UNIVERSITY OF SOUTHAMPTON

FACULTY OF ENGINEERING AND THE ENVIRONMENT

National Centre for Advanced Tribology at Southampton (nCATS) and Fluid Structure Interaction research groups

Ultimate Strength and Mechano-Electrochemical Investigations of Steel Marine Structures subject to Corrosion

by

Yikun Wang

Thesis for the degree of Doctor of Philosophy

April 2015

UNIVERSITY OF SOUTHAMPTON

ABSTRACT

FACULTY OF ENGINEERING AND THE ENVIRONMENT

National Centre for Advanced Tribology at Southampton (nCATS) and Fluid Structure Interaction (FSI) research groups

Thesis for the degree of Doctor of Philosophy

Ultimate Strength and Mechano-Electrochemical Investigations of Steel Marine Structures subject to Corrosion

Yikun Wang

It is well known that ageing steel marine structures are susceptible to corrosion in its all manifestations. The most critical areas are cargo and ballast tanks of merchant ships. However, due to the regulations such as the Performance Standard for Protective Coatings, which requires a 15-year target life of coating in ballast tanks, plus the cathodic protection systems, the internal structures within cargo holds have become more problematic but poorly studied. In the underdeck area and bottom plating, the structures are not normally fully protected. Also, the complex structural arrangement may place difficulties in inspection and repair. In extreme cases, it has been reported that the corrosion rate in these areas could be 5 to 7 times higher than a normal value, and has led to catastrophic structural failures. Currently, the classification societies apply both visual and gauging methods for corrosion inspection during ship surveys. However, it is time consuming especially for large vessels and is highly experience dependent. Therefore, to improve the survey efficiency, facilitate economical maintenance decisions, and even extend the structural life, it is essential to investigate the ultimate strength of such aged and corroded steel structures. Based on the identification of existing corrosion issues in cargo tanks of oil tankers and bulk carriers and the state-of-art of corroded marine structural strength assessments, a nonlinear finite element method was adopted to investigate the influences of pitting and grooving corrosion on the structural integrity. Two full-field experimental techniques were used for a complete validation of the numerical models. Based on the repair conditions provided by classification societies, the numerical results showed that 25% locally corroded area of a plate (800 mm × 800 mm × 15 mm) with 3.75 mm remaining thickness may reduce the ultimate strength by up to 20% compared to a uniformly corroded plate. The weld-induced grooving corrosion of a width of 59 mm and a remaining thickness of 3.75 mm would cause up to 26% strength capacity reduction for a stiffened plate (4750 mm × 950 mm × 15 mm). Moreover, it was shown

that the corrosion depth had a greater influence on structural performance compared to corrosion area for the same volume/material loss. By combining mechano-electrochemical protocols with the stress and strain results obtained from the modelling, it enables predictions of the 'hot spot' locations of mechanically-induced corrosion acceleration. Results showed that the anodic current density inside grooving corrosion damage (24 mm in width and 3.75 mm in depth) was 7 times greater *vis-a-vis* the unstressed condition for the stiffened plate at its ultimate strength state. The results, which are closely related to the industrial corrosion inspection and repair requirement, will not only benefit the shipping industry, but are also applicable to a whole range of marine structures (offshore platforms and steel bridges).

Table of Contents

List of tables

List of figures

DECLARATION OF AUTHORSHIP

I, Yikun Wang

declare that this thesis entitled:

Ultimate Strength and Mechano-Electrochemical Investigations of Steel Marine Structures subject to Corrosion

and the work presented in it are my own and has been generated by me as the result of my own original research.

I confirm that:

1. This work was done wholly or mainly while in candidature for a research degree at this University;
2. Where any part of this thesis has previously been submitted for a degree or any other qualification at this University or any other institution, this has been clearly stated;
3. Where I have consulted the published work of others, this is always clearly attributed;
4. Where I have quoted from the work of others, the source is always given. With the exception of such quotations, this thesis is entirely my own work;
5. I have acknowledged all main sources of help;
6. Where the thesis is based on work done by myself jointly with others, I have made clear exactly what was done by others and what I have contributed myself;
7. Parts of this work have been published as:
   (1) Wang, Y., Wharton, J.A. and Shenoi, R.A. (2014) Ultimate strength analysis of aged steel-plated structures exposed to marine corrosion damage: A review, Corrosion Science, 86: 42-60 (doi: 10. 1016/j.corsci.2014.04.043).
   (2) Wang, Y., Wharton, J.A. and Shenoi, R.A. (2014) Influence of localised pit distribution and bench-shape pits on the ultimate compressive strength of steel plating for shipping, CORROSION, 70: 915-927 (doi:http://dx.doi.org/10.5006/1223).

(3) Wang, Y., Wharton, J.A. and Shenoi, R.A. (2014) Ultimate strength assessment of steel stiffened plate structures with grooving corrosion damage, Engineering Structures, 94: 29-42 (doi: 10.1016/j.engstruct.2015.02.028).

(4) Wang, Y., Wharton, J.A. and Shenoi, R.A. (2014) Ultimate strength and mechanoelectrochemical modelling of corroded steel structural members, Corrosion Science (Submitted).

(5) Sultana, S., Wang, Y., Sobey, A.J., Wharton, J.A. and Shenoi, R.A. (2014) Influence of corrosion on the ultimate collapse strength of steel plates and stiffened panels, Engineering Structures (Submitted).

(6) Wang, Y., Wharton, J.A. and Shenoi, R.A. (2014) The influence of localised pit distribution and bench-shape pits on the ultimate compressive strength of ship platings, Poster, University of Southampton Engineering and the Environment Theme Conference, Southampton, UK.

(7) Wang, Y., Wharton, J.A. and Shenoi, R.A. (2014) The influence of localised pit distribution and bench-shape pits on the ultimate compressive strength of ship plating for shipping, in Proceedings of NACE (National Association of Corrosion Engineers) CORROSION 2014 Conference and Expo, San Antonio, US.

(8) Wang, Y., Wharton, J.A. and Shenoi, R.A. (2013) The influence of localised pit distribution and bench-shape pits on the ultimate compressive strength of ship platings, Poster, Postgraduate Conference, Southampton, UK.

(9) Wang, Y., Wharton, J.A. and Shenoi, R.A. (2013) The influence of localised pit distribution on the ultimate strength of ship structural members, in Proceedings of 4th International Conference on Integrity, Reliability & Failure, Funchal, Portugal.

(10) Wang, Y., Wharton, J.A. and Shenoi, R.A. (2013) Influence of ultimate strength on aged and corroded ships, Poster, FSIRG Away Day, Southampton, UK.

Signed: …… ……..

Date: ……19th Dec 2014……..…

Acknowledgements

The author would like to thank Dr Julian Wharton and Prof. Ajit Shenoi at the University of Southampton, without whose support and time this project would not have been possible. The author would also like to thank Dr Brian Mellor for his critical comments and advice at the nine-month and transfer viva, which helped progress the research in the best direction. Thanks also go to Dr James Underwood and Dr Mamadou Bah for their suggestions (or indeed a piece of coding) on the FEA modelling from scratch. The author would like to thank Wei Wang, Dr Andy Robinson, Dr Tim Woolman, Haibin Zhu, Dr Dan Bull, Dr Jurgita Zekonyte and the Engineering Development and Manufacturing Centre team at the University of Southampton for the training, advice and manufacture for the experimental work.

The author would also like to thank her parents for being finantially but more importantly mentally supportive throughout this research, for cheering her progress and consoling her demorilasation. Thanks are also due to Benjamin Paget-Woods, Yang He, Binyan He, Rong Jiang, Martin Evens, Richard Critchley, Feifei Zhang, Pawee Kucita and Le Zhong for the parties and laughters, which enriched the three-year research life.

Last but not least the author would like to acknowledge the University of Southampton and Lloyd's Register Foundation Univeristy Technology Centre (LRF UTC) for their sponsorship; as well as the meeting with David Howarth and Richard Dawson in the Lloyd's Register.

Nomenclatures

α	Structural aspect ratio
$\bar{\alpha}$	Coefficient describing of mobile dislocation density dependence on strain (10^9 and 10^{11}) / cm^{-2}
α_T	Coefficient of thermal expansion / K^{-1}
β	Slenderness ratio
$\Delta\gamma$	Plastic shearing strain
$\Delta\varepsilon$	Macro plastic strain
ε_x	Strain in *x*-direction
κ^2	Shear correction factor
λ	Column slenderness ratio
λ_e	Effective column slenderness ratio
λ_y	Ratio between the transverse and longitudinal in-plane stresses
ν	Poisson's ratio
ρ	Density of the material / kg m^{-3}
σ_1	1st principal stress / MPa
σ_2	2nd principal stress / MPa
σ_3	3rd principal stress / MPa
σ_{cr}	Critical buckling strength / MPa
σ_E	Elastic buckling stress / MPa
σ_F	Generalised yield stress in Jonson-Ostenfeld formula / MPa
σ_m	Spherical stress in the solid phase / MPa
σ_{max}	Maximum von Mises stress/ MPa
σ_n	Nominal axial compressive stress / MPa
σ_{rc}	Compressive residual stress / MPa
σ_{rt}	Tensile residual stress / MPa
σ_u	Ultimate strength for a structural member with corrosion / MPa
σ_{u0}	Ultimate strength for a structural member without corrosion / MPa
σ_y	Yield stress of the material / MPa
$\Delta\tau$	Hardening / MPa
υ	Orientation-dependent factor
$\Delta\varphi_{Total}$	Total change in the equilibrium potential of a stressed electrode / V
$\Delta\varphi_e$	Change in the equilibrium potential of an elastically stressed electrode / V
$\Delta\varphi_p$	Change in the equilibrium potential of a plastically stressed electrode / V

a	Plate length / mm
A	Cross-sectinoal area of a structural member / mm^2
A_0	Original cross-sectional area / mm^2
$A_{0\mathrm{m}}$	Normalised deflection amplitude / mm
A_r	Smallest cross-sectional area after corrosion / mm^2
b	Plate width / mm
b_e	Effective width of the plating / mm
b_f	Flange width / mm
B	Width between two longitudinal girders / mm
C_p	Specific heat at a constant pressure
d_∞	Long-term thickness of the corrosion wastage / mm
$d(t)$	Mean value of the thickness reduction / mm
D	Flexural rigidity of a plate / GPa
D_M	Moulded depth / m
E	Young's modulus / GPa
E_t	Tangent modulus / GPa
F	Faraday constant / C mol^{-1}
g	Grid spacing
G	Shear modulus / GPa
h_w	Web height / mm
i_a	Anodic current density of a stressed electrode / A m^{-2}
$i_{\mathrm{a}0}$	Anodic current density of a non-stressed electrode / A m^{-2}
I	Moment of inertia / mm^4
J_2	2nd deviatoric component of the Cauchy stress tensor
k	Boltzmann constant for a system of particles representing unit dislocations / J K^{-1} cm
K	Thermoelastic constant of a material
K_t	Effective stress concentration factor
L	Vessel length / m
m	Corresponding half-wave numbers in the *x*-direction
ΔN	Increase in the dislocation density at the hardening / cm^{-2}
N_0	Dislocation density when no hardening / cm^{-2}
N_max	Maximum possible dislocation density / cm^{-2}
n	Number of dislocation in planar pile-ups
P	External load / N
r	Radius of gyration / mm

r_0	Initial corrosion rate in Melchers' model / mm y^{-1}
r_1	Radius of inner pit / mm
r_2	Radius of outer pit / mm
r_a	Accelerated corrosion rate in Melchers' model / mm y^{-1}
R	Gas constant / J mol^{-1} K^{-1}
R_a	Surface roughness / mm
$ROTX$	Rotation about *x*-direction / rad
$ROTY$	Rotation about *y*-direction / rad
t	Structural service time / y
t_0	Original plate thickness / mm
t_1	Remaining thickness of inner pit / mm
t_2	Remaining thickness of outer pit / mm
t_a	Changeover time from oxidation to anaerobic condition in Melchers' model / y
t_f	Flange thickness / mm
t_{gc}	Remaining thickness due to grooving corrosion / mm
t_p	Thickness reduction due to pitting corrosion / mm
t_w	Web thickness / mm
T	Absolute temperature / K
T_0	Coating duration (no corrosion) / y
T_A	End of corrosion acceleration in Qin and Cui's model / y
T_{cr}	Critical buckling load / kN
T_L	End of corrosion deceleration in Qin and Cui's model / y
T_t	Transition time in corrosion prediction models / y
UX	Translation in *x*-direction / mm
UY	Translation in *y*-direction / mm
UZ	Translation in *z*-direction / mm
RS	Residual stress / MPa
U	Position along the length of the stiffener / mm
ΔV	Volume loss due to corrosion / mm^3
V_0	Initial plate volume / mm^3
V_m	Molar volume / m^3 mol^{-1}
V_x	Displacement vectors in *x*-direction
w_{0cm}	Maximum column-type initial deflection / mm
w_{0plm}	Maximum plate initial deflection / mm
w_{0sm}	Maximum sideways initial deflection / mm
w_c	Column-type initial deflection / mm

w_{gc}	Groove width / mm
w_{pl}	Plate initial deflection / mm
w_s	Sideways initial deflection / mm
z	Number of electrons within the partial electrochemical reaction

ABS	American Bureau of Shipping
AFM	Atomic force microspocy
APDL	ANSYS parametric design language
AS	Annual Survey
CCD	Charge-coupled device
CL	Correlation length
CSR	Common Structural Rules
CVI	Close Visual Inspection
DIC	Digital image correlation
DNV	Det Norske Veritas
DOF	Degrees of freedom
DOP	Degree of pitting
DWT	Deadweight tonnage
FEA	Finite element analysis
FI	Full integration
FPSO	Floating production storage and offloading
GVI	General Visual Inspection
HAZ	Heat-affected zone
IACS	International Association of Classification Societies
IMO	International Maritime Organisation
IS	Intermediate Survey
LR	Lloyd's Register
LSM	Least squares matching
MIC	Microbiologically-induced corrosion
MWHC	Maximum water holding capacity
PIF	Plate-induced failure
RMS	Root mean square
PSC	Plate-stiffener combination
PSPC	Performance Standard for Protective Coatings
RI	Reduced integration

SKPFM	Scanning Kelvin probe force microscopy
SEM	Scanning electron microscope
SIF	Stiffener-induced failure
SPM	Stiffened panel model
SRB	Sulphate-reducing bacteria
SS	Special Survey
TSA	Thermoelastic stress analysis
TSCF	Tanker Structure Co-operative Forum
VLCC	Very large crude carrier
ULS	Ultimate limit state

Chapter 1 Introduction

1.1 Background

Ever since the Roman philosopher Pliny (AD 23-79) tried to explain the rust on iron weaponry metaphysically, corrosion has been considered to be financially costly, a waste of natural resources and life-threatening. Marine platforms (ships and offshore structures) and steel bridges are at higher risk of corrosion, particularly after 15 to 20 years in service. Apart from the aggressive environment (temperature fluctuation, service stress, relative humidity, seawater et cetra), the cargoes on-board ships, including iron ore, coal and crude oil can also be corrosive. Catastrophic incidents such as Erika in 1999 [1] and Castor in 2000 [2] have highlighted the on-going corrosion issues.

For shipping alone, in 2011 the total cost of corrosion over the world is estimated to be \$7.5 billion y^{-1} for new construction and \$5.4 billion y^{-1} for repair and maintenance [3]. The primary areas of corrosion occurrence aboard steel-based ships are ballast water tanks, cargo holds, external hulls, machinery, piping systems and super structures, among which the ballast tanks and the cargo holds in oil tankers and bulk carriers are found to be the most susceptible to corrosion damage. Due to the increase in the size and complexity of modern marine structures, the use of high-tensile steels and the ballast water exchange practices, difficulties have been established in the coating application/maintenance, corrosion inspection and material coupling. As a result, localised corrosion has become the dominant corrosion type. For the Castor failure [2], it was reported that in the ullage space (under deck area), localised 'super-rust' was observed with the corrosion rate being 5 to 7 times higher than the normal value (0.1 mm y^{-1}) (Figure 1.1); 65% of the deck plating and longitudinals were corroded away. In addition, severe corrosion may be found in the heat-affected zone (HAZ) along welds. In 2008, a 5 m vertical crack was found on the side of a 26-year-old bulk carrier, resulting in severe leakage (300 m^3 h^{-1} water ingress) [4]. The probable cause of this incident was reported to be the grooving corrosion at the joint of the stiffener and the plate (Figure 1.2), which had been left unattended over years and ultimately led to a crack to propagate. Severe localised corrosion attack has also been observed on the bearing stiffeners of steel bridges [5]. Since corrosion can lead to material degradation, crack initiation/propagation, brittle fracture and unstable failure [6], the structural integrity can be reduced considerably. The finite element analysis (FEA) conducted by Paik et al. [7] showed that 30% area of through-thickness pits would reduce the ultimate strength of a steel plate (800 mm × 800 mm × 15 mm) by up to 50%.

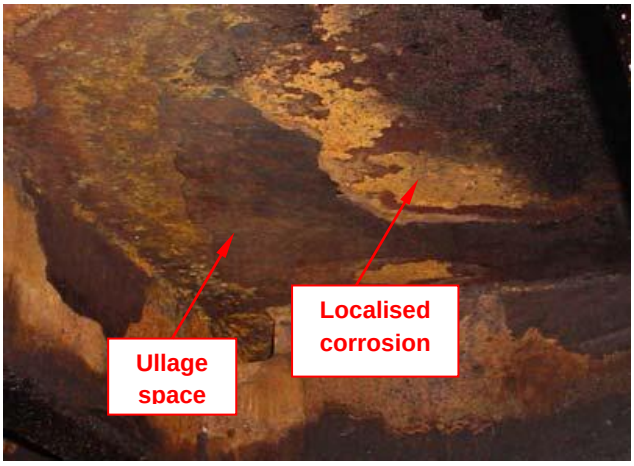

Figure 1.1. Corrosion on the under deck plate surface of a crude oil tanker [3].

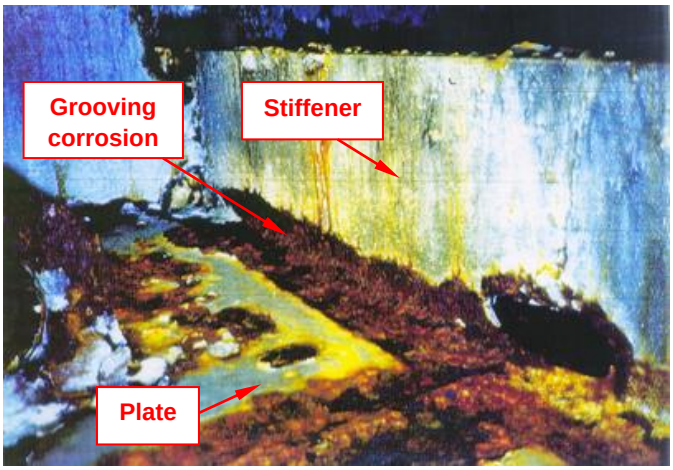

Figure 1.2. Grooving corrosion observed on a stiffened panel inside a ballast tank [4] (typical height of the stiffener: 138 mm to 580 mm).

Due to the ever-increasing concerns about the safety at sea, more regulatory agencies are involved in the design, operation and maintenance of marine structures [8]. Specifically, classification societies, which are led by the International Association of Classification Societies (IACS), establish regulations. Flag states are responsible to enforce the regulations by carrying out periodic surveys to guarantee that a vessel is in a well maintained condition. Also, the International Maritime Organisation (IMO) plays an important role aiming to enhance the efficiency of safety improvement at an international level. The Enhanced Survey Programme was developed as a set of guidelines particularly for inspections of bulk carriers and oil tankers. Organisations such as the Tanker Structure Cooperative Forum (TSCF) issued by IACS were established at an industrial level for general cargo ships and bulk carriers.

The design of ship scantlings are required to contain a certain corrosion allowance for the potential corrosion wastage. The value of the corrosion allowance varies depending on the vessel type and the structural location, and may not be reduced due to the presence of a coating. Classification societies have regulated the corrosion waste allowances together with repair methods. The Common Structural Rules (CSR) require that the strength of local structural members is assessed using the required net thickness and to deduct half the corrosion addition for assessing the hull girder ultimate strength. This approach, termed 'net scantling approach', is aiming to ensure that the structures meet the minimum strength requirement. However, the assessment criteria are somewhat different for every classification society. Also, the CSR is currently only applied for oil tankers and bulk carriers. In terms of corrosion protection systems, regular surveys may be required in association with visual inspections (guided by coating failure diagrams) and ultrasonic thickness measurements when the coating is not considered to be in a satisfactory condition. At present, the typical requirement is a five-point pattern (five thickness measurements per m^2) per plating during a survey [9]. Regardless of any inspection errors, the density of readings could lead to thousands of measurements for a ship hull (internal and external) and hence it is a highly time-consuming process.

Therefore, to improve the survey efficiency, facilitate economical maintenance decisions, and even extend the structural life, it is becoming essential to investigate the ultimate strength (strength capacity) of such aged and corroded steel structures based on a comprehensive understanding of the corrosion mechanisms in marine environment.

1.2 Aims and objectives

This research aims to explore the interactions between mechanical and electrochemical performances of thin-walled steel structures subject to corrosion damage in marine environments.

In order to achieve the research aim, the following objectives have been developed:

(1) Undertake a comprehensive literature review including: marine corrosion mechanisms; corrosion prediction; methods to assess the corrosion-induced strength degradation; mechano-electrochemical performance on a metallic surface and classification society regulations for corrosion inspection/repair;
(2) Conduct a systematic validation of the nonlinear FEA modelling technique via eigenvalue buckling analysis and replication of models from the literature;

(3) Utilisation of full-field experimental methods to examine the elastic and plastic stress/strain on the surface of steel samples with idealised corrosion features;
(4) Develop a nonlinear finite element model to assess the mechanical behaviour (stress/strain concentrations and ultimate strength) of local steel structures (plate and stiffened plate). The studied parameters are as follows:
    (a) Pitting and grooving corrosion features;
    (b) Initial deflections;
    (c) Weld-induced residual stresses;
    (d) Weld connection imperfections (root opening).
(5) Develop a numerical method based on analytical formulas for a multi-component stress condition to predict corrosion acceleration ‘hot spots’ induced by mechanical stress and deformation, as well as to quantify the corrosion rate increment.

Chapter 2 Literature review

2.1 Corrosion in the marine environment

2.1.1 Corrosion classification

Corrosion is defined as the degradation of a metal by an electrochemical reaction with its surrounding environment [10]. There are a number of corrosion types. Specifically, within the maritime engineering, DNV (Det Norske Veritas) suggests that corrosion may be divided into the following four types [11]:

General corrosion: the degradation is uniformly distributed on the surface of a metal.

The corrosion mechanisms of carbon steels in marine environments have been extensively studied and discussed in Refs. [10,12,13]. General corrosion may be found in the ullage space in cargo oil holds due to the volatile gas diffused from the crude oil [3]. It is currently required to maintain an oxygen level below 5% to avoid combustion of hydrocarbons [3]. However, other corrosive gas such as SO_3, SO_2 and CO_2 are not required to be controlled. Once a condensation film or dew is formed on the deck plate as a result of temperature fluctuations, the corrosive gas can dissolve in this water layer and create an acidic environment to corrode steel. Moreover, H_2S from the oil may also be a source of hydrogen ions and react with iron to form sulphide compounds, which will further react with oxygen to generate iron oxides and sulphur. Corrosion product as a combination of rust and sulphur may detach from the plating and expose a fresh steel surface, which could lead to further accelerated corrosion.

The lower stools of a bulk carrier may also be prone to general corrosion, since they are normally left uncoated [14]. According to Ref. [14], the detection of FeOOH and iron sulphate compounds indicated the presence of chloride and sulphate anions, which were believed to be from the coal cargoes. The overall cathodic reaction was determined by the pH level of the moisture within the cargo holds. The pH value is dependent on the relative rates of the supply of pyrite (FeS_2) and carbonates (mainly $CaCO_3$) from the coal [15]. Compared to coal, iron ore is usually transported in a dry state and the only corrosive element is sulphur but in a minor concentration (normally less than 0.1%) [16]. However, corrosion can occur if the structural surface is wetted, for instance from cleaning

operations. The resulting contact between the steel surface and iron ore particles may lead to differential aeration zones and form distinct anodic and cathodic regions.

Pitting corrosion: randomly distributed corrosion area (tens of millimetres in diameter) with localised material degradation.

In ships, pitting is usually in association with a protective coating breakdown [17], ineffective cathodic protection systems, or bacterial activity under anaerobic conditions. Particularly, the bacterial corrosion or microbiologically-induced corrosion (MIC) was first observed by Southwell et al. [18] based on a 16-year immersion test of steels in the Panama Canal. For an anaerobic environment and sufficient nutrients (including iron, organic carbon and nitrogen) in the rust after a period of immersion, sulphate ions may be reduced to sulphide ions during the metabolism of anaerobic bacteria (90% being sulphate-reducing bacteria (SRB)). The metabolites (typically hydrogen sulphide) can be very aggressive to most metals including iron/steel, and may lower the pH to 2 [19] in the ambient environment. It is believed that there are also interactions between SRB and other bacteria, which provide nutrients and maintain the cycling of sulphur [20]. The SRB activities were also observed in the very early stage of immersion due to the development of localised anaerobic conditions in quickly colonised biofilms [21]. However, the influence on steel is negligible [21].

Pitting corrosion is more likely to occur on the bottom plating of cargo oil tanks and horizontal surfaces in ballast tanks [22,23]. A layer of water (condensate or from the oil production process) is normally found at the bottom of cargo oil tanks. The quantity of this water layer may be up to 20% of the total tank volume, and can be highly corrosive. Although the bottom plates may be covered in a thin layer of oil which can behave as a protective coating, severe localised corrosion will occur once this layer is thinned or damaged. However, according to Ref. [3], it is the MIC that dominates the corrosion process in these areas. Condensate water with low oxygen levels and various chemical nutrients provides an ideal anaerobic condition for bacteria to proliferate. In addition, the warm oil and heating facilities (typically 44℃ to 66℃ for oil transfer operation) also contribute to the bacterial corrosion, since it has been found that temperature between 20℃ and 50℃ is the optimum condition for SRB metabolisms [22]. Conversely, a three-year study conducted by Katoh et al. [24] showed that the pH inside pits ranged from 2 to 4, which was too low for MIC to occur. However, they failed to provide an explanation of the pitting mechanism.

In terms of the horizontal surfaces with a protective organic coating (commonly a coal tar epoxy) in a ballast tank, blisters may occur when moisture and oxygen penetrate through the film or soluble materials leach out from the coating. Water and contamination will accumulate at the interface of the coating and steel, and force the polymeric film to form either a neutral or alkaline blister. When neutral blistering occurs, a differential aeration cell at the interface [25] may be established, resulting in localised corrosion underneath. An alkaline blister is formed when cations such as Na^+ accumulate at the interface and react with hydroxyl ions (OH^-) in the cathodic area. In this case, pits are unlikely to form in this region due to the highly alkaline blister fluid, unless the blisters are mechanically damaged [26].

Grooving corrosion

Grooving corrosion (also referred to as preferential weld line corrosion, knife-line or trench-like corrosion), is a selective and rapid damage along a weld joint (Figure 2.1) [11] and [27]. This effect is from time to time referred to as “necking”. It may be caused by the galvanic current generated due to the difference of the metallographic structure between the welds, HAZ and the base metal. Also, coating of the welds is generally less effective. Figure 2.2 shows the 3D surface of a butt-welded steel plate. The weld imperfections (spatter) subsequently mean a thickness fluctuation of an applied protective coating, and hence exacerbate corrosion [28]. In addition, the increased deformation of a corroded stiffener may cause coating break-off. Grooving corrosion was also observed on the weld [27]. Manganese sulphide (MnS) inclusions were reported to develop preferentially in the weld due to the rapid heating and cooling for carbon steel [27]. The surrounding sulphide-enriched portion was anodic to MnS and induced grooving corrosion [27]. During welding, the base metal is likely to expand and be restrained by the adjacent metal. On cooling, local shrinkage will induce high residual tensile stresses. Further discussion specifically addressing this mechanical stress effects on grooving corrosion will be reviewed in Section 2.3. It can be seen that welding will introduce a number of variables to the corrosion mechanism. However, little literature has been found related to the weld-induced or residual-stress-induced corrosion process of ship structures.

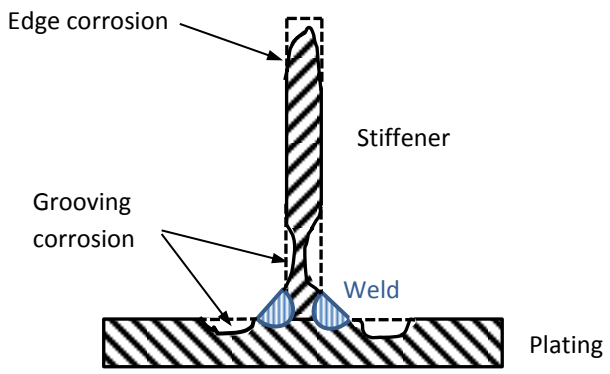

Figure 2.1. Schematic of grooving and edge corrosion on the cross-section of a stiffened plate.

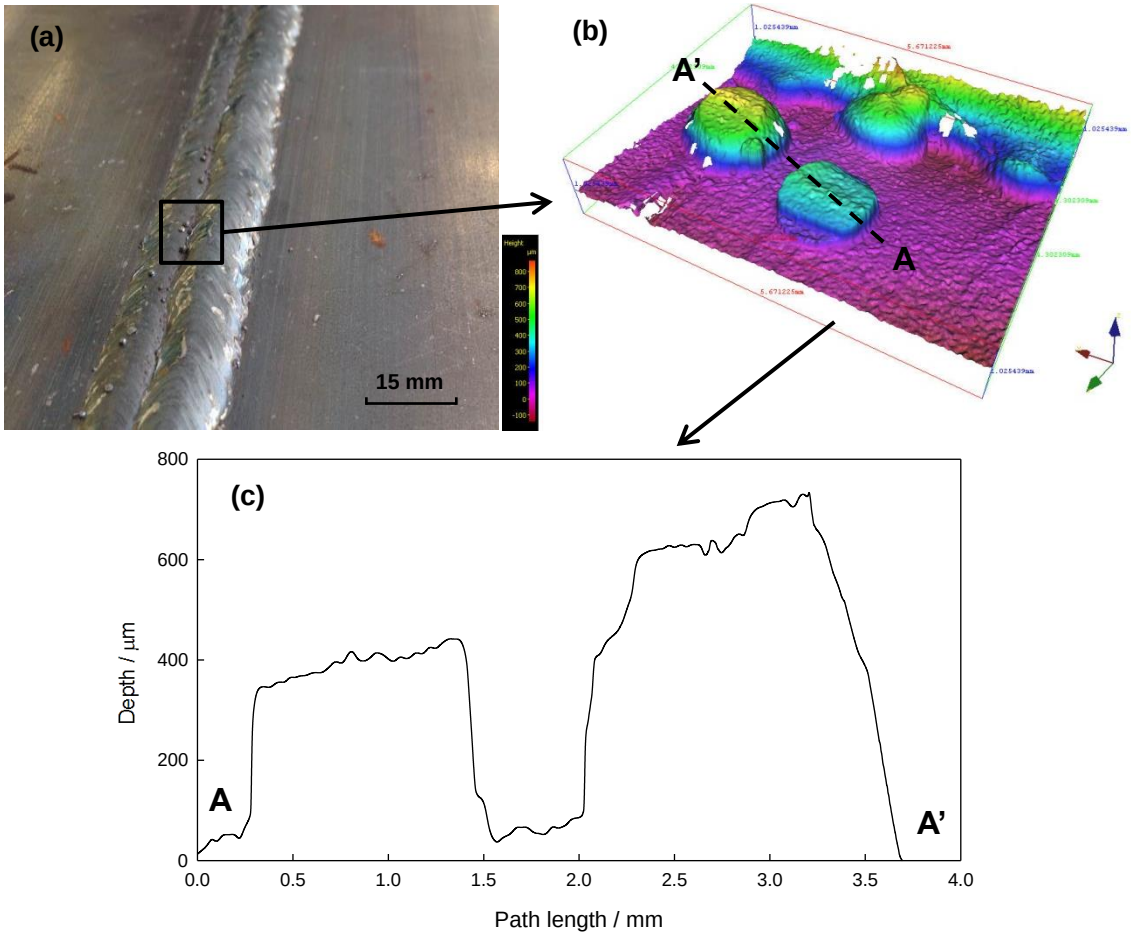

Figure 2.2. Imperfections on the butt welds of a ship grade steel plate: (a) welded plate sample; (b) three-dimensional surface profilometry (scan area: 5.7 mm × 4.3 mm); (c) profile along Line A-A'.

Edge corrosion

Edge corrosion is normally found at the free end of stiffeners and around cut outs (Figure 2.1). The complex structural geometry may result in a thinner coating, which makes these regions more vulnerable to corrosion.

2.1.2 Corrosion configuration

In recent strength assessments considering corrosion attack [29-31], researchers have found that the random distribution of thickness diminution over the structural surface may markedly reduce its strength compared to that of the hypothetically uniformly corroded structures. Thus, a localised corrosion pattern is considered significant for a more accurate strength capacity estimate.

In 2007, a series of corrosion morphologies on mild steel coupons were published [21]. The coupons were immersed in sub-tropical coastal seawater for up to 36 months. The most interesting finding was the development of bench-shape broad pits due to the SRB activities in long-term immersion (Figure 2.3). Such corrosion damage was also found on the inner bottom plating of a 15 to 16 years old bulk carrier (Figure 2.4), where broad pits with vertical walls can be readily observed.

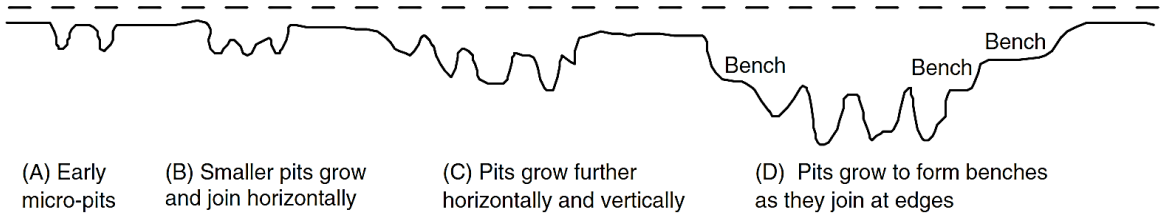

Figure 2.3. Sketch of the development of the bench-shape broad pits [21].

The corrosion configuration is also largely dependent on the coating condition. According to TSCF [32], tank bottom structures with a zinc coating showed patches of scaly areas with only minimal thickness loss, while for coal tar epoxy coated tanks, deep conical pits were observed within limited areas. For coal tar epoxy coated hold frames of bulk carriers, Nakai et al. [33] reported that conical pits appeared initially, followed by a general damage of the surrounding regions. The ratio of pit diameter to depth ranged from 8 to 10 with the maximum diameter observed being 50 mm. Figure 2.5 shows the pitted area (black shade) on a web plate with the cross-sectional view of the pits. Due to the complexity of the marine environment and the different corrosion protection systems, it is increasingly

challenging to identify and even to simplify the most common corrosion pattern for a steel structure.

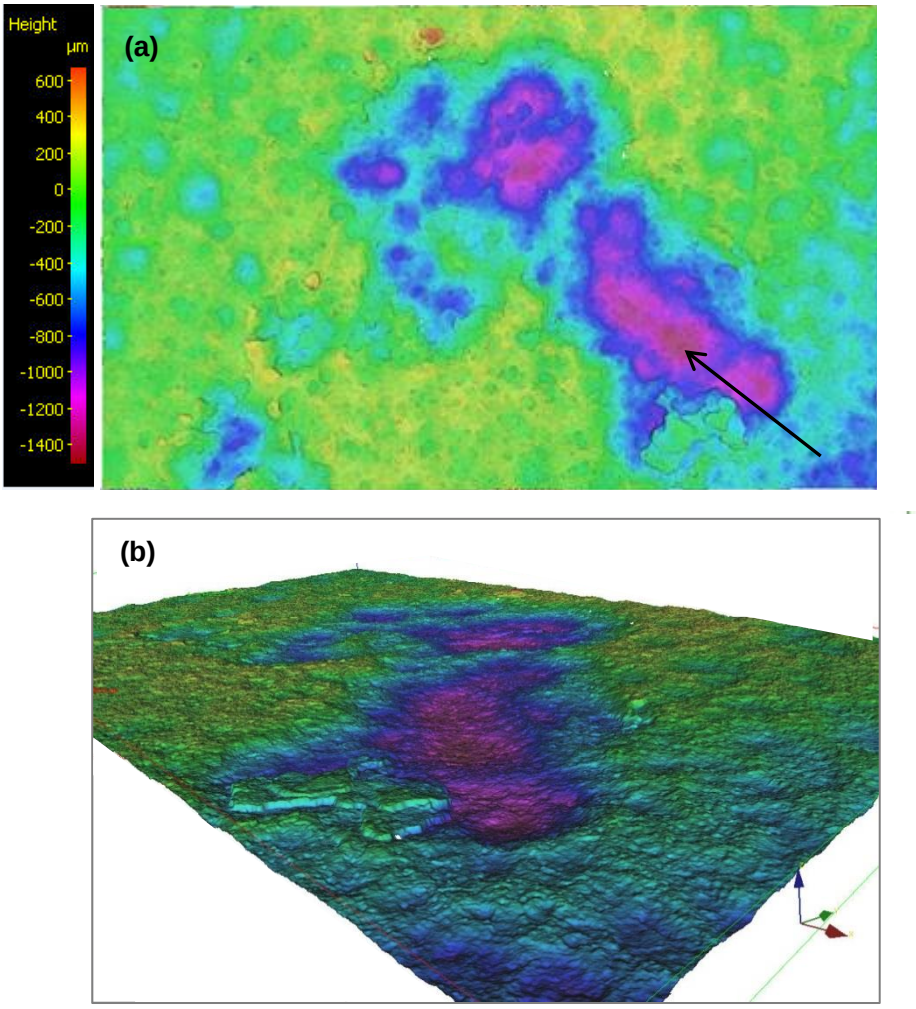

Figure 2.4. Surface profilometry of bench-shape broad pits on the inner bottom plating of an aged bulk carrier: (a) two-dimensional top view; (b) three-dimensional view of a pit along the direction of the arrow in (a). Scan area: 6 mm × 4 mm.

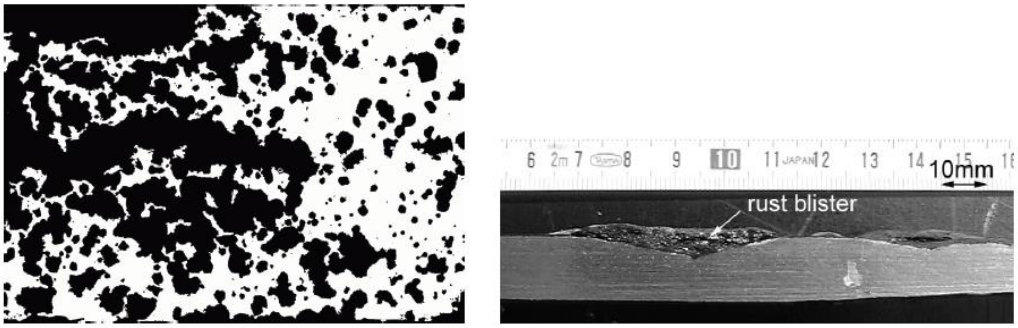

Figure 2.5. Pitting area (left) and the cross section view (right) on a web plate of a hold frame in a bulk carrier [33] (scan area: 500 mm × 700 mm).

2.1.3 Corrosion prediction

Either at the early design stage or under the operation/maintenance condition, it is essential to predict the potential corrosion damage for a safer scantling design and an adequate protection system. The parameter, corrosion rate (mm y^{-1}), defined as the material degradation with time, has therefore been extensively examined on marine structures. Typical corrosion rates of steel structures in a ship hull are listed in Table 2.1 [3,34,35]. It can be seen that the corrosion rate may vary over a wide range, indicating high variance in the corrosion processes. In this section corrosion prediction models based on either collected data or first principles will be summarised and critically assessed, along with a summary of influencing factors.

Table 2.1. Typical corrosion rates of ship steel structures

Conditions	Corrosion rate / mm y^{-1}
Immersed steel specimens in seawater	0.05 - 0.20
Ballast tank	0.046 - 0.289
Crude oil tank	0.08 - 0.21
Ullage space in cargo oil tanks	0.24 - 5.00
Uncoated bottom plate in cargo oil tanks	2.00 - 3.00
Main frames in bulk carriers	0.30
Coated tank bottom	Up to 9.00

2.1.3.1 Corrosion database

Due to the difficulties in extrapolating laboratory data to a large structure/time scale, corrosion measurements collected from a ship survey is of great importance and more practical to help predict the corrosion damage. However, only a limited number of corrosion data sets are currently available in the published literature, mainly from bulk carriers (Table 2.2) and oil tankers (Table 2.3). Paik and Kim published a set of corrosion measurements from ballast tanks of ships aged 11 to 27 years old [36] but without indicating the presence of a coating. In addition, the corrosion data for double-hull oil tanker is lacking, thus leading to errors in attempting to predict corrosion of this vessel type using data from single-hull tankers, which have been phased out since the 1990s.

Table 2.2. Corrosion data sets for bulk carriers

Year	1998 [37]	2003 [38]	2004 [39]	2008 [40]
Number of vessels	44	109	5	3
Ship size		6095 – 138655 DWT	38000 DWT	25000 DWT
Years in service	26	26	25	25
Thickness measurements*	7503	12446	2098	1404
Notes		Include repaired members	Deck plates	Deck plates

*: total number of measurements for all vessels per study.

Table 2.3. Corrosion data sets for oil tankers

Year	1992 [32]	2001 [41]	2003 [42]	2005 [43]
Ship type	Single-hull	Single-hull	Single-hull	Single-hull
Number of vessels	52	197	230	140
Ship size	>150000DWT	100 – 400 m		168 – 401 m
Years in service	25	23	12 - 26	12 – 26, 32
Thickness measurements*		>250000	33820	110082
Notes				Not include scraped ships or the presence of coating

*: total number of measurements for all vessels per study.

2.1.3.2 Corrosion prediction models

From the various corrosion mechanisms and the scattered measurement readings, it seems insufficient to assume a constant corrosion rate as ships age. Thus, a variety of empirical/mathematical models have been proposed. Initially, a linear relationship of corrosion wastage with time was explored by Southwell et al. [18]:

$$d(t) = 0.076 + 0.038t \tag{2.1}$$

where $d(t)$ is the mean value of the thickness reduction (mm) and t is the time (y). Subsequently, a bilinear model was introduced in 1995 by Melchers [34]:

$$d(t) = \begin{cases} 0.09t & 0 < t \leq 1.46 \text{ years} \\ 0.76 + 0.038t & 1.46 < t < 16 \text{ years} \end{cases} \tag{2.2}$$

However, both the linear and bilinear models tend to overestimate the corrosion wastage at the initial stage of exposure [34] and [44], probably due to the exclusion of coating effects. Thus, a modified nonlinear model was proposed [34]:

$$d(t) = 0.084t^{0.823} \tag{2.3}$$

In 1987, Ohyagi [45] reported values of 0.1 mm y^{-1} for the mean corrosion rate and 0.34 mm y^{-1} for the maximum rate based on measurements from 519 different ships. Mateus and Witz [46] compared Ohyagi's model with Melchers' experimental data and found that the actual thickness reduction could be three times more severe than the values from steel specimens. This substantial difference may be due to the anaerobic attack and the iron oxide layer break-off induced by enhanced lateral deflections.

More recently in 1998, Paik and co-workers [37,47] proposed a linear probabilistic model which was later modified [48] by separating the corrosion process into three successive stages: (1) no corrosion: 0 to T_0; (2) transition between coating durability and corrosion initiation: T_0 to $(T_0 + T_t)$; (3) general corrosion. For the third stage, it was suggested that three types of corrosion rate would exist: the convex type (gradual build-up of rust layer will prevent metal from further corrosion); the concave type (likely to happen under dynamically load exposing fresh areas to corrosion); the linear type (rust layer are continually removed due to abrasion or wear). The schematic of the model is illustrated in Figure 2.6.

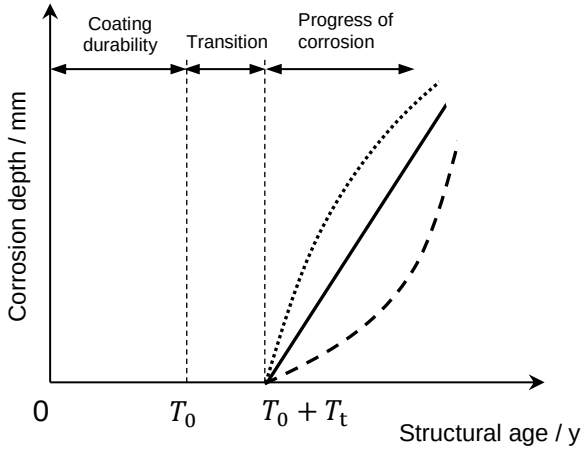

Figure 2.6. The Paik and Thayamballi model [48].

In the Paik and Thayamballi model, the coating duration was estimated using a lognormal distribution [48-50]. Regarding the transition period for bulk carriers, Yamamoto and Ikegami [50] suggested three values for bulk carriers: T_t = 3 y for deep tank bulkheads; T_t = 2 y for watertight bulkheads and T_t = 1.5 y for stools. The corrosion rate is no longer constant:

$$d(t) = C_1(t - T_0 - T_t)^{C_2} \quad (2.4)$$

where C_1, C_2 were obtained based on collected corrosion data. Previous studies have indicated that C_2 may be in the range of 0.3 to 1.5 [34,50], and C_2 = 1.0 or 0.33 could be taken as the usual value at the design stage [47,48]. A Weibull density function was adopted to evaluate C_1 [51]. An example of the model fitting to a set of corrosion measurements on outer bottom plates of bulk carriers can be found in Ref. [48]. However, the actual measruemnts are much more scattered and the maximum corrosion depth could be 4 times higher than the predicted one. Moreoer, it is unrealistic to assume that no corrosion damage occurs during the transition period. Also, it may not be straightforward to determine the starting point of general corrosion period.

In 1999, Guedes Soares and Garbatov [44] proposed a model (Equation 2.5) which also includes no corrosion and transition periods. However, they believed that the corrosion would gradually come to a halt at a depth of d_∞, due to corrosion product accumulation. Any disturbance, or indeed removal, of this oxide layer could lead to a re-initiation of the corrosion process. Figure 2.7 shows the corrosion wastage with time.

$$d(\mathrm{t}) = d_\infty \left[1 - \exp\left(-\frac{t - T_0}{T_t}\right)\right] \quad (2.5)$$

where d_∞ is the long-term thickness reduction (mm), T_0 is the coating life (y) and T_t is the transition time (y).

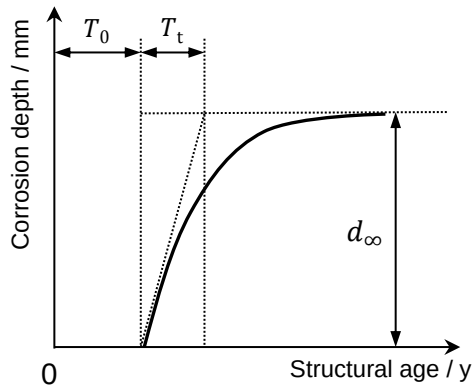

Figure 2.7. The Guedes Soares and Garbatov model [52].

In 2007, Garbatov et al. [52] fitted the Guedes Soares and Garbatov model to a set of corrosion data of cargo tank deck plating of oil tankers provided by the American Bureau of Shipping (ABS). In 2008, this model was used to fit two data sets collected from bulk carrier deck plates [40]. The values of T_0, T_t and d_∞ for different corrosion data sets are summarised in Table 2.4. The corrosion rate in cargo tanks was higher compared to ballast tanks. Also, the coating duration in bulk carriers is generally longer than oil tankers. The transition time for bulk carriers is significantly shorter than that for oil tankers. The standard deviation of the model fitting ranged from 0.2 to 1 mm in general. Nevertheless, fewer data points were used in comparison to Ref. [48]. Ivanov et al. [53] verified the model in Ref. [44] and described the transition period as a linear relation of the thickness reduction with time. However, it is difficult to distinguish the transition period from the third period.

Table 2.4. Parameters for Garbatov et al.'s model

	Structural location	T_0 / y	T_t / y	d_∞ / mm
[44]		1.5 – 15.5	4 - 5	5
[52]	Deck plates of ballast tanks in oil tankers	10.54	17.54	1.85
	Deck plates of cargo tanks in oil tankers	11.49	11.23	1.91
[40]	Hatch cover plates of bulk carriers	15.05	3.27	0.99
	Deck plates of bulk carriers	13 - 13.35	4.8 - 5.51	1.45 - 2.21
	Plates between hatch covers of bulk carriers	13.56	4.3	1.98

Considering that the corrosion mechanism may be very different for short-term exposure compared to long-term, a long-term prediction of corrosion wastage was proposed in Refs. [6,54,55] by adding a weighting factor, which represents the relative duration of different short-term intervals. However, this long-term corrosion model was not further validated due to the lack of suitable measurements.

Qin and Cui [56-58] proposed a more flexible model for marine corrosion of mild steels using a Weibull function (Equation 2.6). Unlike the corrosion process described in Ref. [37] or [44], they believed that after the no corrosion period (0 - T_0), corrosion would accelerate (T_0 - T_A) until general corrosion initiated, and then decelerate (T_A - T_L) over the service life (Figure 2.8). The model can be transformed to the previously published models by applying different parameter values. However, it was fitted to a hypothetical corrosion data set instead of real measurements, which makes it difficult to determine its reliability.

$$d(t) = d_{\infty}\left\{1 - \exp\left[-\left(\frac{t - T_{\mathrm{st}}}{\eta}\right)^{\beta}\right]\right\} \tag{2.6}$$

where d_{∞}, β, η and T_{st} can be determined by the corrosion data.

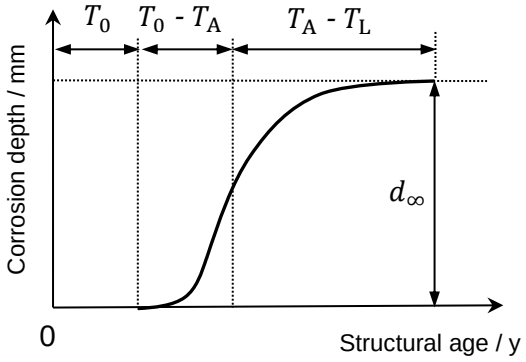

Figure 2.8. The Qin and Cui model [56].

Unlike the empirical models discussed above, which are based purely on corrosion measurements, an alternative multi-phase corrosion model for mild steel at sea immersion conditions has been developed and refined by Melchers and co-workers since 1999, based on a series of *in situ* coupon experiments [12,34,59-66]. They argued that short-term laboratory data would be misleading for estimating the long-term corrosion loss. According to Melchers, the long-term corrosion process can be separated into five phases (shown in Figure 2.9):

Phase 0: corrosion controlled by complex interactions between bacterial colonisation and electrochemical processes; do not affect the long-term corrosion behaviour;

Phase 1: kinetic conditions, where the corrosion rate is controlled by diffusion of oxygen under the concentration gradient adjacent to the metal surface (r_0 is the corrosion rate (mm y^{-1}));

Phase 2: oxygen diffusion controlled period, where corrosion rate declines as the oxygen diffusion is gradually impeded by the built-up of corrosion product (t_{a} is the changeover time from oxidation to anaerobic condition (y));

Phase 3: SRB growth due to the formation of micro-niches in the corrosion deposit layers, especially close to the metal surface (r_{a} is the accelerated corrosion rate (mm y^{-1}));

Phase 4: corrosion rate controlled by the nutrient supply and the rate of loss of corrosion deposits due to mechanical damage.

For the first time a bacterial effect was incorporated in a corrosion prediction model. Via calibration to the collected field experimental data, this model is believed to be able to describe multiple corrosion situations, including mild and low alloy steels in seawater immersion, tidal zone, coastal/inland atmospheric exposure and soil, as well as pitting of stainless steels [20]. Specifically, for ballast and de-ballast operations during a ship voyage, Gudze and Melchers [64] conducted a series of experiments by attaching coupons to the internal surfaces of the ballast tank operations and stated that the model could accurately represent the corrosion loss in ballast tanks. However, in spite of the uncoated condition, the effects of stress and orientation were not appropriately simulated. The coupons were attached to a PVC test pod, which was suspended between the internal stiffeners. As such, the stress state of the coupons cannot reflect the actual condition experienced by internal hull structures. Also, this model has not been checked against actual corrosion data provided by ship surveys.

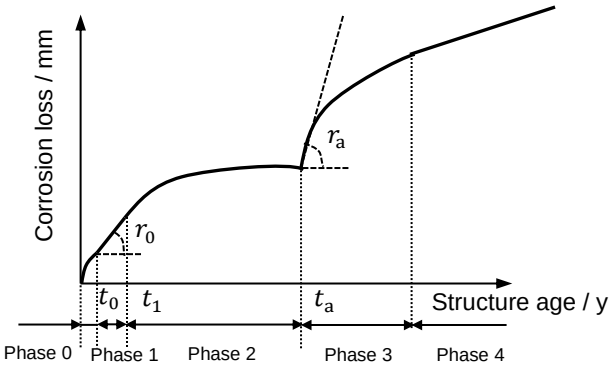

Figure 2.9. The Melchers model [67].

Recently in 2012, an empirical model (Equation 2.7) was reported in Ref. [36], which is based on corrosion measurements collected from ballast tanks of ships aged between 11 to 27 years old. A Weibull function was used to estimate the corrosion depth (pit depth) with time t / y.

$$d(t) = \frac{\alpha}{\beta}\left(\frac{t}{\beta}\right)^{\alpha-1} \exp\left[-\left(\frac{t}{\beta}\right)^{\alpha}\right] \tag{2.7}$$

where $\alpha = 0.002t^3 - 0.0994t^2 + 1.5604t - 6.0025$, $\beta = 0.0004t^3 - 0.0248t^2 + 0.4793t - 2.3812$. By fitting to the same data set as presented in Ref. [48], the standard devisation

was below 1 mm [36]. However, the database used in this study does not indicate the coating condition, for which the authors assumed that the coating life was zero. Due to the requirement for a fully coated condition in ballast tanks by classification societies since 2006 [68], a consideration of coating life is necessary for estimation of corrosion damage at such locations. Also, a validation against other data sets is lacking.

A comparison of the relative performance of the Guedes Soares and Garbatov model (Figure 2.7) and Melchers model (Figure 2.9) was reported in Ref. [69], especially for Phases 3 and 4. The discrepancy increases to 20% between these two models at the long-term corrosion condition. Moreover, it was stated that compared to the Melchers model, which is based on corrosion mechanisms and coupon tests, the Guedes Soares and Garbatov model was more versatile for a wider range of ship type, age and structural locations.

2.1.3.3 Influencing factors

For marine structures, Loseth et al. [70] reported that the corrosion rate would be affected by a host of factors, including material composition, coating, cathodic protection, percentage of time in ballast, relative humidity, frequency of tank washing, temperature, clean or dirty ballast, cargo composition, speed, trade route and composition of inert gas. In addition, salinity, marine fouling, water velocity, mechanical abrasion, local structural flexibility, repair methods, structural location/orientation may also affect the corrosion process [37,48,71-73].

Steel composition

Regarding the influence of the composition and fabrication of ship grade steels on the corrosion rate, it was reported [74,75] that under charge transfer control or even oxygen diffusion control (provided that the diffusion barrier layer remains essentially unchanged), the corrosion rate was unlikely to be affected by the steel composition for common situation for natural sea water. Subsequently, Wang et al. [76] conducted a series of corrosion tests on mild steel, manganese steel and chromium steel in the marine immersion environment and found that carbon, sulphur, manganese and chromium contents in steels may affect the corrosion behaviour. However, to date, the measurements used for corrosion prediction do not specify the constructural materials. Moreover, the corrosion addition values are not determined according to different steel compositions. Therefore, the steel composition is consididered to have minor long-term

effect on the corrosion performance of marine structures [77]. The compositions of frequently used ship grade steels are listed in Table A1.1 in Appendix 1.

Environmental factors

Due to the complexity of the marine environment, it was considered to be important to modify the corrosion prediction models with various environmental factors, some of which have already been repeatedly studied [34,54,67,78,79], including temperature, dissolved oxygen, salinity, pH and water velocity.

The temperature is highly dependent on the trade route. In open seawater, the corrosion rate increases with increasing temperature [80]. If the dissolved oxygen level remains constant, the corrosion rate of low-carbon steel will approximately double for every 30℃ rise [81]. Melchers [67] categorised seawater into moderate temperature and low temperature. For moderate condition, it was observed that the corrosion rate was higher in warmer months. In low temperature seawater (Arctic condition), corrosion tends to increase when the temperature is lower than 5 – 10℃ [82]. However, it is not clearly explained the underlying reason for such corrosion rate change. The influence of temperature is in fact a complex interplay with the oxygen concentration, the diffusion coefficient of oxygen and salinity [77]. Plus, changes in the value and properties of corrosion products may also contribute to the abnormal increase in the corrosion rate at low temperature. A linear relationship between the corrosion rate and the temperature ($< 80℃$) was proposed in Ref. [75]. Apart from its influence on corrosion kinetics and oxygen diffusion, temperature will also affect the bacteria activity. Based on field observations, Melchers and Jeffrey [83] reported that warm surface seawater could lead to higher corrosion loss compared to cold deep water due to the higher metabolism of bacteria. The amount of dissolved oxygen is a function of a series of variables such as temperature, water movement, plant photosynthesis and bacteria activities [75]. In very quiescent waters the corrosion rate can be limited [67]. When oxygen and temperature vary together, as in the actual sea, the oxygen effect tends to be dominant. Reduced oxygen concentration would lead to lower corrosion loss and corrosion rate [83]. Guedes Soares et al. [54] suggested that the oxygen concentration was the major governing factor for corrosion at sea. Linear relationships between dissolved oxygen and the corrosion rate were reported in Refs [67,75]. The salt content in open seawater is normally in the range of 33‰ to 38‰, where S ‰ denotes the weight of dry salts in grams contained in 1000 g of seawater (parts per thousand) [75]. The effect of salinity was reported to be of only marginal importance for corrosion of steels under short-term immersion in seawater

[74,82]. However, greater salinity changes could be found in coastal and brackish areas, which may substantially affect the corrosion rate [80]. It is generally agreed that the surface pH of seawater lies between 8.1 and 8.3 [59,75]. As the depth increases, the pH value may drop due to the decomposition of organisms [59]. Enhanced temperature, pressure and plant photosynthesis may also lead to a change of pH [67,75]. When natural seawater is considered, pH seems to no longer affect the corrosion of carbon steel [80]. Therefore, Guedes Soares et al. [75] assumed that there was no influence from pH between 4 to 10, while Wang et al. [76] reported that the maximum pitting corrosion loss was proportional to pH. In terms of water velocity, many studies have revealed that higher water velocity will lead to an increase in corrosion rate of carbon steel [60,75,84].

Operational factors

Apart from the environmental factors, ship structure corrosion will also be influenced by various operational parameters, such as the corrosion protection condition, percentage of time in ballast, cargo content, tank cleaning and structural orientation.

The efficiency and duration of coating typically depends on the coating type, application details, maintenance and locations. Normally, the thickness of a coating in ships ranges from 200 μm to 500 μm [35]. IMO groups the coating system as types I, II and III, where the corresponding expected duration is 5, 10 and 15 years, respectively. The coating selection is primarily economical orientated. For instance, for ballast tanks and double-side-skin spaces of bulk carriers, 15 years is the recommended target life according to IMO PSPC (Performance Standard for Protective Coatings). In reality, Loseth et al. [70] state that a coal tar epoxy coating life is normally between 8 to 13 years for oil tankers, and 5 years for bulk carriers. Paik et al. [42] used the corrosion data collected from single-hull oil tankers and FPSOs (floating production storage and offloading) and found that the typical coating life was 7.5 years. Wang et al. [43] assumed that the coating life was 5 years in their deck plating analysis of oil tankers. Guo et al. [85] believed that the coating would break down locally when a ship was between 2 to 10 years old. Generally, coating failures start at welds, cut-outs and exposed edges of plating, however, the actual coating life varies significantly. Also, there is little agreement on how to accurately predict coating degradation and the interactions between the influencing factors.

For bulk carriers, due to their long operation period and corrosivity of cargoes, the structural integrity is of great concern. However, sophisticated investigations in the corrosion behaviour are limited [14,37,71]. Corrosion in bulk carriers is highly related to

the on-board cargoes. Paik et al. [37] stated that a bulk carrier typically spent around 40% of the service life carrying coal, 35% carrying iron ore and 20% carrying grain. Cargo coal contains sulphur, high humidity (sometimes at high temperature) and is considered to be the greatest threat to the structures and weld joints in cargo holds. Also, Paik et al. [37] found that the corrosion rate of inner bottom plating was considerably high probably due to the mechanical damage during the loading and unloading of the cargoes. The high corrosion rate of the side shells was thought to be a result of high humidity and/or high temperature of the cargo. Nakai et al. [17] observed that, for a 14-year-old bulk carrier, accelerated corrosion occurred at the lower and middle parts of the coal tar epoxy coated hold frames. A mean corrosion rate of 0.3 mm y^{-1} was recorded at the lower end of the main frames especially towards the hopper tank [22]. In Refs. [14,71], Gardiner and Melchers analysed the characteristic corrosion patterns in cargo holds. The key points are summarised in Table 2.5 based on structural locations.

Table 2.5. Characteristic corrosion patterns in bulk carriers

No	Locations	Corrosion Protective System	Corrosion type	Corrosion rate
1	**Tank top plating**	Upper surface is uncoated; under surface is coated	General corrosion on the upper surface; coating break-down on the under surface (indentation and plate dishing)	Constant general corrosion; coating failure depends on the cargo change frequency
2	**Sideshell frames**	Coated	Localised corrosion	High at the lower bracket connection
3	**Lower stools**	Uncoated or short life coating (2.05 years [51])	Uniformly distributed with thick rust layer	Decreases over time
4	**Corrugated bulkhead plating**	Coated	Corrosion on lower plating is more severe	Vary with vertical position
5	**Ballast tanks**	Coated	Localised coating break-down	Higher in top side tank than double-bottom ballast tank; also depend on the corrosion protection system and tank status

Laboratory tests of mild steel were conducted to investigate the effects of cargo particle size and moisture content on the corrosion rate [15]. It was found that decreasing particle size would increase the corrosion rate, with the maximum corrosion rate at 60% to 80% MWHC (maximum water holding capacity). Also, shipboard experiments [15] in the lower region of a cargo hold in a bulk carrier showed that the mean corrosion rate was 0.1 mm y^{-1} and the standard deviation was 0.014 mm y^{-1}. Typical trends of corrosion rate with the MWHC are shown in Figure 2.10.

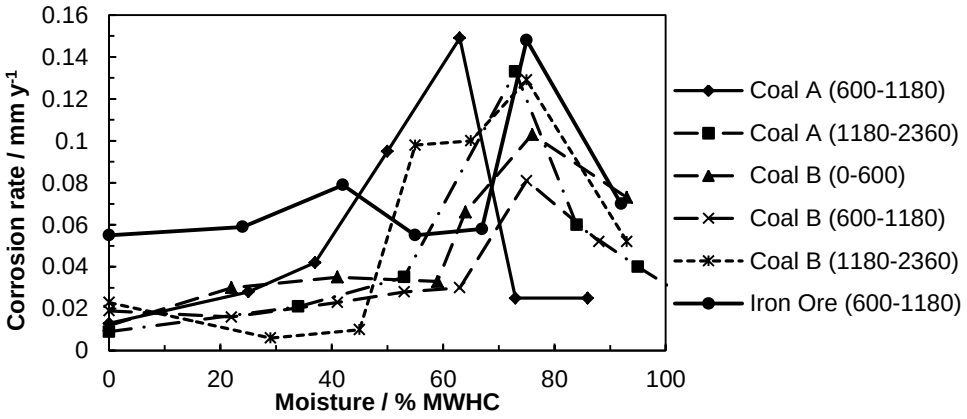

Figure 2.10. Experimental corrosion rates for coal and iron ore exposure (particle size varies from 0 to 2360 μm) [71], where MWHC is the maximum water holding capacity.

It can be seen that when the moisture level is low, the low corrosion rates probably indicate that the underlying steel are fully aerated, which means that the corrosion rate is limited by the electrical conductivity. As the moisture increases, the conductivity also increases, resulting in a higher corrosion rate. With further increase in moisture, the oxygen diffusion becomes limited and restricts the cathodic reaction kinetics, which leads to a reduction in the corrosion rate. Other operational parameters were also investigated in Ref. [14] including cargo and ballast ratio, trade route, coal corrosivity and frequency of cargo changes. However, the study of influence of the moisture content and particle size under acidic moisture condition is lacking in the published literature. Moreover, there has been no formulated correction factor proposed for these influences.

Together with the bulk carrier, the oil tanker is the other ship type with regulated corrosion additions by CSR due to its highly corrosive environment and the severe impact on human life and the marine organisms once structural failure occurs. The causes of corrosion in oil cargo holds can be the various chemical components contained in the oil, high temperature environment, tank wash, loading/unloading frequency and voyage duration, among which the chemical components, temperature and tank wash have been considered to be the major threats and widely studied in the literature. In the cargo oil tanks, H_2S, CO_2, O_2, S, Na^+ and Cl^- are frequently found in high concentrations. Apart from the basic corrosion mechanisms described in Section 2.1.1, the presence of sulphur on the steel surface under oil coat will significantly accelerate corrosion [24]. According to Ref. [3], for cargo oil tanks, the heating facilities and the warm crude oil will raise the temperature of the bottom plates and hence accelerate the corrosion rate due to the enhanced bacterial activities. Excessive washing will remove the oil ‘coating’, which could have as high a corrosion resistance as a coal tar epoxy coating [24]. This operation may

expose bare steel to the corrosive environment [3]. After tank wash, there could be a certain amount of water remaining at the tank bottom, which may also contribute to bottom plating corrosion [6].

2.2 Ultimate strength of corroded structures

2.2.1 Fundamentals

Unlike the conventional allowable stress design, the limit state design has gradually become dominant in structural design. According to Paik and Thayamballi [86] a limit state is defined as a condition for which a particular structural member or an entire structure fails to perform the function that is expected. Ultimate limit state (ULS) is typically the collapse of a structure because of a loss of stiffness and strength; attainment of the maximum resistance due to gross yielding or fracture and instability in part of the structure due to buckling and plastic collapse of adjacent structural members. In metallic structures, especially ductile steel structures, local yielding along with a reduced stiffness will occur as the external loading increases. With further increases in the external load, the ultimate strength will be reached after a degree of yielding. Figure 2.11 illustrates the stress-strain relationships of different kinds of steel plates under compressive loading [86]:

Perfect thin plate: for an ideal thin plate without any initial imperfections (geometrical deflection and/or weld-induced stresses), elastic buckling is expected;
Perfect thick plate: instead of elastic buckling, elasto-plastic bucking is typical for thick perfect plates, due to their high elastic buckling strength. Under this condition, ultimate strength will be reached simultaneously with gross yielding;
Imperfect plate: for plates taking into account the initial imperfections, the elastic buckling phenomenon may not exist. Plates start to deform at the onset of the external loading.

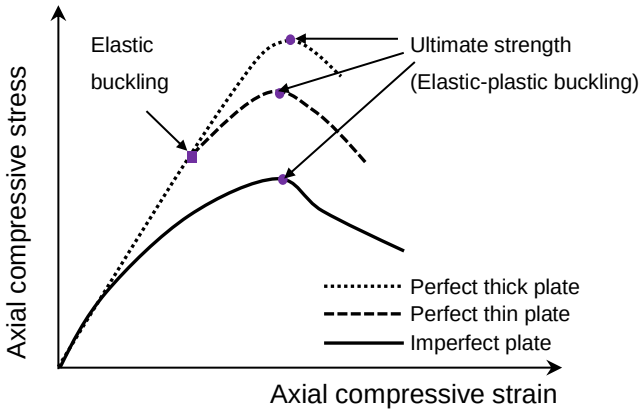

Figure 2.11. A schematic of the stress-strain relationship of a steel plate [86].

Traditional ULS design simply estimates the elastic buckling strength corrected by a plasticity factor. Critical buckling strength σ_{cr} is given by the well-known Jonson-Ostenfeld formula [86] to address the elastic and elastic-plastic buckling problem:

$$\sigma_{\mathrm{cr}} = \begin{cases} \sigma_{\mathrm{E}} & \sigma_{\mathrm{E}} \leq 0.5\sigma_{\mathrm{F}} \\ \sigma_{\mathrm{E}}\left(1 - \dfrac{\sigma_{\mathrm{F}}}{4\sigma_{\mathrm{E}}}\right) & \sigma_{\mathrm{E}} > 0.5\sigma_{\mathrm{F}} \end{cases} \tag{2.8}$$

where σ_{E} is the elastic buckling stress in MPa; $\sigma_{\mathrm{F}} = \sigma_{\mathrm{y}}$ under compressive loading and $\sigma_{\mathrm{F}} = \sigma_{\mathrm{y}}/\sqrt{3}$ under shear loading (σ_{y} is yield stress of the material). However, based on nonlinear FEA results, Paik & Thayamballi [86] reported that σ_{cr} given by Equation 2.8 might be greater than the real ultimate strength for thick and perforated plates. In spite of the effects of the initial imperfections, the thickness variation due to corrosion implies a necessity to assess the maximum load-carrying capacity (ultimate strength) to rationalise the structural design/maintenance rather than the elastic buckling approach with the plasticity correction. Consequently, the ultimate strength analysis of aged and corroded ships has gained increasing attention.

2.2.1.1 Material properties

Three types of material models (Figure 2.12) are often considered in the strength analysis of carbon steel structures [87], specifically aiming to simplify the problem without losing much accuracy.

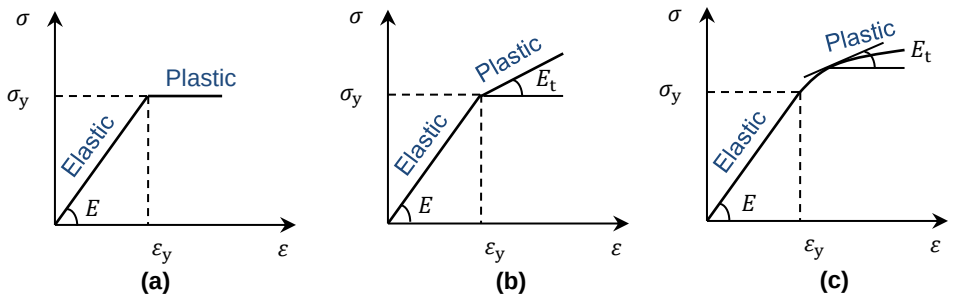

Figure 2.12. Material models used for strength analysis [87].

It is argued that although the strain hardening effect (tangent modulus E_t) would lead to a higher ultimate strength value, this increase is fairly marginal for plates under compressive loading [86,90,91]. In addition, the failure mode will not change [92]. Conversely, in 2011, Khedmati et al. [93] reported that E_t had a slight effect on the ultimate compressive strength of thin plates, while affecting thick plates significantly. However, Rahbar-Ranji [29,94] studied both models (a) and (b) with a conclusion that the tangent modulus had little effect on the strength reduction due to corrosion. Thus, the material model (a), termed elastic-perfectly-plastic model, has been considered sufficient for a conservative compressive strength study, and was generally used in the previous numerical analysis. Table 2.6 summarises the material models used for numerical strength analysis for damaged structures in the literature. It can be seen that most studies ignored the tangent modulus for compressive strength assessment. For tensile and bending strength, the actual stress-strain curves are more readily used since there is often experimental work involved to provide the material properties.

Table 2.6. Summary of the material models used for numerical analysis

	Model (a)	Model (b)	Model (c) - measured
Compressive strength	[7], [17], [48], [29], [95], [96], [97], [94], [98], [99], [100], [101], [102], [103] and [104]	[29], [93], [91], [94], [105], [106], [107], [108] and [109]	[46]
Tensile strength	-	-	[49] and [110]
Shear strength	[111] and [112]	-	-
Bending strength	-	[107], [113] and [114]	[110]

Apart from the strain hardening effect, effort has also been made to investigate the influence of yield strength on the strength reduction. Ok et al. [88] summarised that the frequently used grades of steel for ship structures are mild steel with a yield strength σ_y of 235 MPa and high-tensile steel with yield strengths σ_y of 315 MPa (AH32, DH32, EH32)

and 355 MPa (AH36, DH36, EH36). In addition to the traditional steel grades, a newly developed steel termed Corrosion Resistant Steel with a typical yield stress of 432 MPa has been accepted by IMO [89] specifically for bottom plating of cargo oil tanks. When a corroded plate is under compression, Mateus and Witz [46] stated that the yield strength significantly affected the initial plate stiffness and the out-of-plane displacement at the collapse point.

2.2.1.2 Geometrical properties and initial imperfections

A ship hull is normally composed of a number of plated-structures (Figure 2.13), which consist of three types of structures members: (*i*) plate panels (plating, stiffened panel and corrugated plate); (*ii*) small support members (stiffener, beam and column); (*iii*) main support members (girder) [86]. Plates can be considered as the basic element, and are predominantly subject to in-plane loads (tension and/or compression). The support members are designed to withstand lateral loads, shear and bending. Plates and plate-stiffener combinations are frequently used for corrosion effect analysis. The simplicity of these structural models has enabled researchers to concentrate on the influence of the corrosion damage. The main geometrical parameters, including the plate aspect ratio (α), plate slenderness ratio (β) and column slenderness ratio (λ) are defined as follows:

$$\alpha = \frac{a}{b} \tag{2.9}$$

$$\beta = \frac{b}{t_0}\sqrt{\frac{\sigma_y}{E}} \tag{2.10}$$

$$\lambda = \frac{a}{\pi r}\sqrt{\frac{\sigma_y}{E}} \tag{2.11}$$

where a, b and t_0 are length, width and original thickness of the plate respectively, σ_y is the yield strength, E is Young's modulus and $r = \sqrt{I/A}$ is the radius of gyration, where I is the moment of inertia and A is the cross-sectional area as the sum of the plate and stiffener(s). Hughes and Paik [116] categorised plates as follows: slender plates ($\beta > 2.6$), intermediate plates ($1 < \beta \leq 2.6$) and sturdy plates ($\beta \leq 1$). For ship hull and offshore structures, β typically ranges from 1.5 to 3.5 [86]. The stress-strain relationship, ultimate strength and the failure mode of an intact plated structure are largely dependent on the slenderness ratio when compression is the predominant loading [44,115].

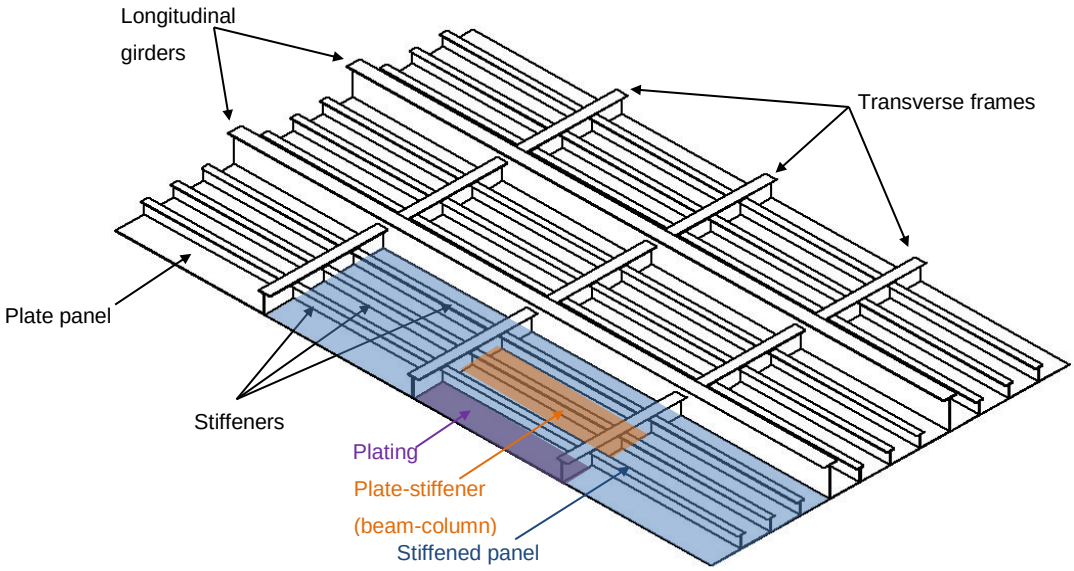

Figure 2.13. Typical plated-structure (grillage) in a ship hull.

The geometric properties have been widely studied for corroded structural members. The influence of the aspect ratio was reported to be significant [93,106,108]. Conversely, Rahbar-Ranji [29,94] and Paik et al. [7] stated that the aspect ratio had little effect on the strength reduction. β is believed by many researchers to be a dominant parameter for the reduction of compressive ultimate strength [29,93,94,97,106,108], while Huang et al. [95], Ok et al. [88,117] and Paik et al. [111] argued that the effects on the compressive and shear strength reduction were negligible. The contradictory conclusions are mainly drawn from numerical studies, implying the underlying uncertainties of the numerical modelling approach as well as the complex interactions amongst the various chosen parameters.

In addition to the basic geometric properties, due to the limitations of fabrication, geometric distortions should be considered in the strength analysis. The distortion shape/amplitude can be determined experimentally, however, to simplify the problem, the initial deflection is usually assumed to follow a Fourier function [116]:

$$\text{Plate:}\quad w_0 = w_{0\text{plm}} \sum_{m=1}^{M} A_{0\text{m}} \sin\frac{m\pi x}{a} \sin\frac{\pi y}{b} \tag{2.12}$$

$$\text{Column-type:}\quad w_{0\text{c}} = w_{0\text{cm}} \sum_{m=1}^{M} A_{0\text{m}} \sin\frac{m\pi U}{a} \tag{2.13}$$

$$\text{Stiffener sideways:}\quad w_{0\text{s}} = w_{0\text{sm}} \frac{z}{h_{\text{w}}} \sum_{m=1}^{M} A_{0\text{m}} \sin\frac{m\pi U}{a} \tag{2.14}$$

where a and b are the length and width of a plate. $w_{0\mathrm{plm}}$, $w_{0\mathrm{cm}}$ and $w_{0\mathrm{sm}}$ are the maximum initial deflections for each imperfection type. $A_{0\mathrm{m}}$ is the normalised deflection amplitude. m indicates the corresponding half-wave numbers in the *x* direction, determined as the minimum integer satisfying $a/b \leq \sqrt{m(m+1)}$. U is the position along the length of the stiffener. z is the vertical position and h_{w} is the height of the web plate. Different values have been assigned by researchers and classification societies for the maximum initial deflection, as summarised in Table 2.7. The value of M is normally taken as 1, but can also be determined based on the "thin-horse" mode, which is a sum of several sinusoidal components. Ueda & Yao [118] reported that $M = 21$ with $m = 1, 3, 5\ldots$. Subsequently, an idealised thin-horse mode was proposed by Yao et al. (1992) with $M = 11$ with $A_{0\mathrm{m}}$ given for different deflection shapes [86].

The geometric imperfection is normally taken into account for numerical studies for compressive and bending strength reduction due to corrosion damage. It has a significant influence especially on the compression strength, since that the ultimate strength could be substantially reduced due to the premature buckling. The difference in compressive ultimate strength of stiffened panels with $w_{0\mathrm{plm}}$ of $0.025\beta^2 t$ and $0.3\beta^2 t$ was found to be 12.5% in Dunbar et al.'s study [100].

Table 2.7. Summary of the frequently used maximum initial deflections

		[115]	[119]	CSR	DNV
$w_{0\mathrm{plm}}$		$t_{\mathrm{w}} < t_0$: $k\beta^2 t_{\mathrm{w}}$ $t_{\mathrm{w}} > t_0$: $k\beta^2 t_0$	Slight: $0.025\beta^2 t_0$ Average: $0.1\beta^2 t_0$ Severe: $0.3\beta^2 t_0$	b/200	b/200
$w_{0\mathrm{cm}}$	$\lambda > 0.2$	-	Slight: 0.00025 a Average: 0.0008 a Severe: 0.002 a	0.0015 a	0.001 a
	$\lambda > 0.4$	-	Slight: 0.00025 a Average: 0.0012 a Severe: 0.0038 a		
	$\lambda > 0.6$	-	Slight: 0.00025 a Average: 0.0015 a Severe: 0.0046 a		
$w_{0\mathrm{sm}}$		-	-	0.0015 a	0.001 a

Notes: t_{w} is the thickness of stiffener web. $\beta \leq 3$: $k = 0.12$; $\beta > 3$: $k = 0.15$.

2.2.1.3 Weld-induced residual stress

Apart from the geometric imperfection, residual stresses are inevitable due to cutting and welding of steel panels. In the HAZ after welding, locally shrinkage and residual tensile stresses (up to the yield stress) are generated in these areas, while in adjacent areas

residual compressive stresses will occur. Examples of measured weld-induced residual stresses on mild steel and high tensile steel are shown in Figure 2.14.

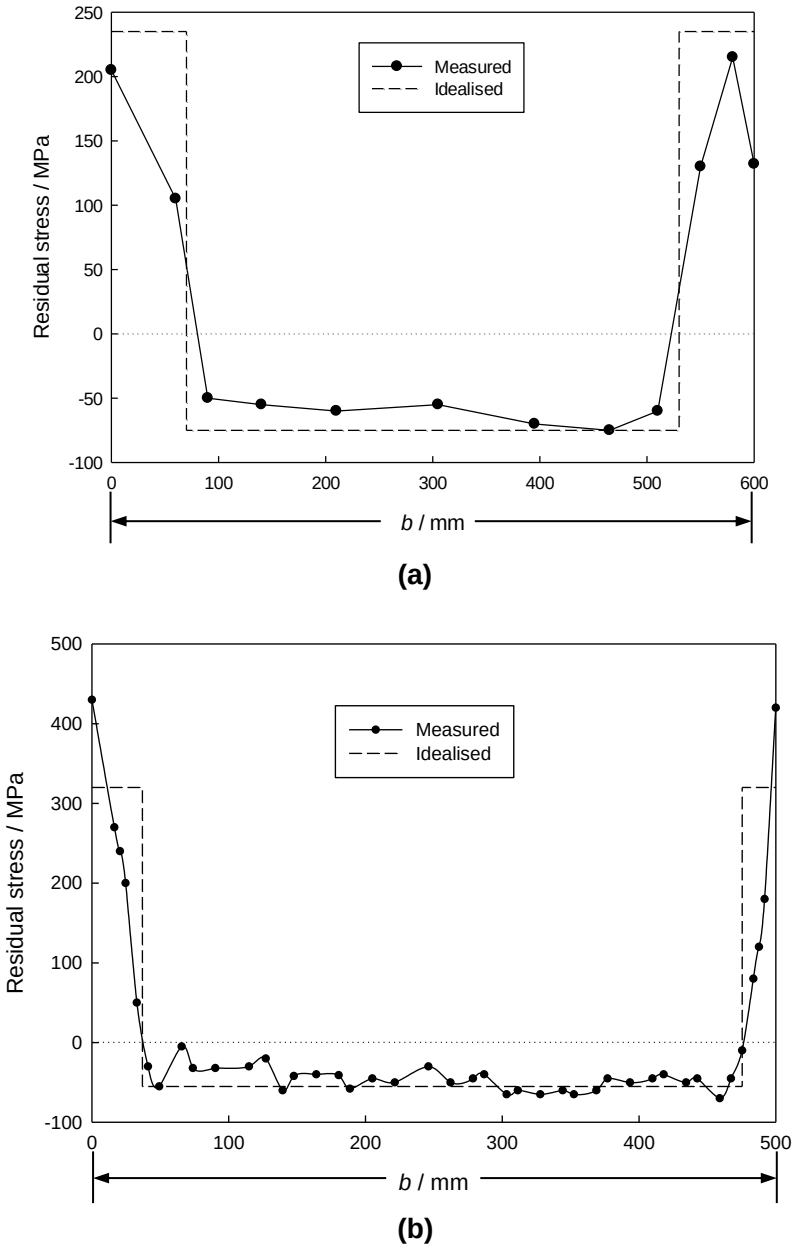

Figure 2.14. Examples of weld-induced residual stresses on plate between stiffeners between two welds (*b* is the width of the plate): (a) mild steel [120]; (b) high tensile steel [121].

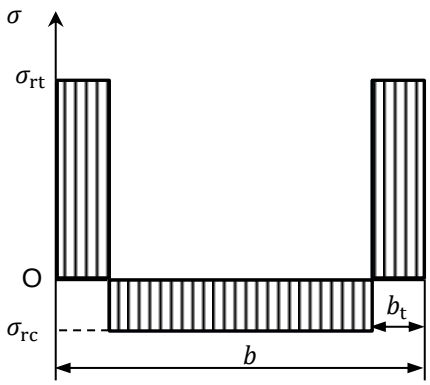

Figure 2.15. Idealised weld-induced residual stress distribution.

To simplify the problem, an idealised residual stress distribution is widely used (Figure 2.15). Assuming b is the width of a plate, the residual stresses and b_t are given as follows [86,119]:

$$\sigma_{rt} = \sigma_y \tag{2.15}$$

$$\sigma_{rc} = \begin{cases} -0.05\sigma_y & \text{Slight level} \\ -0.15\sigma_y & \text{Average level} \\ -0.3\sigma_y & \text{Severe level} \end{cases} \tag{2.16}$$

The actual distribution could be much more complex when fabricating large structures or more than one weld pass is used at the joint [122]. In terms of corrosion effect studies, only Refs. [100,104] applied the residual stresses for stiffened panel and plate models, respectively. Corrosion features were located in areas with either compressive or tensile residual stress. Dunbar et al. [100] concluded that corrosion in the tensile region mainly reduced the post-collapse strength and would enhance buckling when corrosion occurs in the compression region. Tamagawa and Kim [104] reported that the ultimate strength would be further reduced by residual stresses regardless of the corrosion severity. But the reduction diminished when the corrosion damage became significant. Neverthless, the weld effect has been ignored in most cases. Researchers argued that the residual stresses were not as important, since the corrosion feature was the primary concern [7]. Moreover, Nakai et al. [107] studied the residual stresses on an intact plate and concluded that their effect could be neglected. Another reason for not considering the residual stresses is the shakedown effect. As a ship ages, the structural members experience constant loading and unloading, and due to the plasticity of the materials the residual stresses will decrease. Paik and Thayamballi [86] suggested that a reduced tensile

residual stress (e.g., 80% σ_y) could be used to address such issues. However, there has been no published data that considers both the shakedown and corrosion effects.

2.2.1.4 Boundary conditions

The boundary conditions for either experiments or modelling are primarily dependent on the location of the structural members of interest. For a continuous plated structure (Figure 2.13), the stiffeners may or may not be treated as properly designed, which will lead to idealised boundary conditions such as simply supported and clamped [86]. Different boundary conditions could essentially lead to a different failure mode and ultimate strength. For uniaxial compression or edge shear condition, the ultimate strength of a plate can be increased by up to 18% (especially for thin plates) by keeping the unloaded edges straight [46,86]. Strong support members (longitudinal and transverse girders) are normally assumed to remain in plane with high bending rigidity. In general, almost all published research on corroded plates and stiffened panels under axial compression or shear loading has applied a simply supported boundary condition. However, hardly any studies use exactly the same method to achieve such constraint. Indeed, more often, the boundary conditions were not clearly stated.

2.2.2 Investigation method – experiments

Although time consuming, costly and limited in test matrix and conditions, experimental methods for assessing the progressive collapse behaviour of structures are always vital, particularly for validation of numerical modelling and understanding the failure mode of new structural designs [123]. Artificial/idealised corrosion patterns were frequently applied to the samples to control the studied parameters. The stress-strain relationship (load-shortening curve) was normally monitored by placing strain gauges at discrete locations on the sample surface. To better measure the average strain change of an irregular cross-section, vision sensor system was also adopted in Ahmmad and Sumi's tests [49].

Compression tests were carried out by Paik et al. [7] and Nakai et al. [17]: Paik et al. applied compressive loading on welded box-type plated structures (Figure 2.16 (a)) with regularly distributed artificial pits (through-thickness). Nakai et al.'s tests (Figure 2.16 (b)) were performed on web plates clamped along both the loading edges. Paik et al. tested two degrees of pitting (DOP, ratio of damaged area to entire area), and showed that with about 10% DOP the plate's ultimate strength was decreased by 20%. In Nakai et al.'s

experiments, regularly distributed artificial pits (non-through-thickness) were milled on a web plate, varying DOP and locations. The ultimate strength obtained was less than or equal to that of a uniformly corroded specimen. The plate with pits concentrating at both ends had a lower ultimate strength compared to pits at the centre. Moreover, the strength values of both cases were lower than that of plate with pits periodically scattered over the surface.

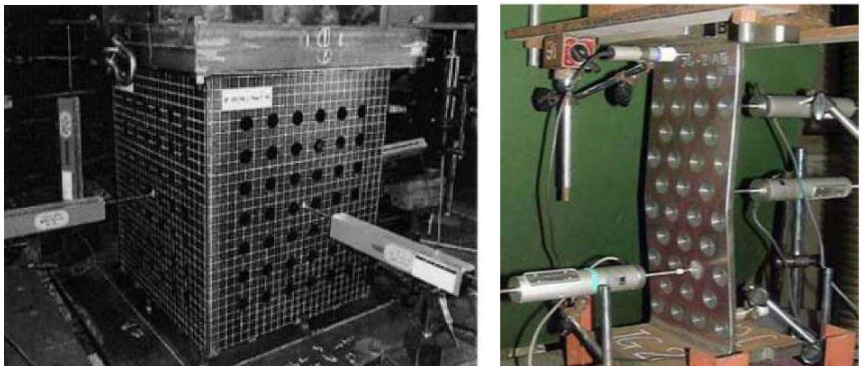

(a) **(b)**

Figure 2.16. Compression test specimens with (a) through-thickness damage [7] and (b) non-through-thickness damage [17].

Tensile experiments are more frequently documented in the literature for corroded specimens. Three sets of tests were conducted by Nakai et al. [17,107], Sumi et al. [49,110] and Appuhamy et al. [99,124] based on the standard tensile test procedure. Specimens with actual or idealised corrosion damage were involved in all three tests. The studies by Nakai et al. and Sumi et al. focused on ship structures while Appuhamy et al. investigated corroded steel bridges. The results showed that the nominal tensile strength and elongation were decreased by corrosion. Pitting would further reduce the tensile strength compared to a uniform thickness reduction. The fracture area corresponded to either a minimum thickness point or a minimum average thickness cross-section. It was interesting to find that orderly distributed pits with fixed diameter could simulate random pitting when the average pit diameter was the same. However, it is not clear why the tensile strength values of minor and moderate corrosion specimens (ratio of minimum thickness to original thickness = 0.5 to 1.0) are higher than that of the corrosion-free specimen in Appuhamy et al.'s work. Also, Nakai et al. [107] concluded that tensile strength is more vulnerable to pitting corrosion compared to compressive and bending strength while Sumi et al. suggested that Paik et al.'s empirical formula [7] for compression reduction could be applicable for tensile strength of plates with either conical or ellipsoidal pits, which indicated little difference of corrosion effects was found on plate's tensile and compressive strength.

Bending tests were also performed for ultimate strength analysis not only on plate elements but also on stiffened plate (plate stiffener combination) models. In Refs. [113,114], three-point and four-point bending tests were carried out with artificial corrosion features on the web plates. It was found that the buckling mode was lateral-distortion under four-point bending and local face buckling under three-point bending. Pitting had little effect on the lateral-distortional buckling strength and could be treated as uniform corrosion with the same average thickness loss. The four-point bending tests conducted on plate elements [110] showed little difference in bending strength between pitted plates under tension and compression. The bending strength reduction is higher due to pitting compared to compressive/tensile/shear strength, which contradicts Nakai et al.'s findings [107].

2.2.3 Investigation method – numerical modelling

The experiments summarised above were all followed by numerical studies under a similar test condition. However, due to the large size and complexity of ship structures, numerical methods, nonlinear FEA in particular, have become more commonly used within various commercial software, such as ANSYS, DNV PULS (Panel Ultimate Limit State), ALPS/ULSAP, MSC/MARC and ABAQUS. In 2008, Paik et al. [125,126] published a series of papers assessing the applicability of some candidate software for intact plated-structures. They concluded that compared to the more refined software such as ANSYS, both DNV PULS and ALPS/ULSAP were computationally efficient and accurate enough for ultimate strength assessment of unstiffened and stiffened panels.

For FEA modelling, convergence difficulties may be encountered due to errors including wrong input data, inappropriate element type, poor element shape/size (free mesh or mapped mesh), wrong boundary/loading conditions and inappropriate calculation strategy. Also, different commercial programmes may generate different outputs even under the same test condition, due to a lack of understanding of the implemented element behaviour and settings. Thus, a comprehensive validation is always essential for the reliability of numerical methods. In this section, numerical studies in the literature will be reviewed focusing on various corrosion features, software, element selection, presence of validation and key findings.

2.2.3.1 General corrosion

General corrosion has been extensively studied in the literature. Methods to simulate general corrosion vary from uniformly reducing the plate thickness to complex rough surfaces, since that the uniform corrosion pattern is generally agreed not to be able to reflect the local plastic hinges (deformation of a section where plastic bending occurs) due to surface unevenness and may underestimate the strength reduction [30,31,46,109]. A summary of the general corrosion modelling is shown in Table 2.8. The main findings are as follows:

(1) Under compressive loading, with the same corrosion-induced volume loss (corrosion wastage), a random surface will lead to a lower ultimate strength value (up to 10%) compared to uniform corrosion [46,109], while Teixeira et al. [31] and Rahbar-Ranji [29,94] argued that the strength value of random corrosion could be higher than or equal to that of uniform corrosion for small corrosion damage;
(2) Corrosion on one side of the plate may further lower the ultimate compressive strength than that for both-side corrosion [106];
(3) A rough surface feature will further distablise the structure in its post-ultimate strength region [108];
(4) For tensile strength, minimum remaining thickness and minimum cross-sectional area are the dominant parameters while the volume loss dominates the compressive ultimate strength;
(5) Apart from a direct scan of a corroded plate surface, various mathematical functions have been applied to generate a rough surface in the models. However, further discussion is needed to justify the practical meaning of the random surface realisations;
(6) Both shell and solid elements (will be discussed in detail in Chapter 4) have been used to model rough surfaces. However, the modelling methods are not always clearly stated. Together with a lack of validation for compressive loading condition, the conclusions drawn in the literature remain debatable;
(7) Weld-induced residual stresses have not been considered;
(8) Various corrosion prediction models (Section 2.1.3.2) have been adopted to inform the average thickness degradation with time. As a result, the strength reduction change with time is largely dependent on the corrosion prediction models.

Table 2.8. Numerical analysis of general corrosion of steel plates

Year	1998 [46]	2010 [49]	2010-2011 [98] [99] [102]	2012 [29] [94]	2010-2012 [93] [106] [108]	2013 [109]	2008, 2013 [30] [31]
Structural model	Square plate with four edges simply supported	Rectangular plate with two short edges clamped	Rectangular plate with two short edges clamped	Plate with four edges simply supported	Rectangular plate and stiffened panel with four edges simply supported	Rectangular plate with four edges simply supported	Square plate with four edges simply supported
Loading	Uniaxial compression	Uniaxial tension	Uniaxial tension	Uniaxial compression	Uniaxial compression	Uniaxial compression	Uniaxial compression
Software	ABAQUS	LS-DYNA	LUSAS	ANSYS	ANSYS	ANSYS	ANSYS
Initial imperfections	$0.1\beta^2 t \sin\frac{\pi x}{a}\sin\frac{\pi y}{b}$	No	No	$0.1\beta^2 t \sin\frac{m\pi x}{a}\sin\frac{\pi y}{b}$	$\sum_{1}^{11} A_{0m} \sin\frac{m\pi x}{a}\sin\frac{\pi y}{b}$	$0.1\beta^2 t \sin\frac{\pi x}{a}\sin\frac{\pi y}{b}$	$0.1\beta^2 t \sin\frac{\pi x}{a}\sin\frac{\pi y}{b}$
Element type	8-node quadratic plate element	8-node brick element	8-node solid hexahedral element	SHELL181	SHELL181	SHELL181	Shell and solid elements
Corrosion model	Ohyagi's model [45]	Yamamoto & Ikegami's model [50]	No	Yamamoto & Ikegami's model [50] – bulkhead plates of ballast tanks in bulk carriers	Ohyagi's model [45]	Garbatov et al.'s model [52] – deck plates of ballast tanks	Garbatov et al.'s model [52] – bottom plates of bulk carriers
General corrosion realisation	Quasi-random thickness model (one-side)	Scan of actual corrosion pattern → CAD → 40% scale (both-side) 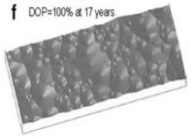	Scan of actual corrosion pattern (both-side) 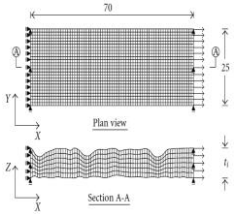	Power spectrum (both-side symmetrical) 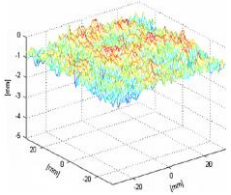	One-side and both-side symmetrical 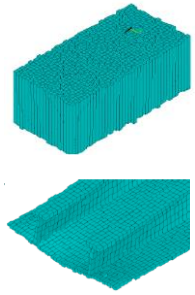	Hexahedron type (both-side symmetrical) 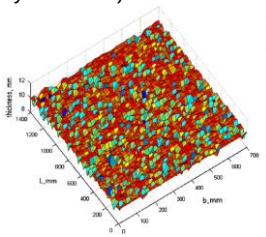	One-side numerical generation 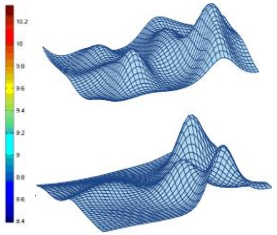
Validation	Intact plate against experiments	Corroded plate against experiments	Corroded plate against experiments	Intact plate against empirical formulas	Intact plate against experiments	No	No

2.2.3.2 Pitting corrosion

Due to the increasingly stringent requirements by classification societies for the use of protective coatings, pitting corrosion is more frequently observed during ship surveys. Acting as potential stress raisers, localised pits can be detrimental to the structural strength. Therefore, a large number of numerical studies have been carried out on pitting corrosion by varying DOP, pit depth, shape, size, distribution and location. Table 2.9 to Table 2.11 summarise the modelling studies of strength reduction due to pitting corrosion. It can be seen that the corrosion effect have been studied mainly on plate elements under compression, tension, shear or bending. The localised corrosion pattern is either rectangular area or circular pits with various shapes (cylindrical, conical, semi-sphere or ellipsoidal). Parameters such as aspect ratio and slenderness ratio have also been considered together with the corrosion damage. Key observations are listed below:

(1) **Coating**: all structural members were modelled as uncoated. However, the corrosion locations are often not supported by *in situ* observations;

(2) **Aspect ratio and slenderness ratio**: Paik et al. [7] suggested that the effects of plate aspect ratio and slenderness ratio on ultimate strength reduction could be neglected. Jiang and Guedes Soares [96,97,101] believed that the aspect ratio could be negligible when the DOP was unchanged, but slenderness ratio governed the failure mode. Khedmati et al. [106] concluded that the effects of aspect ratio and slenderness ratio were different, but cannot be overlooked;

(3) **Initial imperfections**: various shapes of geometric imperfections have been applied, however, with limited work considering weld-induced residual stresses;

(4) **Pitting morphology**: pit shape is thought to be an essential parameter in Refs. [17,33,107] and hence should be carefully modelled according to the location of the structural members, while Paik et al. [7] and Huang et al. [95] stated that the pit shape would have negligible effect on the strength reduction and could be simply treated as cylindrical;

(5) **Governing parameters**: different governing parameters for the corrosion-induced strength reduction under different loading conditions. Particularly, for compressive loading, volume loss [88,95-97,100,101,105,109,117], DOP [103,107] or the smallest cross-sectional area [7] was thought to be dominant. For tensile loading, it is generally concluded that the smallest cross-sectional area was the dominant parameter [49,110]. DOP was thought to be controlling for shear strength reduction [111], while the equivalent thickness or the smallest cross-sectional area [110] was the most important for bending strength [113,114]. However, the

conclusions vary depending on the selection of studied parameters and the interactions between them;

(6) **Validation**: experimental validation of the modelling is lacking especially for compression and shear conditions. The comparisons between shell and solid elements may not be adequate as an effective validation since the constitutive equations imbedded in FEA are the same for different element types.

Overall, investigations into general corrosion using numerical methods have recently gained greater emphasis due to improved computational capabilities. However, regardless of the feasibility of the numerous simulated rough surfaces to represent a naturally corroded surface, the corrosion protection requirements have shifted the situation from general to localised corrosion, thus indicating that greater attention is needed on the localised corrosion effects. Indeed, since 2002 pitting corrosion investigations have been a major portion in the strength reduction assessments. Researchers have attempted to simplify the pitting areas to facilitate a parametric analysis and reduce the computational costs. However, depending on how the actual pitting patterns are interpreted (either distributed over the structural surface or a more localised area), there has not really been a significant advancement in the simulation technique until 2013, when the coalescence of individual pits was modelled by Silva et al. [109]. Compression (uniaxial and biaxial) has been the most interested test condition for both general corrosion [29-31,46,93,94,106,108,109] and pitting corrosion [7,48,88,93,95-97,100,101,103-105,107,109,117]. In terms of the conclusions, the differences in the parameter selection and loading conditions could lead to inconsistent findings. Researchers tend to specify a limited number of variables aiming to focus on the most important ones such as the slenderness ratio, DOP and the volume loss. Unfortunately, the lack of appropriately reported validation remains a major issue for numerical analysis, which has affected the reliability and crucially in some instances the validity of the key findings.

Table 2.9. Numerical analysis of pitting corrosion of steel plates (1)

Year	2002 [105]	2002 [48]	2003 [7]	2004 [111]	2004 [113]	2004 [100]
Structural model	Square/rectangular plate; simply supported	Rectangular plate; simply supported	Square/rectangular plate; simply supported	Square/rectangular plate; simply supported	Plate-stiffener	Square plate and plate-stiffener; simply supported
Loading	Uniaxial compression	Uniaxial compression	Uniaxial compression	Shear stresses	3- and 4-point bending	Uniaxial compression
Software	ALGOR	ANSYS	ANSYS	ANSYS	MSC/MARC	NISA/VAST
Initial imperfections	?	$0.1\beta^2 t \sin\frac{m\pi x}{a}\sin\frac{\pi y}{b}$	$0.1\beta^2 t \sin\frac{m\pi x}{a}\sin\frac{\pi y}{b}$	$0.1\beta^2 t \sin\frac{m\pi x}{a}\sin\frac{\pi y}{b}$	$w_0 = a/1000$ $\theta = \theta_0 \sin\frac{\pi x}{a}$	$w_{\text{plate0}} = 3$ mm $w_{\text{stiffener0}} = 1.1$mm; Welding residual stress for plate-stiffener
Element type	4-node shell element	?	SHELL181	?	4-node thick shell element	Quadrilateral shell element
Studied variables	Aspect ratio, DOP, pit depth, corrosion location	DOP, pit depth, corrosion location	Aspect ratio, DOP, pit depth, pit distribution	Aspect ratio, DOP, β, pit depth	DOP, pit depth, corrosion location	Volume loss
Pitting corrosion realisation	One-side rectangular pits 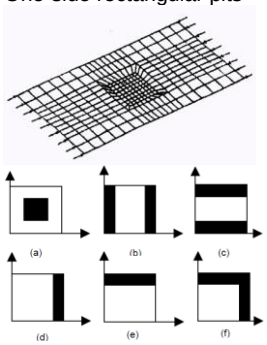	One-side rectangular pits 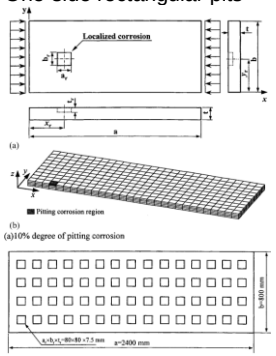	One-side cylindrical pits 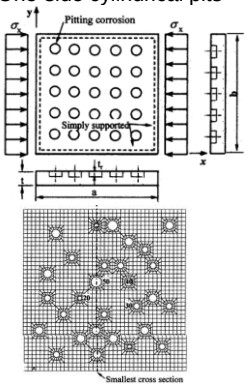	One-side cylindrical pits 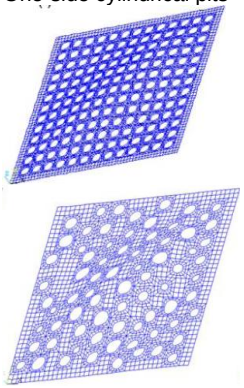	One-side and both-side (symmetrical) conical pits 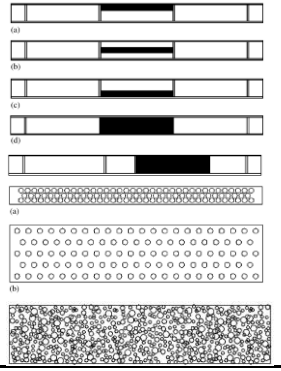	One-side square pit in the centre of the plate; Both-side rectangular pit on face plate of the plate-stiffener 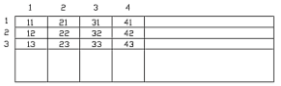
Validation	No	No	Plates with artificial damage against experiments	No	Plate-stiffener with artificial damage against experiments	Elastic buckling strength against analytical solution and intact plate-stiffener against experiments
Governing parameter	Volume loss		Smallest cross-sectional area	DOP	Average thickness loss	Volume loss

Table 2.10. Numerical analysis of pitting corrosion of steel plates (2)

Year	2006 [107]	2006 [114]	2007 [88] [117]	2009 [103]	2009, 2012 [96] [97] [101]	2010 [104]
Structural model	Square plate; simply supported	Stiffened panel	Square plate; simply supported	Square/rectangular plate; simply supported	Square/rectangular plate; simply supported	Square plate; simply supported
Loading	Uniaxial compression + bending	4-point bending	Uniaxial compression	Uniaxial compression	Uniaxial/biaxial compression	Uniaxial compression
Software	MSC/MARC	MSC/MARC	ANSYS	ANSYS	ANSYS	?
Initial imperfections	$0.01t \sin\frac{\pi x}{a} \sin\frac{\pi y}{b}$	$0.01t_w \sin\frac{\pi x}{a} \sin\frac{\pi y}{b}$	$0.1\beta^2 t \sin\frac{\pi x}{a} \sin\frac{\pi y}{b}$	$0.1\beta^2 t \sin\frac{m\pi x}{a} \sin\frac{\pi y}{b}$	$0.005b \sin\frac{m\pi x}{a} \sin\frac{\pi y}{b}$	$(a/150) \sin\frac{\pi x}{a} \sin\frac{\pi y}{b}$ Welding residual stresses
Element type	4-node thick shell element	4-node thick shell element	SHELL181	SOLID95	SHELL93, SHELL181	8-node solid element
Studied variables	DOP, pit diameter, stress gradient	Pit location and distribution	β, pit location, pit size	Aspect ratio, DOP, β	Aspect ratio, β, DOP, pit depth, pit diameter, stress ratio	Corrosion location (tension or compression region), pit depth, plate length
Pitting corrosion realisation	Both-side (symmetrical and non-symmetrical) conical pits 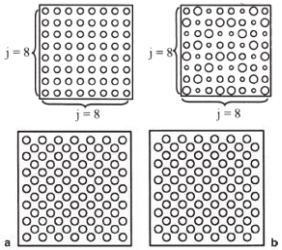	One-side and both-side (symmetrical) conical pits on web plate 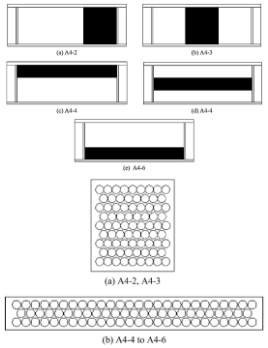	One-side rectangular pits 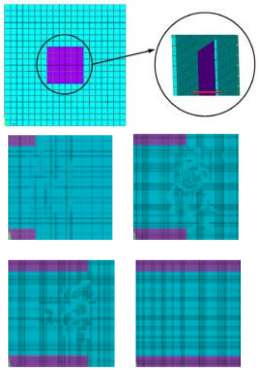	Both-side cylindrical pits	One-side and both-side (symmetrical) circular pits 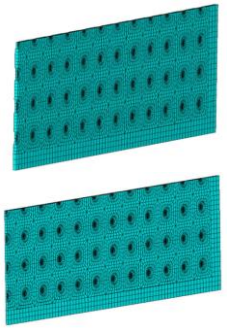	One-side square pit 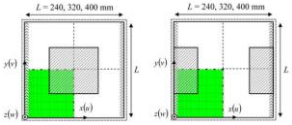
Validation	Compared with 8-node solid element	Plate with artificial damage against experiments	No	No	No	No
Governing parameter	DOP, equivalent thickness	Average thickness loss	β, volume loss	DOP	β, volume loss	?

Table 2.11. Numerical analysis of pitting corrosion of steel plates (3)

Year	2010 [95]	2010-2011 [49] [110]	2011 [93]	2011 [110]	2012 [112]	2013 [109]
Structural model	Square plate; simply supported	Rectangular plate; clamped	Rectangular plate; simply supported	Rectangular plate	Rectangular plate; simply supported	Square plate; simply supported
Loading	Biaxial compression	Uniaxial tension	Uniaxial compression	4-point bending	Elastic shear stress	Uniaxial compression
Software	ANSYS	LS-DYNA	ANSYS	LS-DYNA	ANSYS	ANSYS
Initial imperfections	$0.05\beta^2 t \sin\frac{\pi x}{a}\sin\frac{\pi y}{b}$	No	$0.1\beta^2 t \sin\frac{m\pi x}{a}\sin\frac{\pi y}{b}$	No	$0.1\beta^2 t \sin\frac{m\pi x}{a}\sin\frac{\pi y}{b}$	$0.1\beta^2 t \sin\frac{\pi x}{a}\sin\frac{\pi y}{b}$
Element type	Shell element	8-node brick element	SHELL181	8-node brick element	SHELL63	SHELL181
Studied variables	Pit shape, pit depth, pit distribution, β, stress ratio, stress gradient	Pit shape, size and distribution	Aspect ratio, β, pit depth, DOP	Aspect ratio, DOP, β	Aspect ratio, β, DOP	Volume loss
Pitting corrosion realisation	Cylindrical, semi-sphere and conical pits 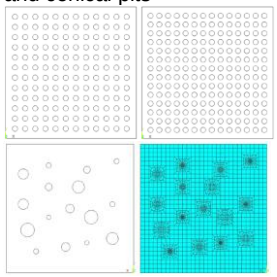	Conical and ellipsoidal pits 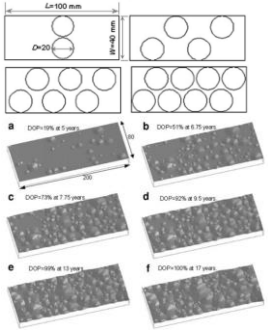	One-side conical pits 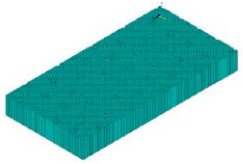	One-side and both-side ellipsoidal pits 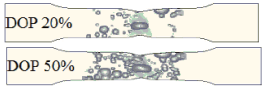	Both-side (symmetrical) rectangular pits with a rough surface 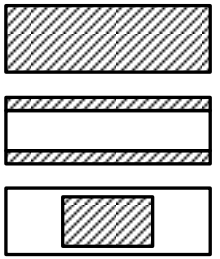	One-side ellipsoidal pits 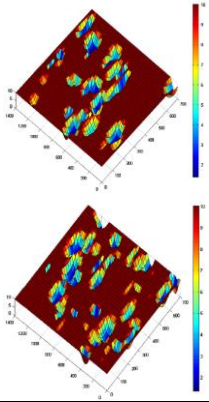
Validation	Compared with solid element	Plate with artificial damage against experiments	Intact plate against experiments	Plate with artificial damage against experiments	Against analytical solution	No
Governing parameter	Volume loss	Smallest cross-sectional area	β, aspect ratio	Smallest cross-sectional area	Volume loss	Volume loss

2.3 Mechano-electrochemistry

The combined influence of mechanical and chemical/electrochemical effects (which is often termed mechano-chemical or chemo-mechanical changes in physico-mechanical properties and the deformation of the solid) have been studied since the beginning of the 19th century [127]. Previous studies have focused on stress corrosion cracking [128,129], corrosion fatigue [130] and hydrogen-induced cracking [131-133]. However, there is yet to be an agreement on the synergistic effect of elastic stress and electrochemical process. In addition, various theories have been proposed to explain the influence of plastic strain on corrosion enhancement, which is largely dependent on the studied materials and the test environment. In this section the mechano-electrochemical analysis will be reviewed focusing on the elastic stress and plastic deformation effects from the viewpoint of thermodynamics.

2.3.1 Influence of elastic stress

An early study carried out by Despic et al. [131] in 1968 established that during corrosion, only the rate of hydrogen evolution was affected by tensile elastic stress. The chemical potential of hydrogen was believed to decrease under stress, which lowered the activation energy barrier for hydrogen-metal discharge and hence enhanced the cathodic reaction. Conversely, Gutman concluded that both tensile and compressive elastic stress would equally and directly affect the anodic reaction by increasing the surface chemical potential and decreasing the equilibrium potential [127]. The promoted cathodic reaction was reported to be due to the localisation of anodic area and increased cathodic area during loading [127]. Movachan et al. argued that the compressive stress would cause even higher corrosion damage in the elastic region [134]. Zhang et al. reported that the elastic load would only affect the anodic polarisation [135]. Moreover, a cyclic tensile stress caused more serious corrosion compared to unstressed and statically stressed low carbon low alloy steels, since the load increased the surface activity, lowered the reaction energy and led to a more porous corrosion product film.

Theoretically, when considering a point within a solid as an infinitely small cube, the macroscopic stress state (Cauchy stress tensor) can be expressed as a combination of the hydrostatic pressure/stress and deviatoric stress [136]. When a solid surface is elastically stressed, Gutman [127] reported that the chemical potential of an atom of a

solid would be increased by the spherical part of the macroscopic stress tensor, i.e., the hydrostatic pressure, and hence leading to increases in macroscopic chemical potential in the solid surface, regardless of the stress sign. The introduced mechanochemical behaviour will result in a mechano-electrochemical response and a decrease in the equilibrium potential $\Delta\varphi_{\mathrm{e}}$ [127]:

$$\Delta\varphi_{\mathrm{e}} = -\frac{\sigma_{\mathrm{m}} V_{\mathrm{m}}}{zF} \tag{2.17}$$

where $\Delta\varphi_{\mathrm{e}}$ is the change in equilibrium potential (V), respectively. σ_{m} is the absolute value of the spherical stress in the solid phase (MPa), V_{m} is the molar volume (m^3 mol^{-1}), z is the number of electrons within the partial electrochemical reaction and F is the Faraday's constant (96485 C mol^{-1}). When considering metal dissolution, only the anodic current density is directly affected by the mechano-electrochemical action [127]:

$$i_{\mathrm{a}} = i_{\mathrm{a0}} \exp \frac{\sigma_{\mathrm{m}} V_{\mathrm{m}}}{RT} \tag{2.18}$$

where i_{a0} is the anodic current density of a non-stressed electrode (A m^{-2}); R is the ideal gas constant (8.314 J mol^{-1} K^{-1}) and T is the temperature (K). Qiao and Mao [137] also proposed a theoretical expression of elastic stress effect on the anodic current density, which was modified by also considering the volume change [138]:

$$i_{\mathrm{a}} = i_{\mathrm{a0}} \exp \frac{3(1-2\nu)\sigma_{\mathrm{m}}{}^2 V_{\mathrm{m}}}{ERT} \tag{2.19}$$

where E is the Young's modulus and ν is the Poisson's ratio. However, principal stresses σ_1, σ_2 and σ_3 were used to calculate the hydrostatic stress, which inappropriately include the shear stresses for the volume dilation. Moreover, there is a lack of validation against experimental measurements.

From the literature it was found that the influence of elastic stress may vary significantly but is limited in magnitude. For example, both experiments and theoretical estimate have indicated that for carbon steel with a yield stress of 450 MPa under uniaxial elastic bending (420 MPa), the ratio of stress and unstressed equilibrium potential is around 1.8 [127], with $\Delta\varphi_{\mathrm{e}}$ of approximately 15 mV (Equation 2.17). In addition to the stress sign (tensile/compressive), the discrepancy could be due to the differences in sample microstructure, preparation, corrosion mechanism and application of the elastic stress.

Table 2.12 summarises typical materials and solutions used in the abovementioned studies. In fact, the observed mechano-electrochemical performance is likely to be a combination of the surface physical property change, microstructural heterogeneity and the deformation of oxide film induced by the external loading. When a passive film is present, the load may also alter the surface film state and the adsorption of the surface active elements [127]. It is difficult to individualise the influence of each parameter.

Table 2.12. A summary of typical studied material for elastic stress effect

Year	Ref.	Material	Solution
1968	[131]	Armo iron; Copper (99.95% Cu); Nickel (99.97% Ni); Molybdenum (99.9% Mo).	0.1N H_2SO_4; 0.1N H_2SO_4 + 0.1 $CuSO_4$; 0.1N H_2SO_4; 1N KOH
1994	[127]	Carbon steels; Martensitic steel; Aluminium	30% HCl; 20% H_2SO_4 (+ 30 g L^{-1} NaCl); 3% NaCl + 0.1% H_2O_2 and 1N NaCl + 1% HCl
1995	[137]	310 austenitic stainless steel	Boiling LiCl
2009	[138]	X60 pipeline steel	NS4 solution (0.122 g L^{-1} KCl, 0.483 g L^{-1} $NaHCO_3$, 0.181 g L^{-1} $CaCl_2$, 0.131 g L^{-1} $MgSO_4$)
2013	[135]	Bainitic steel; Dual phase steel	3.5 wt.% NaCl; 3.5 wt.% NaCl

2.3.2 Influence of plastic deformation

Investigations of plastic deformation effects have been carried out by applying external loading, cold work or welding, which leads to direct and/or residual plastic strain. For external loading, it has been generally agreed that the plastic strain will significantly enhance corrosion by directly influencing the anodic reaction [129,131,134,138-141] while the hydrogen evolution was reported to increase as well [133,138]. Despic et al. [131] observed that a negative corrosion potential ship by up to 30 times, with a marked increase in the anodic current density at the onset of the tensile plastic strain and reached an asymptotic value gradually. However, Lu et al. observed a very limited effect of plastic deformation on metal dissolution [132]. The anodic current density due to tensile plastic deformation was found to increase to a value and then decrease regardless of the surface film condition [139,140]. A tensile strain was found to be more effective than compressive strain [141]. Conversely, the tensile and compressive plastic strain was reported to have the same effect on electrochemical properties [127,138], since different types of plastic deformation are all realised as micro-shears within the crystalline microstructure [127]. More recently, due to the increase in the computational capability, research of mechano-

electrochemistry has been achieved numerically with implementation of Gutman's formulas [127] to provide more detailed information on the corrosion enhancement [142,143]. However, the validation of the numerical work was not clearly presented. Also, the multi-component stress condition needs to be appropriately addressed.

The plastic strain effects are mainly related to the dislocations on the solid surface. When slip planes occur during plastic deformation, the formed steps or planar dislocation pile-ups will produce new charged double layers, increasing the surface roughness and creating edges, for which the metal dissolution increases [131,141]. The increase in the dislocation density would lead to sites with more active electrons [138,141]. The heterogeneity of dislocations was reported to be the major contribution to the mechano-electrochemical effect compared to uniformly distributed dislocations [132] and [138]. Moreover, for metals with high index slip planes, the binding energy of the surface atoms tends to be lower and hence more active for corrosion process [131]. At a later stage, the active planes that dissolve initially become stable, which results in an asymptotic value [131], while the decreased current density was explained as the dislocation cross-slip and partial annihilation that destroyed the planar pile-ups during the dynamic recovery stage [139,140]. The increased hydrogen adsorption is due to the increase in the crystalline imperfections caused by plastic deformation [138].

The theoretical formulas proposed in Ref. [131] were validated against experimental data. However, the parameters such as integral double layer capacity, roughness factor and current density corresponding to high-index plane dissolutions were not clearly reported. A local change in the equilibrium potential induced by plastic deformation $\Delta\varphi_{\mathrm{p}}$ is given in Ref. [127] as follows:

$$\Delta\varphi_{\mathrm{p}} = -\frac{n\Delta\tau R}{\bar{\alpha}kN_{\max}zF} \tag{2.20}$$

where n is the number of dislocations in planar pile-ups; $\bar{\alpha}$ is equal between 10^9 and 10^{11} cm^{-2}; k is the Boltzmann constant for a system of particles representing unit dislocations and $N_{\max}$ is the maximum possible dislocation density. By assuming $n \leq 10$, $\bar{\alpha} = 10^{11}$ cm^{-2}, $N_{\max} = 10^{12}$ cm^{-2} for iron at $\Delta\tau$ = 190 MPa, $\Delta\varphi_{\mathrm{p}}$ was estimated to be -73 mV [127]. The consideration of plastic strain was also expressed by the volume expansion ΔV_{p} due to microvoids [132]:

$$\Delta V_{\mathrm{p}} = -\frac{V_{\mathrm{m}}\varepsilon_{\mathrm{p}}}{\varepsilon_{\mathrm{f}}}\,\bar{V}_{\mathrm{p,max}} \tag{2.21}$$

where ε_{p} is the plastic strain, ε_{f} is the fracture strain and $\bar{V}_{\mathrm{p,max}}$ is the maximum volume change of plastically deformed metal. The change in the internal energy ΔU_{p} and entropy ΔS_{p} due to the plastic strain is:

$$\Delta U_{\mathrm{p}} + \Delta S_{\mathrm{p}} = V_{\mathrm{m}} e_{\mathrm{p}} \tag{2.22}$$

where e_{p} is the density of stored plastic strain energy. Therefore the anodic current density change can be expressed as:

$$i_{\mathrm{a}} = i_{\mathrm{a0}}\exp\left(-\frac{V_{\mathrm{m}}\varepsilon_{\mathrm{p}}}{\varepsilon_{\mathrm{f}}}\,\bar{V}_{\mathrm{p,max}} + V_{\mathrm{m}} e_{\mathrm{p}}\right) \tag{2.23}$$

However, the hydrostatic pressure is related to the volume change of the solid, and it is the distortion of the solid that is associated with plastic deformation [136]. Also, Equation 2.21 is based on an empirical approximation for aluminium alloy 6061. Evidence of appropriate validation was not systematically shown in Ref. [132], and it is unclear whether or not the parameters from aluminium alloy can be directly applied for other materials.

By cold working, the effect of oxide film stability can be largely eliminated. An early study by Migai et al. in 1971 [133] reported that cold working, similar to uniaxial tension/compression, led to an altered microstructure of steel KH18N10T (formation of *α* phase) and hence an increase in the corrosion rate. The increased current density at an early stage of cold rolling and a decreased value in the dynamic recovery stage of the hardening process corroborated the observations under external loading [144]. However, according to the theoretical study in Refs. [132,138], a compressive plastic strain would cause corrosion deceleration. Their experiment showed a reduction in the corrosion current density with increased cold working, which was considered to relate to the presence of CO_2 in the surrounding environment [132]. Although the slip-out of dislocations beneath the surface over time (ageing effect) will reduce the number of active sites [138], the interaction between cold working and CO_2 was not fully examined.

In terms of welded specimens, electrochemically more negative potentials have been detected in the vicinity of the weld boundary using either a micro-capillary probe in an

electrolyte or a Kelvin probe [127,145,146], as shown in Figure 2.17. The relatively high potential on the weld bead was reported to be induced by a thick oxide film [146] as well as a lower reisudal stress in compreson to the base metal [127]. Areas with lower potentials will preferentially act as anodes, which could induce grooving or knife-line corrosion. Although the electrochemical heterogeneity is introduced by the welding material and in particular welding materials, after annealing, levelling of potential on the weld and base metal was observed [139], indicating that there are interactions between the electrochemical performance and the stress state.

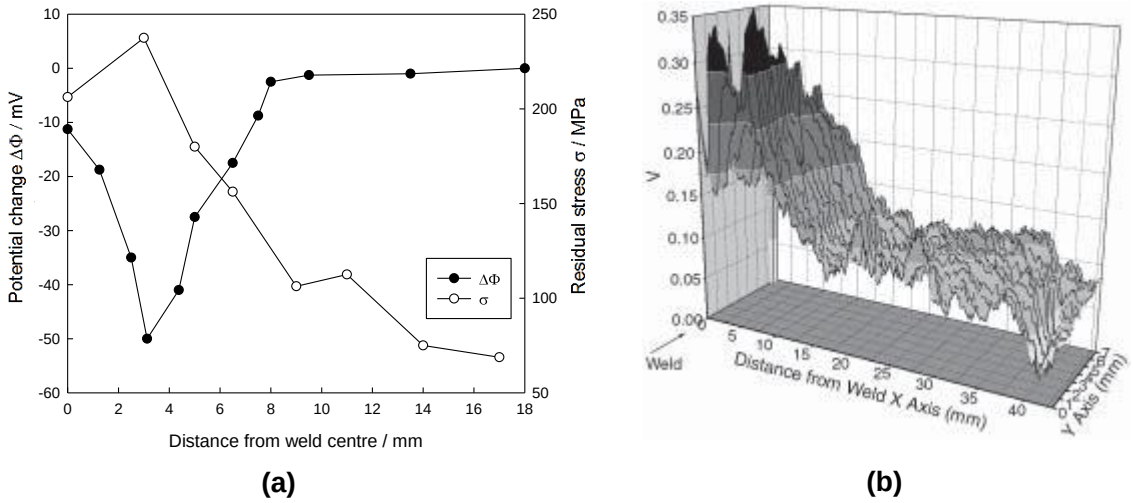

Figure 2.17. Electrochemical and mechanical heterogeneity of steel weld joint: (a) surface potential change and residual stress distribution across a butt weld [127]; (b) local Volta potential across a butt weld [146].

It can be seen that great effort has been made to investigate the interaction between plastic strain and the electrochemical properties of a solid surface. However, various parameters have been considered to be controlling the process, such as dislocation density, high-index slip plane, change in microstructures and microvoid-induced volume change. The studied materials and test solutions in the literature are summarised in Table 2.13. In addition, the presence of a weld introduces extra heterogeneity in the microstructure at the HAZ. On the other hand, research has shown that dislocations would increase the oxygen adsorption and hence facilitate the formation of oxide layer [147,148], which could potentially retard the corrosion process. Further investigation is needed based not only on the fundamental thermodynamics but also on the interpretation and transformation from micro-stress/strain of a single crystal to macro-stress/strain of a metallic structural surface.

Table 2.13. A summary of studied material for plastic strain effect

Year	Ref.	Material	Solution
1968	[131]	Armo iron; Copper (99.95% Cu); Nickel (99.97% Ni); Molybdenum (99.9% Mo).	0.1N H_2SO_4; 0.1N H_2SO_4 + 0.1 $CuSO_4$; 0.1N H_2SO_4; 1N KOH
1971	[133]	Stainless steel KH18N10T	5% H_2SO_4
1994	[127]	Low carbon steel; Stainless steel (18Cr-8Ni); Molybdenum (99.9% Mo); Copper; Aluminium; X52 pipeline steel	7N H_2SO_4; Boiling $MgCl_2$; 1N HNO_3; 10% H_2SO_4; H_2S + HCl; 0.9N H_2SO_4
1996	[139]	316L stainless steel;	0.1N Na_2SO_4 + 5% H_2SO_4
2002	[140]	Mg alloys (AM60 and AZ91D)	NaCl + $Mg(OH)_2$
2006	[129]	AA2024-T3	1M NaCl
2007	[144]	Stainless steels (AISI 304 and AISI 430)	0.5M NaCl
2009	[138]	X60 pipeline steel	NS4 solution (0.122 g L^{-1} KCl, 0.483 g L^{-1} $NaHCO_3$, 0.181 g L^{-1} $CaCl_2$, 0.131 g L^{-1} $MgSO_4$)
2011	[147]	Nickel (99.999% Ni)	40% H_2SO_4
2012	[142]	X100 pipeline steel	0.483 g L^{-1} $NaHCO_3$, 0.122 g L^{-1} KCl, 0.181 g L^{-1} $CaCl_2$ and 0.131 g L^{-1} $MgSO_4$
2013	[132]	API X70 steel	0.483 g L^{-1} $NaHCO_3$, 0.122 g L^{-1} KCl, 0.181 g L^{-1} $CaCl_2$ and 0.131 g L^{-1} $MgSO_4$

2.4 Ship survey criteria, inspection and maintenance

Ship surveys generally consist of Annual Surveys (AS), Intermediate Surveys (IS) and Special Surveys (SS) [26]. An AS, which typically lasts for one or two days, is conducted every year to check the condition of external hull structures and piping surfaces. An SS, which takes one or two weeks, is carried out every five years. Vessels are dry-docked and all structures are examined in detail. Whilst an IS, lasting normally three or four days, takes place at the mid-point between the AS and SS, involving the same inspection areas as in the AS plus ballast tanks and cargo tanks. During an SS, General Visual Inspections (GVI) and Close Visual Inspections (CVI) are included to assess coating condition and material degradation. Ultrasonic thickness measurement (gauging), in conjunction with GVI and CVI, provides quantitative information of the corrosion condition of ship structures. The thickness measurement is also included especially for ships of more than ten years in service.

A set of parameters such as the average thickness, maximum pit depth and pit intensity are required by the classification societies during a corrosion inspection [149,150]. The accuracy of the corrosion prediction and strength assessment are affected directly by the quality of the collected corrosion data. However, the underlying uncertainties, including instrument error, remaining rust and human error, can all contribute to the large scatter of the data. Teixeira and Guedes Soares [30,151] carried out a study on the inspection quality on corroded ship plates and found that the accuracy of different measurement pattern of the plate thickness was different. For certain purposes, such as to measure a highly localised corrosion field, an appropriate measurement pattern needs to be adopted to increase the accuracy.

2.4.1 Coating inspection

Recently, the application of coating in ballast tanks and double-side-skin spaces in bulk carriers are required by IMO PSPC [68] to reach its target life of 15 years. The application of IMO PSPC is mandatory according to IACS CSR for oil tankers of 150 m in length and above, and bulk carriers of 90 m in length and above. IACS requires the protective coating in ballast tanks of all types of ships except oil tankers to maintain in at least a 'Fair' condition. A 'Good' condition is required for oil tankers and chemical carriers. The rating conditions are listed in Table 2.14 [26] and Table 2.15 [152].

Table 2.14. Coating and rust rating for ballast tanks of all ship types except oil tankers [26]

Rating/condition	Good	Fair	Poor
Spot rusting	Minor	<20%	
Edges and welds		Local break down	
Hard scale			≥10%
General breakdown			>20%

Table 2.15. Coating and rust rating for ballast tanks of oil tankers and chemical carriers [152]

Rating/condition	Good	Fair	Poor
Breakdown of coating or area rusted	<5%	5% - 20%	>20%
Area of hard rust scale		<10%	≥10%
Local breakdown on edge or weld lines	<20%	20% - 50%	>50%

To facilitate the coating condition inspection, various coating failure scale diagrams have been produced by the classification societies, for example Figure 2.18 from ABS [26]. Providing that material degradation often occurs at the areas where coating fails, the diagrams may be seen as rationally simplified corrosion features on local structures.

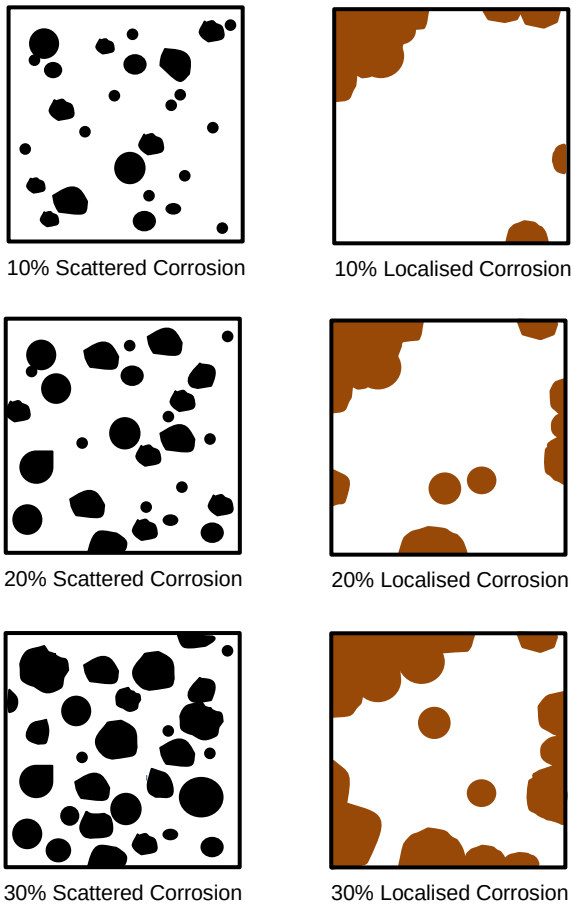

Figure 2.18. Replica of scattered (left) and localised (right) coating failure scale diagrams at various DOP values [26].

2.4.2 Design, thickness diminution and maintenance

In addition to applying a protective coating, the design of ship scantlings are required to contain a certain allowance for corrosion wastage, including the corrosion addition (Figure 2.19). The value of the corrosion addition varies depending on the vessel type and structural locations, and is not reduced due to the presence of coating, since the coating will eventually breakdown and it is not always possible to recoat in time.

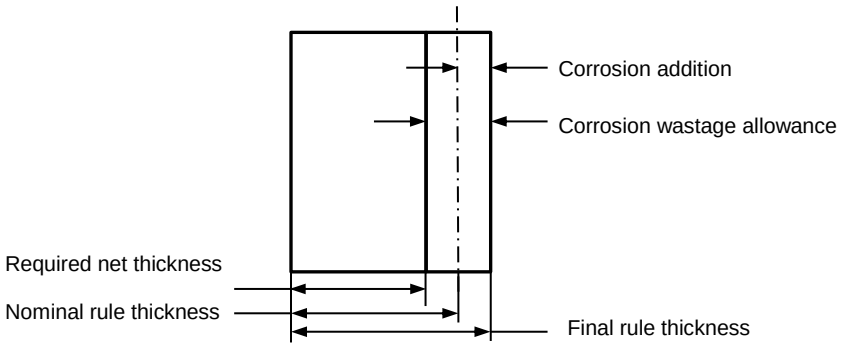

Figure 2.19. Corrosion addition and wastage allowance [32].

The corrosion wastage allowance is normally expressed as a percentage of as-built scantlings. The values of general trading ships are in the range of 15% - 25% for local structural members. Substantial corrosion with wastage of more than 75% of the allowance needs to be recorded by classification societies [8]. Based on an extensive collection of investigation (e.g., [38,42,86,153]), CSR established the corrosion addition for different structural locations. However, such rules are only applied for bulk carriers and oil tankers [154].

Classification societies have issued different maximum allowable thickness diminutions, in association with the ultrasonic thickness measurements during ship surveys, to determine the repair time point. Typical values from Lloyd's Register (LR) and DNV are summarised below.

For general corrosion, LR [155] categorises ships into three groups: (1) oil tankers, chemical tankers, dry bulk cargo ships, combination carriers and liquefied gas ships with a length $L \geq 90$ m; (2) all remaining ship types not included in (1) with a length $L \geq 90$ m; (3) all ship types having a length $L < 90$ m. The maximum permissible diminution of individual plates and stiffeners are listed in Table 2.16.

DNV [11] simply divides vessels into two groups: vessels with a length $L < 100$ m or $L \geq 100$ m. For the former group, the allowable diminution of plate thickness is generally up to 20% and 25% for the hull envelope. However, the plating thickness should also be no less than $0.9 \times (5.5 + 0.02L)$ for the deck and $0.9 \times (5.0 + 0.04L)$ for the side/bottom. When vessels are longer than 100 m, the allowable thickness diminutions for structural members within 0.4*L* amidships are listed in Table 2.17. In terms of repairs, CSR states that repair is needed when the remaining corrosion addition is about 0.5 mm [156]. According to IACS, areas found with inacceptable thickness diminution are normally repaired with inserted material of the same grade and scantlings as original.

Table 2.16. Maximum thickness diminution of individual plates and stiffeners [155]

Structural member	Category (1)	Category (2) & (3)
Hull envelope: plates, shell and deck plating	20%	30%
Hull envelope: transverse section	20%	30%
Longitudinal structures: deck and shell longitudinal stiffeners, longitudinal bulkhead plating and stiffeners, inner bottom plating and stiffeners, hopper sloping plating and stiffeners.	Plating 20% Stiffeners 30%	Plating 30% Stiffeners 25%
Transverse structural members in cargo oil and ballast tanks	20%	25%
Ballast tanks and oil tanks transverse bulkheads	Plating 25% Stiffeners and corrugated bulkhead plating 25%	Plating 30% Stiffeners and corrugated bulkhead plating 25%
Cargo hold transverse frames and end brackets	20%	25%

Table 2.17. Maximum thickness diminutions of structural members [11]

Structural member: longitudinal	Thickness diminution
Strength members within 0.15D_{M}* from deck and bottom	Plating 20% Stiffeners 25% Girders and stringers 20%
Side and longitudinal bulkhead between 0.15D_{M} and 0.85D_{M} from bottom	Plating 20% Stiffeners 25%
Other longitudinal structure between 0.15D_{M} and 0.85D_{M} from bottom	Plating 20% Stiffeners 25% Girders and stringers 20%
Structural member: transverse	
Deck plating between hatches	Plating 20% Stiffeners 25%
Transverse bulkheads	Plating 25% Plain bulkhead 25% Corrugated bulkhead plating 20%
Frames/Stiffeners	25%

*D_{M}: moulded depth

Regarding pitting corrosion, the LR Guidance Information for steel ships states [157]:

(1) Shallow pitting less than 0.33t_0, where t_0 is the original thickness of structural members, may be repaired by filling with a suitable epoxy compound;

(2) Isolated deep pits greater than 0.33t_0 may be repaired by welding, provided the thickness of material left at the bottom of the pit exceeds 6 mm;

(3) Where the pitting intensity is found to be extensive (above 25% of the surface area) in association with deep pits (over 50% of the original thickness), or where the thickness of material left at the bottom of the pit is less than 6 mm, the affected plating should be cropped and renewed.

DNV [11] gives the maximum allowable thickness diminution: $0.4t_0$ when the pitting area is less than 20%, provided the remaining thickness is no less than 6 mm. For the following condition, repair is necessary:

(1) Widely scattered pitting (less than 5%) and the remaining thickness in pitted area is no less than 6 mm, the use of either a plastic compound filler or welding may be applied;
(2) For larger pitting areas, plates and stiffeners may be renewed by inserts.

For groove and edge corrosion, within the HAZ, repairs are required when corrosion is beyond 20% on the weld line [152]. According to LR [155], when grooving corrosion is greater than 15% of one side of the web plate, thickness measurements need to be taken. The minimum acceptable remaining thickness in any groove is:

(1) $0.75t_0$ for grooving in the cargo hold side frame webs and flanges;
(2) $0.70t_0$ for grooving in the side shell, hopper tank and topside tank plating attached to the cargo hold side frame, over a width up to 30 mm from each side of it.

The maximum acceptable breadth of groove given by DNV [11] is 15% of the web height, but no more than 100 mm with the remaining allowable thickness in the grooved area being $0.7t_0$, but no less than 6 mm. The acceptable extent of corrosion at the free edge of longitudinals, according to DNV [11], is defined as:

(1) The overall height of the corroded area is less than 25% of the stiffener web height;
(2) The edge thickness is no less than $0.33t_0$;
(3) The remaining thickness in the corroded area is above the minimum allowable thickness for general corrosion.

Re-welding and renewal by inserts are required by DNV for grooving and edge corrosion.

2.5 Conclusions

From the literature review it can be seen that a good prediction of the strength capacity of steel structures is largely dependent on the accuracy of the corrosion prediction, including the corrosion pattern, location and rate. The general procedure adopted in the literature to predict corrosion is identified in Figure 2.20, based on which the main conclusions are summarised as follows:

(1) While the general corrosion mechanisms for steel have been systematically explored, the application of corrosion protection systems, welding and stress conditions of ships structures have presented uncertainties in terms of the localised corrosion. For example, the influence of environmentally assisted

cracking and microbial effects. More detailed investigation of the corrosion mechanisms is needed, specifically concentrating on localised corrosion with regard to the diverse range of coated internal tank structures;

(2) Corrosion data sets provided by ship surveys show large scatter patterns predominantly due to the complex environmental and operational conditions, or indeed any associated human and gauging errors, which are not normally noted in the survey reports. Also, complete data sets are rarely available in the public domain, and even if present are often limited to ship types (i.e., there is sparse information for double-hull tankers);

(3) There is a debate concerning whether a corrosion prediction model should rely on mechanistic principles or actual measurments collected from ship surveys. For the former (Melchers' model), the coating effect is excluded. As such, steel coupons may not be able to represent the corrosion behaviour of ship structures at larger scales or under stress. Moreover, no validation against survey data has been conducted, which lowers its practicability. Whereas in the latter, the quality of the model is entirely dependent on the corrosion data for which it may lose the adaptability to represent wide range of structures;

(4) The influencing factor (environmental and operational) is the most debatable aspect in corrosion predictions. To date, mathematical expressions of the corrosion rate have been corrected for environmental factors including temperature, dissolved oxygen, salinity and water velocity. However, it is not always easy to determine the parameters in these functions. The effect of the coating, as an operational factor, has been considered in some models, but at a rather empirical level. The corrosion mechanism of coated steels is not yet fully understood. Mathematical relations between chemical components and the corrosion rate for oil tanks have been proposed. However, the influence of the other operational factors can only be considered qualitatively. Factors such as the stress and strain experienced by the structural members, structural orientation, tank wash, ballast frequency, cleanliness of ballast water, and trade route have not been studied in detail, not to mention the correlations among them. It is worth thinking about the significance of the corrosion rate correction, and which parameter(s) has/have the most influence and cannot be ignored.

(5) The overall quality of a corrosion prediction model can be determined from two key aspects: (*i*) researchers seek models which are able to fully reflect the physical phenomenon by considering a number of variables and uncertainties; (*ii*) from an industry perspective where a corrosion model should be capable of predicting corrosion loss as accurately as possible given the fewest conditions. Thus, it is

essential to not only have a better understanding of the degradation mechanisms but also associate it with industries (ship design, survey, inspection and repair) effectively.

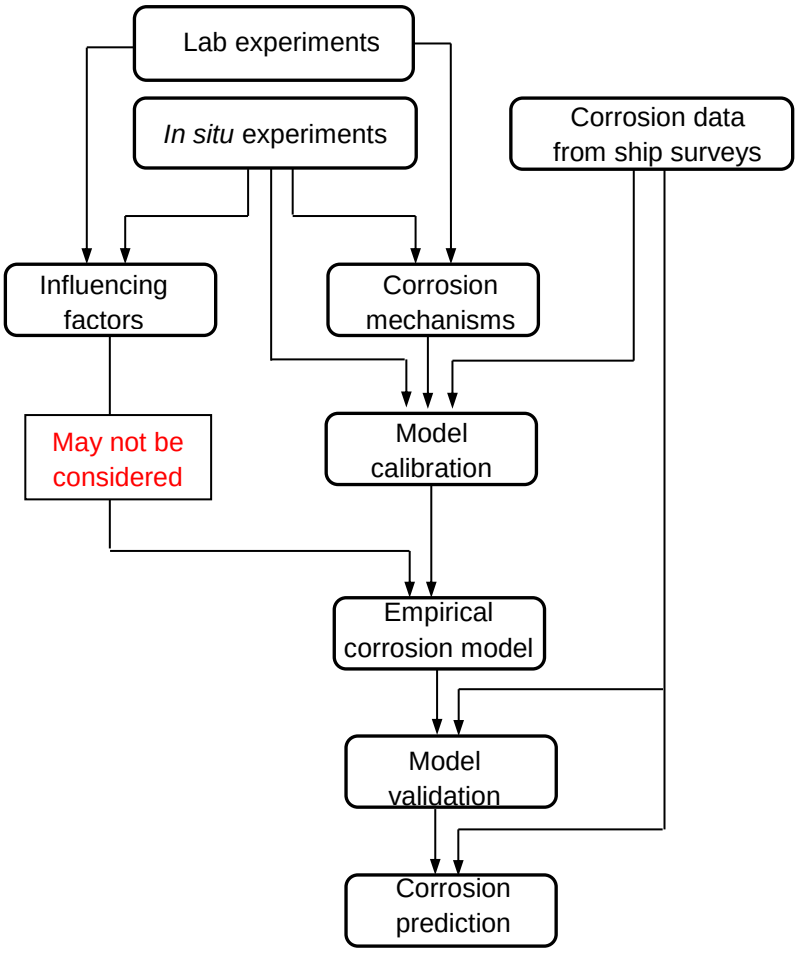

Figure 2.20. General procedure of corrosion prediction in the literature.

The strength capacity analysis of steel structures subject to corrosion damage has been reviewed covering both experimental and numerical methods. The experimental work is summarised in Table 2.18 and shows that tension and bending are the most frequently tested conditions. However, experiments are only able to provide the stress-strain relationship at discrete locations on specimens from strain gauges, with no information of the stress/strain distributions on an irregular surface. This research has proposed two novel full-field experimental techniques for steel plate specimens with damaged surface under uniaxial compression (shaded section in Table 2.18).

Table 2.18. Summary of the experimental analyses

	General corrosion		Localised corrosion	
	Plate element	Plate-stiffener	Plate element	Plate-stiffener
Compressive test	-	-	[7] [17]*	-
Tensile test	[49]* [99]* [110] [124]*	-	[17]* [49] [99]* [107] [110] [124]*	-
Shear test	-	-	-	-
Bending test	[110]	[113]	[110]	[113] [114]

*: samples with an actual corroded surface.

Table 2.19 outlines the numerical studies, where the nonlinear FEA is the preferential approach. Considerable effort has been made to assess the ultimate strength degradation induced by corrosion for both local structural members and global structural systems. However, to date, the effects of microbiological attack and stress-induced corrosion degradation which are often considered to be important mechanisms at an extended time scale have not been effectively incorporated. Also, the localised corrosion morphology has not been closely related to actual observations either from experiments or a ship survey. Welding effects including the residual stresses and grooving corrosion are routinely ignored. Uniaxial loading condition has been frequently used in modelling studies. However, the structural strength response to corrosion under combined loading has not been fully investigated. Most importantly, the numerical techniques vary significantly in detail, for example, iteration algorithm, element feature (type, size, aspect ratio) and boundary conditions. As models with greater complexity are being developed, the modelling techniques, which may significantly influence the result accuracy, were often not systematically reported and validated. Therefore, this research has first explored the modelling technique in detail, followed by simulation of localised corrosion (including microbial effect) informed by the coating failure diagram (Figure 2.18) and repair rules issued by classification societies. The weld-induced grooving corrosion was then studied on a plate-stiffener combination model with both geometric and welding imperfections (shaded sections in Table 2.19). The modelling studies have not only assessed the ultimate strength reduction related to corrosion, but also examined the stress concentrations and plastic strain distributions in detail.

Table 2.19. Summary of the numerical analysis

			Plate element			Plate-stiffener	
			No imperfection	Initial deflection	Initial deflection + residual stresses	Initial deflection	Initial deflection + residual stresses
Localised corrosion	Pitting	No use of corrosion prediction model	[105] [110]*	[7]* [48] [88] [93] [95] [96] [97] [101] [103] [107] [109] [111] [112] [117]	[104]	[113]* [114]*	[100]
		Use of corrosion prediction model	[49]* [110]*	-	-	-	-
	Grooving		-	-	-	-	-
	Edge		[105]	[88] [112] [117]	-	-	[100]
General corrosion	Actual corrosion pattern		[49]* [98]* [99]* [102]*	-	-	-	
	Mathematical surface determined by corrosion model		-	[29] [30] [31] [46] [93] [94] [106] [108] [109]	-	[108]	-

*: with experimental validations.

The mechano-chemistry theory provides greater insights into the material degradation scenario – synergistic effect of mechanical and chemical/electrochemical properties of a solid surface. To explore the fundamental changes in a stressed surface from the thermodynamic perspective, the phenomenon of environmentally assisted cracking has not been included in the review. Even though, the influence of elastic stress and plastic strain vary significantly owing to the selection of test materials/solutions and loading conditions. The former is directly associated with microstructural heterogeneity and the oxide film formation while the latter introduces complications in stress state, deformation of oxide layers and may alter the microstructures. The mechano-electrochemical performance of a metal surface can be sensitive to different factors and it is difficult to determine the individual influence. Also, there is yet an agreement on the quantification of such influences, for example, plastic strain. Theoretical methods have been proposed together with empirical estimations. However, most validations of such protocols are unclearly stated. A better understanding of the mechano-electrochemical mechanism is no doubtfully very beneficial to accurately estimate the enhanced corrosion rate or reduced corrosion potential, and hence to lead to more targeted corrosion inspections and optimised maintenance schedules. The mechano-eletrochemical formulas have been imbedded in the modelling work in this research to generate a map of corrosion acceleration locations and quantify the increased corrosion rate.

Although a regular ship survey is required by classification societies, the inspection frequency and locations are largely based on the previous experience. Further effort is essential to clearly identify the extent of corrosion damage, check the strength capacity (ultimate strength) of the corroded members, and most importantly predict the ‘hot spot’ locations of corrosion acceleration especially for the internal structures within ships, which are often failed to be maintained properly by the owners/operators [92].

Overall, there is an increasing necessity to seek new insights between the state-of-the-art and the practical aspects of structural assessment [122], and determine the partial safety factor associated with the uncertainties of corrosion.

Chapter 3 Methodology

As discussed in Chapter 1 and the end of Chapter 2, this research will focus on the mechanical and mechano-electrochemical performance of local thin-walled steel structures subject to corrosion damage. Nonlinear FEA was adopted as a primary tool to conduct the strength assessment. Experimental techniques including thermoelastic stress analysis (TSA) and digital image correlation (DIC) were also used to provide full-field measurements of surface stress/strain distributions as a validation of the models as well as a physical measurement of stress concentration and deformation. In addition, a numerical methodology was developed to estimate the mechano-electrochemical properties based on the FEA results, aiming to predict corrosion acceleration at 'hot spot' locations induced by mechanical stress and deformation and to quantify the increased corrosion rate.

3.1 Nonlinear FEA

A static analysis was performed in ANSYS 14.0 [158] using ANSYS parametric design language (APDL). Large deflection option was used to achieve the geometric nonlinearity, while bilinear isotropic hardening option was adopted for the material nonlinearity. Bilinear isotropic hardening material model uses the von Mises yield criteria coupled with an isotropic work hardening assumption and is preferred for large strain analysis [158]. The Full Newton-Raphson solver was used to calculate the plasticity during the loading process. Automatic time stepping and line search were activated to help achieve the convergence. The convergence values (tolerance) for both displacement and force were set to be 5% (mm and N). A typical procedure of the nonlinear FEA is outlined in Figure 3.1 with detailed settings given in Table 3.1. Since this study has focused on the buckling collapse of structures, instabilities were observed for some situations due to a large displacement for a small load increment, resulting in converging difficulties. To tackle this issue, an artificial damper element was introduced in each node based on an energy dissipation ratio, which ranges from 0 to 1. A high ratio could result in a better convergence, in expense of a stiffer structure and hence may affect the accuracy. Throughout the numerical studies, the energy dissipation ratio was kept to be around 0.01%, which is below the suggested 1% in Ref. [158].

For thin-walled structures, shell and solid elements are frequently used depending on the complexity of the structural geometry and the degree of details required from the results.

The behaviour and selection of the element types will be explored in detail in Section 4.1. Initial geometric imperfections were applied based on the frequently observed deflection shapes for all models as well as to initiate the buckling phenomenon. The application of the initial deflection was achieved by assigning the desired values as displacement loading for every node. After solving the constrained model, only the nodal locations (geometry) were updated and the degrees of freedom (DOFs) were cleaned up. Residual stresses can be introduced by performing a thermal FEA to simulate the welding procedure with a series of temperature-dependent thermal/mechanical properties of steel, a certain welding condition (current, voltage, heating time, speed, et cetera) and using element birth/death to represent the welding material. However, the magnitude of the residual stresses and deformation will entirely depend on the material properties and the welding condition used. Besides, the benchmark study reported in Ref. [92] shows both the thermal FEA and a representative residual stress matrix as introduced in Section 2.2.1.3 result in similar residual stress profile and stress-strain behaviour. Therefore, it was decided to explicitly prescribe representative residual stresses to the structure by keeping the initial deflection unchanged. Based on the stress equations (Equations 2.15 and 2.16) a stress matrix was formed consisting of stress records for every integration point in every element depending on the location of the element centroid. After the application of the initial deflection, the initial stress matrix was read and solved with all DOFs constrained in order to obtain the reaction force records for all elements. Next, the constraints needed to be cleared up and replaced with the real boundary conditions, followed by a calculation producer with two load steps. The initial stress matrix and the reaction force matrix needed to be read again in the first step to achieve the initial stress application with negligible additional deformation ($\times 10^{-5}$ mm). The external load was then added at the second step as an elastic-plastic analysis. It needs to be noted that the element size and number are essential for the residual stress application since the tensile/compressive area is judged by the element centroids. A coarse mesh especially at the HAZ boundary (change in the stress sign) will lead to an unbalanced internal stress and hence a false result. Once the nonlinear FEA was completed, the stress/strain values of the plates were derived for each substep in order to determine the load shortening or stress-strain curves and the ultimate strength.

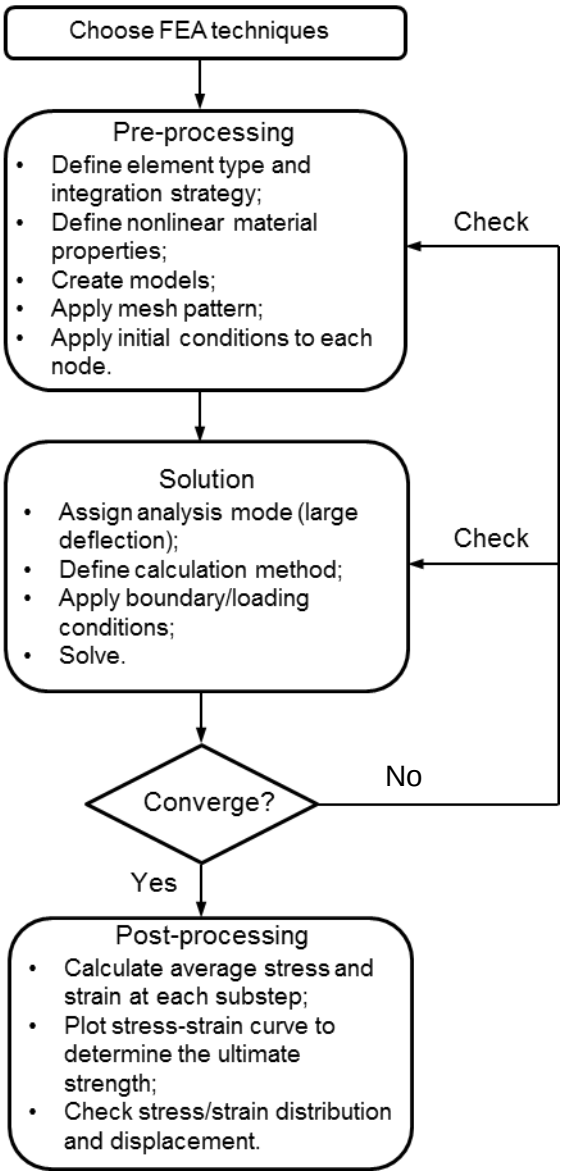

Figure 3.1. Flow chart of FEA procedure.

Table 3.1. Setting details for the Newton-Raphson solver

Options	APDL
Automatic time stepping	AUTOTS,ON
Substep number = 500	NSUBST,500
Write results for every substeps	OUTRES,ALL,ALL
Line search	LNSRCH,ON
Full Newton-Raphson	NROPT,FULL,,ON
Maximum iteration number = 500	NEQIT,500

3.2 Experimental technique – TSA

Based on the thermoelasticity theory, which was established in 1853 by Lord Kelvin [159], TSA is a well-established non-contacting technique, and is able to provide a full-field measurement of principal stresses over the specimen surface [160]. It has been widely used for structural analysis [160-163] to assess stress concentration and propagation around crack tips, manufacturing defects and development of fatigue damage. TSA technique is based on three assumptions [160]:

(1) The material behaviour is linearly elastic;
(2) The relevant material properties such as Young's modulus are not temperature dependent;
(3) The temperature change in the material is under an adiabatic condition.

For the isotropic material used in the experiments, the TSA technique is based on a first-order relationship between the principal stress (σ_1 and σ_2) change and the temperature change, using the following expression [164]:

$$\Delta T = -\frac{\alpha_{\mathrm{T}} T}{\rho C_{\mathrm{p}}} \Delta(\sigma_1 + \sigma_2) \tag{3.1}$$

where α_{T} is the coefficient of thermal expansion, ρ is the density of the material, C_{p} is the specific heat at a constant pressure, T is the absolute temperature of the specimen surface and $\Delta(\sigma_1 + \sigma_2)$ is the sum of the principal surface stresses. The expression $\alpha_{\mathrm{T}}/(\rho C_{\mathrm{p}})$ is referred as the thermoelastic constant of the material and is often denoted by K. Therefore, Equation 3.1 can be simplified as:

$$\Delta T = -KT\Delta(\sigma_1 + \sigma_2) \tag{3.2}$$

To calibrate and process the thermoelastic signals, the constant K can be determined experimentally from a standard uniaxial tensile test on a calibration specimen. Knowing the cross-sectional area and applied tensile load, σ_1 can be obtained and hence the K value. Once K is known, the TSA data can be transformed to give a full-field stress contour plot.

A cyclic loading is necessary to ensure an adiabatic thermal condition, under which the surface temperature change associated with the stress change can be monitored by an infrared detector. Most infrared detectors implement a charge-coupled device (CCD) to

obtain the digital signal which is proportional to the illumination intensity. Figure 3.2 illustrates the procedure of a single point of light being converted to a digital signal. To achieve the full-field measurement, it is necessary to use a CCD array consisting of multiple squares of semi-conductor material. Therefore multiple points of light intensity can be detected, and hence a full-field map. The resulting digital signals are then processed into either temperature or phase data. Particularly, the number of pixels within the CCD array and the image frequency/capture rate are the two most important parameters to determine the TSA image resolution. A certain degree of noise always exists in CCD arrays but can be reduced when CCD is cooled.

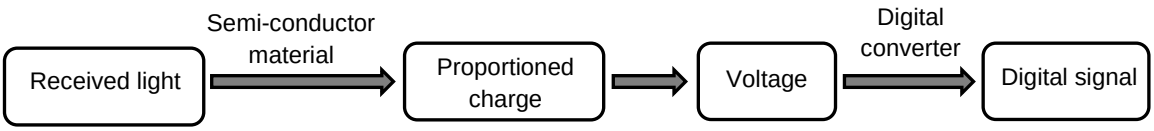

Figure 3.2. CCD process of a single light point.

TSA requires a uniformly high emissivity over the specimen surface for which the radiant energy can be measured quantitatively. For metallic materials, a thin layer of matt black paint needs to be applied on the tested area to standardise the emissivity. A higher emissivity will generate a more accurate signal especially when the temperature change is small. Any variation of the emissivity across the specimen surface could lead to non-stress-related temperature changes [165]. In addition, a surface finish of poor quality may result in a too reflective surface and a radiation from ambient sources other than the specimen. The loading frequency and the painting thickness have no direct effect on the temperature results. However, the frequency should be sufficiently high to ensure minimal heat loss to the ambient environment. If the frequency is too high, there will be insufficiently heat flow through the coating to maintain the temperature change, while an overly thick coating could act as a thermal insulator and result in temperature attenuation. Therefore, to achieve a result of high accuracy, the loading frequency and coating thickness were applied based on a previous comprehensive TSA study for steel specimens [165].

Since the mechanical behaviour in the elastic regime is less dependent of the load direction (tensile/compressive), a servo-hydraulic test machine (Instron 8802) was used in this study to provide a sinusoidal cyclic tensile loading (20 ± 15 kN at 10 Hz) and hence the adiabatic thermal condition The temperature change was captured by an infrared detector with a 320×256 pixel field of view at 383 Hz. The detector is calibrated annually

therefore the error in the temperature data could be neglected compared to the system noise. The inbuilt 27 mm lens was used in the tests at a distance of 150 mm. Steel rigs were designed for TSA specimens to transform the load from the test machine to a uniform stress along the specimen edges by using three M8 bolts on each side. In order to maintain a uniaxial loading direction, two lubricated (copper grease) free-rolling pins were adopted to connect the rigs and the test machine jaws. The experimental set-up is shown in Figure 3.3. Matt black paint with a thickness of 10 to 25 μm was applied over the specimen surface. Software Altair was used to process the data.

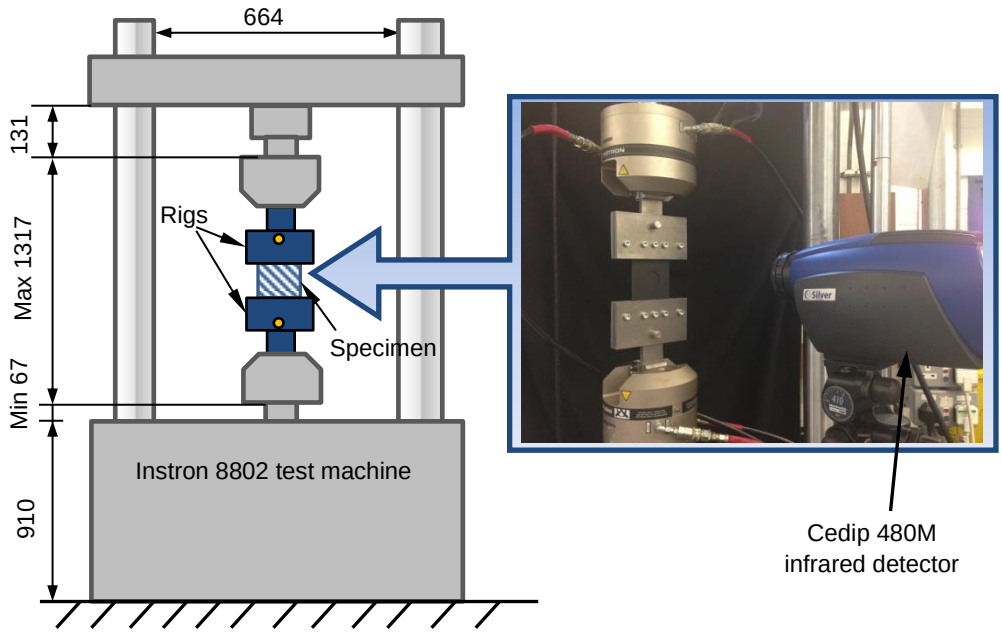

Figure 3.3. TSA experimental set-up (all dimensions are in mm).

3.3 Experimental technique – DIC

DIC enables a full-field measurement of deformation and displacement and has been successfully utilised in monitoring crack propagations [166-168] and large plastic deformation of various materials [169,170]. The concept is to evaluate the object deformation by tracking deformation of a random pattern in an image (Figure 3.4). Each pixel within an image has a gray value. Generally, it is impossible to identify one pixel in the reference image and in the deformed image, since the same gray value can be found for a significant number of other pixels. To overcome the correspondence problem uniquely during a deformation, DIC applies a stochastic speckle pattern to provide information of a small aperture (subset or interrogation cell) for pattern matching on the

specimen surface. The speckle pattern is typically achieved using black paint spatter on a white paint or vice versa, so that each subset would be statistically different from any other ones [171]. The motion estimation method is based on minimising the squared difference in gray values, namely a summation of squares deviation. The correlation function is expressed as [172]:

$$C(m,n,u,v) = \sum_{i,j=-N/2}^{N/2} [G(m+u+i, n+v+j) - F(m+i, n+j)]^2 \quad (3.3)$$

where m and n denote the pixel location in the reference image; u and v represent the displacements of the subset centre from the reference (undeformed) image to the deformed image; N is the size of the subset; G and F are the gray value matrices of deformed and reference images, respectively. Detailed information of DIC can be found in Ref. [172].

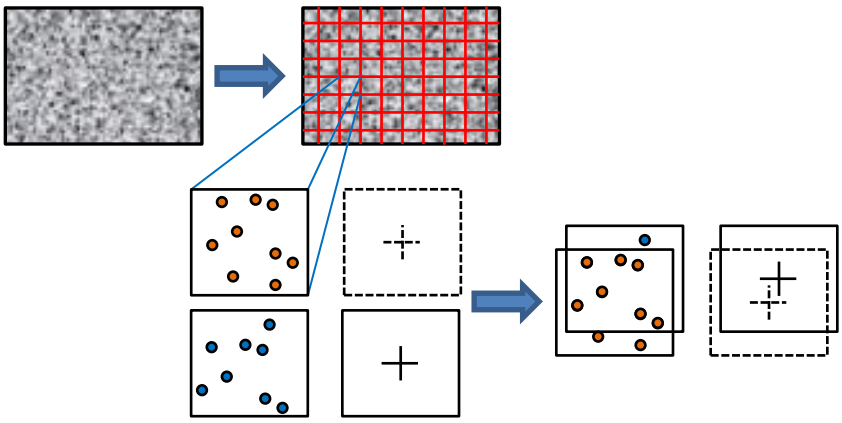

Figure 3.4. Pattern matching of DIC technique [173].

The calculation of the correlation between subsets in the reference image and the deformed image can be carried out using various algorithms such as the least squares matching (LSM), Bayesian probability methods and fast Fourier transform. For the current study LaVision DaVis 8.1.0 correlation software was adopted to employ a LSM algorithm and iteratively approximate the deformation [173]. The iteration starts from the selected seeding point(s) and the analysed region grows with the existing information being used as a predictor for a possible match. Once identifying all subsets in the deformed image, the displacement data can be converted to Lagrangian strain tensor or engineering strain for the area of interest. Once the surface deformations are obtained, DaVis uses a central difference scheme to compute the strain values [173]. For instance, at any location (m,n),

strain in *x*-direction $\varepsilon_x(m,n)$ is evaluated numerically using the displacement vectors to the left $V_x(m-1,n)$ and right $V_x(m+1,n)$ (or top and bottom for *y*-direction):

$$\varepsilon_x(m,n) = [V_x(m+1,n) - V_x(m,n) + V_x(m,n) - V_x(m-1,n)]/2g \quad (3.4)$$

where g is the grid spacing determined as $g = \text{Subset size}/[100/(100 - \text{Overlap})]$ with overlap in percentage. When assessing the edge of the grid, a simple forward differencing is used instead whereby the strain is calculated using the difference between immediate neighbouring displacement vectors. As described above, a single CCD camera is sufficient to capture in-plane displacements. However, it cannot distinguish uniform strain from uniform out-of-plane displacement [166]. By using a two-camera stereo set-up, the calibration process helps build a 'working volume' and informs the positions of the two cameras relative to each other [174] to calculate the out-of-plane deformation.

The experimental considerations for DIC include the surface preparation, the brightness and post-processing settings [174]. In order to capture the physical movement of the specimen and enhance contrast, a surface preparation of a random speckle pattern (black speckles on white or vice versa) is of vital importance. The speckle size needs to be increased as the field becomes large. The optimum size for the speckles is a few pixels across. Smaller speckles may lead to a loss in the pattern contrast while less information is obtained using overly large speckles [166]. A detailed analysis of the speckle pattern quality can be found in Ref. [175]. The illumination and contrast condition need to be checked before recording to avoid saturation. In post-processing, the precision of the displacement measurements and the spacial resolution are largely dependent on the subset size and the number of pixels within the image [168]. Since every single subset represents the average displacement values of all features included, it should be large enough (minimum 2 × 2 to 4 × 4 pixels^2) to incorporate sufficient information for the system to recognise in the next image. Thus, a larger subset results in a higher precision in the displacement/strain results but with compromising the spatial resolution and the computing time. In general, maximising the number of pixels in one subset and the number of subsets for the whole image should be well balanced. For LSM algorithm used in this software, seeding points are needed as starting points to determine the deformation. Ideally, seeding points should be located in the viewing area where minimal movement is expected [173]. However, within each region the subset match may not be calculated robustly, resulting in some regions not analysed. Therefore, the definition of multiple seeding points may be necessary to enlarge the analysis area.

In this study, the servo-hydraulic test machine Instron 8032 was used to provide a quasi-static uniaxial compressive loading by displacement control (1 mm min^{-1}). The weight of the specimen and the rigs was balanced out prior to external load. Prior to the buckling tests, the initial deflections of all specimens were measured using an Aberlink 3D Faro Arm at discrete locations (Figure A4.1 in Appendix 4). To facilitate the modelling process for comparison, surface fittings were performed to obtain a polynomial function (Figure A4.2 in Appendix 4), based on which the nodal location was updated to generate a plate model with real deflection. The 3D DIC system was adopted to capture the out-of-plane deformation due to buckling failure. Two 5 MP 12 bit monochromatic LaVision E-lite CCD cameras were used with two Sigma 105 lenses (Figure 3.5 (b)). The cameras were positioned with the viewing directions 30° relative to each other in front of the specimen. A floodlight was used to enhance the illumination. The deformation was recorded at a frequency of 1 Hz, including the load and displacement provided by the Instron machine. Steel rigs were designed specifically for such thin plate compressive tests, as shown in Figure 3.5 (a), where the two lubricated pillars were press fit at the bottom and free slide at the top, aiming to achieve a uniform in-plane compressive stress. For specimen surface finish, black paint with white speckles was applied. The average speckle size was five pixels across and the spatial resolution was 24.4 pixels mm^{-1}.

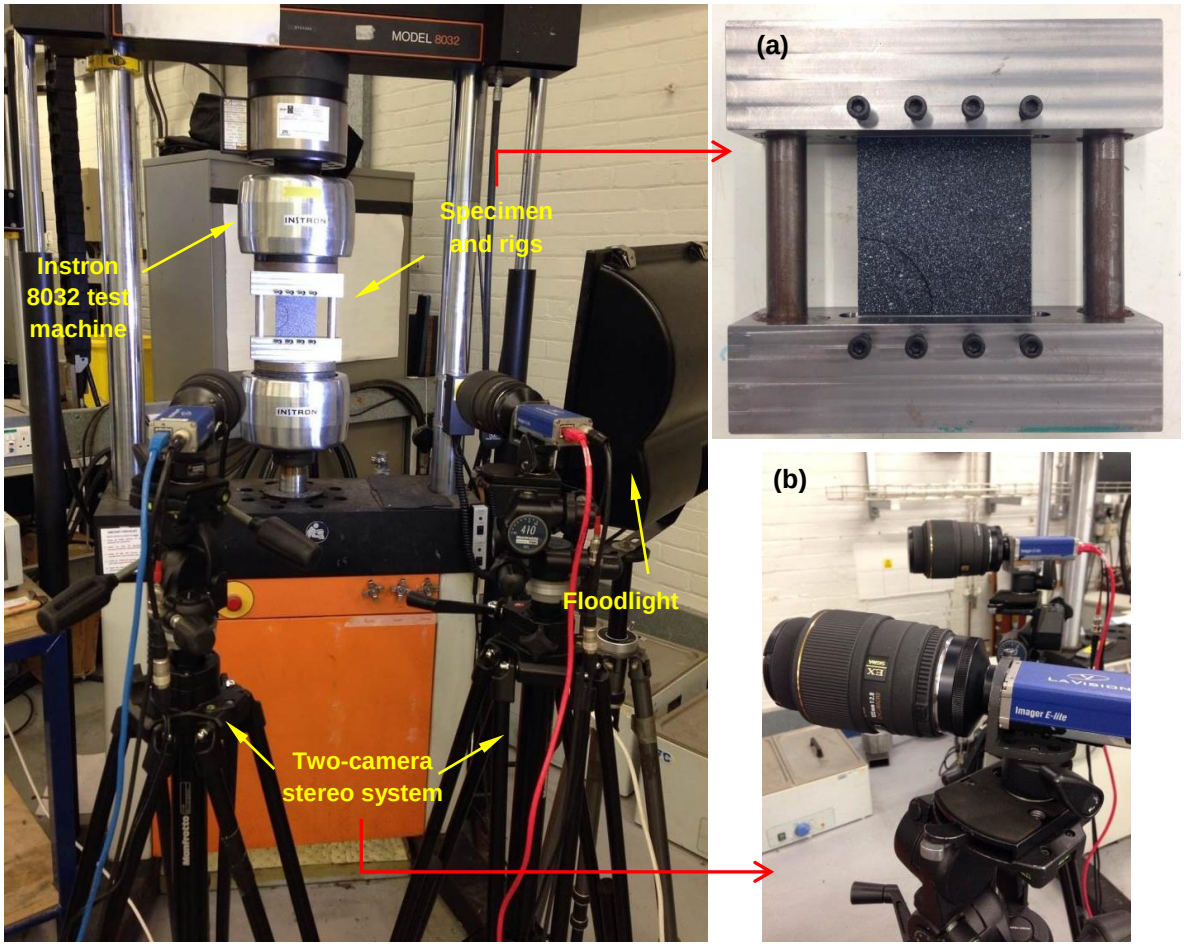

Figure 3.5. 3D DIC experimental set-up: (a) specimen and rigs; (b) a 3D camera system including two Sigma 105 mm lenses and two 5 MP 12 bit monochromatic LaVision E-lite CCD cameras.

3.4 Mechano-electrochemical analysis

The mechano-electrochemical analysis was carried out numerically based on Gutman's methods introduced in Section 2.3 and the FEA results. Based on Gutman's theory [127], when a solid surface is elastically stressed, the spherical part of the macroscopic stress tensor (hydrostatic pressure) will increase the macroscopic chemical potential in the surface and increase the corrosion kinetics (Equations 2.17 and 2.18). When further increases in the load occur, a local change in the equilibrium potential induced by plastic deformation is given as Equation 2.20. The plastic deformation is realised as micro shear strain $\Delta\gamma$ and the increase in the dislocation density ΔN (cm^{-2}) with hardening stress $\Delta\tau$ (MPa) is [127];

$$\Delta N = N_0 \left(\exp \frac{n\Delta\tau}{\bar{\alpha} k N_{\max} T} - 1 \right) \tag{3.5}$$

where N_0 is the dislocation density (cm^{-2}) at $\Delta\tau = 0$ (approximately 10^8 cm^{-2} [127]). n is the number of dislocation in planar pile-ups; $\bar{\alpha}$ is equal between 10^9 and 10^{11} cm^{-2}; k is the Boltzmann constant for a system of particles representing unit dislocations (J K^{-1} cm) and T is the temperature (K). Thus, the macro plastic strain can be expressed as [127]:

$$\Delta\varepsilon = \frac{\Delta\gamma}{\upsilon} = \frac{N_0}{\bar{\alpha}\upsilon}\left(\exp\frac{n\Delta\tau}{\bar{\alpha}kN_{\max}T} - 1\right) \tag{3.6}$$

where υ is the orientation-dependent factor (which is equal to 0.45 for tensile condition [127]). If a steel structure is loaded until it reaches its ultimate strength with plasticity occurring to a certain extent and left under stress, the overall increase in the equilibrium potential of the structure surface should be the summation of the elastic and plastic effects. By taking into account Equations 3.5 and 3.6, the overall enhanced anodic current density is [127]:

$$i_{\mathrm{a}} = i_{\mathrm{a0}}\exp\left(\frac{\sigma_{\mathrm{m}}V_{\mathrm{m}}}{RT} + \frac{n\Delta\tau}{\bar{\alpha}kN_{\max}T}\right) = i_{\mathrm{a0}}\exp\frac{\sigma_{\mathrm{m}}V_{\mathrm{m}}}{RT}\left(\frac{\Delta\varepsilon}{\varepsilon_0} + 1\right) \tag{3.7}$$

where ε_0 represents the onset of plastic strain. From Equation 3.7 it can be seen that the contribution of mechanical property to the potential or current change should consist of the spherical part of the applied stress and the plastic strain. By substituting $V_{\mathrm{m}} = 7.09 \times 10^{-6}$ m^3 mol^{-1} for iron and $\varepsilon_0 = \sigma_{\mathrm{y}}/E$, the ratio of the local anodic current density of a stressed structure to the unstressed condition can be estimated. It needs to be emphasised that when a solid is experiencing a multi-component elastic-plastic stress state due to an out-of-plane deformation, $\Delta\varepsilon$ cannot be taken as the axial plastic strain even though the external loading is uniaxial. Since the von Mises criterion was used to judge the onset of yielding, the plastic strain will only be developed when the equivalent (von Mises) stress is equal to the yielding stress of the material. The concept of equivalent stress/strain is used as a scalar value to simplify the stress state to the uniaxial condition by keeping the unit distortion strain energy the same. Therefore, $\Delta\varepsilon$ was treated as the equivalent plastic strain for this study. It was assumed that the initial structural surface was anodic and the structural members were located in a cargo oil tank, where the average temperature was set to be 60°C. The corrosion process was activation controlled due to the very low oxygen level (below 5%) [3]. The influence of a polymeric coating was not considered here. When the plate was loaded up to the ultimate strength stage, both the hydrostatic stress σ_{m} and the equivalent plastic strain $\Delta\varepsilon$ were readily obtained for every element from

the numerical models. Utilising Equation 3.7, the anodic current density increment ratio ($i_{\mathrm{a}}/i_{\mathrm{a0}}$) can be calculated.

Chapter 4 Validation of nonlinear FEA

To gain familiarity and confidence with the nonlinear FEA method, this chapter details the numerical validation conducted for thin-walled structure simulation. The validation consists of two parts: (1) eigenvalue buckling analysis, which was used to inform the behaviour of various element types commonly used for thin-wall structure analysis; (2) replicated models of local structural members including plates, stiffened plates (plate-stiffener combinations) and a stiffened panel. The application of initial imperfections (deflection and weld-induced residual stresses) was also taken into account.

4.1 Eigenvalue buckling analysis

Elastic buckling behaviour, in which the buckling stress is below the yield stress or the proportional limit of the material, has been extensively studied and documented for thin plates [176-179]. Since the material and geometric nonlinearities and initial imperfections are ignored during the analysis, the eigenvalue buckling load is normally utilised for structural design with a correction factor considering the plasticity behaviour (Equation 2.8) [86]. Although it has been agreed that the ultimate strength is more of a consistent basis for an economical structural design [86], due to the loading similarity with the future nonlinear corrosion models, simple calculation procedure and fast processing time, a series of eigenvalue buckling analysis has been conducted to assess the feasibility of the selection of the element type, element shape/size and boundary condition. The values of the critical loading and the maximum deflection derived from FEA were compared with analytical solutions, which were based on two plate theories, namely classical thin plate theory (Kirchhoff plate theory) and first order shear deformation plate theory (Mindlin-Reissner plate theory). Detailed descriptions of the two theories can be found in Appendix 2. To compensate the actual parabolic transverse shear strain distribution through the thickness, a shear correction factor $\kappa^2 = 5/6$ [180] was used in the Mindlin-Reissner theory.

A square steel plate (Grade 070M20) with dimensions of 90 mm × 90 mm × 3 mm (used for TSA/DIC experiments later on) was taken as an example for modelling. Key properties of the sample plate are listed in Table 4.1. Regarding the element type, shell elements SHELL63, SHELL181 and SHELL281 were assessed initially as predominant element types for thin-walled structural analysis. Solid-shell (SOLSH190) and 3D solid elements

(SOLID185 and SOLID186) were also considered in order to fully define the geometry of a corroded surface.

Table 4.1. Key properties of Grade 070M20 steel plate

Properties	Values
Dimensions / mm	90 × 90 × 3
***E* / Pa**	2.05×10^{11}
***G* / Pa**	7.23×10^{10}
ν	0.3
ρ / kg m^{-3}	7870
***D* / Pa m^3**	464.84
κ^2	5/6

Critical buckling loads were derived for both Kirchhoff and Mindlin plates using Equations 46 and 49 in Appendix 2. The first three buckling modes ($m = 1, 2$ and 3; $n = 1$) were studied (Table 4.2). The mode shapes are shown in Figure 4.1.

Table 4.2. Analytical solution of the buckling load

Buckling mode		$T_{\text{cr (Kirchhoff)}}$	$T_{\text{cr (Mindlin)}}$
m	***n***	**/ kN**	**/ kN**
1	**1**	203.90	201.38
2	**1**	318.59	312.47
3	**1**	566.39	547.33

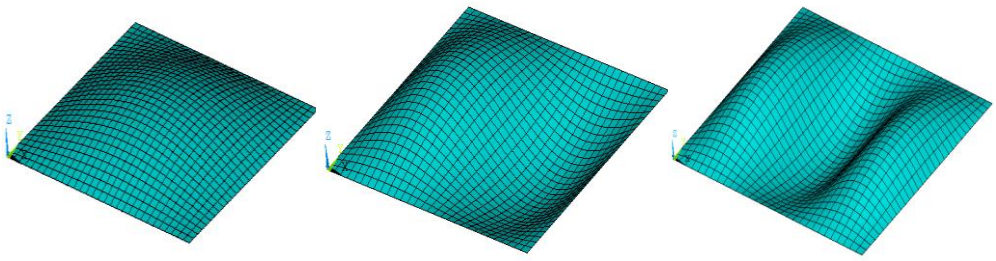

(a) **(b)** **(c)**

Figure 4.1. Buckling mode shapes: (a) the 1st (*m*=1, *n*=1); (b) the 2nd (*m*=2, *n*=1); (c) the 3rd (*m*=3, *n*=1).

4.1.1 Shell elements

In ANSYS, 4-node shell element SHELL63 is based on the thin plate theory (Kirchhoff plate theory) neglecting the effect of shear deflection through thickness. It has six DOFs at each node (translations in x-, y- and z-directions and rotations about the nodal x-, y- and

z-axes). However, SHELL63 is often found not to be able to provide accurate results along plate edges, for plate openings and other kinds of defects. Consequently, based on the thick plate theory (Mindlin plate theory), SHELL181 has been widely used for plate strength analysis considering corrosion damage [88,93,96,97,111,117]. Similarly, SHELL181 also has four nodes with six DOFs at each node. Stress and strain results are provided at mid-thickness of the element. Key option KEYOPT(1) = 2 could be used to evaluate stresses and strains on exterior surfaces. Reduced integration (RI) (KEYOPT(3) = 0) is the default option especially for nonlinear applications. However, full integration (FI) with incompatible modes (KEYOPT(3) = 2) is recommended due to its high accuracy even with relatively coarse mesh [158]. Even so, when mapped mesh or quadrilateral-shaped elements are difficult to adopt for irregular geometric patterns, SHELL181 tends to give poor accuracy regardless of the element size. Therefore, a higher version of shell element SHELL281 with eight nodes and six DOFs was also considered. The triangle-shaped element (six nodes) of SHELL281 was used primarily as a free mesh for the corrosion modelling. Simply supported boundary condition was assigned for the models with six constraining methods tested (Figure 4.2) as frequently used in the literature.

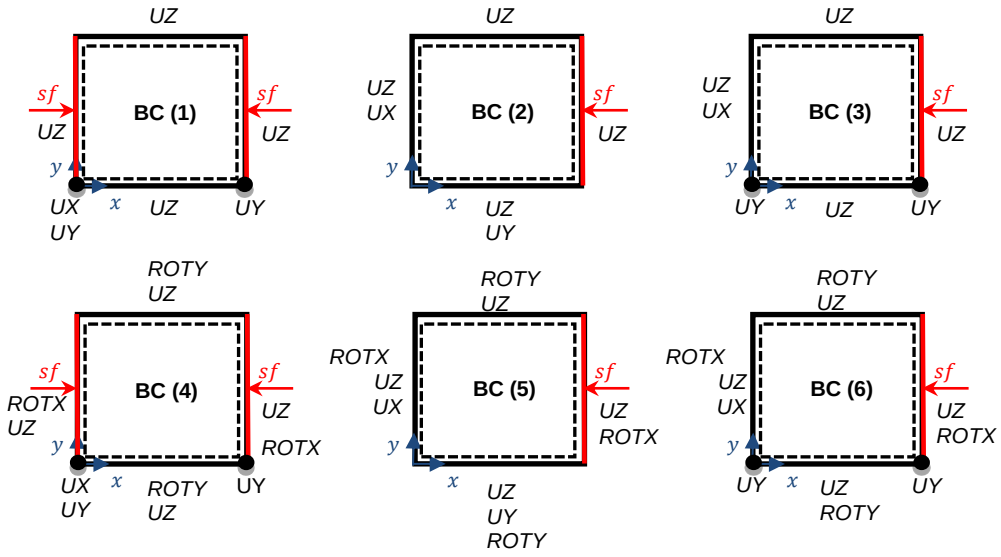

Figure 4.2. Boundary conditions for shell elements (*UX*, *UY*, *UZ*: zero translation in *x*-, *y*- and *z*-directions; *ROTX*, *ROTY*: zero rotation about *x*- and *y*-axis; *sf*: surface load).

Boundary conditions BCs (1) to (3) and (4) to (6) were studied first for both SHELL63 and SHELL181/SHELL281, respectively, using quadrilateral-shaped element with the same element size (3 mm × 3 mm). It was found that SHELL63 gave the similar results under BCs (1) to (3), so did SHELL181 and SHELL281 under BCs (4) to (6). The errors

calculated according to Equation 4.1 are listed in Table 4.3. It can be seen that the boundary conditions used for the modelling correspond well with the theoretical condition.

$$Error\ (\%) = \frac{T_{\mathrm{cr(analytical)}} - T_{\mathrm{cr(numerical)}}}{T_{\mathrm{cr(analytical)}}} \times 100 \tag{4.1}$$

Table 4.3. Boundary conditions check – shell (element size: 3 mm ×3 mm)

Buckling mode		$T_{\mathrm{cr\ (Kirchhoff)}}$	$T_{\mathrm{cr\ (SHELL63)}}$	Error	$T_{\mathrm{cr\ (Mindlin)}}$	$T_{\mathrm{cr\ (SHELL181)}}$	Error	$T_{\mathrm{cr\ (SHELL281)}}$	Error
m	***n***	**/ kN**	/ kN	/ %	**/ kN**	/ kN	/ %	/ kN	/ %
1	**1**	**203.90**	203.77	0.06	**201.38**	203.04	-0.83	202.63	-0.62
2	**1**	**318.59**	318.21	0.12	**312.47**	315.37	-0.93	313.69	-0.39
3	**1**	**566.39**	565.45	0.17	**547.33**	556.67	-1.71	549.24	-0.35

Using the boundary conditions described above, the effect of the element size is shown in Figure 4.3. Both FI and RI were considered for SHELL181. It can be seen that the accuracy of these three shell elements decreases when increasing the element size. In general, SHELL63 tends to provide lower load values compared to the analytical solution while SHELL181 and SHELL281 led to higher estimates, indicating that the modelling results lie in between Kirchhoff and Mindlin solutions. Moreover, the accuracy for higher buckling modes is lower. Particularly, the result of the 3rd buckling mode given by SHELL181 shows a rather high error (up to 14%) when a coarse mesh (large element size) is used. It is believed that for the 2nd and the 3rd buckling modes, more complex mode shapes are generated (Figure 4.1), and the change of the deflection over the plate surface is difficult to be fully described using large element size. In terms of the integration strategy, FI with incompatible modes (KEYOPT(3) = 2) gives slightly better estimates compared to RI (KEYOPT(3) = 0), especially when the element size is increased. The number of integration points through element thickness does not affect the accuracy. Using triangle-shaped elements, SHELL281 gives better prediction compared to SHELL181 in general.

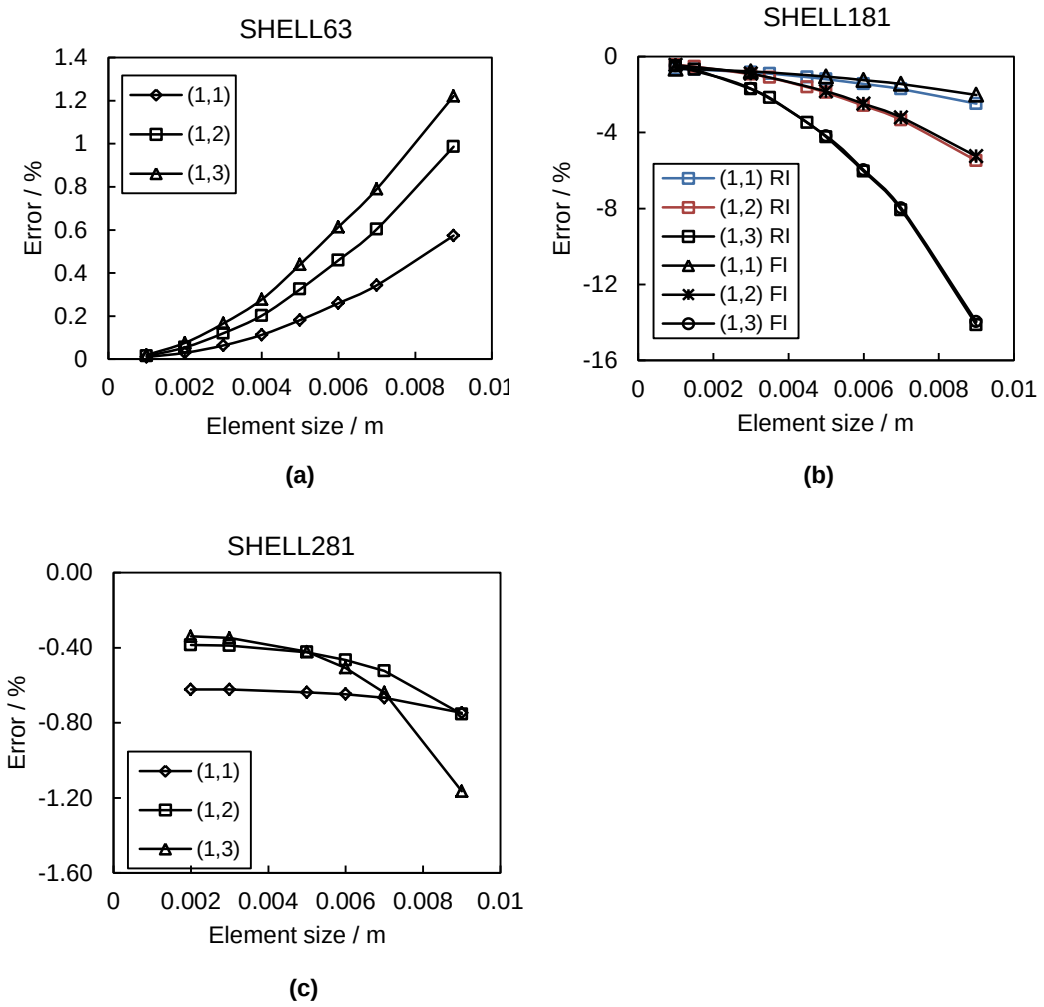

Figure 4.3. Effect of element size: (a) SHELL63; (b) SHELL181 (RI: reduced integration; FI: full integration); (c) SHELL281.

4.1.2 Solid-shell and solid elements

Compared to classical shell elements, which represent the mid-surface of a thin structure with plane stress assumptions, the 3D 8-node solid-shell element SOLSH190 in theory has a better ability to simulate the geometry of a more complex structure and gives more accurate predictions. It has three DOFs (translations in the nodal x-, y- and z-directions) at each node. The Mindlin plate theory is implemented. For a single layer, two integration points are used through the thickness by default. Enhanced transverse shear strains can be activated (KEYOPT(2) = 1) leading to quadratic transverse shear strain distributions through thickness. The SOLSH190 results were compared with the analytical solution using the Mindlin theory. The solid element SOLID185 has also been used for 3D modelling. Similar to SOLSH190, it is also an 8-node element with three translation DOFs at each node. SOLID186, defined by 20 nodes and exhibiting quadratic displacement

behaviour, is the higher-order version of SOLID185. Although it is generally considered that solid elements could provide the most accurate prediction, two numerical problems, namely shear locking and hourglassing, could lead to faulty results. Shear locking particularly refers to an overly stiff response (edges are unable to curve) of first order brick element, such as SOLID185. The RI or the second order solid element (SOLID186) is normally used to overcome such problem. However using RI may suffer the so-called hourglassing problem, by making the element excessively flexible. The number of elements through thickness is predominantly related to this problem. In this section, key settings (boundary condition, number of elements through thickness, integration strategy and size/shape of the element) will be explored to give a better understanding of the behaviour of the abovementioned element types for the future corrosion modelling.

Since more than one element can be defined through thickness, new constraining methods need to be applied to achieve the simply support condition. SOLSH190 was used to test the constraining methods, which are illustrated in Figure 4.4 with two elements through thickness and the element size on surfaces being 3 mm × 3 mm.

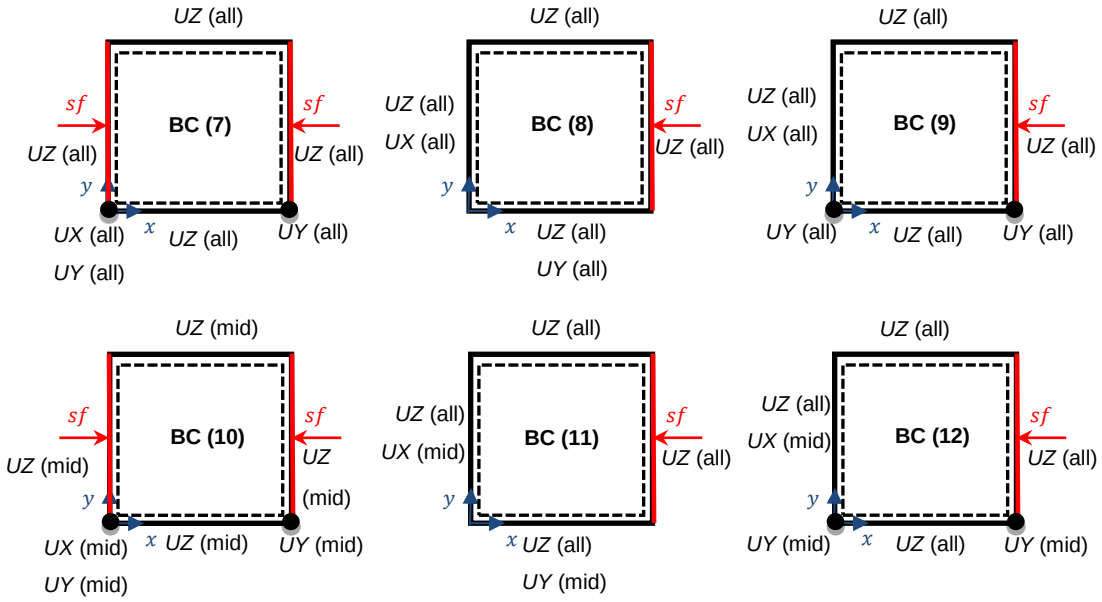

Figure 4.4. Boundary conditions for solid elements: (all) = all nodes through thickness; (mid) = nodes at mid-thickness (*UX*, *UY*, *UZ*: zero translation in *x*-, *y*- and *z*-directions; *sf*: surface load).

Results derived from Equation 4.1 are listed in Table 4.4, from which it can be seen that BCs (7), (11) and (12) give the best predictions. However, BCs (11) and (12) can only be used when the number of elements through thickness is even.

Table 4.4. Boundary conditions check – SOLSH190

Buckling mode		$T_{cr\ (Mindlin)}$	$T_{cr\ BC(7)}$	Error	$T_{cr\ BC(8)}$	Error	$T_{cr\ BC(9)}$	Error
m	***n***	**/ kN**	/ kN	/ %	/ kN	/ %	/ kN	/ %
1	**1**	**203.90**	200.24	0.56	313.71	-55.78	243.77	-21.05
2	**1**	**318.59**	314.38	-0.61	457.89	-46.54	422.47	-35.20
3	**1**	**566.39**	561.99	-2.68	741.74	-35.52	721.37	-31.80

Buckling mode		$T_{cr\ (Mindlin)}$	$T_{cr\ BC(10)}$	Error	$T_{cr\ BC(11)}$	Error	$T_{cr\ BC(12)}$	Error
m	***n***	**/ kN**	/ kN	/ %	/ kN	/ %	/ kN	/ %
1	**1**	**203.90**	199.68	0.84	200.15	0.61	200.13	0.62
2	**1**	**318.59**	313.76	-0.41	314.37	-0.61	314.39	-0.61
3	**1**	**566.39**	561.09	-2.51	562.13	-2.70	562.17	-2.71

The effect of the number of elements through thickness (examples in Figure 4.5) and the integration strategy are shown in Figure 4.6 using BCs (7) and (11). During the test it was found that RI and the default FI could lead to high errors for SOLID185 due to the shear locking and hourglassing problems. Therefore, only FI with enhanced strain formulation (KEYOPT(2) = 2) was shown here for SOLID185. The critical loads of the first buckling mode are plotted. The element size on the surfaces was set to be 3 mm × 3 mm, which leads to good results using SHELL181.

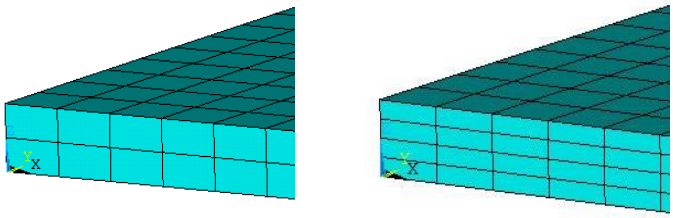

(a) **(b)**

Figure 4.5. Examples of different number of elements through thickness: (a) two elements; (b) four elements.

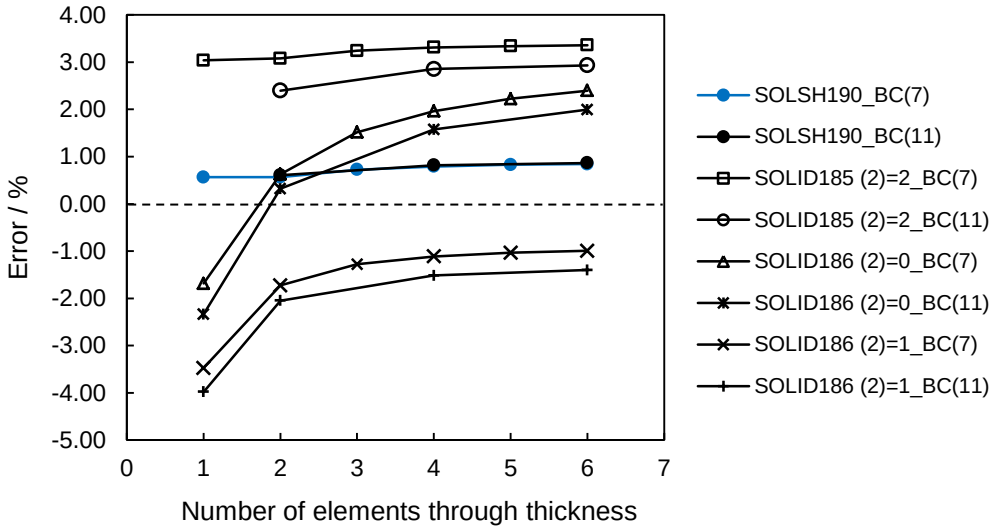

Figure 4.6. Effects of the number of elements and integration strategy (SOLID185 (2)=2: FI with enhanced strain formulation; SOLID186 (2)=0: RI; SOLID186 (2)=1: default FI).

Figure 4.6 shows that SOLSH190 gives the best results compared with solid elements. With mid-nodes in the elements, SOLID186 is more accurate than SOLID185. For the two solid elements, little difference was found between BCs (7) and (11). Similar tests were also carried out using BC (12) with the same accuracy generated as BC (11). The effect of the number of elements through thickness is limited for SOLSH190 and SOLID185, but greater for SOLID186 when using RI. Single layer is not recommended for solid elements. When FI is activated for SOLID186, it tends to overpredict the buckling load compared to the analytical solution. Since the buckling load should be lower than the analytical solution derived based on plane stress assumptions, as a conservative result, RI will be used for SOLID186. Overall, most cases have led to an acceptable error (within 3%) [95].

The effect of the element size on the plate surface was also studied using two elements through thickness for all element types. Boundary conditions BCs (7) and (11) were adopted. Figure 4.7 shows the error change with element size for the 1st buckling mode. The results indicate that SOLSH190 gave the closest predictions even with a coarse mesh on the surface and, interestingly, a finer mesh of the 8-node element (SOLID185) was more accurate and less computationally expensive than a coarser quadratic mesh of the 20-node element (SOLID186) with a comparable number of nodes. Likewise, BCs (7) and (11) provided similar results.

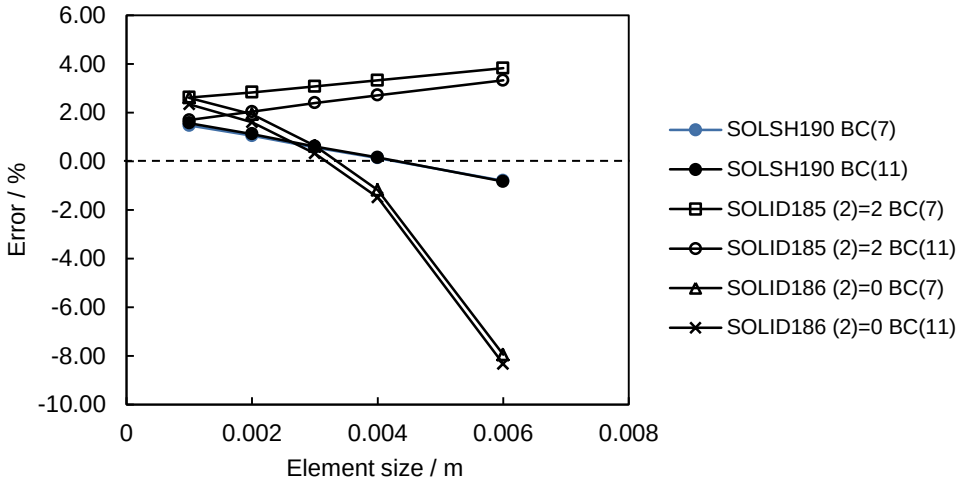

Figure 4.7. Effects of the element size on the plate surface (SOLID185 (2)=2: FI with enhanced strain formulation; SOLID186 (2)=0: RI).

A good mesh should be tailored to the physics of the problem, i.e., fine in the direction of rapidly changing gradients and relatively coarse in the direction with less changed fields. However, the element shape testing provided by Ref. [158] states that the best possible quadrilateral aspect ratio is 1. Since a brick element is made of six quadrilateral faces, it is worth exploring the solid element behaviour when keeping the aspect ratio of each quadrilateral face equal to 1 (a cube). Figure 4.8 shows the errors with the number of elements through thickness. BC (7) was used for this study. Results show that even when keeping a good aspect ratio for every element, one element through thickness is still not able to provide acceptable accuracy. For two and three elements through thickness, the accuracy is no better than that with the fixed element size 3 mm × 3 mm in Figure 4.6. However, predictions from SOLID186 with FI become more conservative, albeit at the expense of much higher computational time. Therefore, mesh for the future corrosion modelling should firstly guarantee to be fine enough in the direction of high change in stress and strain, while keeping the aspect ratio close to 1 without significant reduction in computational efficiency.

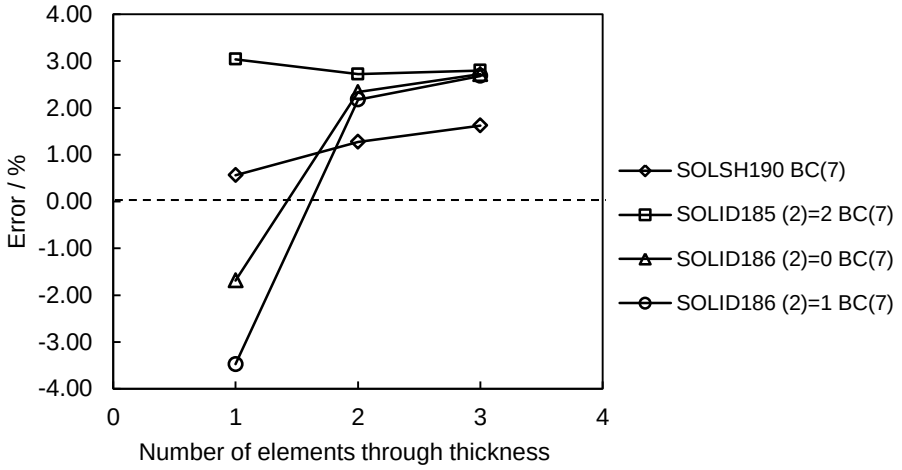

Figure 4.8. Effects of the element size with cubic brick elements.

4.1.3 Summary

Based on the eigenvalue buckling analysis, the key findings are as follows:

Shell elements:

(1) BCs (1) to (3) in Figure 4.2 were found to be suitable as a simply supported boundary condition for SHELL63 while BCs (4) to (6) are feasible for SHELL181/281;

(2) The accuracy of shell elements decreases when increasing the element size;

(3) SHELL63 tends to provide lower load values compared to the analytical solution while SHELL181 leads to higher values;

(4) For SHELL181, FI with incompatible modes (KEYOPT(3) = 2) yields better accuracy compared to RI, especially for a coarse mesh;

(5) Using triangle-shaped elements, SHELL281 gives better prediction compared to SHELL181;

(6) The number of integration points through element thickness does not affect the accuracy.

Solid-shell and solid elements:

(1) BCs (7), (11) and (12) in Figure 4.4 all provide good results with similar accuracy for SOLSH190, SOLID185/186. However, BC (11) and (12) can only be used when the number of elements through thickness is even;

(2) Only FI with enhanced strain formulation (KEYOPT(2) = 2) can provide sufficient accuracy for SOLID185; conversely, RI (KEYOPT(2) = 0) is recommended for SOLID186;

(3) The effect of number of elements though thickness is limited for SOLSH190 and SOLID185, compared to SOLID186 with RI;
(4) A finer mesh of SOLID185 was more accurate and less computationally expensive than a more coarse quadratic mesh (SOLID186) with a comparable number of nodes;
(5) At least two elements through thickness are needed for solid elements;
(6) Mesh should firstly guarantee to be fine enough in the direction of high change in stress/strain, and keep the aspect ratio close to 1 without significant reduction in computational efficiency.

4.2 Replicated nonlinear models

The eigenvalue buckling analysis has provided insight of the element selection and basic settings. However, further validation is necessary for the nonlinear FEA technique outlined in Section 3.1. Due to a lack of analytical solution for nonlinear problems, three sets of numerical models (experimentally validated and benchmark studies) from the literature were replicated. In addition, the application of weld-induced residual stresses was also validated. Element SHELL181 was adopted primarily based on the investigation in Section 4.1.

4.2.1 Plate models

Modelling of a square steel plate with and without pitting corrosion was carried out and compared with Paik et al.'s work [7]. The plate was simply supported along four edges with uniaxial in-plane compressive stress (controlling displacement) applied on two sides and two unloaded edges kept straight. Cylindrical pits were uniformly distributed over the upper surface varying the DOP and pit depth. The geometric and material properties are listed in Table 4.5. For computational simplicity, 1/4 scale was used when constructing the models, as shown in Figure 4.9. FI with incompatible modes was used for SHELL181.

Table 4.5. Input properties of Paik et al.'s models

Model Properties	Values
Dimensions $a \times b \times t_0$ / mm	800 × 800 × 15
E / GPa	205.8
σ_y / MPa	352.8
ν	0.3
E_t	0
Initial imperfection	$w = 0.1\beta^2 t_0 \sin\frac{\pi x}{a}\sin\frac{\pi y}{b}$
Pit diameter / mm	40
Pit depth	$0.25t_0$, $0.5t_0$, $0.75t_0$ and t_0
DOP	4.9%, 9.6%, 15.9%, 23.8% and 33.2%

The average compressive stress and strain were calculated for every load substep and plotted in Figure 4.10 and Figure 4.11, varying DOP and pit depth, respectively. It can be seen that the replicated model shows a very good agreement with Paik et al.'s results. The difference could be from the selection of the element type and the application of constraint/load, which are not clearly stated in the paper. Moreover, for one-side pitting corrosion, Paik et al. set the elastic modulus to be zero at pitting regions, while the replicated model used the section command of shell elements to set different thickness values.

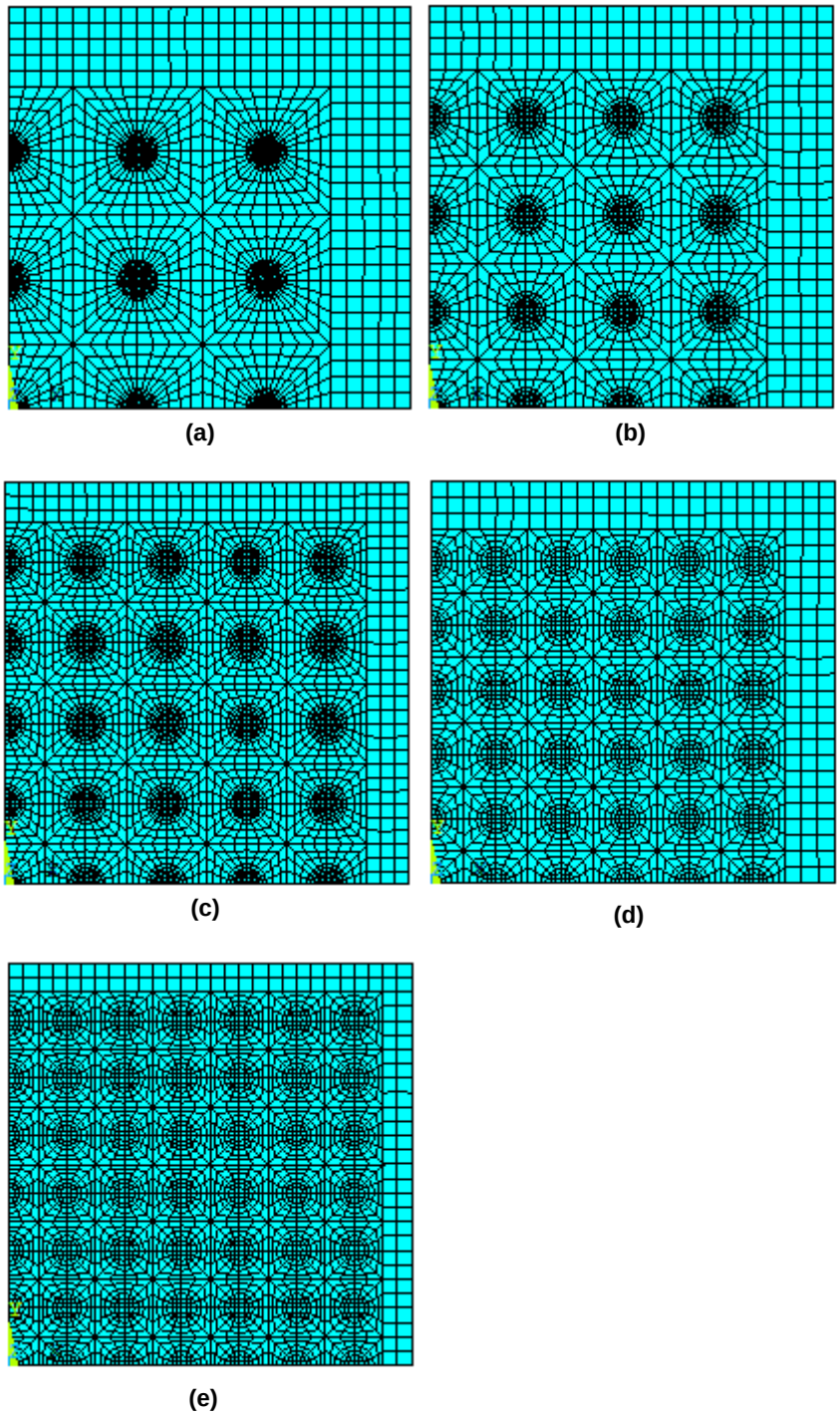

Figure 4.9. Replicated Paik et al.'s model with various DOPs: (a) DOP=4.9%; (b) DOP=9.6%; (c) DOP=15.9%; (d) DOP=23.8%; (e) DOP=33.2%.

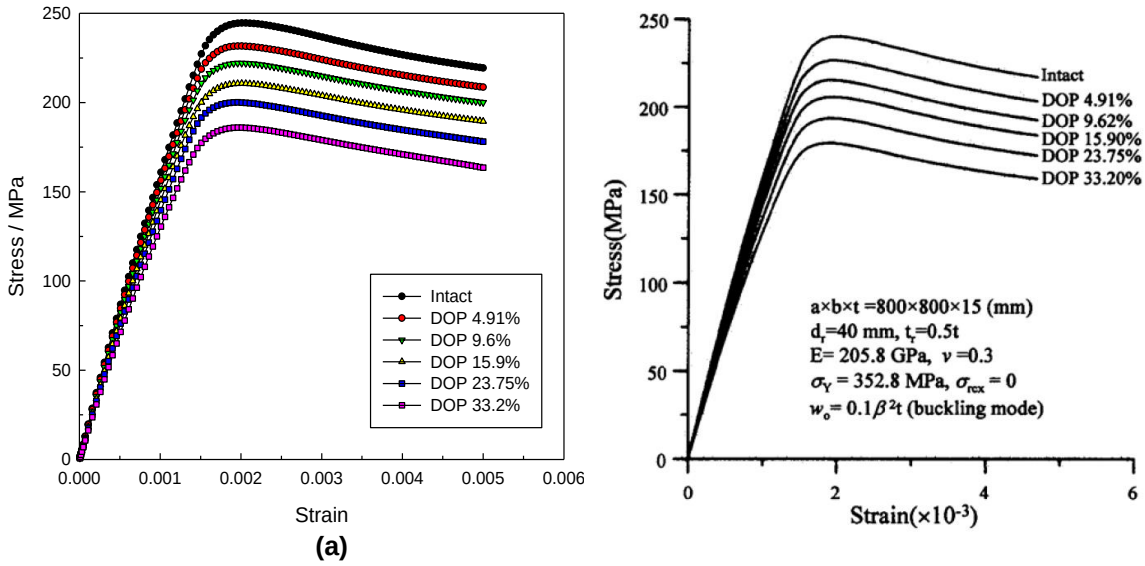

Figure 4.10. Compressive stress-strain relationships: (a) replicated models; (b) models in Ref. [7] varying DOP.

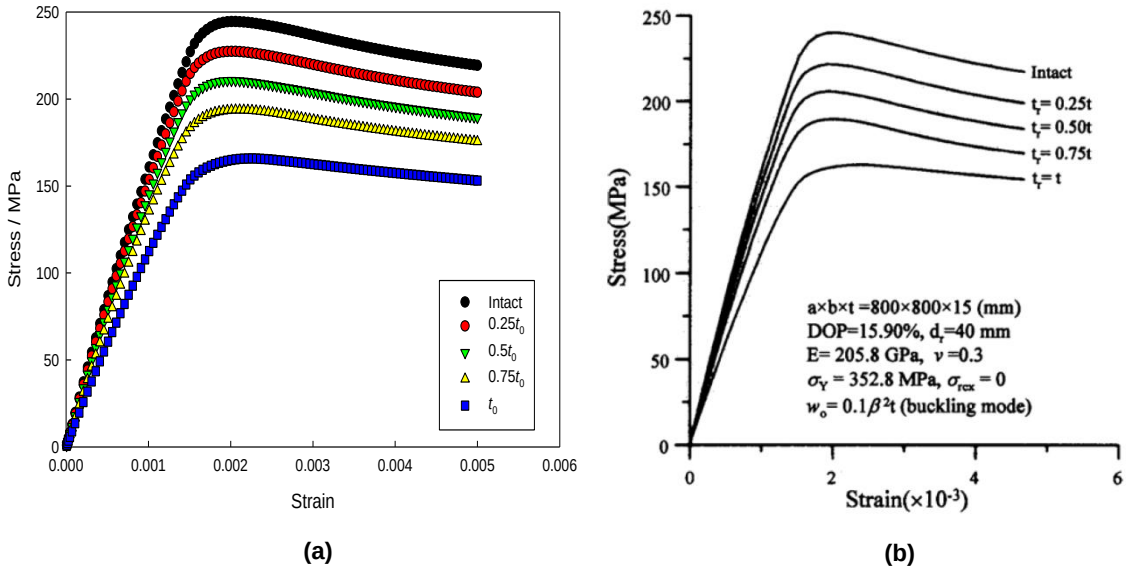

Figure 4.11. Compressive stress-strain relationships: (a) replicated models; (b) models in Ref. [7] varying pit depth.

4.2.2 Plate-stiffener combination models

To gain confidence in modelling plate-stiffener combinations, including the application of initial deflections, boundary and loading conditions, three models were replicated, i.e., a one-bay stiffened panel model (SPM), a two-bay plate-stiffener combination (PSC) and a two-bay SPM [86]. Figure 4.12 illustrates the location and geometric information of each

model and the loading condition. Model details are listed in Table 4.6. An example of the mesh is shown in Figure 4.13. Simply supported boundary conditions were applied along the four edges of each model with a uniaxial compressive load applied by controlling the displacement. The transverse frames were not included in the present model, however with the out-of-plane displacement constrained along the frame locations.

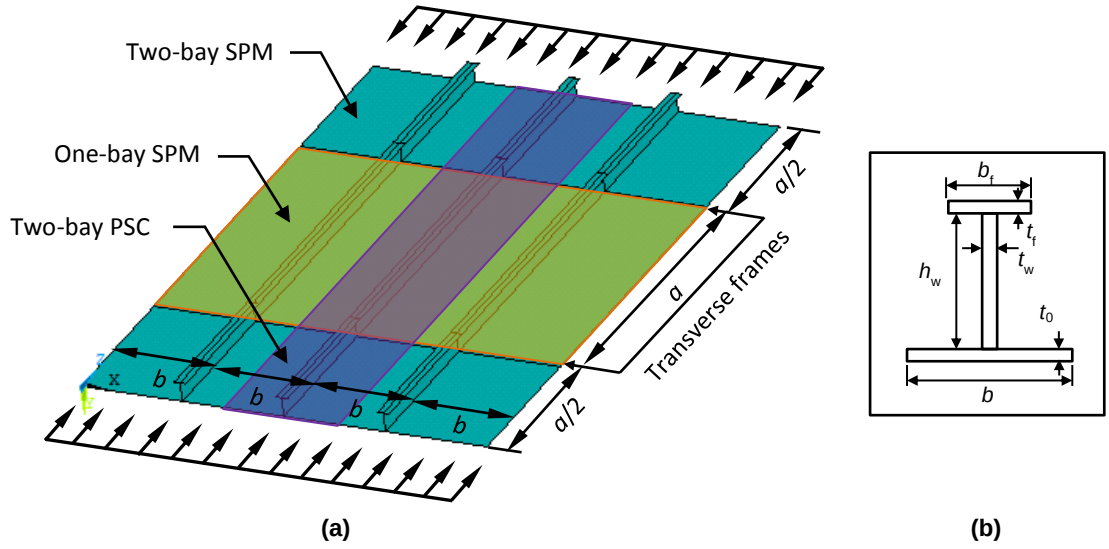

Figure 4.12. Plate-stiffener combination models reported in Ref. [86]: (a) model locations and loading direction; (b) cross-section of a stiffener.

Table 4.6. Model properties used in Ref. [86]

Model Properties	Values
***a* / mm**	2640
***b* / mm**	900
t_0 / mm	21
$h_w \times t_w$ / mm	150 × 12 and 210 × 12
$b_f \times t_f$ / mm	100 × 15
***E* / GPa (both plate and stiffener)**	205.8
σ_y / MPa (both plate and stiffener)	352.8
***ν* (both plate and stiffener)**	0.3
E_t (both plate and stiffener)	0
Plate initial deflection / mm	$w_{pl} = 0.05\beta^2 t_0 \sin\frac{3\pi x}{a}\sin\frac{\pi y}{b}$
Column-type initial deflection / mm	$w_c = 0.0025a \sin\frac{\pi x}{a}\sin\frac{\pi y}{B}$
Sideways initial deflection / mm	$w_s = 0.0025a \frac{z}{h_w}\sin\frac{\pi x}{a}$

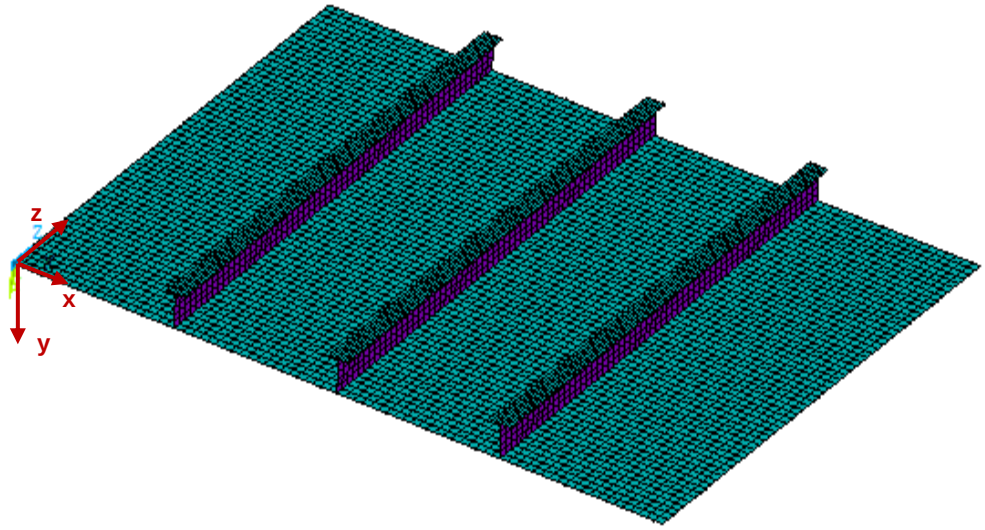

Figure 4.13. Meshed one-bay SPM.

Validation was achieved by comparing the stress-strain relationships for each model with two stiffener heights and two failure modes, namely plate-induced failure (PIF) and stiffener-induced failure (SIF). Comparison results in Figure 4.14 and Figure 4.15 show good agreement between the referenced plate-stiffener combination models and the replicated ones in both elastic and plastic regimes, indicating the feasibility of the adopted nonlinear FEA procedure for modelling various plate-stiffener combination models. The minor variations in results of two-bay models could be caused by the differences in the symmetric boundary conditions, which are not mentioned in the literature.

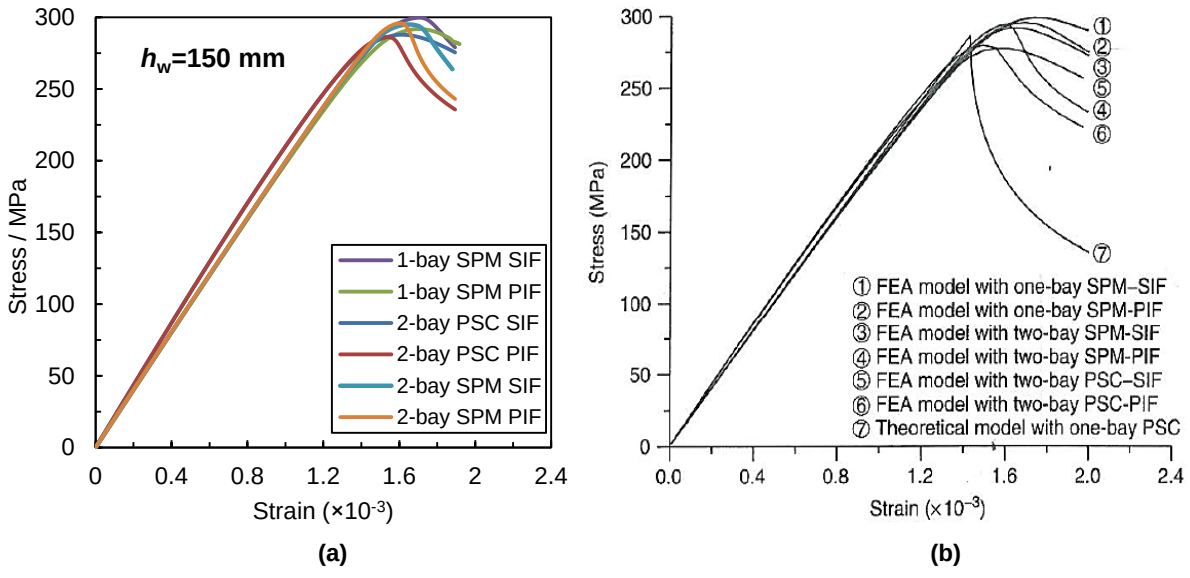

Figure 4.14. Compressive stress-strain relationships: (a) replicated models; (b) models in Ref. [86] with h_w = 150 mm.

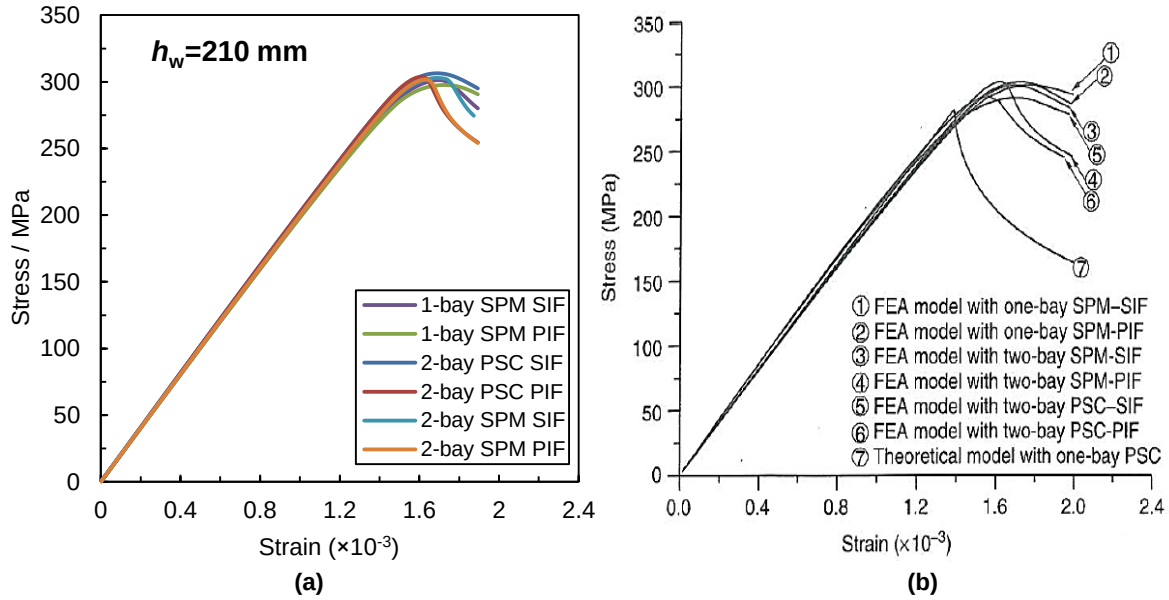

Figure 4.15. Compressive stress strain relationships: (a) replicated models; (b) models in Ref. [86] with h_w = 210 mm.

4.2.3 Two-bay/two-span stiffened panel model

To incorporate the column-type initial deflection, as well as the interactions between plate and transverse/longitudinal girders, a stiffened panel reported as a benchmark model of the deck panel of a VLCC (very large crude carrier) [122] has also been replicated. The model consists of two bays and two spans with each panel containing eight stiffeners with a tee bar cross section. Model properties are listed in Table 4.7 (the parameters are as previously defined in Figure 4.12 (b)). The meshed model is shown in Figure 4.16.

By applying a simply supported boundary condition and uniaxial compressive load along the longitudinal direction, good correlations between the replicated and published stress-strain relationships were obtained (Figure 4.17), indicating that the nonlinear FEA procedure, boundary/loading conditions and the mesh were applied appropriately.

Table 4.7. Model properties used in Ref. [122]

Model Properties	Values
a **/ mm**	4750
b **/ mm**	950
t_0 **/ mm**	15
$h_w \times t_w$ **/ mm**	580 × 15
$b_f \times t_f$ **/ mm**	150 × 20
E **/ GPa (both plate and stiffener)**	205.8
σ_y **/ MPa (both plate and stiffener)**	313.6
ν **(both plate and stiffener)**	0.3
E_t **(both plate and stiffener)**	0
Plate initial deflection / mm	$w_{pl} = 0.1\beta^2 t_0 \sin\frac{5\pi x}{a}\sin\frac{\pi y}{b}$
Column-type initial deflection / mm (*B* / mm: width between two longitudinal girders)	$w_c = 0.0015a \sin\frac{\pi x}{a}\sin\frac{\pi y}{B}$
Sideways initial deflection / mm	$w_s = 0.0015a\frac{z}{h_w}\sin\frac{\pi x}{a}$

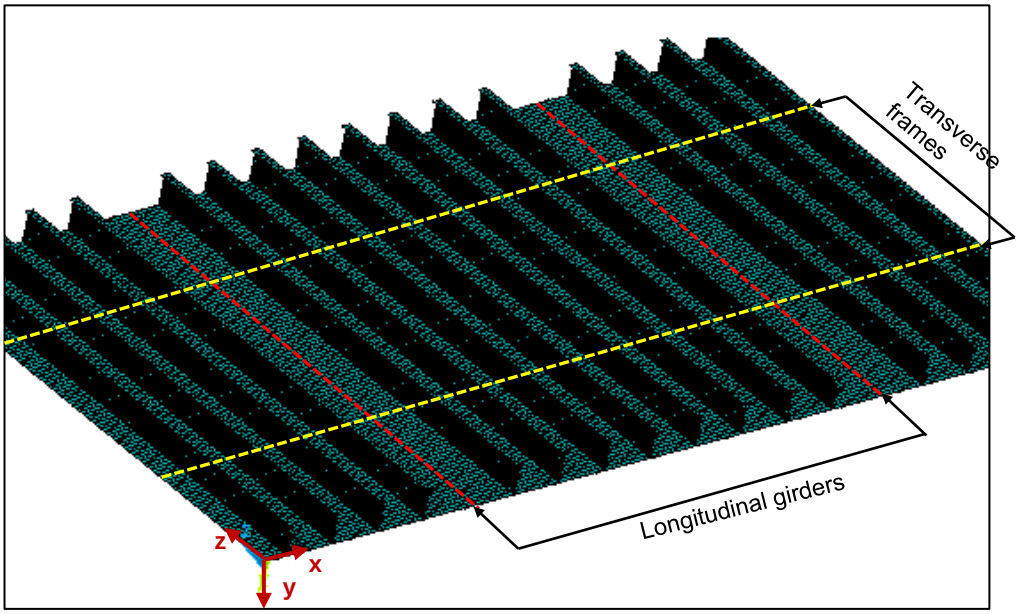

Figure 4.16. Meshed two-bay/two-span model reported in Ref. [122].

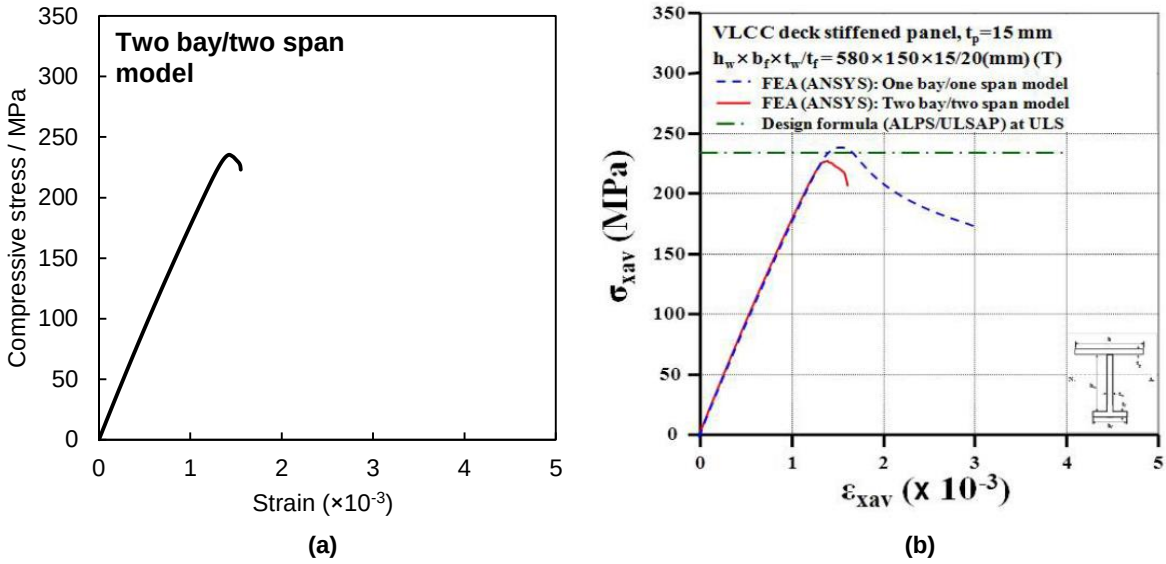

Figure 4.17. Compressive stress-strain relationships: (a) replicated models; (b) models in Ref. [122].

4.2.4 Validation of the residual stress application method

The method to explicitly apply weld-induced residual stresses to a structure (Section 3.1) was validated against Paik and Sohn's modelling of a rectangular steel plate [181]. The plate dimension is 5700 mm × 945 mm × 21 mm with four edges simply supported and uniaxial compressive load applied longitudinally. The plate is made of high tensile steel with E = 205.8 GPa, σ_y = 315 MPa and ν = 0.3. The initial deflection is in a form of $w_{pl} = (b/200)\sin(6\pi x/a)\sin(\pi y/b)$. Three levels of compressive residual stresses (Equation 2.16) were applied in the longitudinal direction. Figure 4.18 illustrates the residual stress distribution.

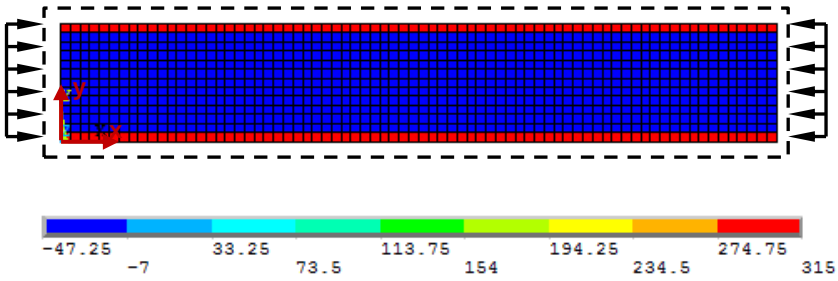

Figure 4.18. Residual stress distribution on a rectangular plate model from Ref. [181] (stress in MPa).

Figure 4.19 is the comparison of the compressive stress-strain results. The transverse residual stresses are not included due to the consideration of the external loading being

predominantly longitudinal. A good correlation has been obtained using SHELL181 indicating the adopted method is appropriate for the residual stress application. The method was also adapted for solid models (SOLID185) to test its feasibility. From the results it can be seen that there is minor difference between the shell and solid elements in both pre- and post-ultimate strength regimes.

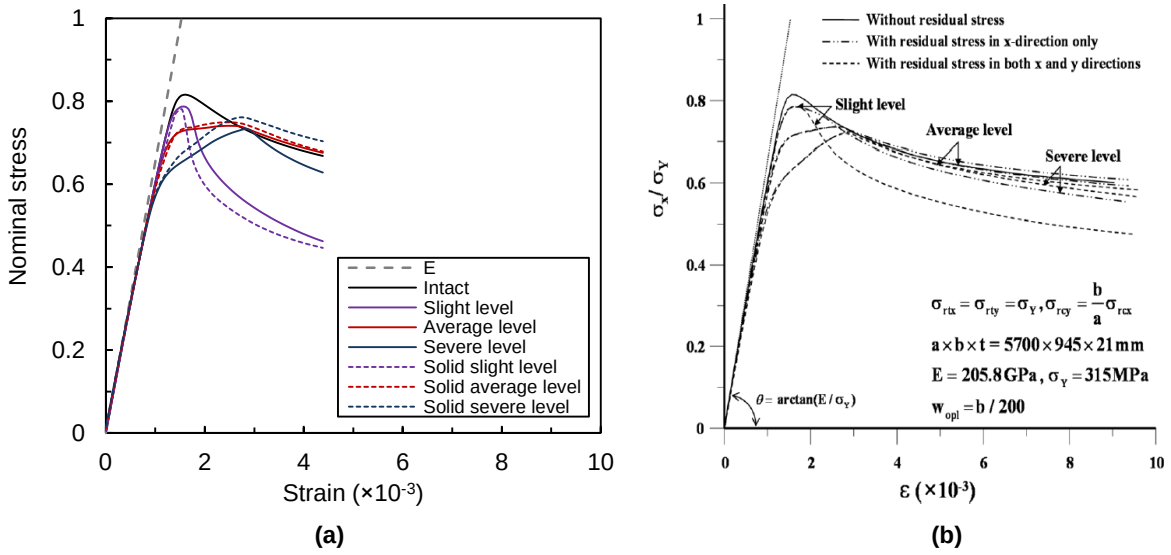

Figure 4.19. Compressive stress strain relationships: (a) replicated models; (b) models in Ref. [181] (nominal stress = stress / σ_y; E: Young's modulus).

4.3 Conclusions

This chapter has firstly detailed the behaviour of various shell and solid elements frequently used for thin-walled structures. Greater insights were gained into the constraining method for a simply supported boundary condition, selection of element type, element size and element shape, number of elements through thickness, and integration strategies, in order to minimise technical errors for future analysis. Regarding the nonlinear FEA considering both geometric and material nonlinearities, validation was carried out by replicating a series of localised steel structural members published in the literature, including plates, plate-stiffener combinations and a two-bay/two-span stiffened panel. The stress/strain relationships showed good agreement between the replicated models and the published ones using SHELL181, which again proves the significance of the eigenvalue buckling analysis. The replicated plate model with weld-induced residual stresses has verified the feasibility of the proposed method to explicitly apply a residual stress matrix prior to external loads for both shell and solid elements.

Chapter 5 Numerical investigation of plate models

Based on the validation reported in Chapter 4, this chapter presents a series of plate models subject to idealised one-side local corrosion damage, focusing on the pit distribution, bench-shape pits induced by MIC and a local rough surface. The coating failure scale diagrams (Figure 2.18) and reported immersion trials [21] were used to inform the corrosion patterns in order to develop a modelling strategy. Inasmuch as the negligible influence of the aspect ratio of a structural member (length to width) when investigating the corrosion effect (Section 2.2.3), the basic structural member was set to be a square plate of shipbuilding high tensile steel for an equivalent Grade ASTM A131. The studied properties are listed in Table 5.1. As discussed in Section 2.2.1.1, although the strain hardening effect of a material would lead to a higher ultimate strength value, this increase is fairly marginal for plates under compressive loading [86,90,91]. In addition, the failure mode will not change due to the tangent modulus. Thus, an elastic-perfectly-plastic material model was considered sufficient for a conservative compressive strength study, and has been adopted in the present modelling. The plate was simply supported along four edges. A uniaxial in-plane compressive load was applied along two parallel plate edges by controlling the displacement with the unloaded edges kept straight. Von Mises criterion was used to assess yielding.

Table 5.1. Basic properties of the plate model

Model Properties	Values
Dimensions $a \times b \times t_0$ / mm	800 × 800 × 15
E / GPa	205.8
σ_y / MPa	352.8
ν	0.3
E_t / GPa	0
β	2.208
Initial deflection / mm	$w = 0.1\beta^2 t_0 \sin\frac{\pi x}{a}\sin\frac{\pi y}{b}$

5.1 Localised pit distribution study

Four idealised pit distributions on one side of a plate were considered (Figure 5.1) based on the coating failure diagram (Figure 2.18), representing either a large corrosion area or a cluster of small pits. In terms of the pit shape, Paik et al. [7] and Huang et al. [95] stated that pit shape would not have much effect on the ultimate strength reduction and hence

the cylindrical shape was applied for simplicity. Although non-realistic sharp corners therefore may be introduced to the model, the analysis was considered to be conservative and valid. The test matrix also contains five DOPs (2%, 5%, 10%, 15% and 25%) and four thickness reductions, t_p (0.25t_0, 0.33t_0, 0.5t_0 and 0.75t_0), where t_0 is the original plate thickness. For the random pitting corrosion pattern, all pits were completely separated with the radius ranging from 10 mm to 30 mm, as frequently observed pit dimentions [32,33]. Plates with uniformly reduced thickness were also investigated by keeping the corrosion-induced volume loss the same for comparison. A mesh convergence study, for example in Figure 5.2 when corrosion is in the middle of the plate, indicates that the deflection ratio UZ_{max}/w_0 (maximum lateral deflection at the ultimate state to the maximum initial deflection) starts to converge when the maximum element size is 50 mm. However, since the initial deflection was applied to every node of the model, to avoid extra geometric discontinuity and achieve a mapped mesh pattern (contains only orthogonal element shape), the maximum element size was set to be 16 mm. Both SHELL181 and SOLSH190 were used to construct the models.

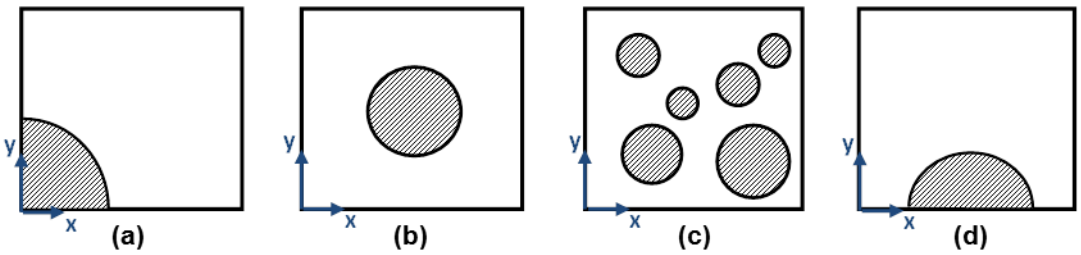

Figure 5.1. Studied corrosion patterns with compressive load in the x-direction: (a) corrosion at the corner (lc); (b) corrosion in the middle (m); (c) random pitting (r); (d) corrosion at the unloaded edge (b).

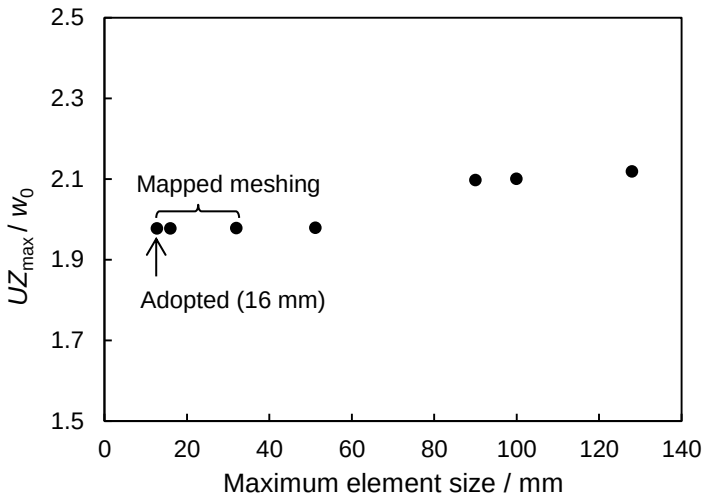

Figure 5.2. Meshing convergence study for numerical modelling (UZ_{max} = maximum lateral deflection at ultimate strength state / mm; w_0 = maximum initial deflection / mm).

Loading was divided into numerous substeps. The nominal axial compressive stress (σ_n) of the plates were derived and extracted according to Equation 5.1 for each substep and plotted versus the axial compressive strain in order to determine the ultimate strength.

$$\sigma_n = \frac{P}{A_0} \tag{5.1}$$

where P is the reactional load value and A_0 is the original cross-sectional area. The axial strain was calculated by dividing the loaded edge displacement in the loading direction by the original plate width. The ultimate strength was the highest stress obtained from a stress-strain curve. The modelling indicated that when taking into account the initial imperfections, the plates started to deform at the onset of the external loading, as shown in Figure 5.3 and Figure 5.4.

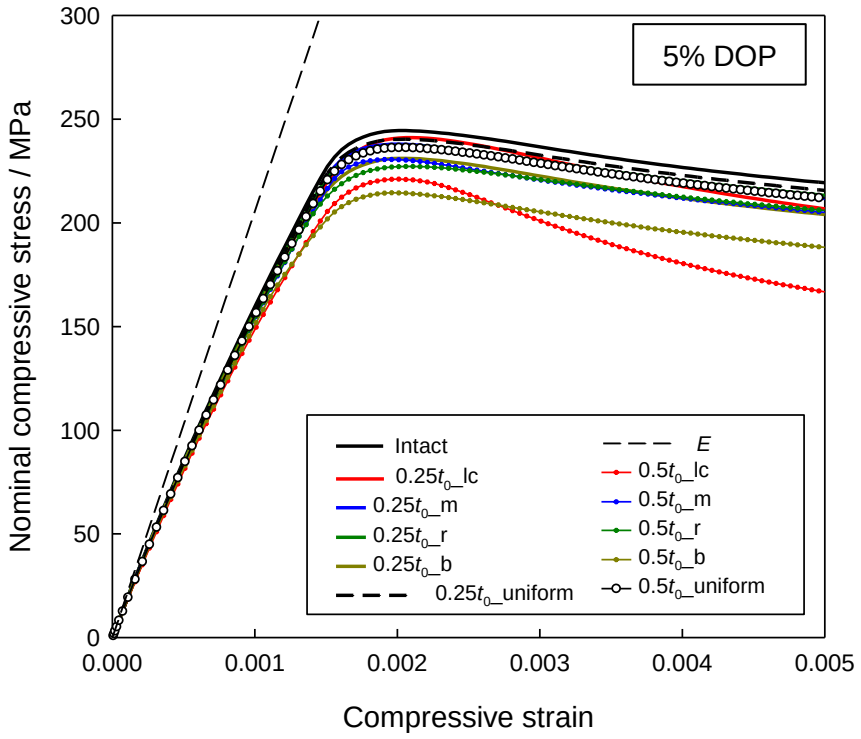

Figure 5.3. Nominal compressive stress-strain relationships (DOP = 5%; pit depth = 0.25t_0 and 0.5t_0) (lc: corrosion at the corner; m: corrosion in the middle; r: random pitting; b: corrosion at the unloaded edge; *E*: Young's modulus of the material).

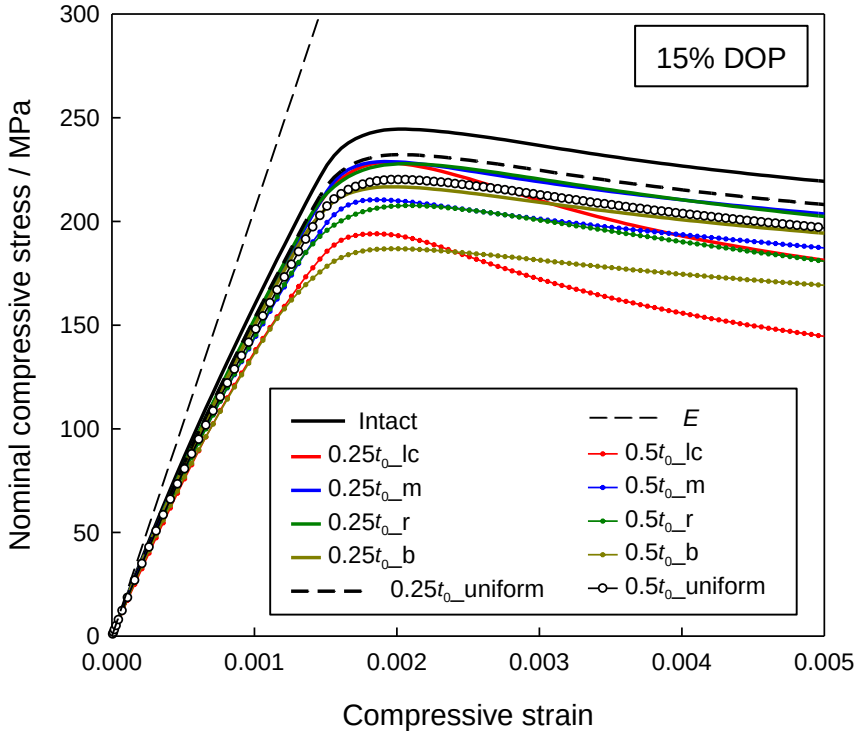

Figure 5.4. Nominal compressive stress-strain relationships (DOP = 15%; pit depth = 0.25t_0 and 0.5t_0) (lc: corrosion at the corner; m: corrosion in the middle; r: random pitting; b: corrosion at the unloaded edge; *E*: Young's modulus of the material).

In total, 81 cases have been considered in this localised pit distribution study. Shown in Figure 5.3 and Figure 5.4 are examples of the stress-strain relationships for the intact plate, uniformly corroded plates and plates with the four pit distributions, two DOPs of 5% and 15% DOP and two pit depths of $0.25t_0$ and $0.5t_0$. It can be seen that the ultimate strength of the four localised corrosion distributions is lower than that for a uniformly corroded plate with the same volume loss. Furthermore, when the corrosion damage is shallow ($0.25t_0$), plates with corrosion in the middle and random pits show a similar stress progression trend as that of the intact and uniformly corroded plates. The ultimate strength values of the middle, random and corner corrosion plates are all similar to each other. Conversely, the ultimate strength of edge corrosion distributions is much lower. In addition, increasing DOP not only leads to a strength reduction, but also enlarges the difference between pit depth of $0.25t_0$ and $0.5t_0$. For a more comprehensive comparison, the normalised reduction results are derived based on Equation 5.2. The normalised ultimate strength reduction and the corresponding lateral deflection compared to the intact plate were derived and plotted versus the pit depth and DOP, as shown in Figure 5.5 (DOP = 5%) and Figure 5.6 (DOP = 15%).

$$X\ (\%) = \frac{X_{\text{Intact}} - X_{\text{Corroded}}}{X_{\text{Intact}}} \times 100 \qquad (5.2)$$

where X represents the reduction of either ultimate strength or lateral deflection.

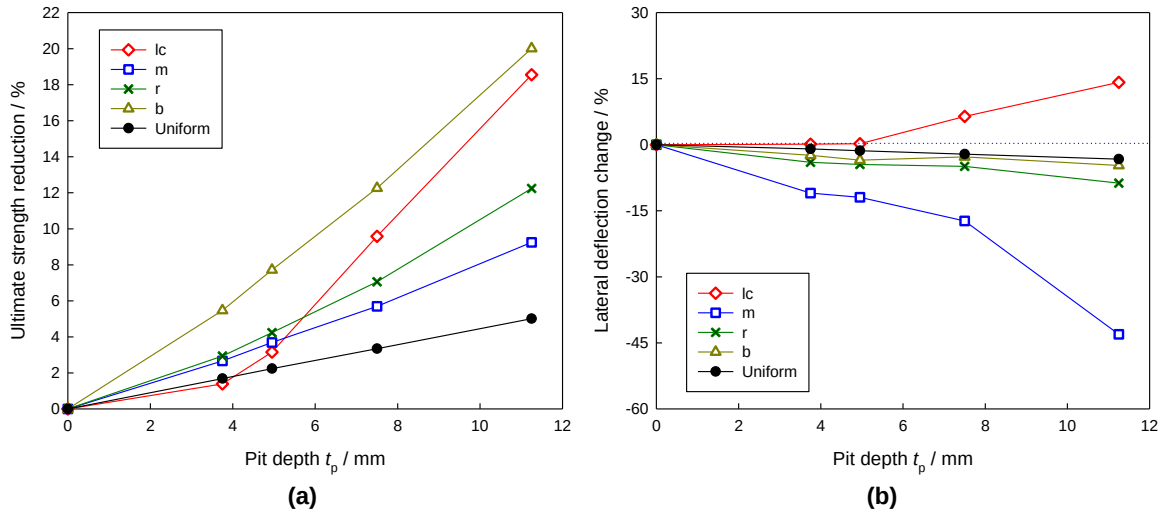

Figure 5.5: (a) Normalised ultimate strength and (b) lateral deflection reductions (DOP = 5%) (lc: corrosion at the corner; m: corrosion in the middle; r: random pitting; b: corrosion at the unloaded edge).

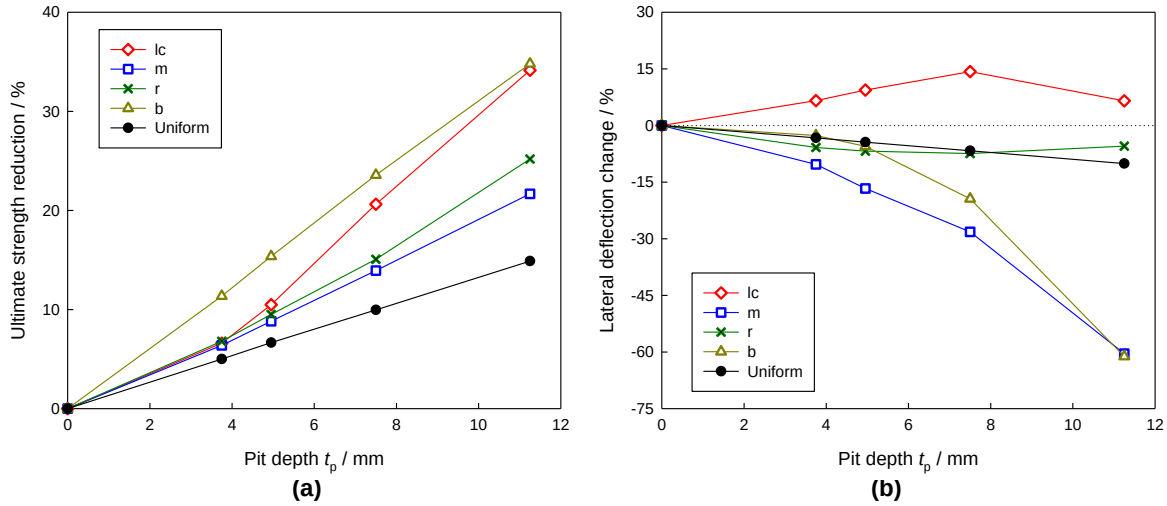

Figure 5.6: (a) Normalised ultimate strength and (b) lateral deflection reductions (DOP = 15%) (lc: corrosion at the corner; m: corrosion in the middle; r: random pitting; b: corrosion at the unloaded edge).

For all pit depths and DOPs, the difference in the strength reduction between middle and random pitting corrosion is small. For every DOP, as the pit depth increases, the strength reduction of corner corrosion shows a more scattered response compared to the other pit distributions. A negative deflection change means that the deflection is increased by the corrosion. It can be seen that random pitted plates show a very similar deflection change as the uniformly corroded plate. Unlike the slight difference of ultimate strength between uniform and middle corrosion, the difference in the lateral deflection is up to 40%, due to

the reduced effect of membrane stress which could stabilise the plate. Conversely, corner corrosion tends to decrease the deflection.

For a compressive loading condition, the corrosion-induced volume loss is generally considered as the governing parameter for strength assessment of corroded structures, as discussed in Section 2.2.3. As such, Figure 5.7 presents the strength reduction change with volume loss (%). It is evident that the strength reduction increases almost linearly with volume loss for uniform corrosion, middle corrosion and random pitting. For corrosion patterns with the same volume loss, the highest reduction is generally for the small and deep pits in comparison with broad and shallow, and this difference is more obvious for the edge and corner corrosion, which leads to greater scatter in the data. For instance, when edge corrosion occurs with a volume loss of 5%, the reduction is 19.4% when DOP = 10% and pit depth = $0.5t_0$, but only 10.3% when DOP = 25% and pit depth = $0.2t_0$. Moreover, a large pit depth could result in a lower strength even with a smaller volume loss. The results show that the localised corrosion may further reduce the ultimate strength by up to 20% compared to a uniformly corroded plate.

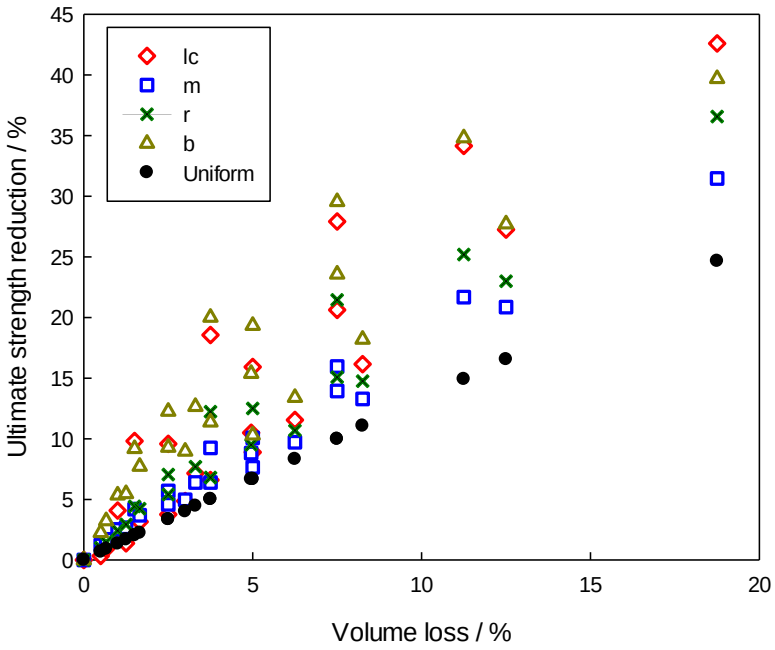

Figure 5.7: Normalised ultimate strength reductions versus volume loss (%) (lc: corrosion at the corner; m: corrosion in the middle; r: random pitting; b: corrosion at the unloaded edge).

5.2 Bench-shape pit distribution study

Based on the observations from immersion trials [21], bench-shape broad pits were simulated on the plate models. Corrosion patterns (a), (b) and (d) shown in Figure 4.1 with two DOPs (15% and 25%) were chosen as basic corrosion locations. Figure 5.8 illustrates the cross-section of a bench-shape pit. The test matrix includes three r_1 ((1/3) r_2, (1/2) r_2 and (2/3) r_2) and six t_1 (2 mm, 3 mm, 3.75 mm, 7 mm, 7.5 mm and 10.05 mm). Five volume losses based on the no-bench studies when DOP = 15% and 25% were used to determine t_2 by keeping the same volume loss. The material properties, boundary and loading conditions were the same as for the no-benched modelling.

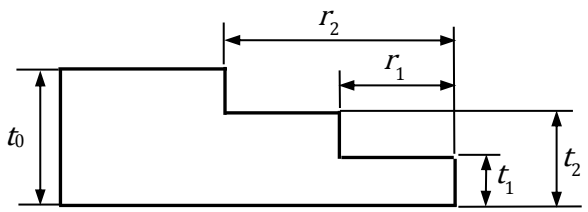

Figure 5.8: Schematic of a bench-shape pit cross-section.

The bench-shape pit study contains 56 cases. The nominal compressive stress-strain relationships were plotted to assess the stress progression. Figure 5.9 and Figure 5.10 are examples for 15%DOP (volume loss = 3.75%) and 25%DOP (volume loss = 6.25%) respectively with three corrosion locations, three r_1 values and one t_1 (7 mm). It is clear that the unloading path of the plate with bench-shape pitting follows a similar trend as the plate without bench. Again, the corrosion at the plate corner shows generally a more unstable behaviour. Apart from the effect on the ultimate strength, bench-shape pits could further reduce the stiffness in the post-ultimate strength regime.

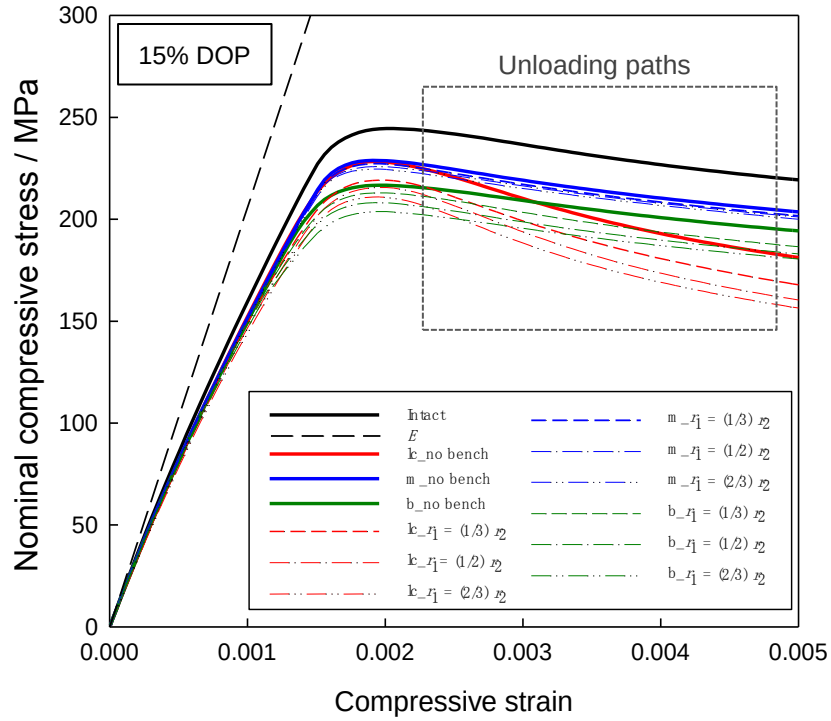

Figure 5.9: Nominal compressive stress-strain relationships for bench-shape pits (DOP = 15%; volume loss = 3.75%; t_1 = 7 mm) (lc: corrosion at the corner; m: corrosion in the middle; b: corrosion at the unloaded edge; *E*: Young's modulus of the material).

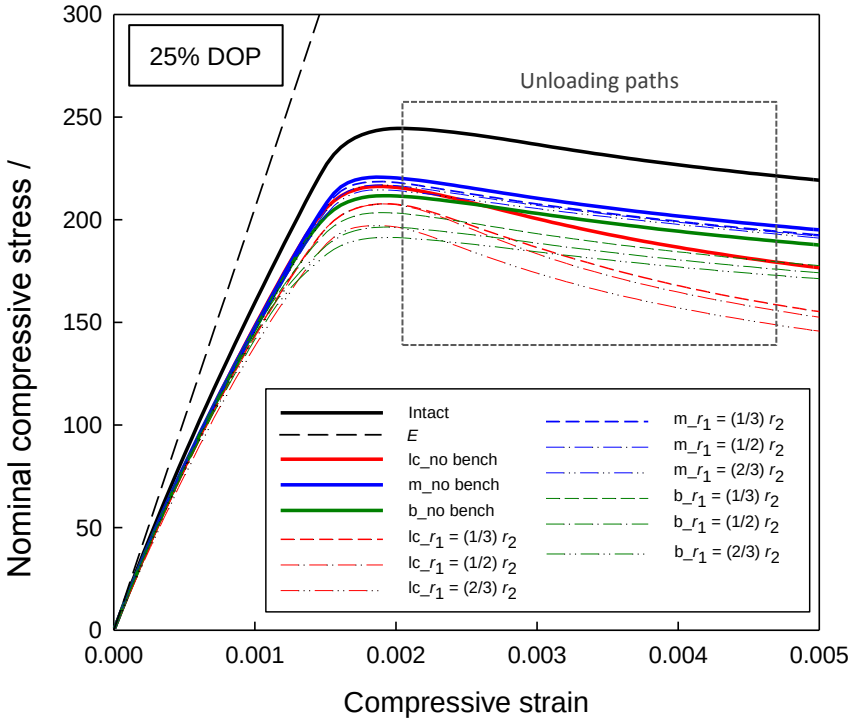

Figure 5.10: Nominal compressive stress-strain relationships for bench-shape pits (DOP = 25%; volume loss = 6.25%; t_1 = 7 mm) (lc: corrosion at the corner; m: corrosion in the middle; b: corrosion at the unloaded edge; *E*: Young's modulus of the material).

The nominalised ultimate strength reductions were calculated using Equation 5.2, in comparison with the results from studies of the no-benched condition. Figure 5.11 shows typical results when $r_1 = (1/2)r_2$ and DOP = 15% at three corrosion locations. For an identical volume loss, the bench will further reduce the strength. However, the overall effect of bench feature diminishes with increasing volume loss. Whereas with increasing DOP, the difference between plates with and without benches becomes significant for all three corrosion locations (Figure A3.7 to Figure A3.11 in Appendix 3). For each DOP, the strength reduction due to benches is much greater when corrosion occurs at the unloaded edge and the corner compared to central corrosion, implying a less severe effect of benches on plates with central corrosion. In terms of the bench configuration, when DOP and volume loss are fixed, a smaller t_1 leads to a lower ultimate strength. This observation is also true for the other two r_1 values. From the results for $r_1 = (1/3)r_2$ and $r_1 = (2/3)r_2$ (Figure A3.7 to Figure A3.11 in Appendix 3), it is found that a larger r_1 may lead to a greater strength reduction. In general, the existence of benches may further reduce the strength by up to 14% compared to the no-bench condition.

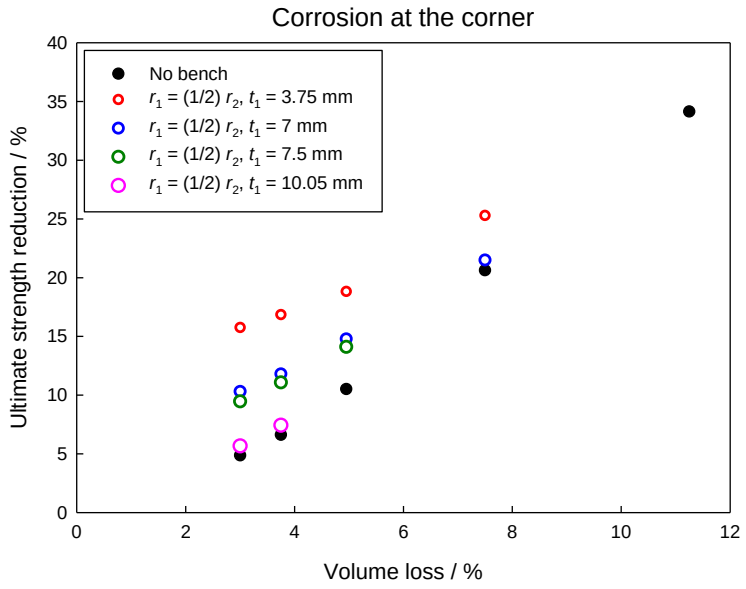

(a)

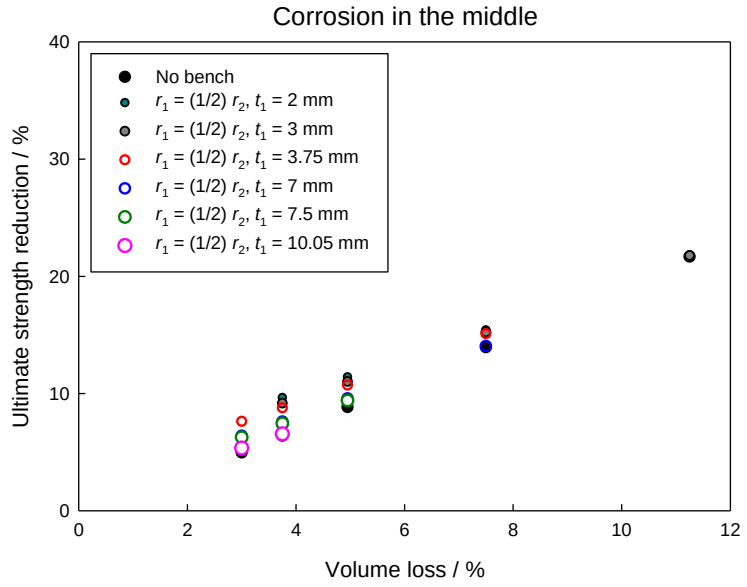

(b)

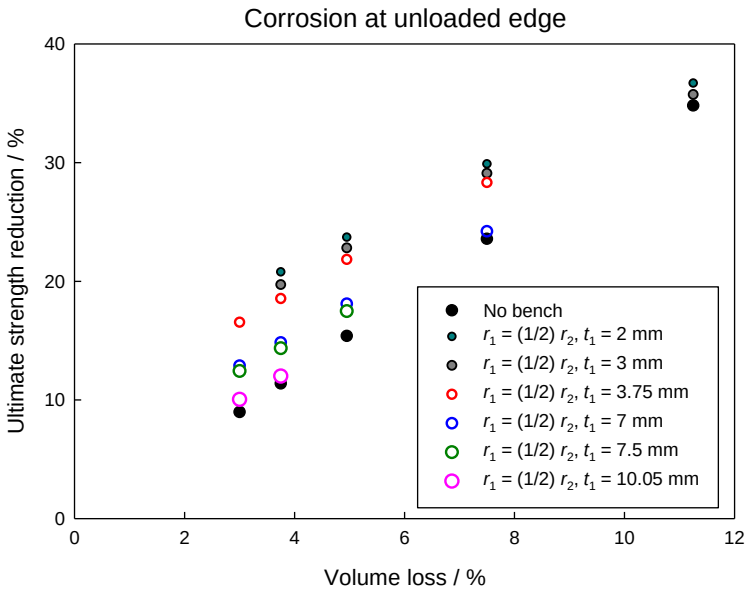

(c)

Figure 5.11: Normalised ultimate strength reduction for bench-shape pit study (DOP = 15%; r_1 = (1/2) r_2): (a) corrosion at the corner; (b) corrosion in the middle; (c) corrosion at the unloaded edge.

5.3 Localised rough surface study

The numerical studies described in Sections 5.1 and 5.2 have adopted idealised corrosion patterns with a flat surface at the bottom of the corroded area. However, corrosion is seldom observed with such a flat surface. Therefore, plates with a rough surface were also investigated to assess the reliability of the corrosion pattern idealisation. A simple Gaussian random surface was generated based on the method outlined in Refs. [182,183]

to quickly introduce a roughness to the surface for a parametric study. Figure 5.12 shows examples of the two random surfaces for the full scale plate with a root mean square (RMS) height of 1.0 mm and two correlation lengths (CL) (10 mm and 50 mm in both *x*- and *y*-directions, correlating with the observed pit diameters in Ref [33]).

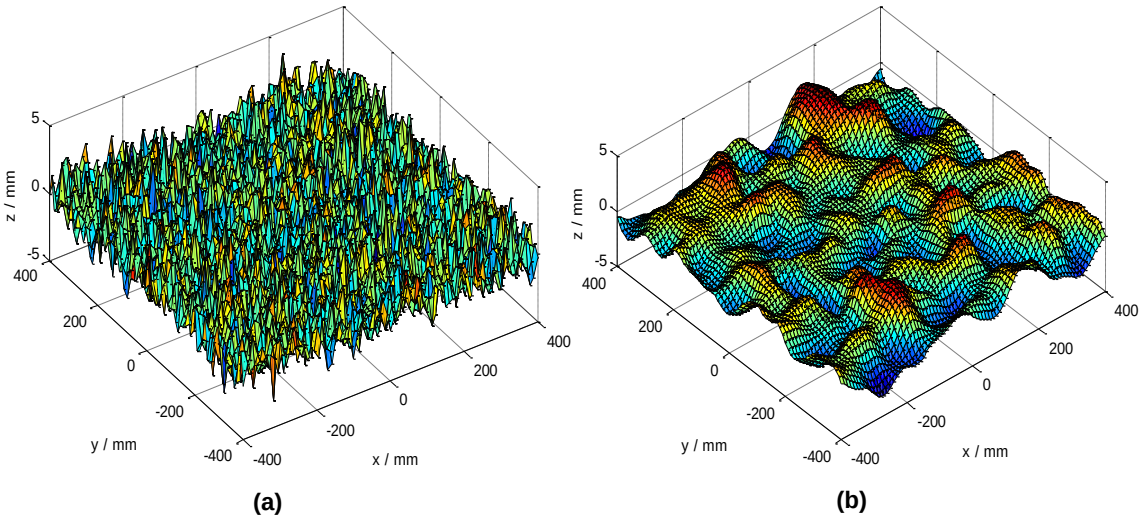

Figure 5.12: Random surface configurations: (a) RMS = 1 mm, CL = 10 mm; (b) RMS = 1 mm, CL = 50 mm (area: 800 mm × 800 mm).

Due to the limitation of the nature of shell elements, only both-side corrosion with identical surface feature could be constructed. Therefore, solid-shell element SOLSH190 was adopted to construct the one-side rough surface model based on the previous corrosion pattern where corrosion was in the middle of the plate, as described in Section 5.1. A rough surface was introduced only to the corroded area. Based on the collected data and the corrosion model proposed in Ref. [52] for cargo tanks, three RMS heights (1 mm, 1.5 mm and 2 mm) were considered. The test matrix also contains four DOPs (5%, 10%, 15% and 25%), one pit depth ($0.5t_0$) and two CLs (10 and 50 mm) in both *x*- and *y*-directions. The roughness R_a values for every surface profile are listed in Table 5.2. Boundary and loading conditions were based on the outcome from the eigenvalue buckling analysis. Figure 5.13 illustrates two examples of the amplified corroded region for DOP = 15% and pit depth = $0.5t_0$. In total, 24 modelling cases were carried out.

Table 5.2. Surface roughness

No.	RMS / mm	CL / mm	R_a / mm
1	1	10	0.924
2	1.5	10	1.389
3	2	10	1.860
4	1	50	0.845
5	1.5	50	1.086
6	2	50	1.537

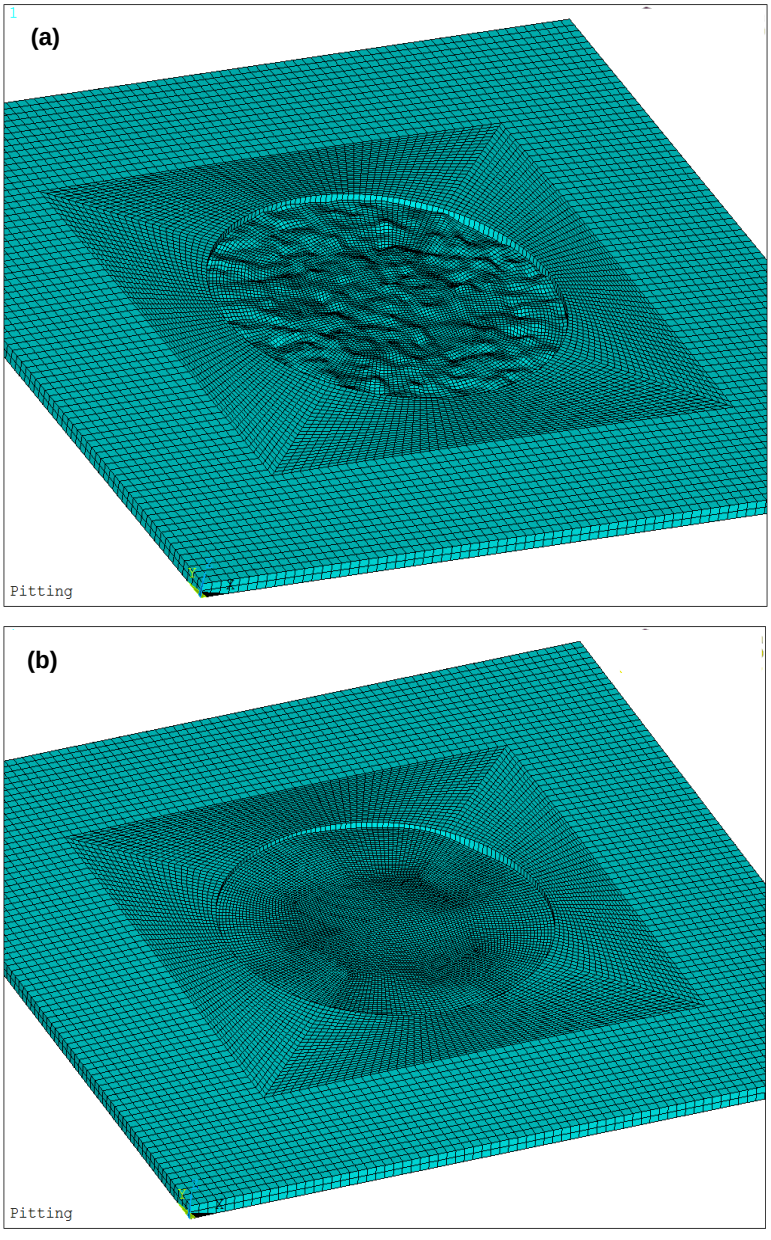

Figure 5.13: Two examples of a rough surface inside a pit (DOP = 15%, pit depth = 0.5t_0): (a) RMS = 1.5 mm, CL = 10 mm; (b) RMS = 1.5 mm, CL = 50 mm.

Figure 5.14 is a comparison of stress-strain relationships between a flat surface and a rough surface conditions for 15% DOP. It can be seen that minor variation has been

induced by the rough surface. The ultimate strength reductions are plotted versus DOP for three rough surfaces, compared to models without a rough surface (also using SOLSH190) (Figure 5.15). It can be seen that when DOP increases, the ultimate strength decreases for all rough surface conditions. However, when the DOP is beyond 15%, the strength difference tends to be stabilised or even lower. In general, increasing RMS leads to an increase in the strength difference, while a high CL together with a high DOP could introduce more complexity in the ultimate strength. However, the strength difference induced by a rough surface remains relatively low (less than 4%).

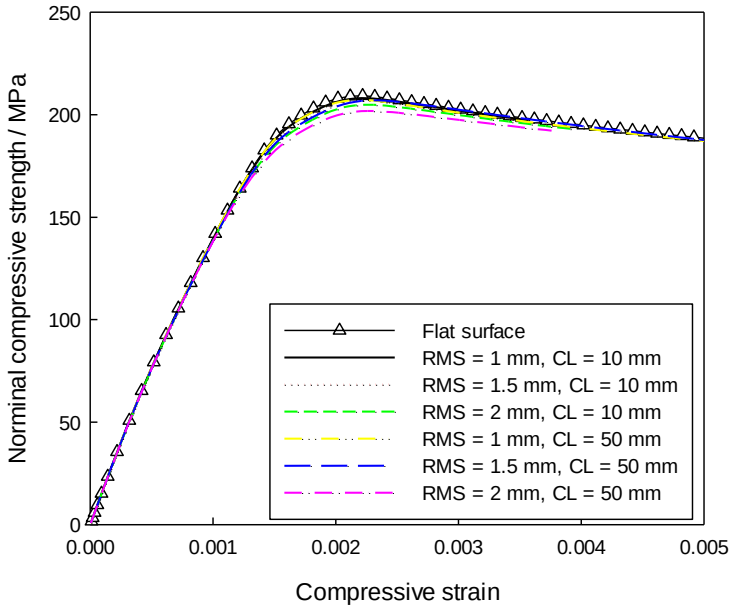

Figure 5.14. Stress-strain relationships for models with 15% DOP, flat and rough surfaces.

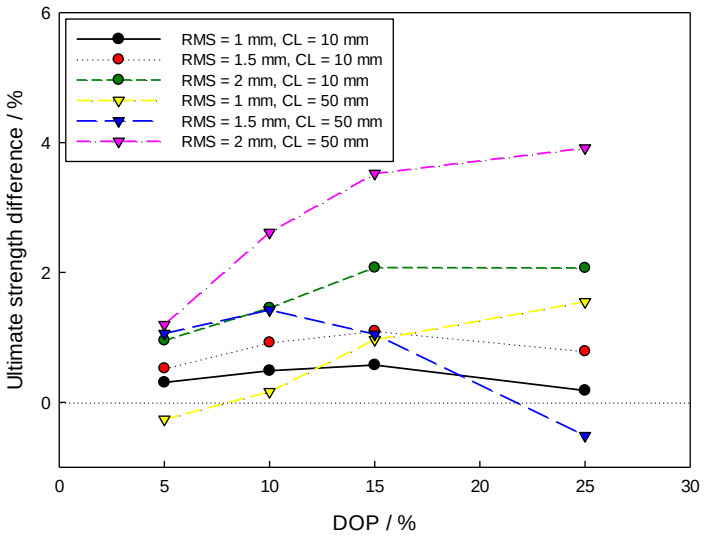

Figure 5.15. Ultimate strength reductions compared to idealised corrosion pattern (RMS = 1 mm, 1.5 mm and 2 mm; CL = 10 mm and 50 mm).

5.4 Discussion

The nonlinear FEA study indicates that the corrosion on the unloaded edge could potentially lead to a much lower ultimate strength compared to the other corrosion locations. For a ductile material, when the applied load increases the straight unloaded edges, which are supposed to be locations where supported members lie, will provide extra strength when the centre of the plate deforms and experiences tensile membrane stresses [86]. For the situations where corrosion occurs in the middle or randomly distributed on the plate surface, the unloaded edges remain intact and are able to provide complete support. The lower strength reduction for corner corrosion may be due to the less damage occurring at the unloaded edge, especially at the yielding area. Also, the lateral deflection is more constrained for corner corrosion (Figure 5.5 (b) and Figure 5.6 (b)) compared to the other situations, which can also contribute to the higher strength. However, the strength data versus pit depth for corner corrosion (Figure 5.5 (a) and Figure 5.6 (a)) indicates that a large pit depth would introduce a greater geometric complexity to the loaded and unloaded boundary conditions (i.e., a change in cross-sectional area at the loaded and unloaded boundaries), and hence a more scattered data. The strength reduction versus volume loss (Figure 5.7) indicates that the pit depth has a greater influence compared to DOP for edge and corner corrosion.

In terms of the post-ultimate strength regime (Figure 5.3 and Figure 5.4), edge corrosion tends to offer a more stable behaviour after the ultimate strength state especially when corrosion becomes severe (pit depth $\geq 0.5t_0$), while plates with corrosion at the corner present a much more rapid drop in the stiffness compared to the other corrosion patterns, implying a higher degree of instability. This is probably due to the eccentricity of loading when corrosion occurs at the loaded edges. This finding is essential because when considering a structural system consisting of a number of different structural members, some members will always reach their ultimate strength first before the whole system collapses. Thus, more unstable post-ultimate strength behaviour would greatly influence the strength of attached members which have not yet failed. When shallow pits exist, although the damage of the plate corner does not severely reduce the ultimate strength, it may significantly affect the effectiveness of the remaining intact structural members.

The influence of the bench-shape pit distribution is considered to be primarily due to the higher geometric discontinuity and hence the stress concentration introduced by the bench. Therefore, the effective stress concentration factor (K_t) defined in Equation 5.3, was obtained and plotted versus the aspect ratio of pits with and without benches.

$$K_{\mathrm{t}} = \frac{\sigma_{\max}}{\sigma_{\mathrm{n}}} \tag{5.3}$$

where $\sigma_{\max} = \sqrt{3J_2}$ (for which J_2 is the second deviatoric component of the Cauchy stress tensor) is the maximum von Mises stress for nonlinear material behaviour and σ_{n} is defined in Equation 5.1. The aspect ratio for the bench geometry was calculated for inner and outer pits, respectively. Figure 5.16 and Figure 5.17 show the influence of pit aspect ratio on K_{t} when corrosion occurs on the unloaded edge, at 15% DOP and $r_1 = (1/2)r_2$. It can be seen that for a fixed DOP value (fixed r_2) and pitting without bench, the stress concentration factor increases when the aspect ratio increases, which is also reported by Horner et al. and Cerit et al. [184,185]. Interestingly, by assessing K_{t} versus the inner and outer pit aspect ratios, it is apparent that a high stress concentration is associated with a high outer pit aspect ratio and a low inner pit aspect ratio when keeping the volume loss the same as the no-bench condition. When the volume loss increases, the outer pit aspect ratio is increased while the inner one is decreased, as illustrated in Figure 5.18, which leads to a smaller difference in the stress concentration factor between the bench and no-bench conditions, and hence a smaller ultimate strength reduction difference (Figure 5.11).

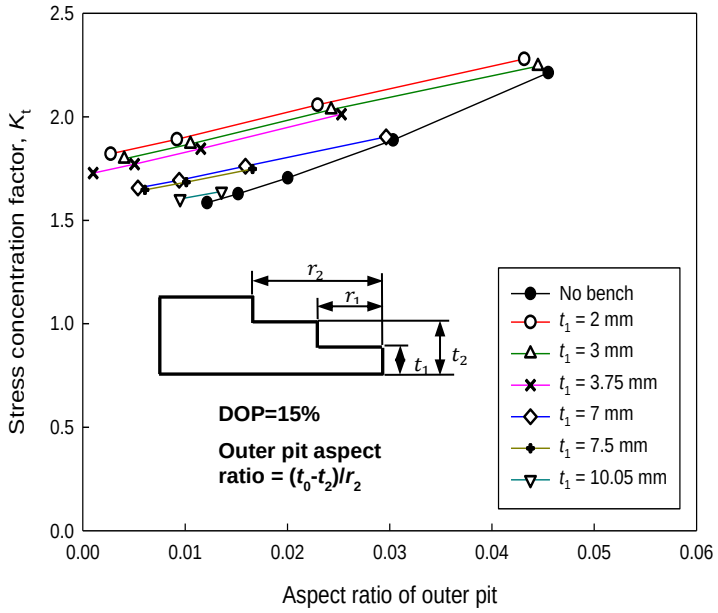

Figure 5.16: Stress concentration factor change versus outer pit aspect ratio (edge corrosion; DOP = 15%; $r_1 = (1/2)r_2$).

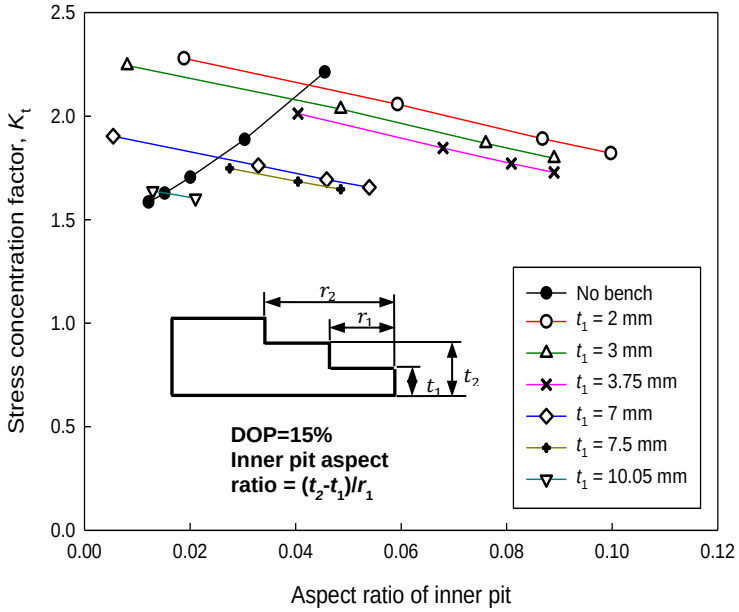

Figure 5.17: Stress concentration factor change versus inner pit aspect ratio (edge corrosion; DOP = 15%; $r_1 = (1/2)r_2$).

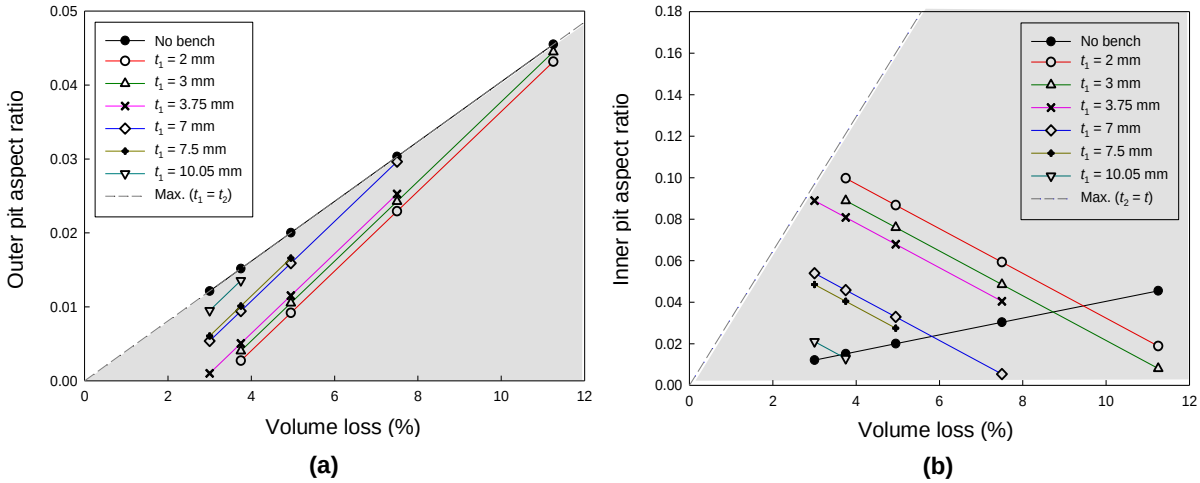

Figure 5.18: (a) Outer and (b) inner pit aspect ratio change versus volume loss (edge corrosion; DOP = 15%; $r_1 = (1/2)r_2$; shaded area: aspect ratio range).

When exploring the influence of the inner pit diameter r_1, Figure 5.19 suggests that for the same outer pit aspect ratio, a higher r_1 is associated with a higher volume loss and a higher stress concentration factor. However, at the same inner pit aspect ratio, little variation is observed for different r_1 (Figure 5.20), due to the little change in the volume loss. Therefore, for both pitting area with and without benches, the pit aspect ratio and more importantly the material degradation (volume loss) determine the strength capacity of the corroded structures.

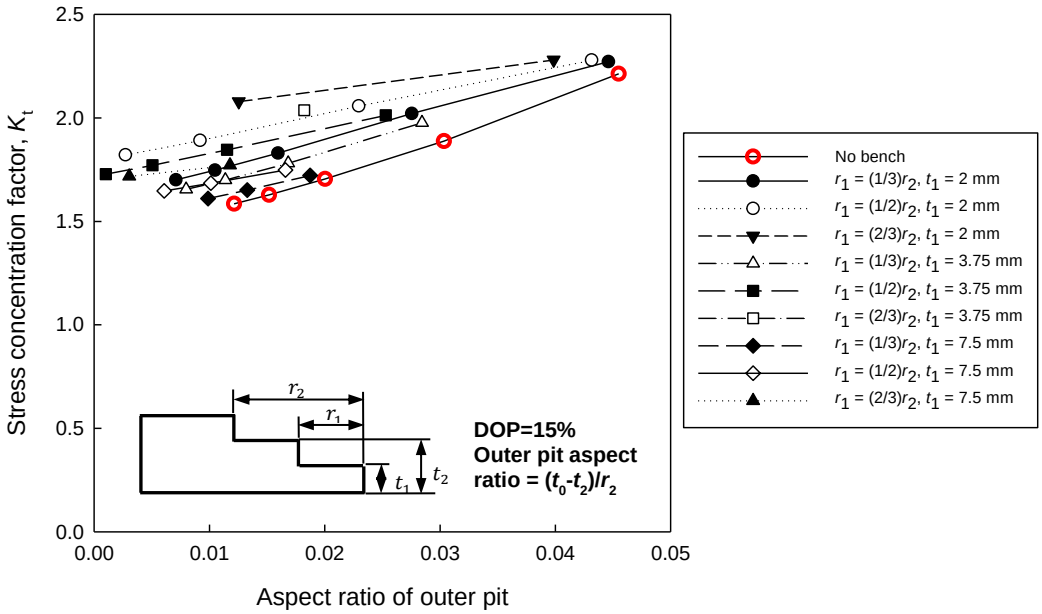

Figure 5.19: Stress concentration factor change versus outer pit aspect ratio for all r_1 values (edge corrosion; DOP = 15%).

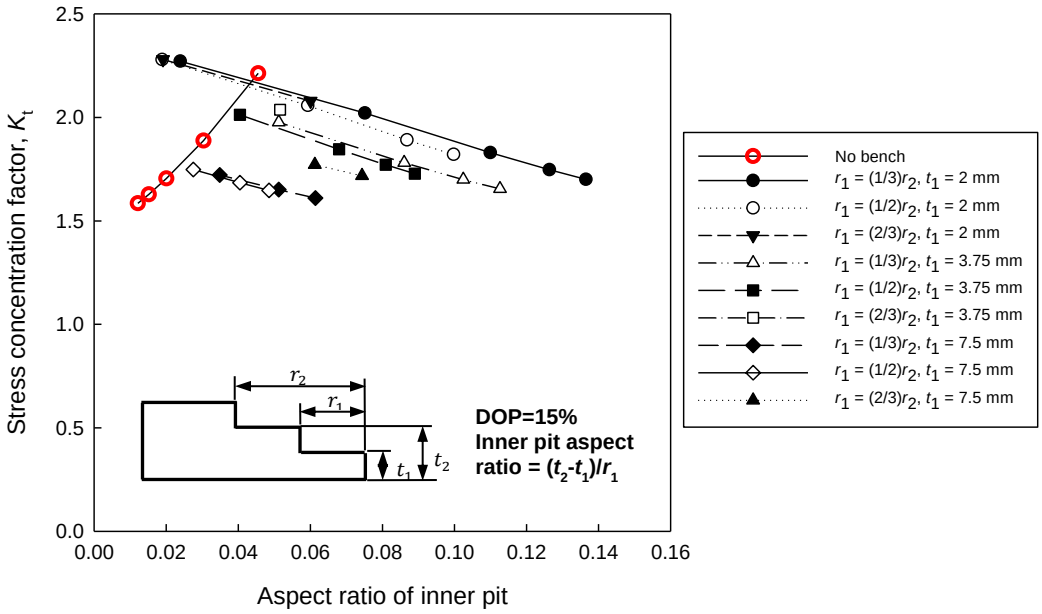

Figure 5.20: Stress concentration factor change versus inner pit aspect ratio for all r_1 values (edge corrosion; DOP = 15%).

In the modelling studies, due to the initial geometric imperfection, a plate under compressive load will experience tension on the corroded surface and compression on the unaffected surface. Since tensile stress could potentially become a source of stress-induced cracks, and concentrated plastic strain is reported to determine the crack initiation associated with pits [186], the first principal plastic strain distributions for the localised corrosion models have been investigated. The results reveal that the highest plastic strain

occurs at the pitted area and the inner pit for plates with no-bench and bench-shape pit respectively. Figure 5.21 is an example of the plastic strain evolution on a cross-section of the model with random pitting (DOP = 15%, pit depth = $0.5t_0$). Clearly, when the structure is elastically stressed (Points 1 in Figure 5.21), the highest strain starts to emerge around the edges of the pits and gradually propagates towards the pit bottom to the intact side of the plate (Points 2 to 3 in Figure 5.21). The model reaches its ultimate strength with the highest strain occurring at both the pit bottom and edge.

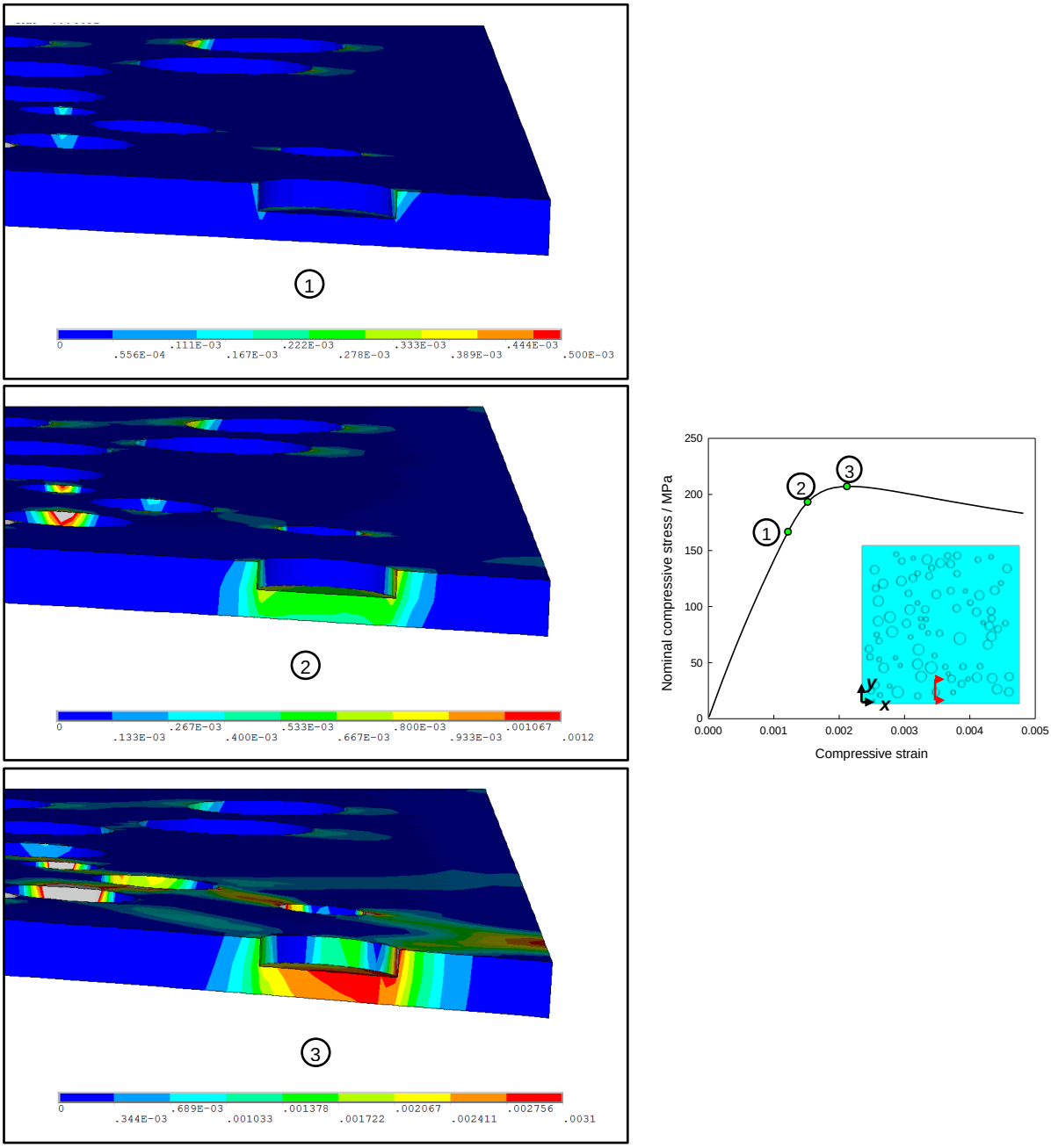

Figure 5.21: First principal plastic strain evolution for a plate with random pitting (DOP = 15%, pit depth = $0.5t_0$).

For bench-shape condition, Figure 5.22 shows the plastic strain distributions at three load steps for plate with bench-shape pitting (DOP = 15%, $r_1 = (1/2)r_2$, t_1 = 3.75 mm and t_2 = 8.75 mm). High strain is initiated just below the inner pit mouth due to the geometric discontinuity, especially at the sharp corners introduced by the pitting configuration (Points 1 and 2 in Figure 5.22). However, when further increasing the external load, the highest value gradually shifts to the pit bottom (Points 3 in Figure 5.22), where the remaining thickness is the lowest. The plastic strain distributions correlate well with previously published results [186] when the structure is elastically loaded globally. However, when it is further loaded until failure, the location of plastic strain concentration is largely dependent on the external load and the location of the damage.

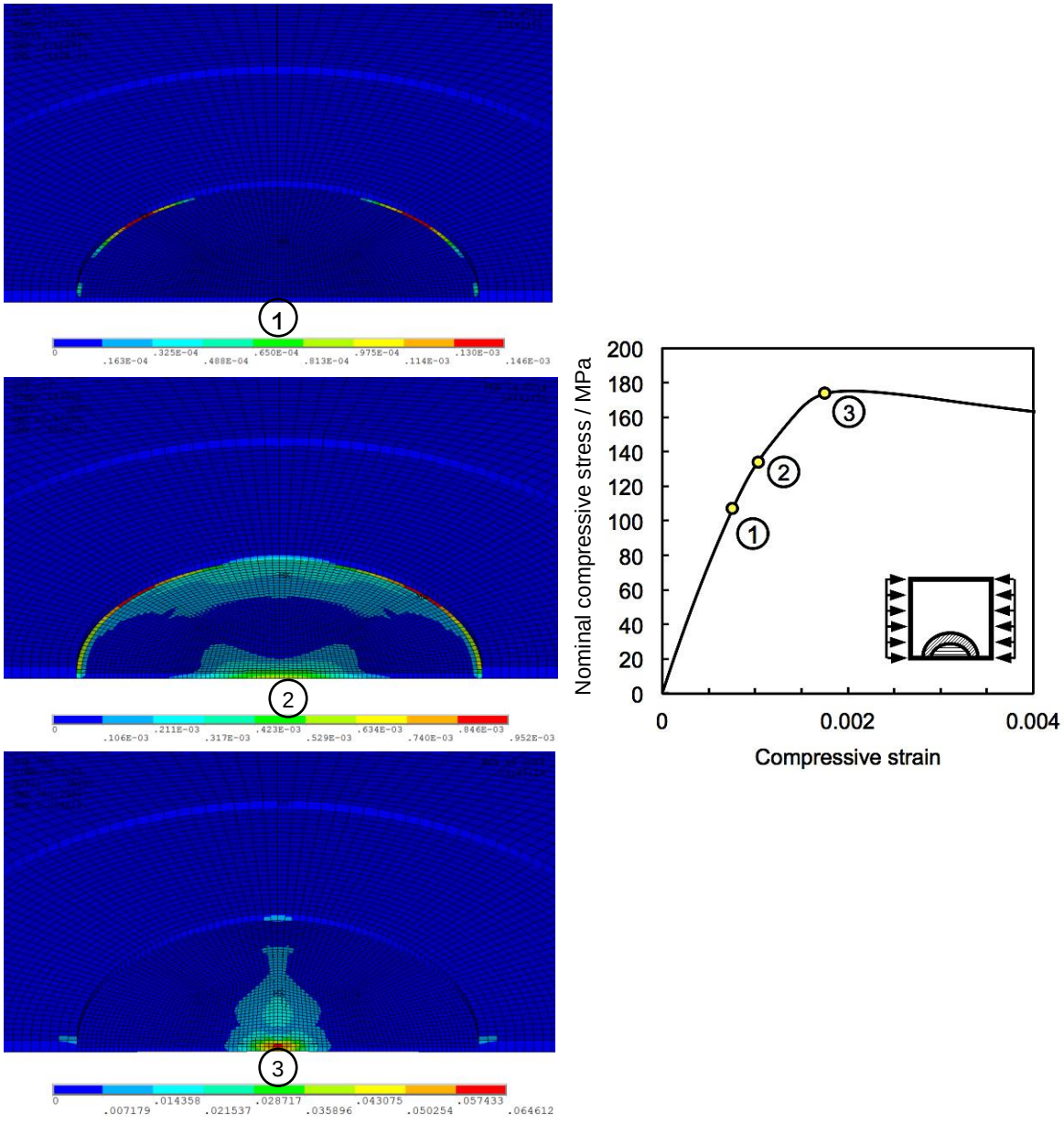

Figure 5.22: First principal plastic strain evolution for a plate with bench-shape pit (DOP = 15%, $r_1 = (1/2)r_2$, t_1 = 3.75 mm and t_2 = 8.75 mm).

In terms of a localised rough surface, the studied surfaces induced up to 4% reduction in the ultimate strength compared to models with a flat surface in the corroded area, whereas for small DOPs, the strength could even be increased, for example when RMS = 1 mm and CL = 50 mm in Figure 5.15. This observation corresponds well with Refs. [29,31,94] with a general corrosion pattern. In addition, the post-collapse behaviour is not greatly affected by the rough surface (Figure 5.14). Although a rough surface may not cause significant ultimate strength reduction, it has a greater influence on the stress and strain distributions. When examining the von Mises stress distribution at the collapse stage (Figure 5.23), it can be seen that multiple localised areas with much lower stress occur due to the rough surface, while the yielding area for the flat surface condition is very much uniform. Earlier in the elastic region, Figure 5.24 shows the stress distributions when keeping the compressive stress the same (163 MPa). It is interesting to note that no obvious yielded area appears on the plate with a flat surface yet initial plastic areas [46] have already formed on the rough surface due to the thickness variation. This early local plasticity is considered to be the major cause for the strength reduction. In addition, the extra stress concentrations could lead to early stress-induced cracks and potential corrosion acceleration. High RMS means a rougher surface (Table 5.2) which leads to more local plastic areas and hence a greater strength reduction. When increasing CL, the yielded area becomes less localised. The general stress profile is not significantly altered in both elastic and plastic regions for all DOPs when CL = 10 mm, which may explain the minor magnitude of ultimate strength reduction. However, the larger yielded area for CL = 50 mm enhances the rough surface effects on the stress distribution for difference DOP and leads to a more random variation of ultimate strength (Figure 5.15).

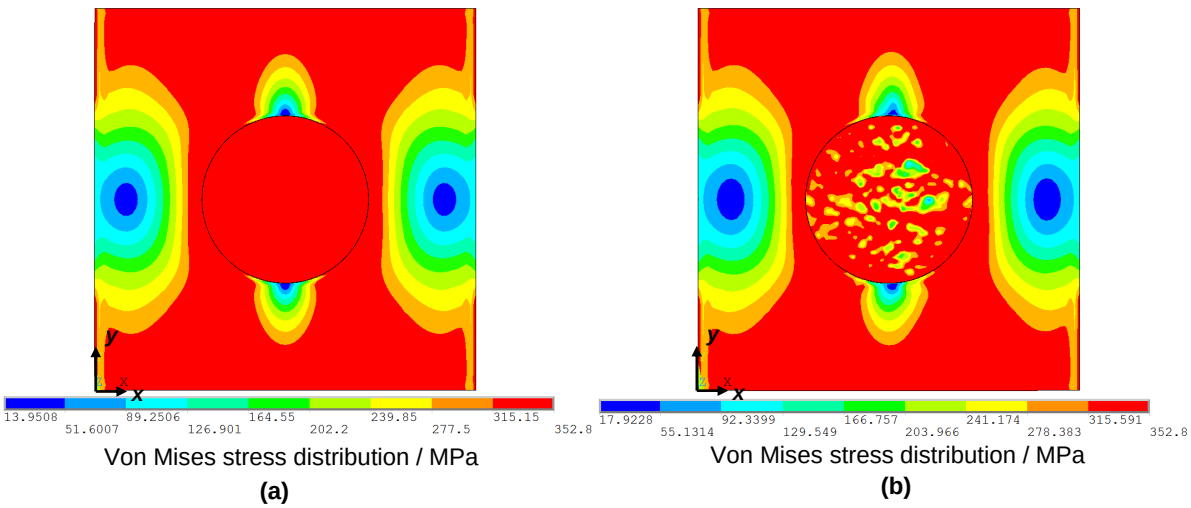

Figure 5.23: Von Mises stress distribution at ultimate strength stage (DOP = 15%): (a) flat surface in the corroded area; (b) rough surface in the corroded area (RMS = 1.5 mm, CL = 10 mm).

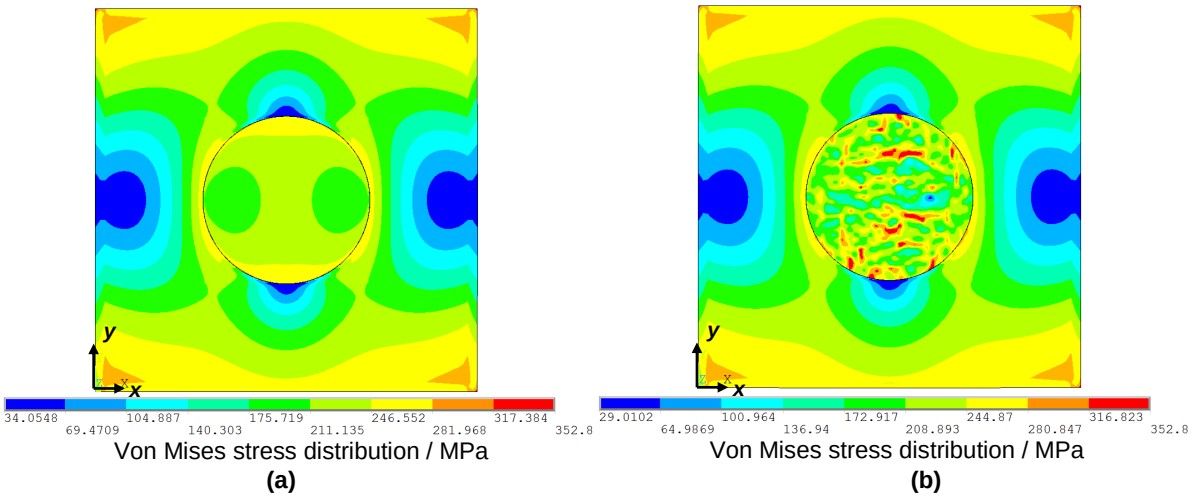

Figure 5.24: Von Mises stress distribution in elastic regime when compressive stress = 163 MPa (DOP = 15%): (a) flat surface in the corroded area; (b) rough surface in the corroded area (RMS = 1.5 mm, CL = 10 mm).

Again, the first principal plastic strain has been investigated for this situation. At the ultimate strength stage, plastic strain appears on the rough surface compared to the flat surface condition where the plastic strain only occurs around the edge. For small CL (Figure 5.25 (a) and (b)), the area with plastic strain is very narrow while larger plastic area was observed for high CL (Figure 5.25 (c) and (d)). However, only a larger DOP can incorporate the rough surface feature when CL is high, which again explains why the strength reduction is more noisy when DOP is beyond 15% for CL = 50 mm.

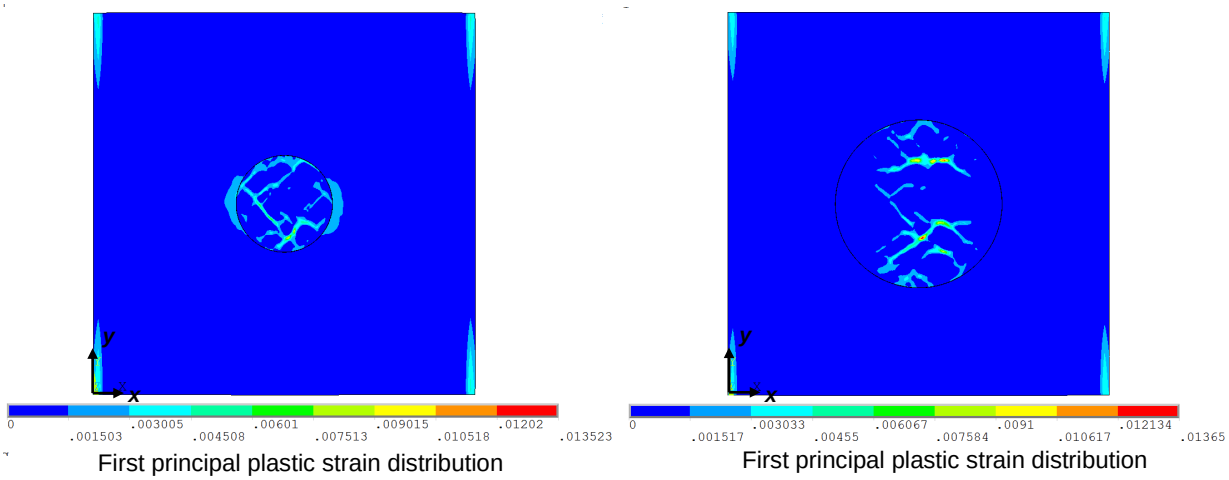

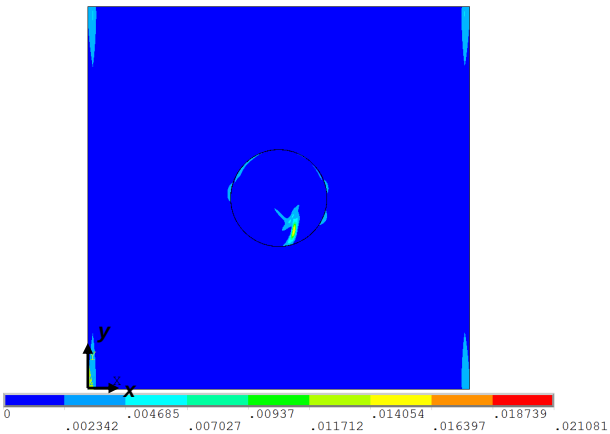

First principal plastic strain distribution

(c)

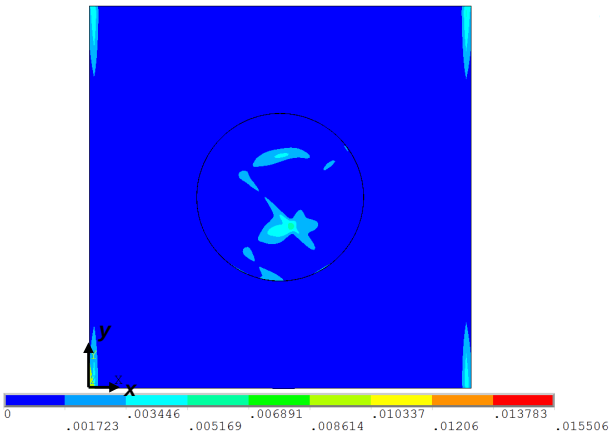

First principal plastic strain distribution

(d)

Figure 5.25: First principal plastic strain distributions at ultimate strength stage (RMS = 1.5 mm): (a) DOP = 5%, CL = 10 mm; (b) DOP = 15%, CL = 10 mm; (c) DOP = 5%, CL = 50 mm; (d) DOP = 15%, CL = 50 mm.

Figure 5.26 presents an example of the plastic strain evolution during the loading process by examining the cross-section perpendicular to the load direction. In correlation with the von Mises stress distribution, the plastic strain starts to develop not only on the intact side of the plate but also on the rough surface when the plate is elastically loaded (Point 1). When the load is further increased, the plastic strain propagates along the path with minimum thickness (Point 2) and gradually forms plastic bands or hinges (Point 3) joining the plastic region on the intact side and at the area with high geometric discontinuity. This finding indicates the plastic strain distribution is not only dependent on the external load and the damage location, which has been found from the bench-shape pit study, but also largely associated with the morphology of a corroded surface. Moreover, when the structure enters its plastic regime, the location of high plastic strain depends on the location with minimum remaining thickness. The overall significance of plastic strain analysis on the electrochemical performance will be discussed in detail in Chapter 8.

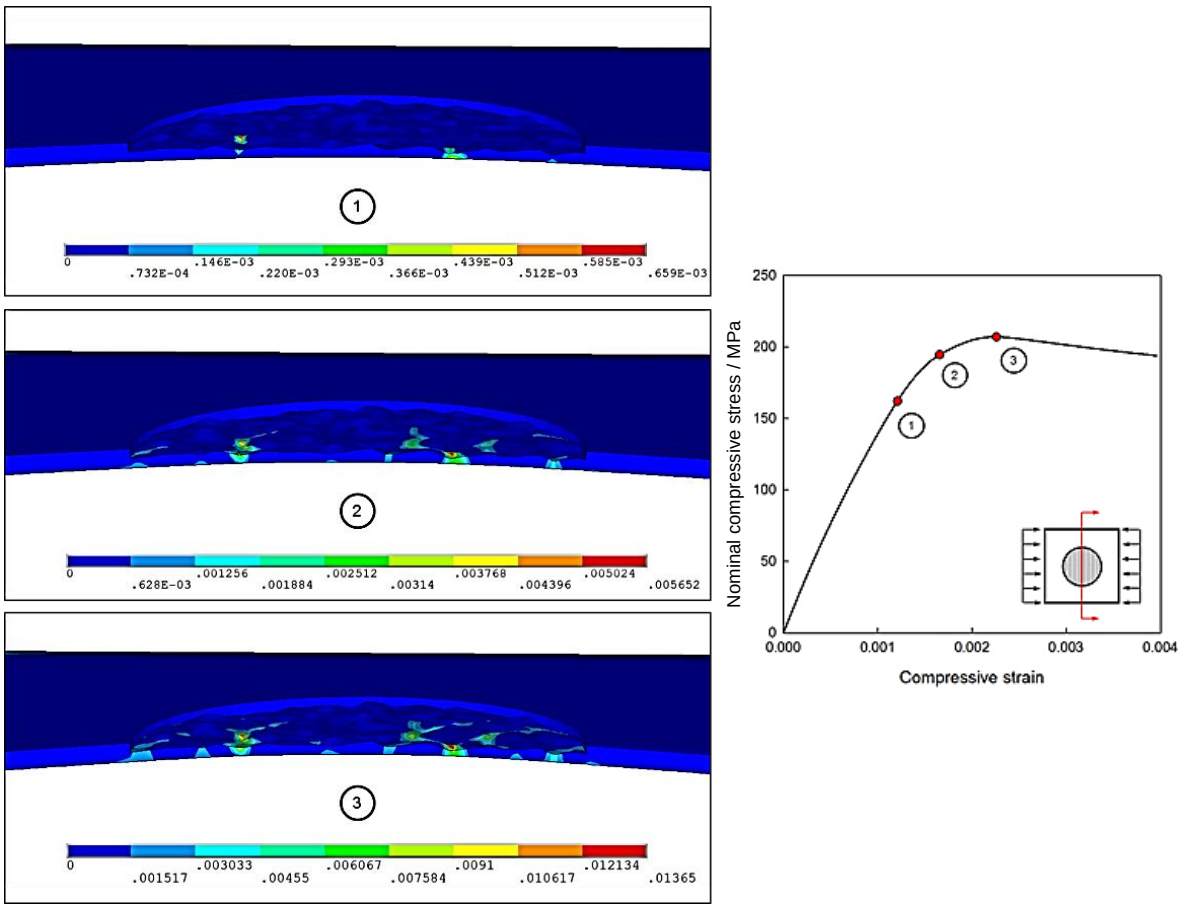

Figure 5.26: First principal plastic strain evolution for a plate with a rough surface (DOP = 15%, RMS = 1.5 mm and CL = 10 mm).

5.5 Conclusions

The utilisation of the classification society rules (coating failure scale diagrams), bench-shape corrosion and a localised rough surface have given the parametric FEA models a more realistic physical meaning for ship structures, but equally this approach could also be adapted for other marine platforms and steel bridges. The frequently detected localised corrosion (diameters in the order of tens of mm) may reduce the ultimate strength by up to 20% compared to a uniformly corroded plate. In addition, the existence of corrosion benches within these features will further reduce the strength by up to 14%. The strength reduction is greatly influenced by the corrosion size (especially the pit depth), the formation of the bench geometry and the corrosion location. In terms of the post-ultimate strength regime, the corrosion at the plate corner shows generally a more unstable behaviour, which may weaken a structural system when the rest of the structural members have not failed. Greater attention during survey and maintenance is thus needed when such pitting features occur at the corner/edge of plate structures, especially

when a bench-shape pit is formed. A rough surface has little impact on the ultimate strength and post-collapse behaviour but will introduce extra stress concentrations and localised plastic strain even when the structure is elastically loaded, which may lead to crack initiation and corrosion acceleration. In addition to strength analysis, the numerical models have provided information of the localised plastic strain distribution when the plate is loaded elastically and plastically, showing that plastic strain is not only dependent on the external load and damage location but also largely associated with the morphology of a corroded surface. Moreover, when the structure enters its plastic regime, the location of high plastic strain depends on the location with minimum remaining thickness.

Chapter 6 Experimental investigations

Although the nonlinear FEA procedure has been validated (Chapter 4) and proven to be able to provide the stress-strain relationships of a range of plates with idealised local corrosion damage (Chapter 5), its reliability remains to be fully verified. Also, due to the geometric complexity of the corrosion damage, identifying the early stress concentrations and the plastic strain around the defects are of equal or even greater importance. However, to date, only numerical modelling has provided such information. From the previously published experiments, strain gauges have been widely used at discrete locations over specimen surfaces [7,49,113], as discussed in Chapter 2. This chapter presents two full-field measurement techniques (TSA and DIC), to not only fully validate the mesh quality of the plate models introduced in Chapter 5, but also physically assess the early stress concentrations and the plastic strain distribution on a specimen with similar damage patterns as used for the modelling.

6.1 TSA experiments

TSA specimens were fabricated from Grade 070M20 steel, which is used for marine application, with a Young's modulus of 205 GPa, Poisson's ratio of 0.3 and a yield stress of 520 MPa. Specimens were scaled down to 90 mm × 90 mm × 3.5 mm to accommodate to the test machine, with the four one-side corrosion patterns shown in Figure 5.1 and three bench-shape corrosion patterns described in Section 5.2. Figure 6.1 illustrates the specimens with various pit locations. For specimens without benches, DOP = 15% and pit depth = $0.5t_0$, while for bench-shape pit, DOP = 15%, $r_1 = (1/2)r_2$ and $t_1 = (1/2)\ t_2 = (1/2)\ t_0$. Specimen (h) was manufactured with three randomly distributed artificial circular defects with a DOP of 5% and three pit depths of $0.33t_0$, $0.5t_0$ and t_0 (through-thickness). The calibration of K (where $K = 3.01\times10^{-12}$ Pa^{-1}) was achieved by testing an intact specimen with known principal stresses. The temperature was 22 °C. Although it has been assessed numerically that the specimen will not develop plastic strain under a maximum load of 35 kN, the cyclic loading could potentially lead to a fatigue problem. Thus, tests were performed within the first ten cycles to minimise the development of fatigue cracks. The specimens were unloaded immediately after data acquisition. Each test condition was repeated three times and the average values are reported below.

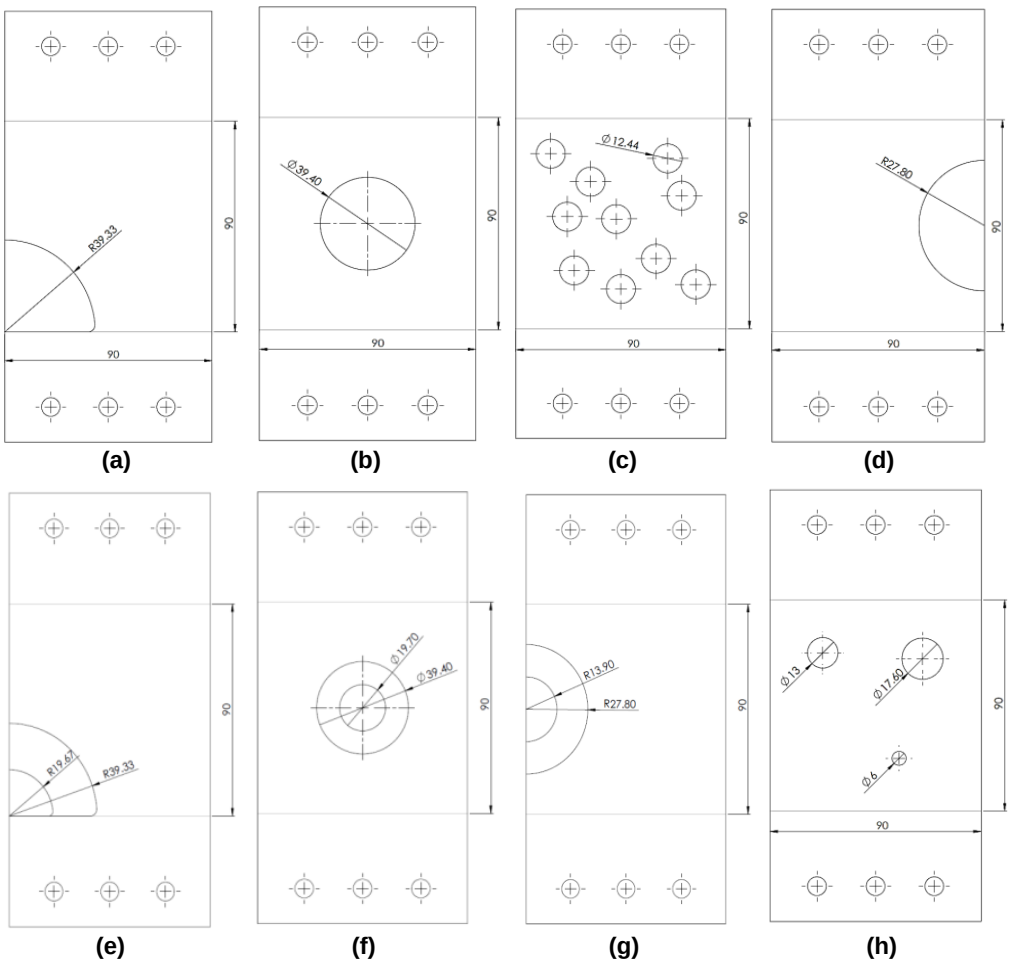

Figure 6.1. Schematic of TSA test specimens (all dimensions are in mm): (a) corrosion at the corner (lc); (b) corrosion in the middle (m); (c) random pitting (r); (d) corrosion at the unloaded edge (b); (e) bench-shape_lc; (f) bench-shape_m; (g) bench-shape_b; (h) specimen with random pits and thickness reductions.

All the temperature data from TSA were processed using Equation 3.2 to generate principal stress maps. The numerical models of the test specimens were built using shell elements (SHELL181/281) with the mesh pattern used in the modelling study. The upper and lower edges were clamped with a uniform tensile pressure applied at the lower edge (the same as for the TSA tests). In the FEA models, the load maximum amplitude difference of 30 kN was applied to achieve the same loading condition as used to calculate the TSA stress results. Figure 6.2 to Figure 6.8 show the principal stress maps from TSA and FEA for all test conditions.

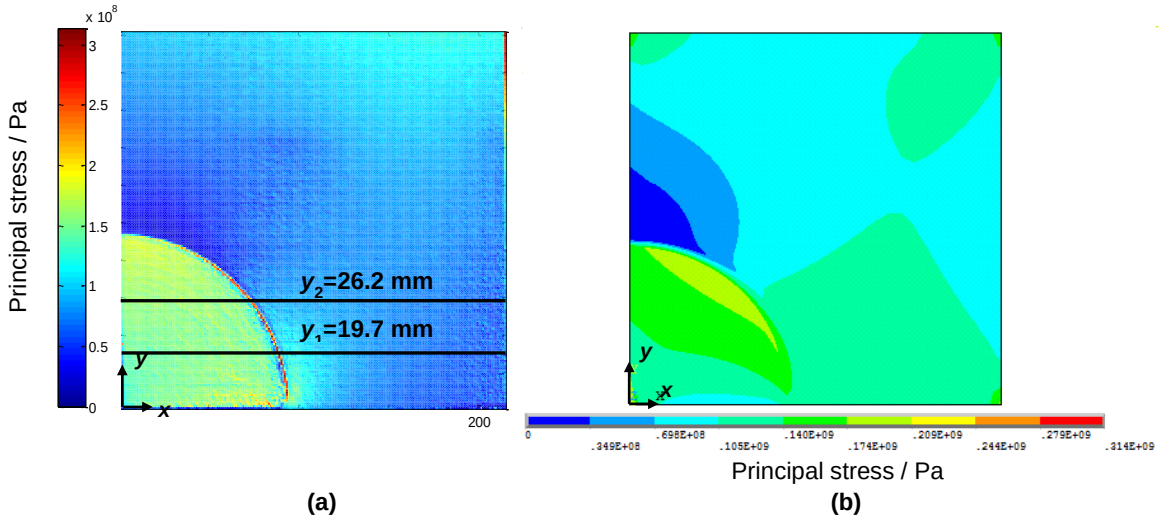

Figure 6.2. Front surface of principal stress from (a) TSA and (b) FEA for Specimen (a) with corrosion at the corner.

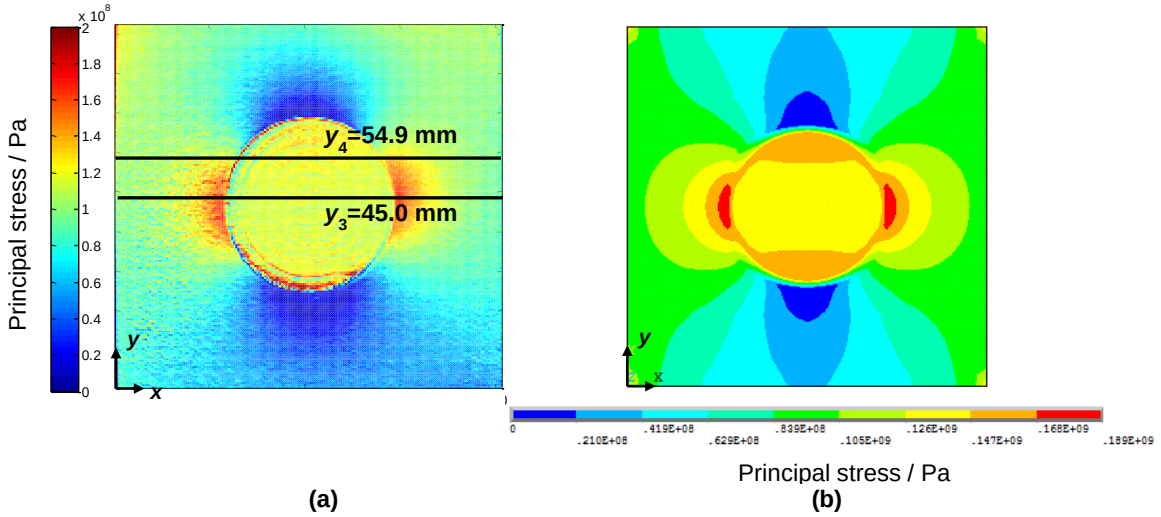

Figure 6.3. Front surface of principal stress from (a) TSA and (b) FEA for Specimen (b) with corrosion in the middle.

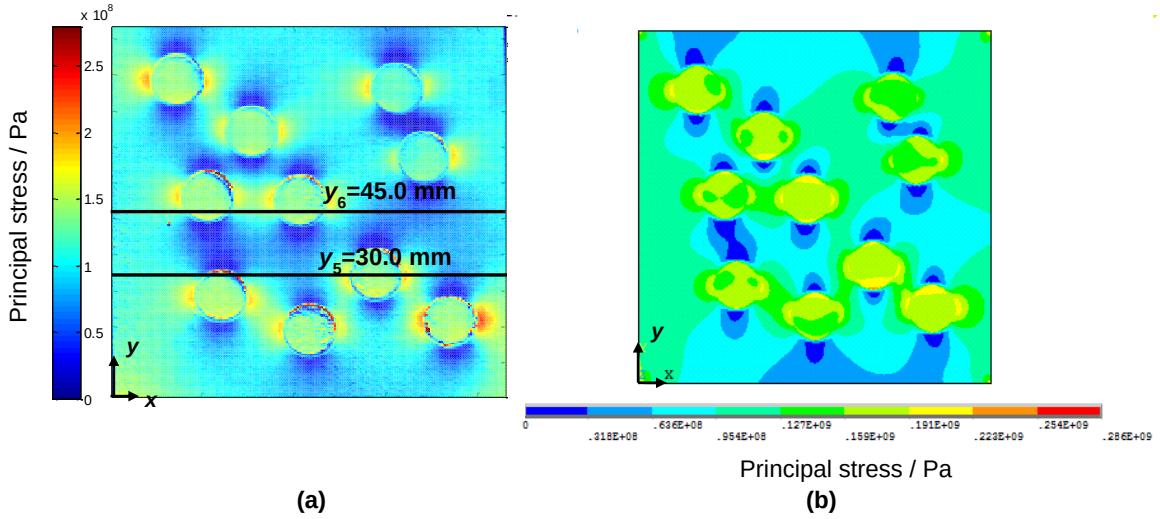

Figure 6.4. Front surface of principal stress from (a) TSA and (b) FEA for Specimen (c) with random pitting.

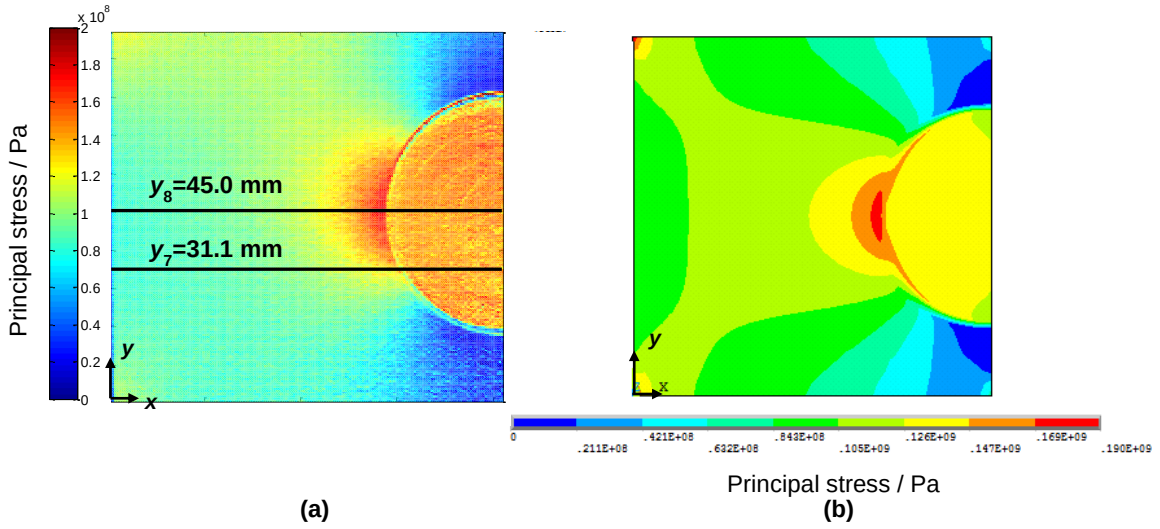

Figure 6.5. Front surface of principal stress from (a) TSA and (b) FEA for Specimen (d) with corrosion at the unloaded edge.

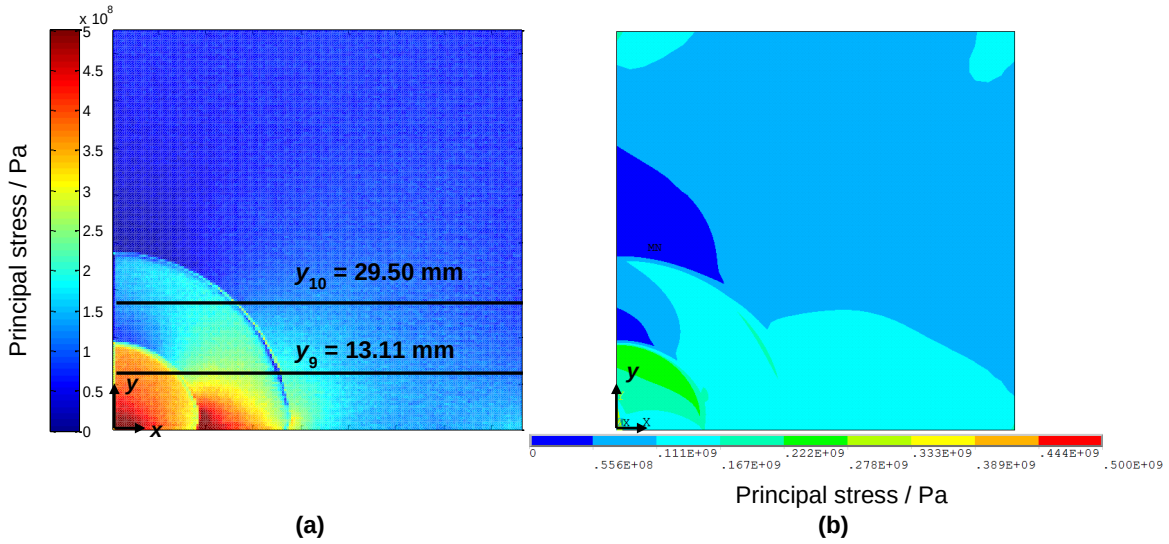

Figure 6.6. Front surface of principal stress from (a) TSA and (b) FEA for Specimen (e) with bench-shape corrosion at the corner.

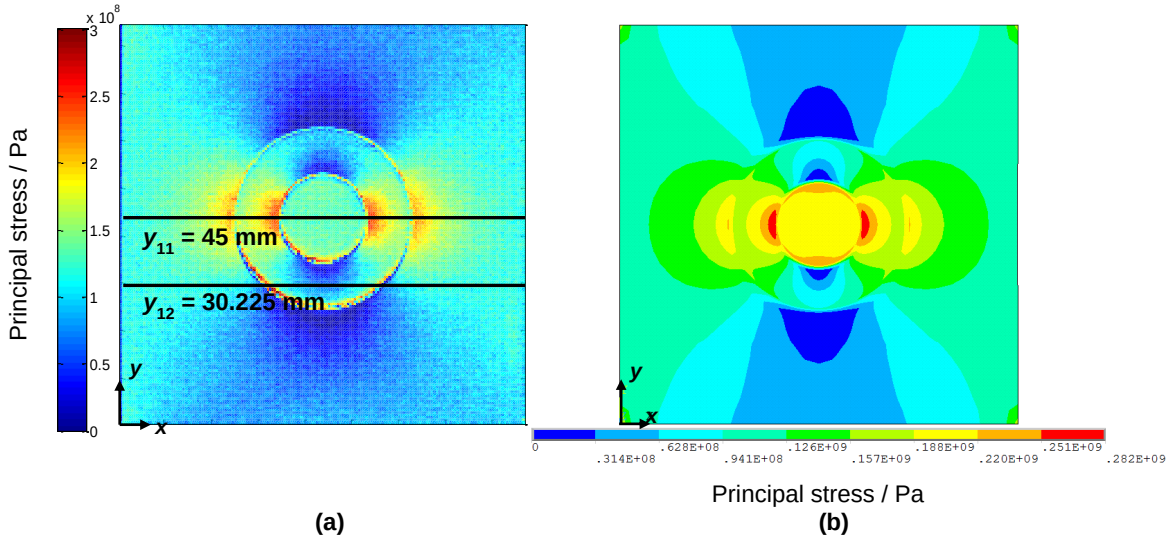

Figure 6.7. Front surface of principal stress from (a) TSA and (b) FEA for Specimen (f) with bench-shape corrosion in the middle.

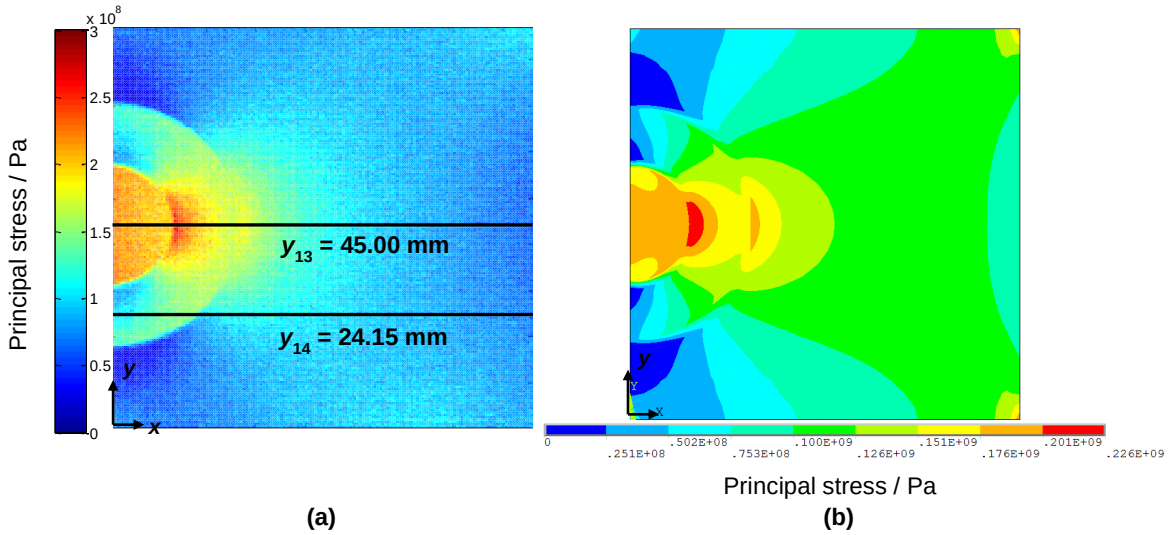

Figure 6.8. Front surface of principal stress from (a) TSA and (b) FEA for Specimen (g) with bench-shape corrosion at the unloaded edge.

TSA was also conducted on the back surfaces of the specimens. Figure 6.9 is an example of the principal stress map of the back surface of Specimen (h). It can be seen that a clear stress change at the back of the non-through-thickness defect is detected.

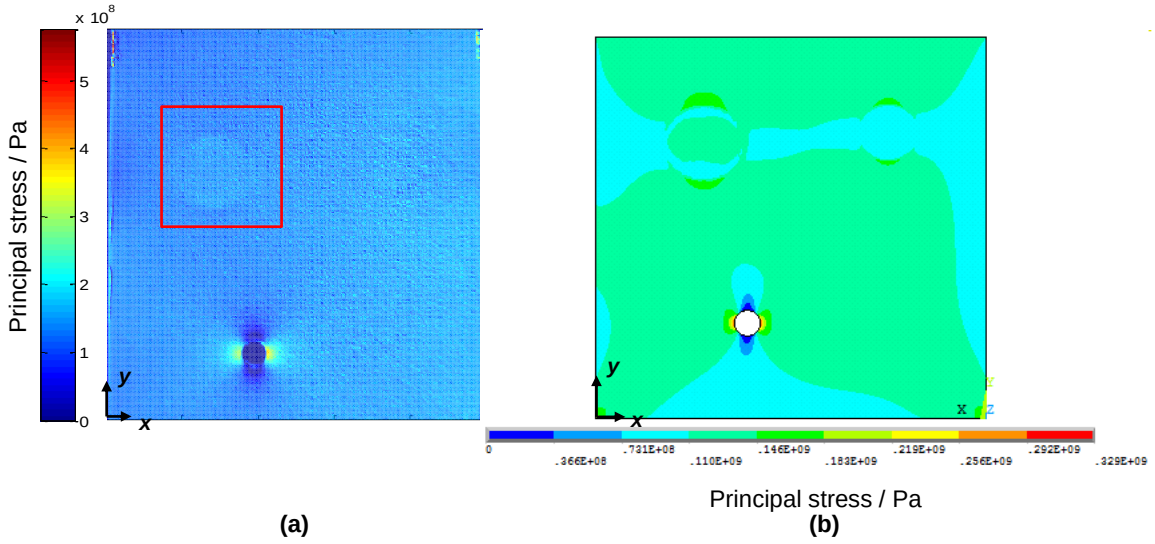

Figure 6.9. Back surface of principal stress from (a) TSA and (b) FEA for Specimen (h) with random pits and thickness reductions.

To further verify the quality of the numerical models, line data at different locations (indicated in Figure 6.2 (a) to Figure 6.8 (a)) were obtained and plotted. Figure 6.10 to Figure 6.16 are comparisons of stress values along the two defined lines for every specimen.

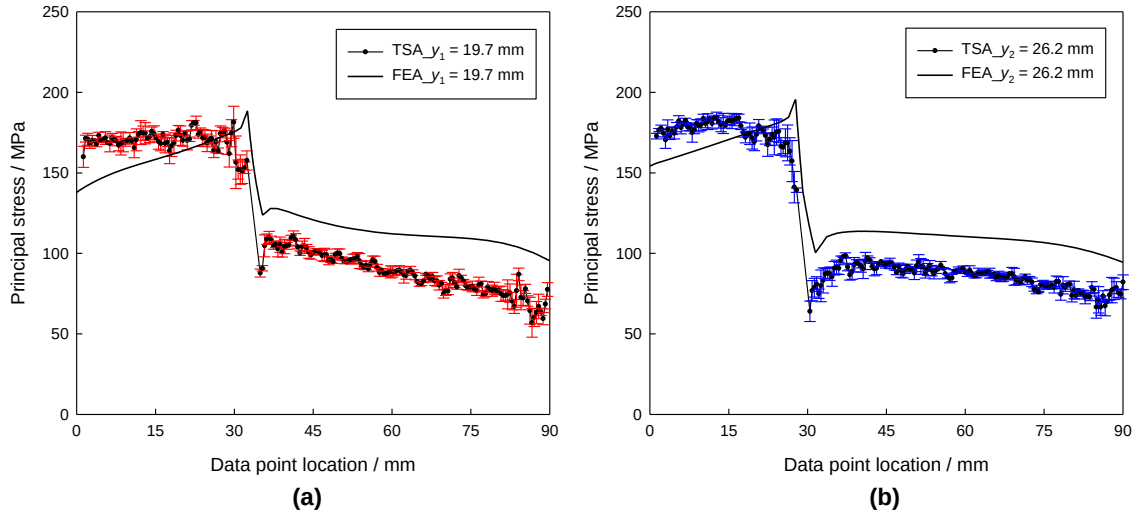

Figure 6.10. TSA and FEA data at (a) y_1 and (b) y_2 in Figure 6.2 for corrosion at the corner (Specimen (a)).

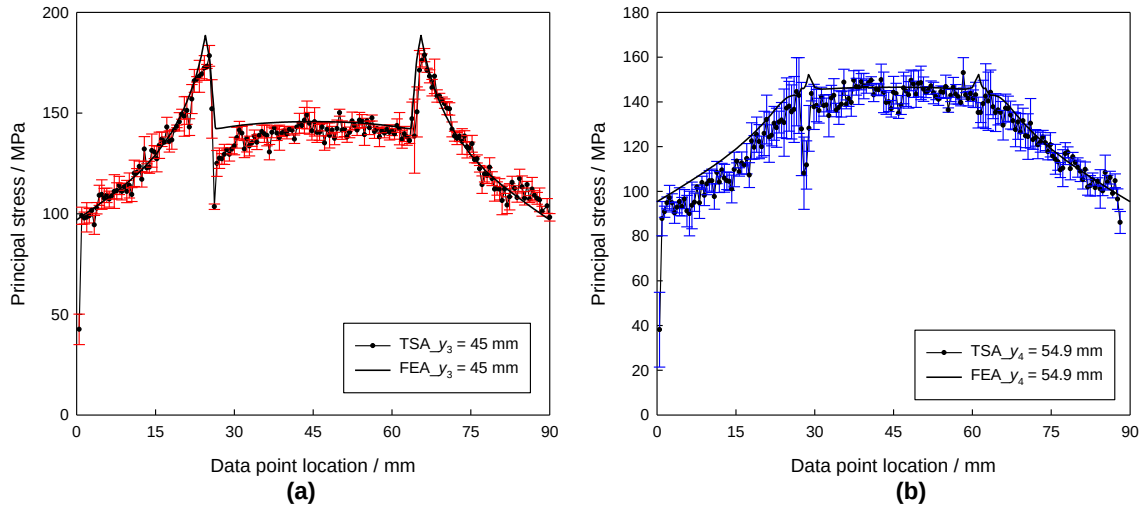

Figure 6.11. TSA and FEA data at (a) y_3 and (b) y_4 in Figure 6.3 for corrosion in the middle (Specimen (b)).

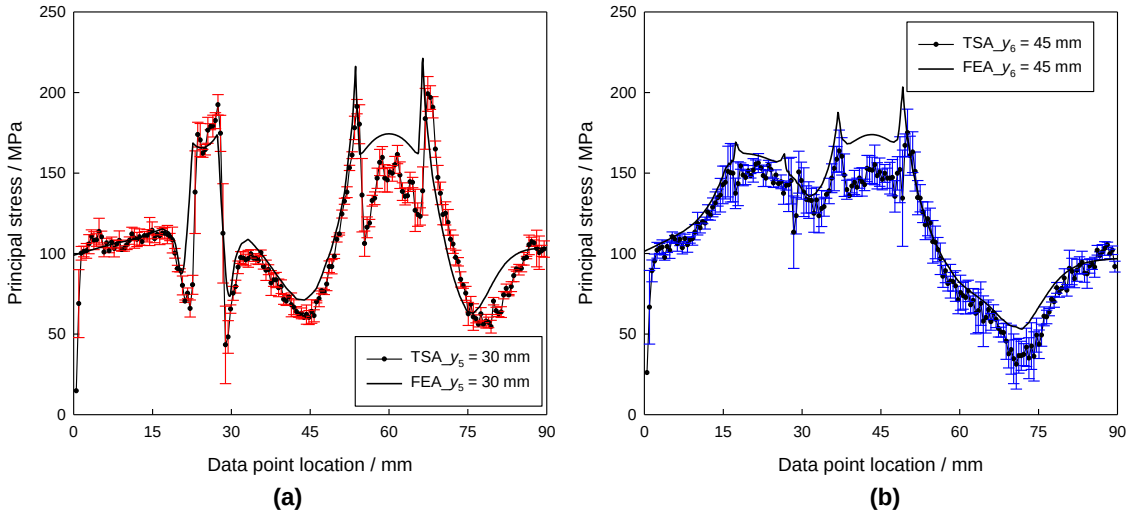

Figure 6.12. TSA and FEA data at (a) y_5 and (b) y_6 in Figure 6.4 for random pitting (Specimen (c)).

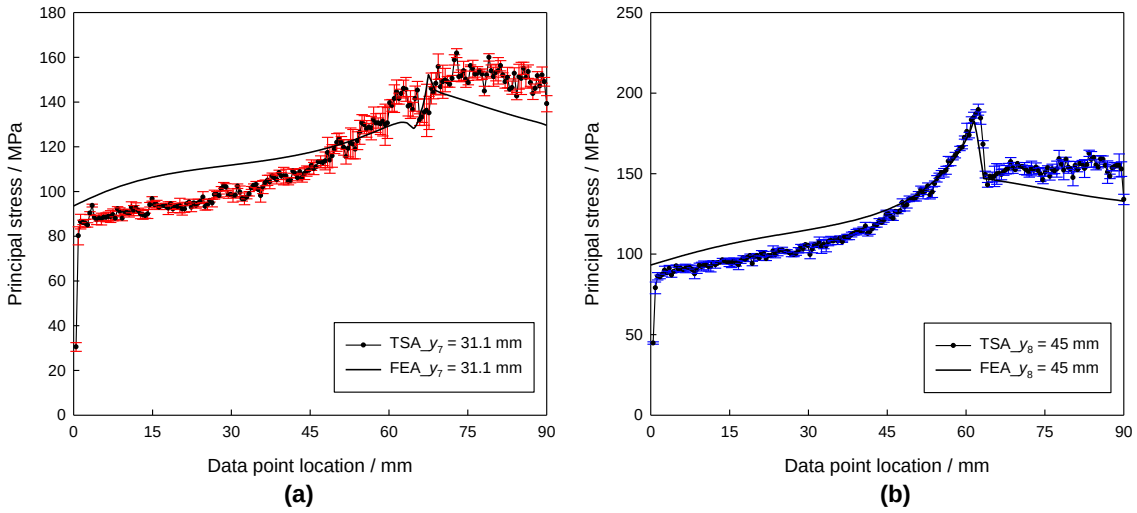

Figure 6.13. TSA and FEA data at (a) y_7 and (b) y_8 in Figure 6.5 for corrosion on the unloaded edge (Specimen (d)).

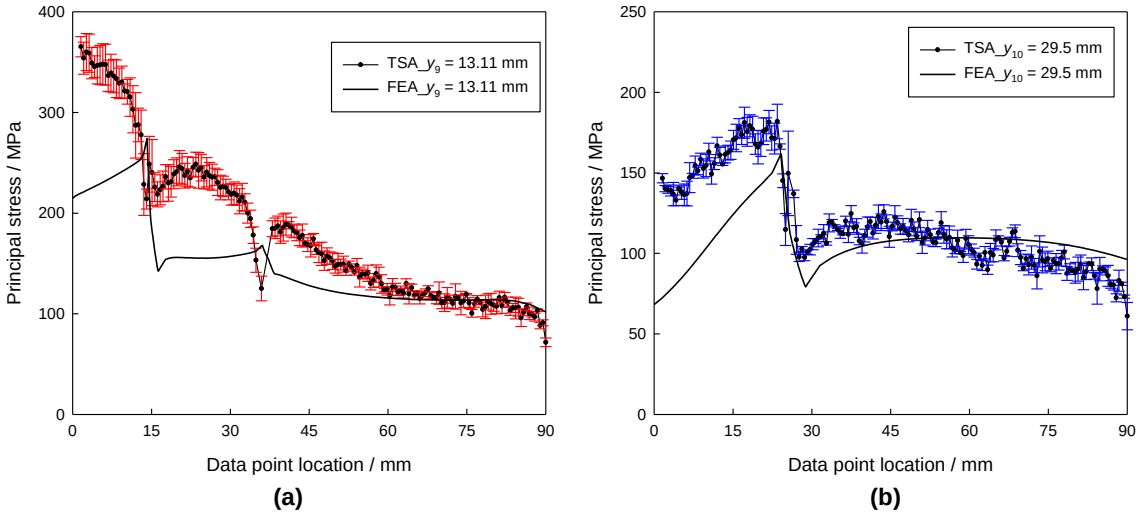

Figure 6.14. TSA and FEA data at (a) y_9 and (b) y_{10} in Figure 6.6 for bench-shape corrosion at the corner (Specimen (e)).

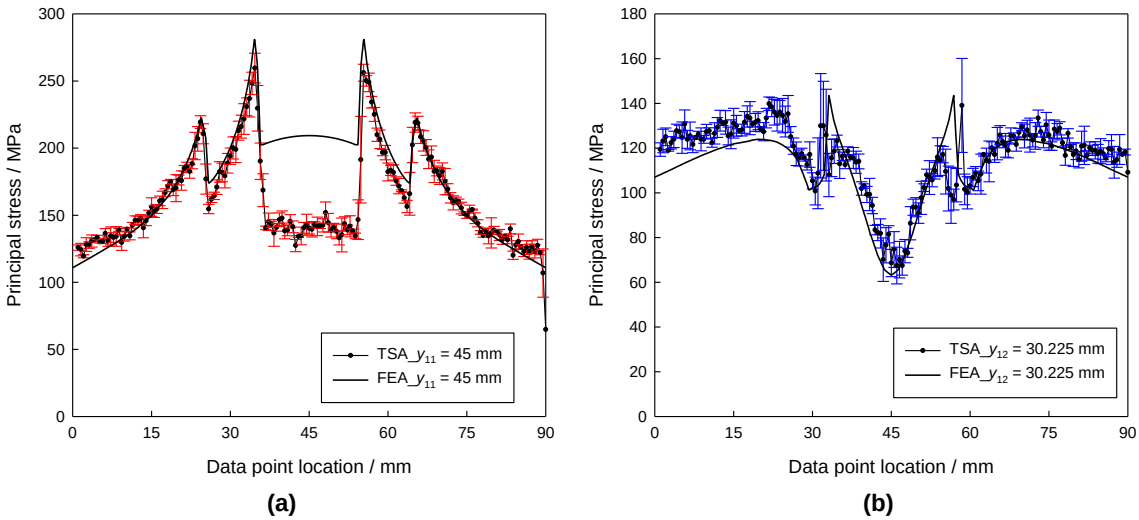

Figure 6.15. TSA and FEA data at (a) y_{11} and (b) y_{12} in Figure 6.7 for bench-shape corrosion in the middle (Specimen (f)).

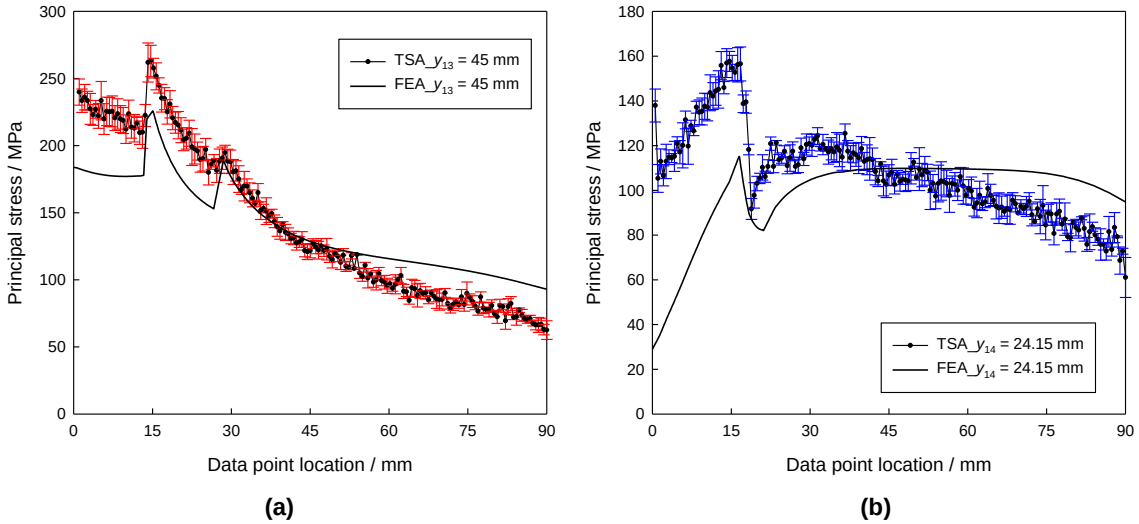

Figure 6.16. TSA and FEA data at (a) y_{13} and (b) y_{14} in Figure 6.8 for bench-shape corrosion on the unloaded edge (Specimen (g)).

6.2 DIC experiments

Four DIC specimens were fabricated from Grade 070M20 steel (used for TSA tests) and scaled down to 110 mm × 90 mm × 3 mm (tested area: 90 mm × 90 mm), with the four one-side corrosion patterns shown in Figure 5.1. Both top and bottom edges of the specimen were clamped to the specifically designed rigs. Similar to the TSA test condition, the DOP was 15% and pit depth was $0.5t_0$ for all DIC specimens. A compressive load was applied quasi-statically at 1 mm min^{-1} with the entire loading procedure monitored by a stereo camera system at 1 Hz in order to capture the ultimate strength point. For data processing, the subset size was set to be 61 × 61 pixels while the step size (grid spacing) was 19 pixels, leading to a 31% overlap. The correlation mode was set to be the sum of differential of the preceding images, which is suitable for large deformation over time. Since the rigs will experience elastic deformations as well during the loading process, strain values instead of displacement along the load direction were examined. Regarding the numerical models, shell element SHELL181 was used to construct the models. The material was set to be elastic-perfectly-plastic. After the application of initial deflection using polynomial functions, both the loaded edges were straightened and the deflections were updated accordingly. Figure 6.17 to Figure 6.20 are the load-strain relationships obtained from DIC and FEA for all the specimens.

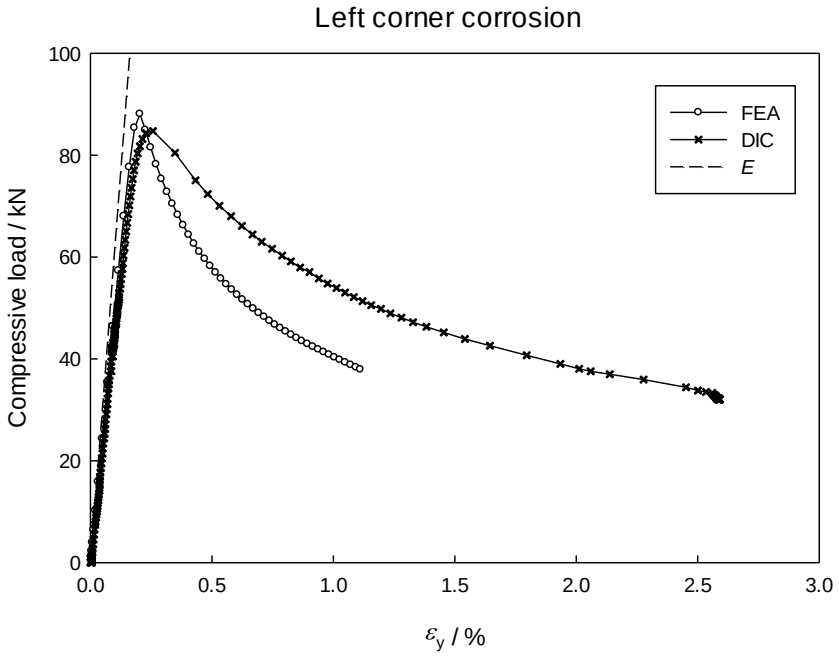

Figure 6.17. Load-strain relationships obtained from DIC and FEA for specimen with corrosion at the corner.

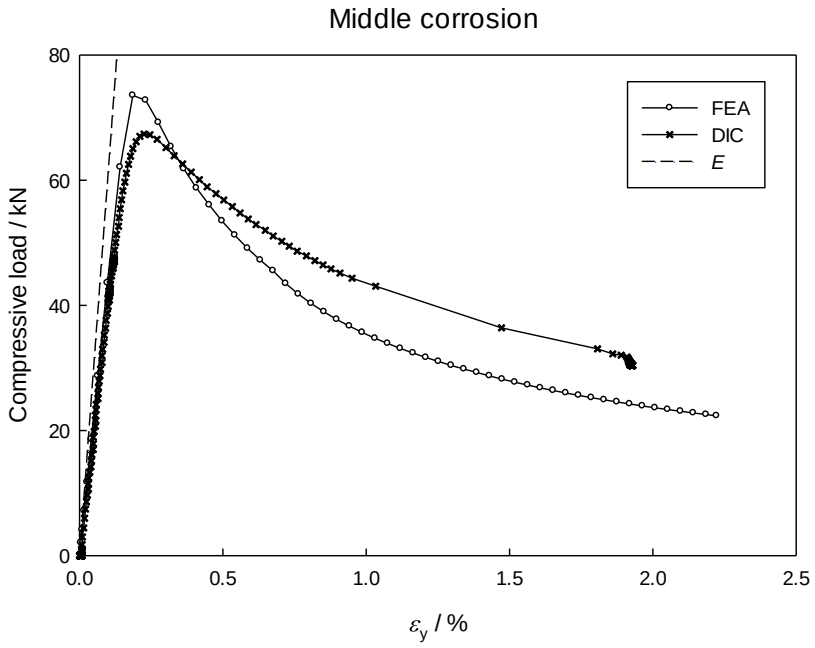

Figure 6.18. Load-strain relationships obtained from DIC and FEA for specimen with corrosion in the middle.

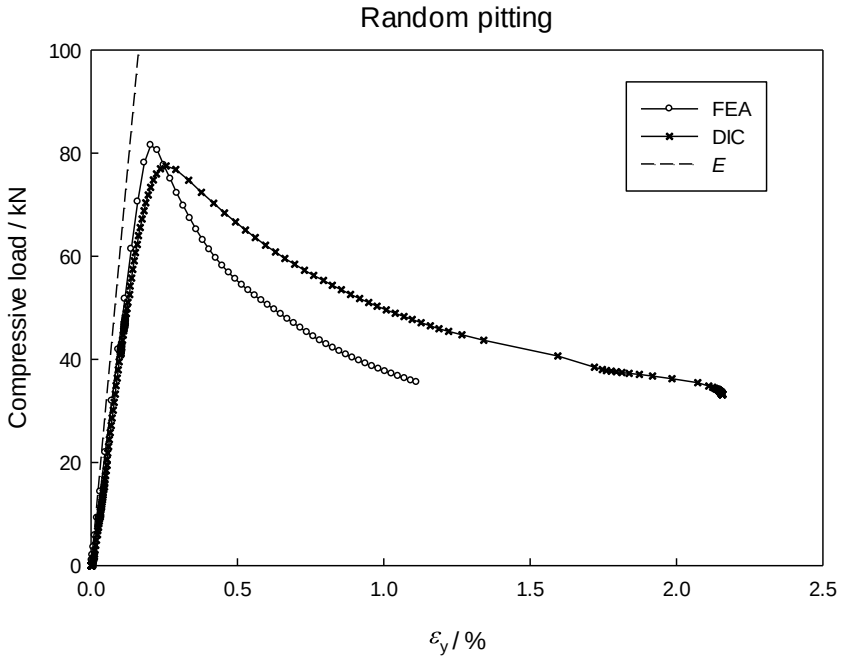

Figure 6.19. Load-strain relationships obtained from DIC and FEA for specimen with random pitting corrosion.

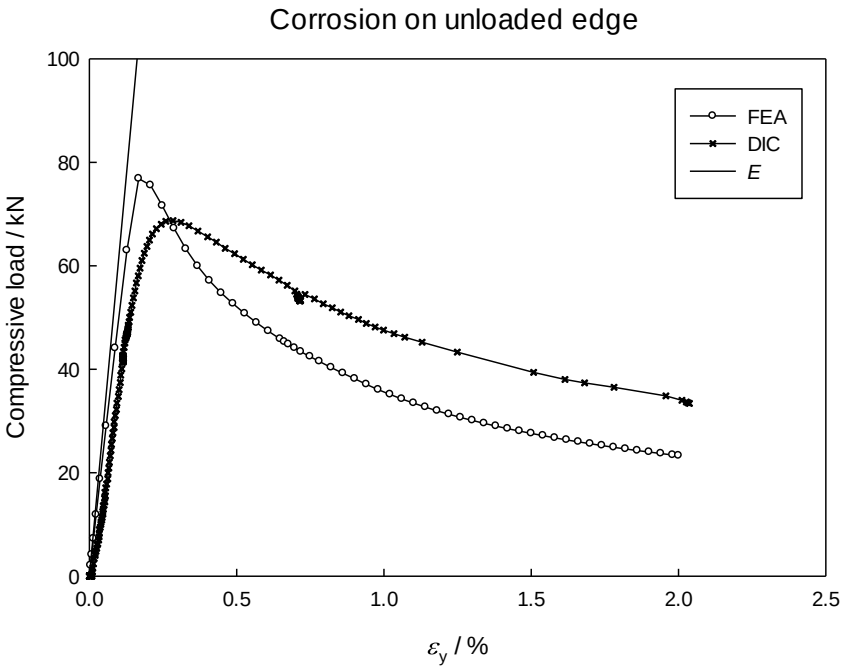

Figure 6.20. Load-strain relationships obtained from DIC and FEA for specimen with corrosion on the unloaded edge.

Based on the load-strain plots, the ultimate strength was determined for all test conditions. Figure 6.21 to Figure 6.28 are comparisons of the out-of-plane deformation and strain in *y*-direction (loading direction) obtained from DIC and FEA for all specimens at their ultimate strength states.

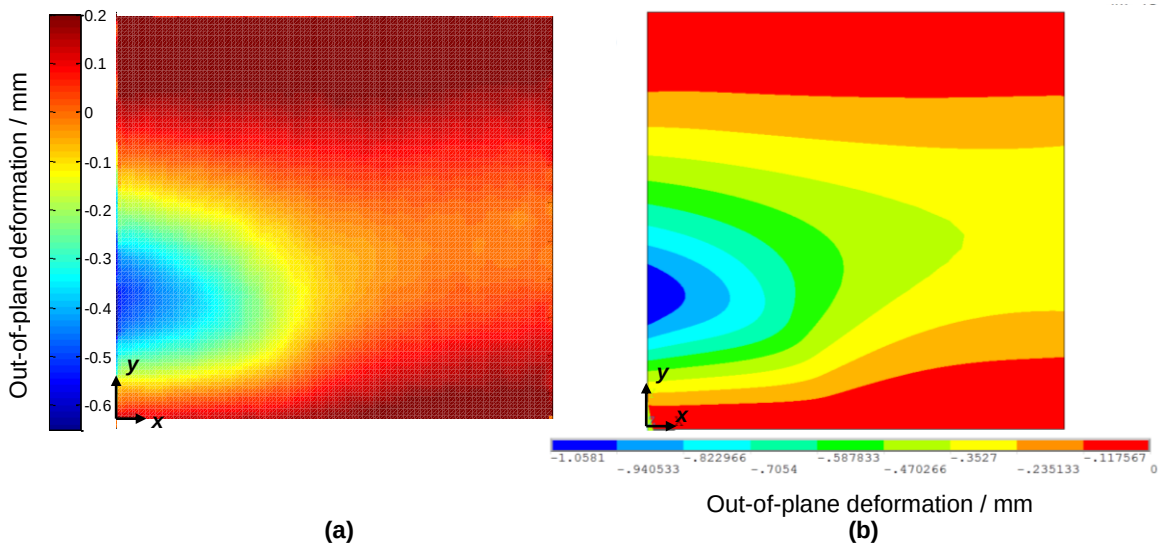

Figure 6.21. Front surface of out-of-plane deformation maps from (a) DIC and (b) FEA for specimen with corrosion at the corner at ultimate strength state.

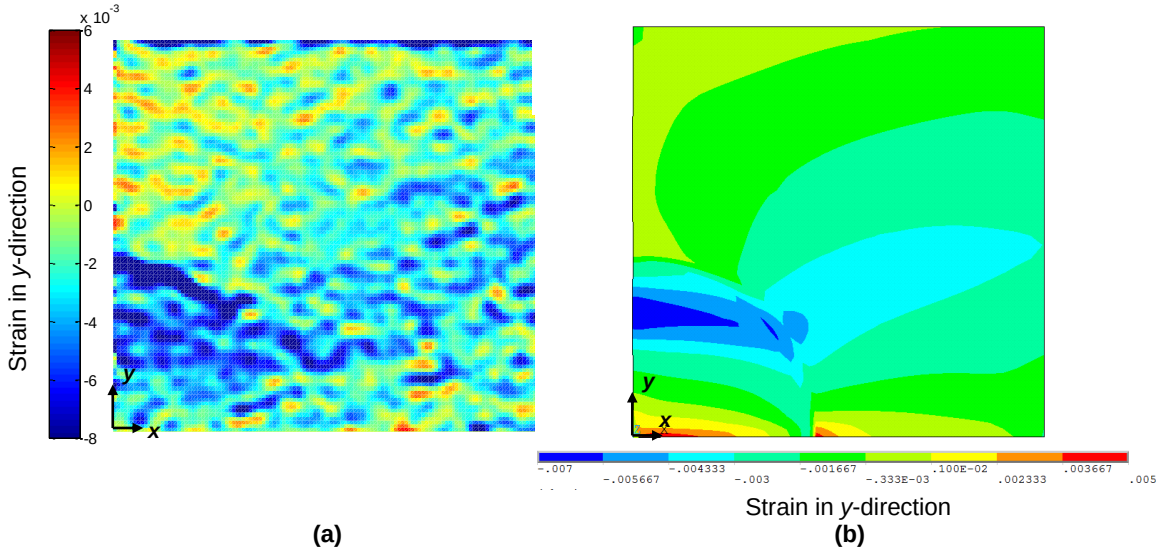

Figure 6.22. Front surface of strain in *y*-direction maps from (a) DIC and (b) FEA for specimen with corrosion at the corner at ultimate strength state.

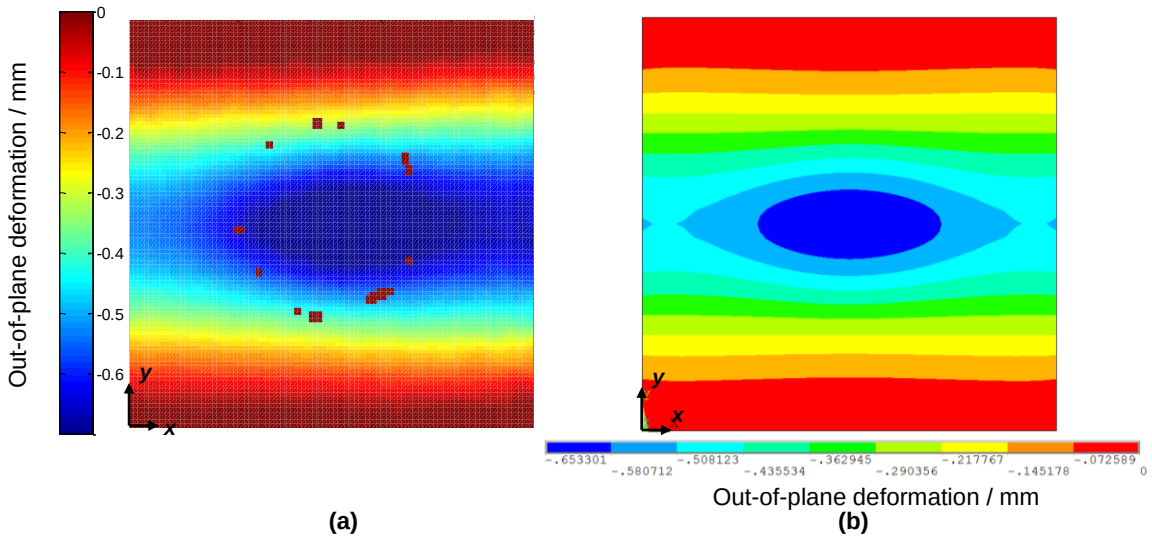

Figure 6.23. Front surface of out-of-plane deformation maps from (a) DIC and (b) FEA for specimen with corrosion in the middle at ultimate strength state.

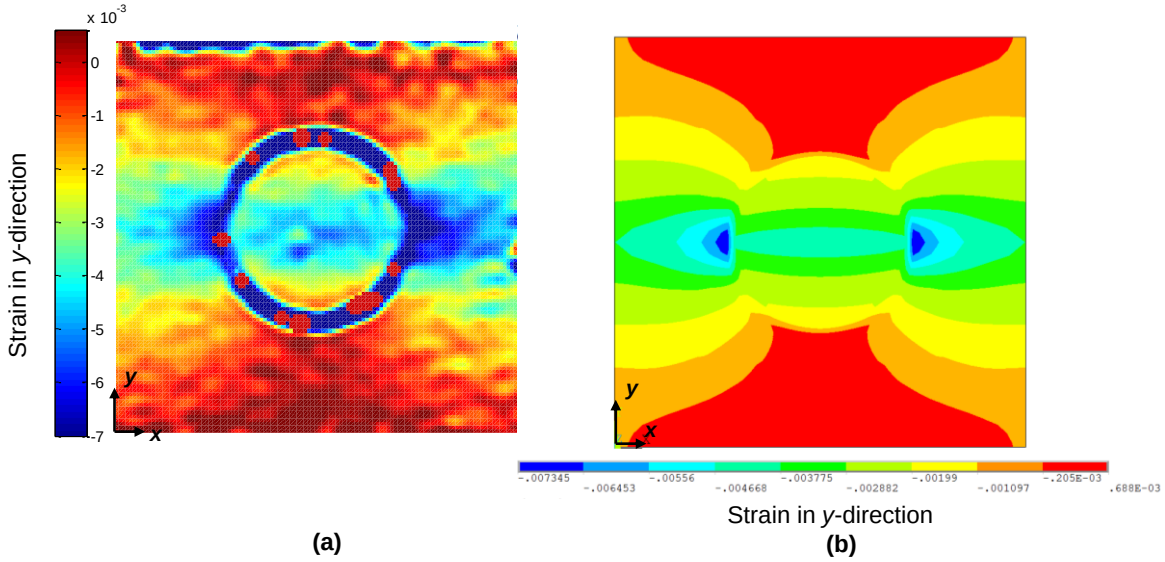

Figure 6.24. Front surface of strain in *y*-direction maps from (a) DIC and (b) FEA for specimen with corrosion in the middle at ultimate strength state.

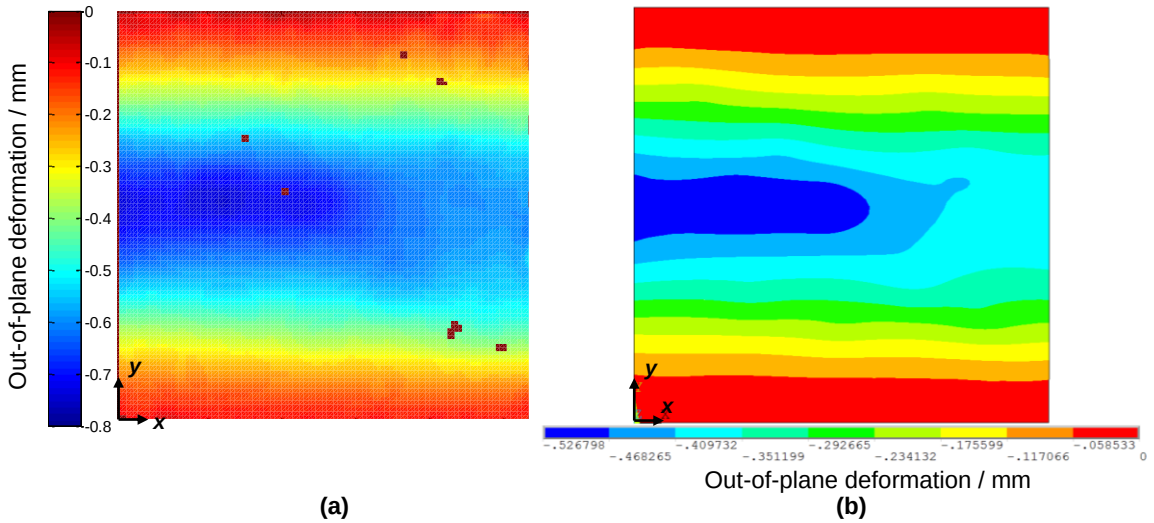

Figure 6.25. Front surface of out-of-plane deformation maps from (a) DIC and (b) FEA for specimen with random pitting at ultimate strength state.

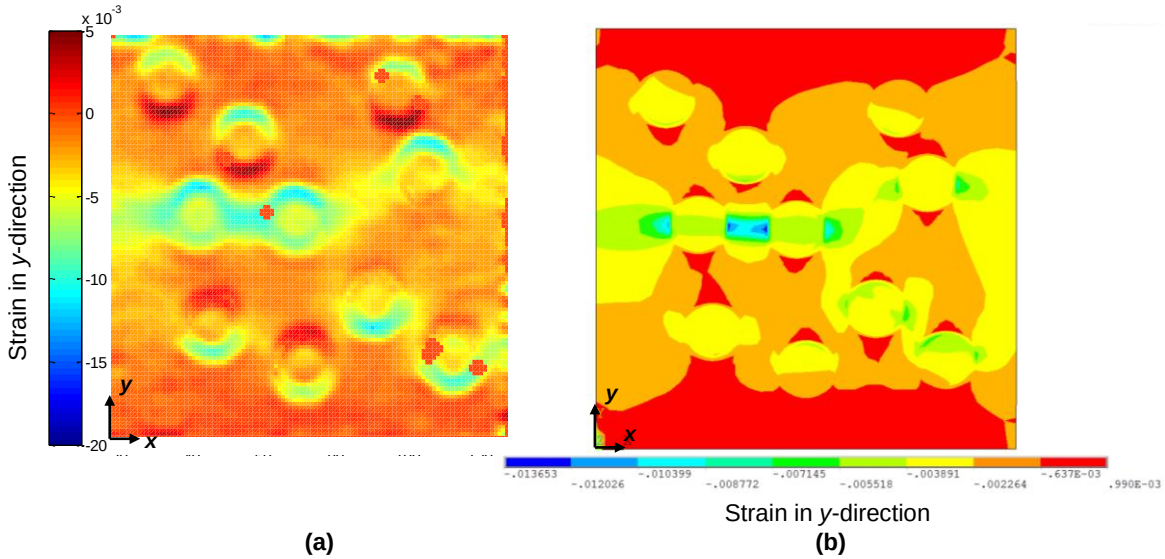

Figure 6.26. Front surface of strain in *y*-direction maps from (a) DIC and (b) FEA for specimen with random pitting at ultimate strength state.

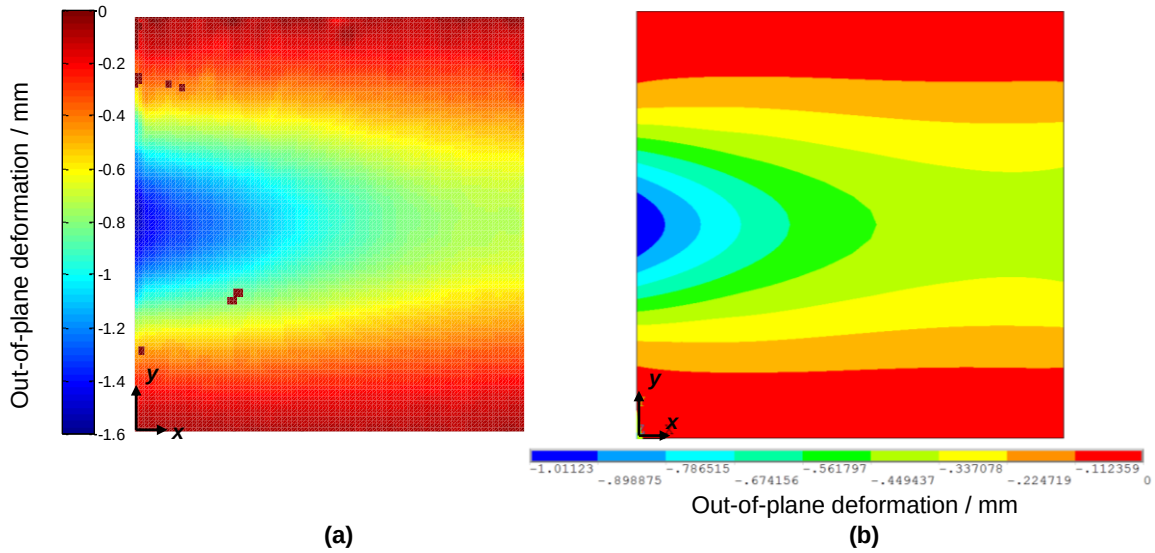

Figure 6.27. Front surface of out-of-plane deformation maps from (a) DIC and (b) FEA for specimen with corrosion on the unloaded edge at ultimate strength state.

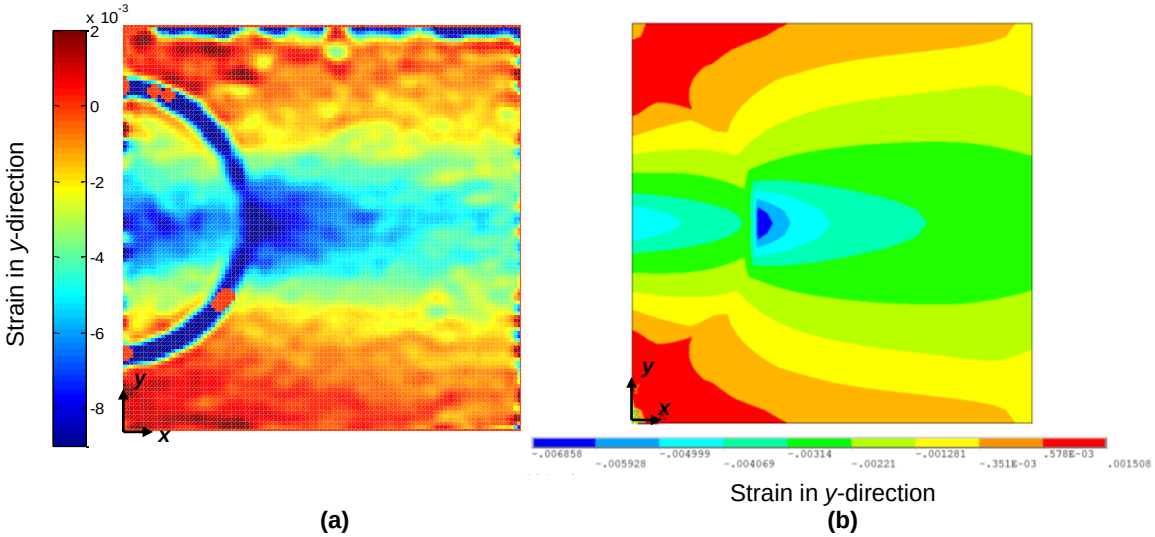

Figure 6.28. Front surface of strain in *y*-direction maps from (a) DIC and (b) FEA for specimen with corrosion on the unloaded edge at ultimate strength state.

Since the beauty of the DIC experiment is to be able to capture the full-field plastic behaviour of a specimen surface, a post-collapse point was also selected according to the load-strain curves to compare with the FEA results by keeping the compressive load the same, as shown in Figure 6.29 to Figure 6.36 for both out-of-plane deformations and strains in the *y*-direction.

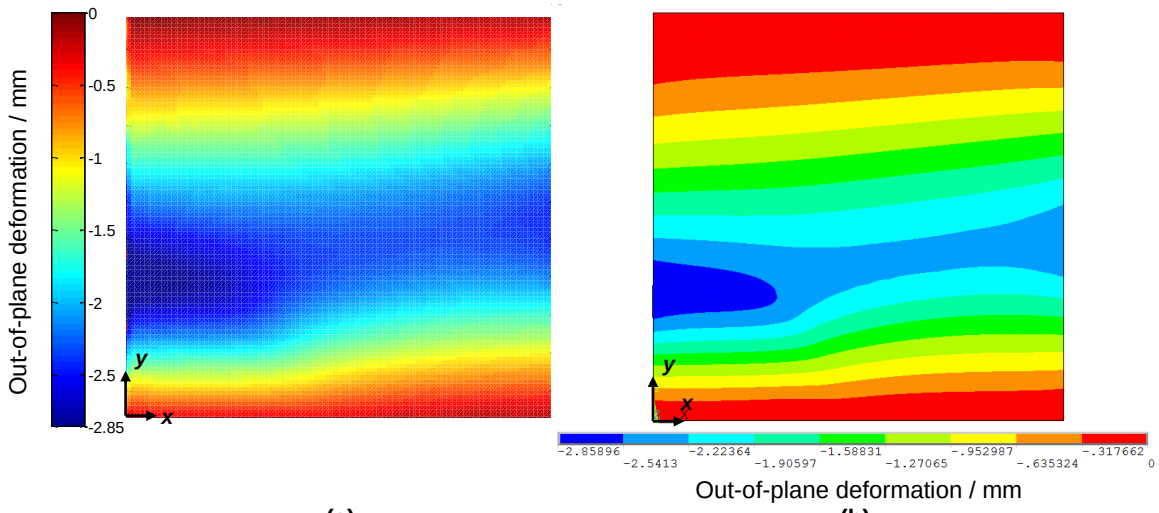

Figure 6.29. Front surface of out-of-plane deformation maps from (a) DIC and (b) FEA for specimen with corrosion at the corner when external load = 60 kN in the post-collapse region.

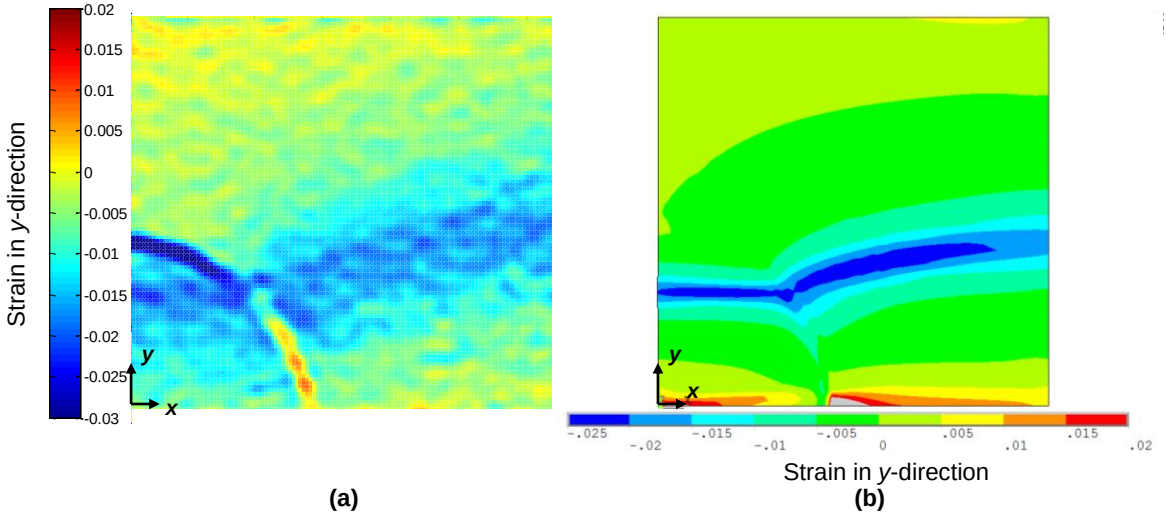

Figure 6.30. Front surface of strain in *y*-direction maps from (a) DIC and (b) FEA for specimen with corrosion at the corner when external load = 60 kN in the post-collapse region.

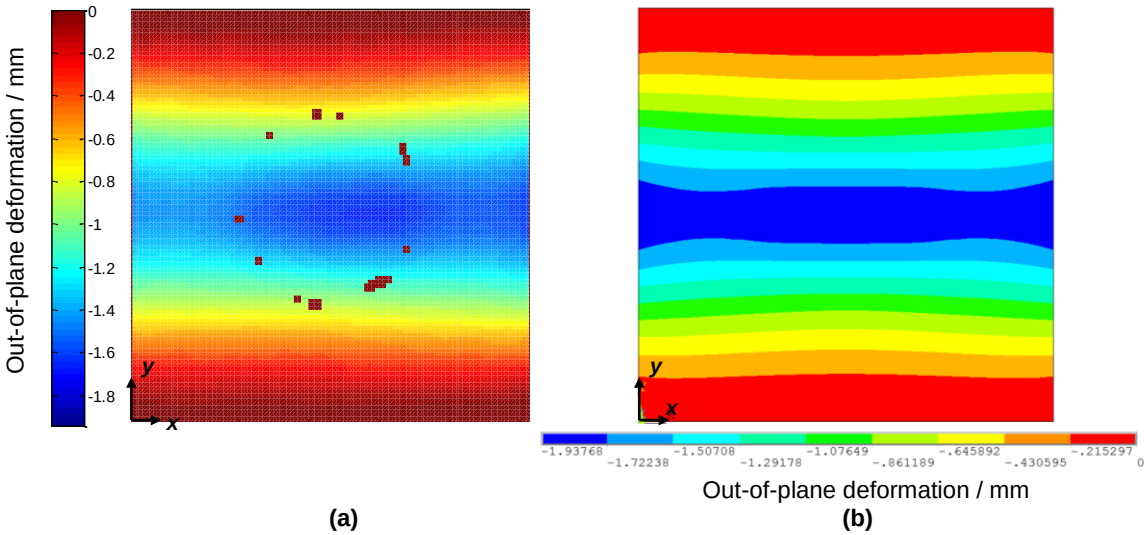

Figure 6.31. Front surface of out-of-plane deformation maps from (a) DIC and (b) FEA for specimen with corrosion in the middle when external load = 63 kN in the post-collapse region.

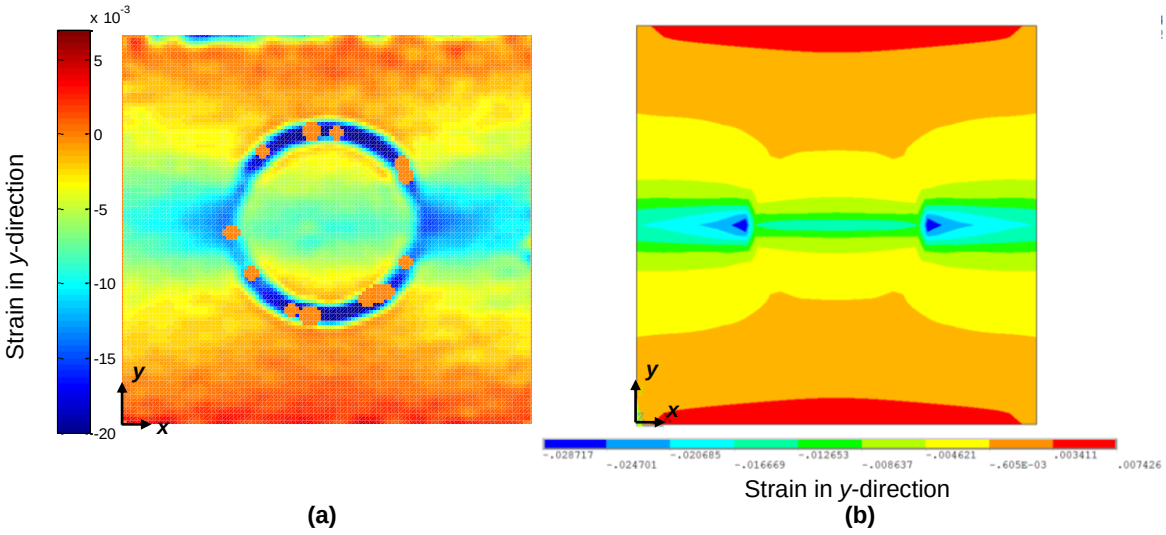

Figure 6.32. Front surface of strain in *y*-direction maps from (a) DIC and (b) FEA for specimen with corrosion in the middle when external load = 63 kN in the post-collapse region.

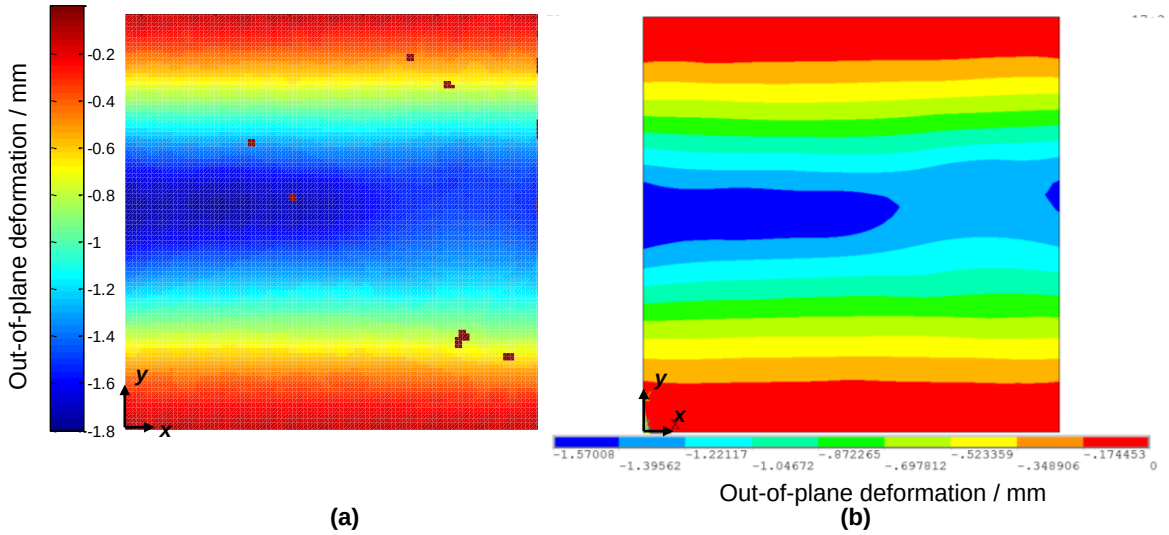

Figure 6.33. Front surface of out-of-plane deformation maps from (a) DIC and (b) FEA for specimen with random pitting when external load = 70 kN in the post-collapse region.

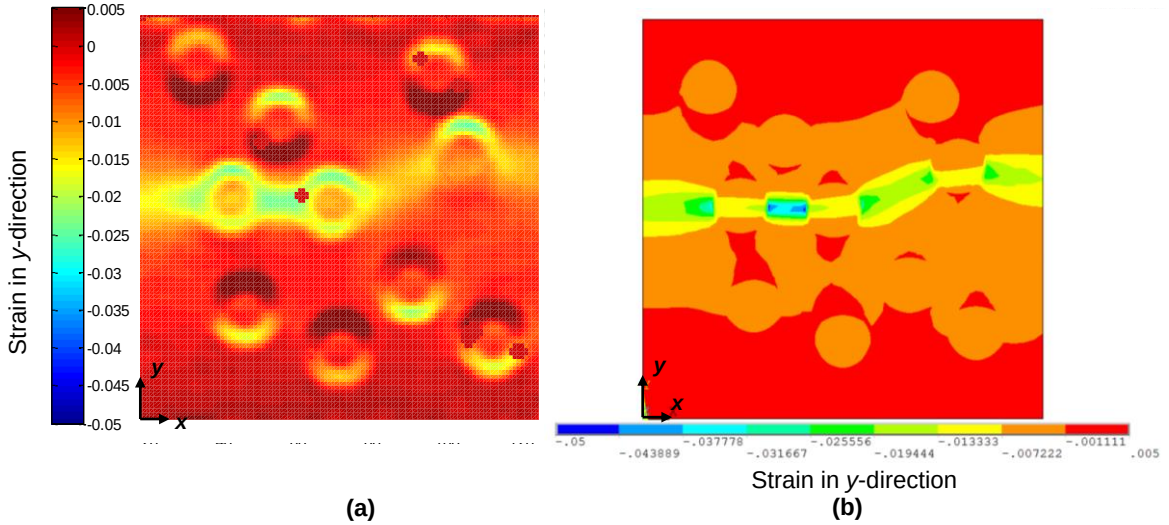

Figure 6.34. Front surface of strain in *y*-direction maps from (a) DIC and (b) FEA for specimen with random pitting when external load = 70 kN in the post-collapse region.

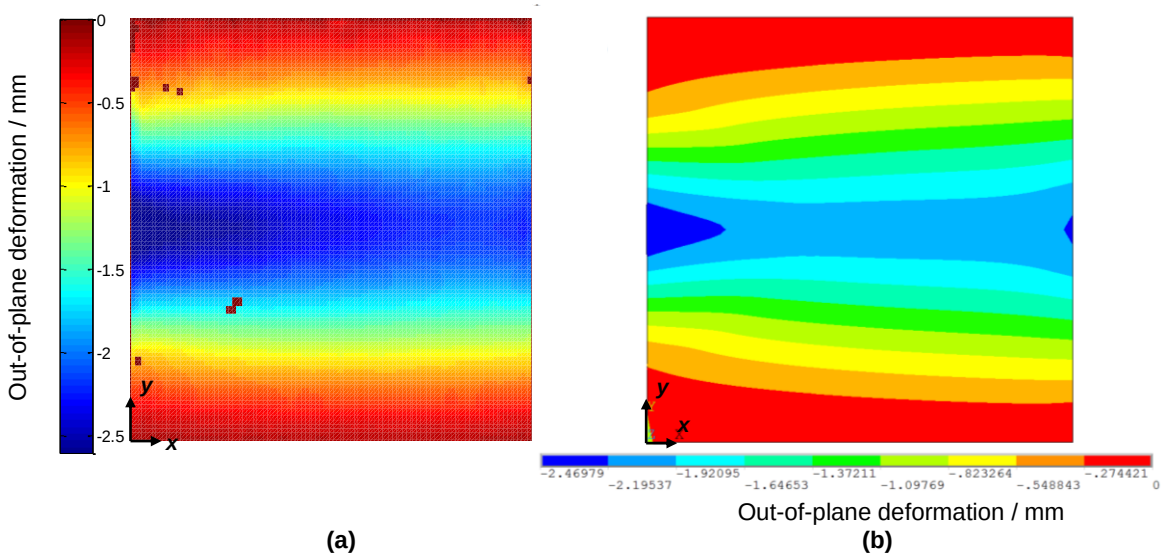

Figure 6.35. Front surface of out-of-plane deformation maps from (a) DIC and (b) FEA for specimen with corrosion on the unloaded edge when external load = 60 kN in the post-collapse region.

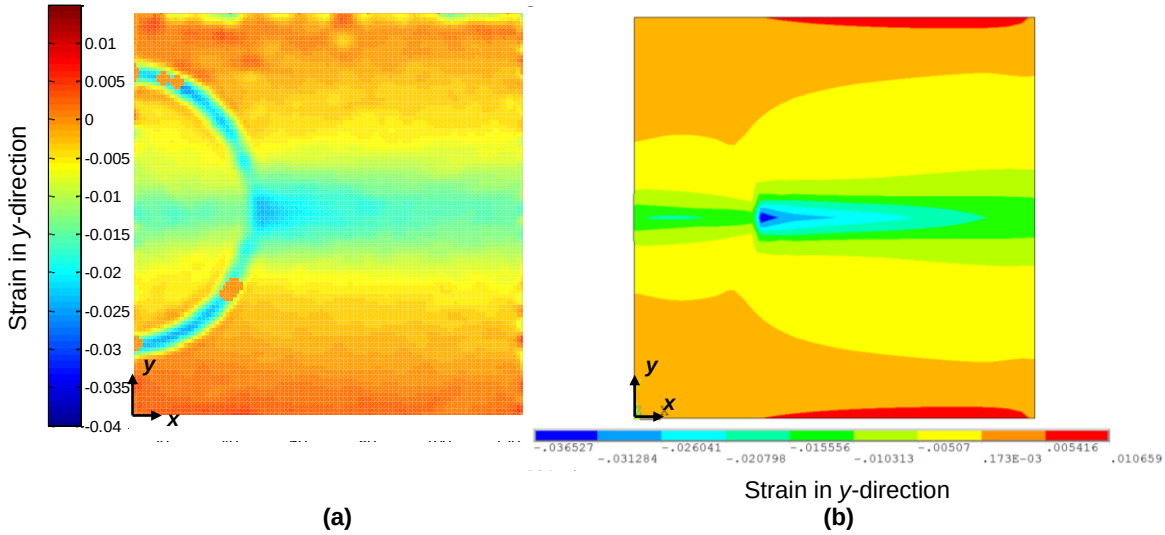

Figure 6.36. Front surface of strain in *y*-direction maps from (a) DIC and (b) FEA for specimen with corrosion on the unloaded edge when external load = 60 kN in the post-collapse region.

6.3 Discussion

TSA successfully detected the stress concentrations around the artificial pit defects and the interactions between them for all specimens. Due to the limitation of the TSA theory, which is only applicable in the elastic region of the material, the compressive load up to the collapse point used in the modelling condition cannot be achieved in these

experiments. However, it is considered that TSA is able to provide a full-field measurement of principal stresses over a corroded surface in the elastic regime as an indicator of the early stress concentration locations and indeed the stress concentration factor, which has mainly been investigated numerically [184-186]. Also, it has validated the mesh pattern for the studied corrosion models, which predominantly governs the accuracy of the FEA results. The line data comparisons (Figure 6.10 to Figure 6.16) show that the experimental and numerical stress change follow the same trend as the geometry changes and correlates well in most of the areas. However, the distance between two pixels in TSA is approximately 0.44 mm while the distance between two integration points in FEA models is 0.09 mm. This difference may be the main source of error at the corrosion defect edges (sharp corners). In addition, the non-adiabatic condition caused by the unevenness of the paint layer at areas with rapidly changing geometry could lead to a variation of the comparison results. Also, the material properties could be influenced by the machining of the pit surface and edges, which was not considered in the models. However, this influence is considered to be marginal.

In terms of the DIC experiments, the load-strain relationships (Figure 6.17 to Figure 6.20) for all specimens present a good correlation in general between DIC and FEA. The difference of the ultimate strength ranges from 3.9% (corrosion at the corner) to 11.8% (corrosion on the unloaded edge) with higher predictions from FEA. In the post-collapse region, FEA tends to underestimate the unloading path. The manufacture of the specimens is considered to be the main source of error. Firstly, initial deflections were introduced randomly during the machining and measured on a coarse grid on the specimens (9 × 9 data points) due to the limitation of the Faro Arm resolution. Although the polynomial functions show a good fitting ($R^2 > 0.95$), the variation around the defect (Figure A4.1 in Appendix 4) may not be included. Secondly, the higher ultimate strength and lower unloading path obtained from FEA could be induced by the pre-stress along the loaded edges. Both edges were straightened in the models. However, the clamped boundary condition was achieved on a 90 mm × 10 mm region using a steel strip and four M6 bolts on each side (Figure 6.37), which would introduce pre-stress to the specimen and lower the ultimate strength. Detailed consideration of the residual stress will be discussed in Chapter 7.

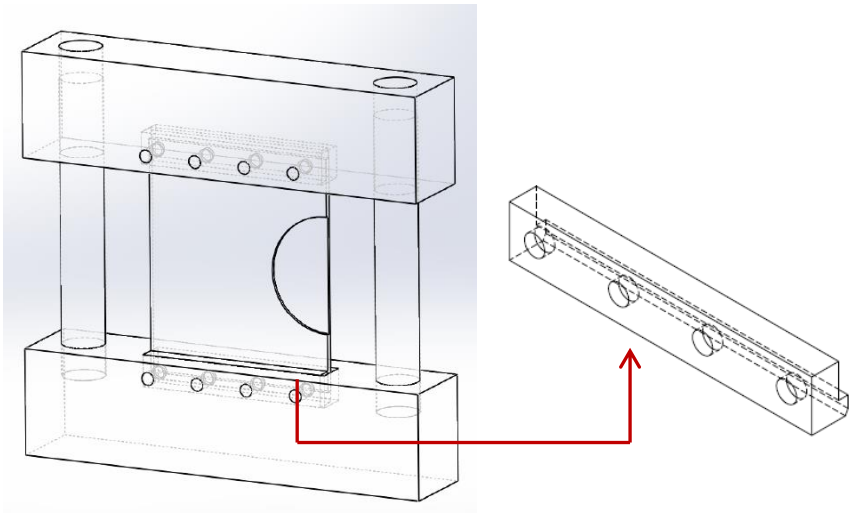

Figure 6.37. Schematic of a specimen and the rigs (dimension of the specimen: 110 mm × 90 mm × 3 mm).

When examining deformation/strain maps, it can be seen that FEA results show a good agreement with DIC in capturing various failure modes as well as the post-collapse deformations depending on the location of defects. When keeping the strength value the same in the post-collapse region, an improvement in the DIC and FEA comparisons can be observed. Although seeding points were carefully selected around the defect edges (thickness discontinuity), there are still some regions that the DIC failed to correlate, for example the red squares in Figure 6.23 (a). Smaller subset size (41 × 41 pixels) was hence tested with little improvement in the correlation area but in compensation of more noisy data. In terms of strain maps, DIC has presented a high strain resolution (in the order of 10^{-3}). However, more noise can be seen since strain values were calculated based on the displacement results for DIC (Section 3.3). Moreover, strains which are unrealistically high in magnitude were obtained around the defect. This is due to the discontinuous deformation inside and outside the defect. Figure 6.38 is an example of the deformation maps in *y*-direction for specimen with corrosion in the middle at the ultimate strength state. According to Equation 3.4, the deformation discontinuity around the defect edge will be averaged and hence an unrealistic region of strains. Overall, the nonlinear FEA has been successfully validated using the DIC experimental method. However, the buckling mode of the specimens is largely dependent on the initial state (geometric imperfection and initial stress) which may be difficult to simulate accurately.

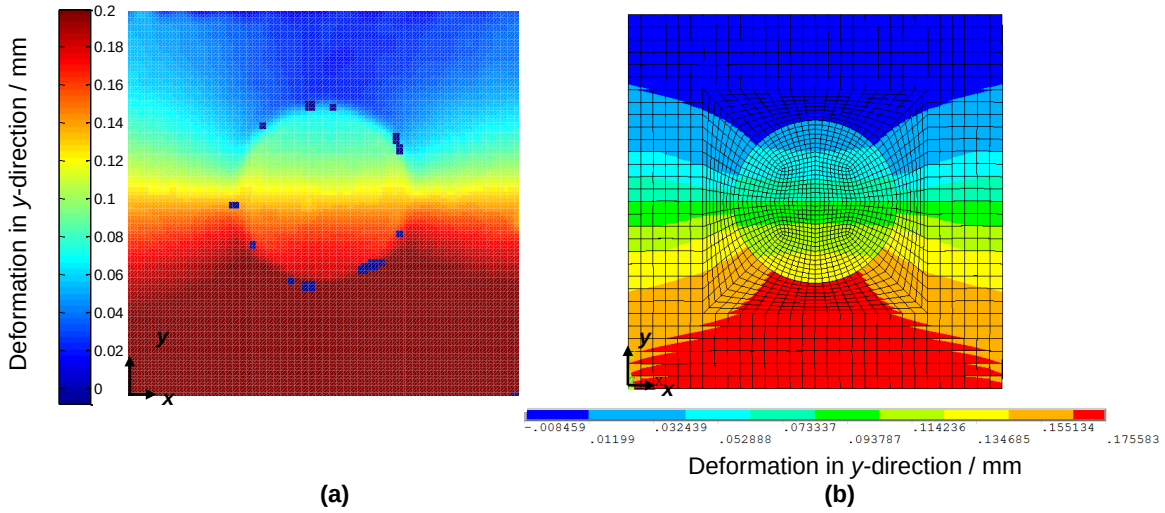

Figure 6.38. Front surface of deformation in *y*-direction maps from (a) DIC and (b) FEA for specimen with corrosion in the middle at ultimate strength state.

6.4 Conclusions

A full-field stress measurement using TSA technique demonstrates that it can be used to validate the mesh quality of FEA models. More importantly, it is able to physically reveal early stress concentration locations of corroded structural surfaces. For a steel plate with various defects representing corrosion damage, DIC experiments have been proven to be a valid novel experimental method to not only assess the buckling strength but also provide a full-field displacement/strain map on specimen surfaces, which can significantly improve the reliability of nonlinear FEA for specimens with non-uniform thickness. Also, strain concentrations can be physically detected around the defects. However, the calculation imbedded in DIC could lead to unrealistic strain values around sharp edges and needs to be treated with caution.

Chapter 7 Numerical investigation of stiffened plate models

In this chapter, a modified approach is proposed to simulate the behaviour of steel stiffened plates with fillet welds subject to weld-induced grooving corrosion using nonlinear FEA. The study considers various initial geometric imperfections, weld-induced residual stresses and the weld connection imperfection (root opening). The influence of such corrosion damage on the load shortening (stress-strain) curves, ultimate strength and the stress/strain distributions has been investigated.

7.1 Model construction

To focus on the corrosion feature, this study examined a simplified plate-stiffener combination (stiffened plate) model instead of a large stiffened panel. According to the benchmark study reported in Ref. [92], a stiffened plate model containing a stiffener and a half of the plating on both sides could provide good accuracy in both pre- and post-collapse phases in the case when the model is undergone a uniaxial compressive loading in the longitudinal direction. Therefore, such loading condition was applied to the models.

The stiffened plate model covers one stiffener and a half plating on both sides from a stiffened deck panel of a double hull tanker [122] shown in Figure 7.1 (a) and (b), with the model properties listed in Table 7.1. The widely used shell element SHELL181 was one option to construct the model assuming perfect connection between the stiffener and the plate by sharing nodes and DOFs without modelling the welds. However, it was realised that modelling of the welds and detailed through-thickness stress data are essential for a weld-induced corrosion analysis. Although shell elements are computationally economical, due to the 2D nature of representing the midplane of a cross-section, it was decided that a solid element SOLID185 was more appropriate for the weld connection simulation, corrosion features and the weld-induced residual stresses. To achieve a simply supported boundary condition, the cross-section of short edges where transverse girders lie was fully constrained in the *y*-direction. Symmetric boundaries along the edges in the longitudinal (*z*-) direction were achieved at the mid-thickness nodes. The compressive load was also applied at mid-thickness by controlling the displacement. The comparison between SHELL181 and SOLID185 is shown in Figure A5.1 in Appendix 5.

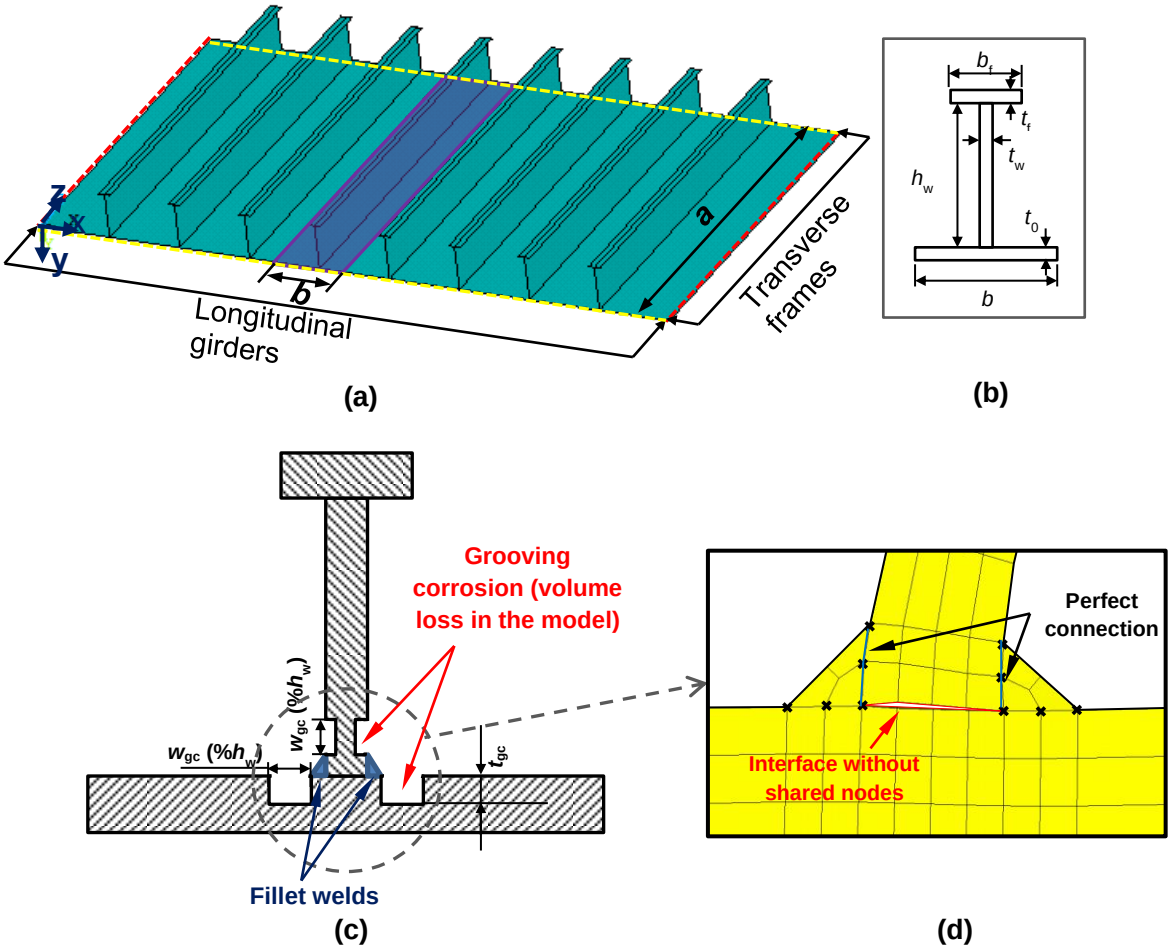

Figure 7.1. The stiffened plate model of interest and the cross-section of the stiffener with grooving corrosion features (dimensions refer to Table 7.1): (a) model location; (b) cross-section of the model; (c) cross-section of grooving corrosion and fillet weld connections; (d) modified weld connection (x: shared nodes).

Numerical studies of weld effects on stiffened plates have recently been carried out using solid elements [187-190], where the interface between the stiffener and the plate has always been modelled with shared nodes/elements. However, in reality this is not the actual condition for fillet welds since it is the weld metal which joins the stiffener and the plating together (Figure 7.1 (d)). Therefore, contact surfaces TARGE170 coupled with CONTA175 were adopted in the current investigation to represent the fillet weld connections, which have not been incorporated in previously reported model construction. CONTA175 associated with TARGE170 represent contact and sliding between two surfaces in 2D or 3D models [158]. The width of the fillet weld cross-section was 6 mm [189-192]. Figure 7.1 (c) shows the cross-section of the model and contact surface locations. For the interface between the stiffener and the plate, Coulomb's friction model was used with the static coefficient of friction of 0.78 and a dynamic value of 0.42 for a high-tensile steel contact [193].

Table 7.1. Model properties used for the stiffened plate model

Model Properties	Values
a / mm	4750
b / mm	950
t_0 / mm	15
$h_w \times t_w$ / mm	235 × 12
$b_f \times t_f$ / mm	90 × 17
E / GPa (both plate and stiffener)	205.8
σ_y / MPa (both plate and stiffener)	313.6
ν (both plate and stiffener)	0.3
E_t (both plate and stiffener)	0
$\beta = \frac{b}{t_0}\sqrt{\frac{\sigma_y}{E}}$ (plate slenderness ratio)	2.472
Plate initial deflection / mm	$w_{pl} = 0.1\beta^2 t_0 \sin\frac{5\pi x}{a}\sin\frac{\pi y}{b}$
Column-type initial deflection / mm (B / mm: width between two longitudinal girders)	$w_c = 0.0015a \sin\frac{\pi x}{a}\sin\frac{\pi y}{B}$
Sideways initial deflection / mm	$w_s = 0.0015a \frac{z}{h_w}\sin\frac{\pi x}{a}$

Initial geometric imperfections were applied based on the frequently used deflection shapes for all models as well as to initiate the buckling phenomenon (Equations 2.12 to 2.14). For the application of weld-induced residual stresses, the representative residual stress distribution suggested in Ref. [122] (Equations 2.15 and 2.16) was applied explicitly in the longitudinal direction with tensile zone reaching the yield stress of the material and an average level of compressive stress ($-0.15\sigma_y$) assigned for the plate and the stiffener, respectively. The transverse residual stresses were not included due to the consideration of the external loading being predominantly longitudinal.

The grooving corrosion was located in the vicinity of the welds on both plating and the web plate, as shown in Figure 7.1 (c) based on the observed corrosion features [11]. In addition to the modelling validation (Chapter 4), a convergence study showed that the difference between results using shell and solid elements was less than 5% (Figure A5.1 in Appendix 5), and did not vary significantly from two elements to four elements through the plate thickness. Thus, two elements through-thickness were used for a lower computational cost. The maximum element length (in *z*-direction) used on the plate was 47.5 mm with six elements along the web height and refinement at the welds. A refined mesh was used in the HAZ to guarantee the equilibrium of the internal stress on the cross-section. The typical element size ranges from 3 mm to 47.5 mm.

7.2 Test matrix information

Based on the inspection and repair criterion outlined in Section 2.4.2, the grooving corrosion width w_{gc} varying from 5% to 50% h_{w} and the remaining thickness t_{gc} of 0.75, 0.5 and 0.25t_0 or t_{w} depending on the corrosion location were examined. In addition to the corrosion features and locations, two failure modes PIF and SIF of the interframe flexural buckling of a stiffened plate were also considered due to the uncertainty of the initial deflection. Depending on the direction of the column-type initial deflection, PIF is likely to occur when the plating is under compression initially, while the stiffener in compression initially will result in SIF. In addition to the commonly used Fourier function in Table 7.1 (the so-called buckling-mode initial deflection defined in Ref. [92]), imperfections with a shape more similar to weld-induced deformations (Equations 2.12) have also been investigated with M = 11 and $A_{0\mathrm{m}}$ listed in Table 7.2 [86].

Table 7.2. Initial deflection amplitudes for welding type initial deflection [86]

A_{01}	A_{02}	A_{03}	A_{04}	A_{05}	A_{06}	A_{07}	A_{08}	A_{09}	A_{010}	A_{011}
1.0	-0.00235	0.3837	-0.00259	0.2127	-0.0371	0.0478	-0.00201	0.001	0.009	0.0005

Also, two weld methods, continuous and intermittent, have been studied (Figure 7.2). Based on the welding regulations provided in Refs. [187,188], the width of the welds w = 75 mm and p = 187 mm for intermittent scenario, leading to 26 welds distributed on each side of the stiffener. The influence of residual stresses was investigated on continuously welded stiffened plates. So far, the abovementioned test conditions are all assuming ideal weld connections, i.e., perfect contact between the stiffener and the plate. However, perfect connection is rarely possible in reality and small gaps exist, which are often called the root opening [194], as illustrated in Figure 7.3. The opening may be of the same size of the fillet weld in extreme conditions and can hardly be observed externally. Throughout the literature there is yet to be an analysis assessing the influence of such weld imperfection. Therefore, in addition to the grooving corrosion features, the root opening was also considered to explore the stress level change both globally and locally compared to perfect weld connection. According to the AWS D1.1-98 Structural Welding Code [194], the size of a fillet weld needs to be increased when the root opening is greater than 1.6 mm. To assess an extreme condition, a 2 mm gap between the stiffener and the plate was introduced to the continuously welded models in this study without residual stresses. In terms of corrosion features, two corrosion locations (on the stiffener or on the plate), two failure modes (PIF and SIF), two types of initial deflection (buckling-mode and weld-

induced), five w_{gc} values (5%h_w, 10%h_w, 15%h_w, 20%h_w and 25%h_w) and one t_{gc} (0.25t_0 or 0.25t_w) were considered. Overall, 212 cases have been analysed.

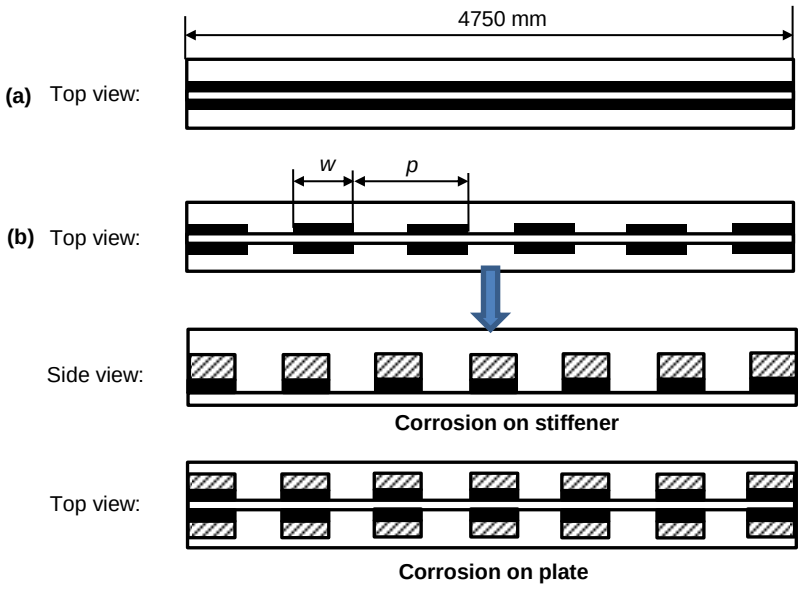

Figure 7.2. Weld methods in the test matrix (black area: weld; shaded area: corrosion): (a) continuous weld; (b) intermittent weld with indication of corrosion locations.

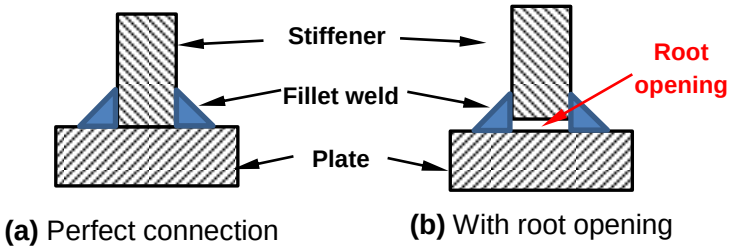

Figure 7.3. Illustration of root opening for a T-joint with fillet welds.

7.3 Results

An external compressive load was applied at numerous substeps. The load shortening curves were derived by recording the reaction force F and the longitudinal displacement UZ at every substep. The nominalised values were calculated based on the following equations:

$$F/F_y = F/(\sigma_y A_0) \quad (7.1)$$

$$UZ/UZ_y = UZ/[a(\sigma_y/E)] \quad (7.2)$$

where A_0 is the original cross-sectional area of the intact model and the other parameters are defined in Table 7.1.

7.3.1 Influence of corrosion location and initial column type deflection (PIF/SIF)

The influence of the corrosion location has been examined on stiffened plates with continuous welds, applying a buckling-mode initial plate deflection and two directions of initial column type deflection (PIF and SIF). Figure 7.4 shows the nominal load-shortening curves for corrosion on the plate (t_{gc} = 0.25t_0) and on the stiffener (t_{gc} = 0.25t_w), respectively. It can be seen that the transition from elastic to plastic region is steady without sudden buckling phenomenon. The deformation starts at the onset of the load due to the coincidence of the Fourier component of the initial deflection and the final collapse mode. Stiffened plates with corrosion at both locations (on both sides of the plate and the stiffener adjacent to the welds in Figure 7.1 (c) follow similar loading and unloading paths as the intact ones. Also, the initial column type deflection does not affect pre-collapse and collapse strength. Regarding the post-collapse region, a stable unloading process can be found for both corrosion locations and two failure modes, as indicated in Figure 7.4.

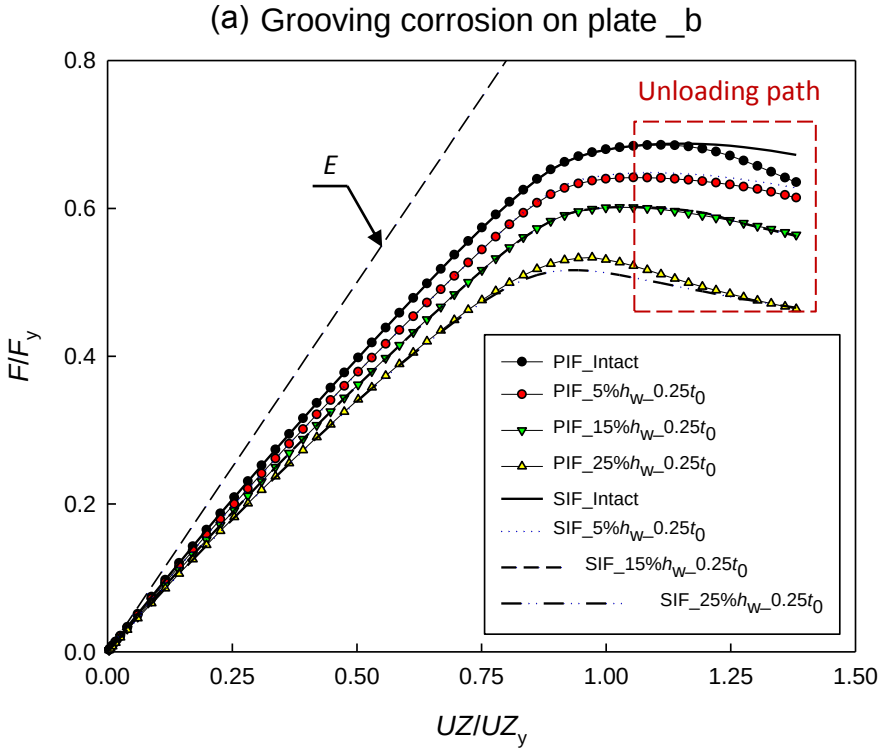

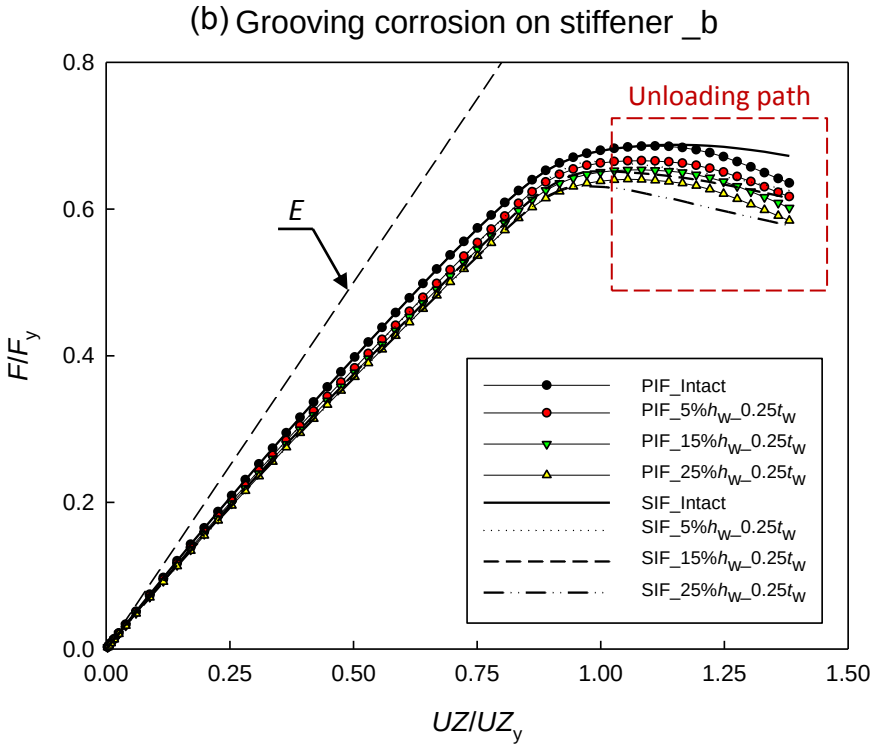

Figure 7.4. Nominal load shortening curves for corrosion on the (a) plate and (b) stiffener (b: buckling-mode initial deflection; *E*: Young's modulus of the material).

The ultimate strength reductions, which were calculated based on the intact value, are also plotted versus percentage volume loss for different groove widths and locations (Figure 7.5). It can be seen that compared to the condition where the corrosion depth is less than half of the original plate thickness (e.g., the first two data points for each corrosion width), when the remaining thickness is reduced to $0.25t_0$ or $0.25t_w$, a greater increase in the strength reduction occurs for all conditions with the exception of the stiffener corrosion (PIF). The much lower ultimate strength for grooving corrosion on the plating is independent of the failure mode.

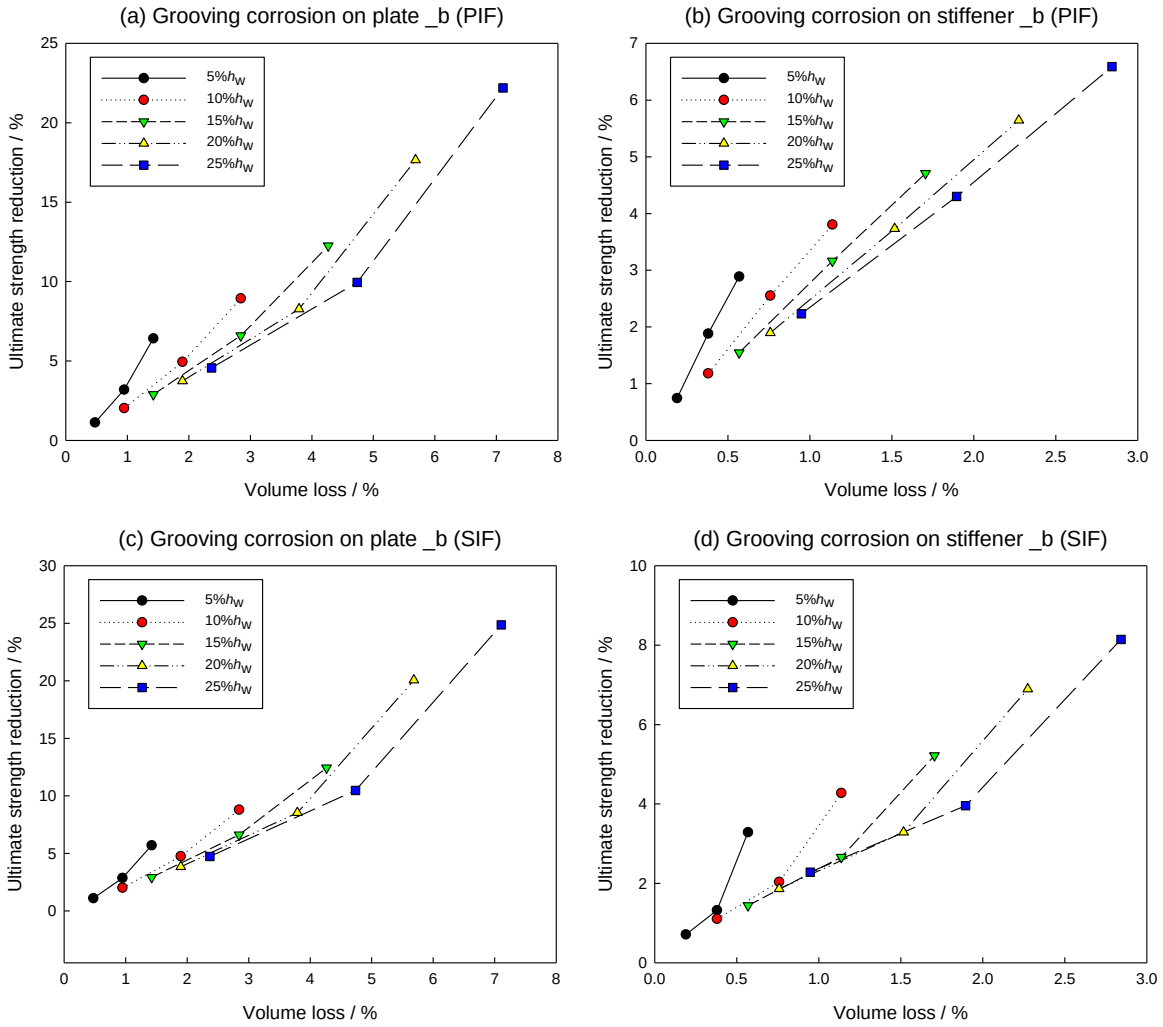

Figure 7.5. Ultimate strength reduction versus volume loss for models without residual stresses for buckling-mode initial deflection and continuous weld (b: buckling-mode initial deflection).

7.3.2 Influence of initial plate deflection and initial column type deflection (PIF/SIF)

The influence of the initial deflection type was also examined on stiffened plates with continuous welds, considering PIF and SIF, five groove widths and four groove depths. In addition to applying an energy dissipation ratio as introduced in Section 3.1, the grooving corrosion was primarily located on the stiffeners since the results could be highly unstable for corrosion on the plate with a welding type initial deflection.

Comparisons of the load-shortening curves between the two initial deformation conditions are presented in Figure 7.6. It is clear that a model with weld-induced deflection behaves more like a perfect thin plate compared to that with a buckling-mode deflection (Figure 2.11). With weld-induced initial deflection, the stress progresses linearly with the slope

close to the Young's modulus of the material up to Point 1, which is the onset of a significant out-of-plane deformation of the plate on one side of the stiffener. As the load increases, instability occurs at Point 2 where the middle area of the plate on the other side of the plating starts to buckle with yielding developed in the compressed regions. From Point 2 the model keeps deforming in the same manner with extensive yielding appearing on the plating and the stiffener until collapse at Point 3.

Further comparisons were achieved against the volume loss (for example Figure 7.7 for corrosion on stiffener). The weld-induced initial deflection results in a greater ultimate strength reduction (up to 26% for corrosion on the plate). However, it follows a similar trend for PIF, whereas for SIF there appears to be a marked increase in the strength reduction from $0.75t_w$ to $0.5t_w$ (first two points for every corrosion width) and then follows the same slope as the buckling type condition with a low corrosion depth.

(a) Grooving corrosion on stiffener (PIF)

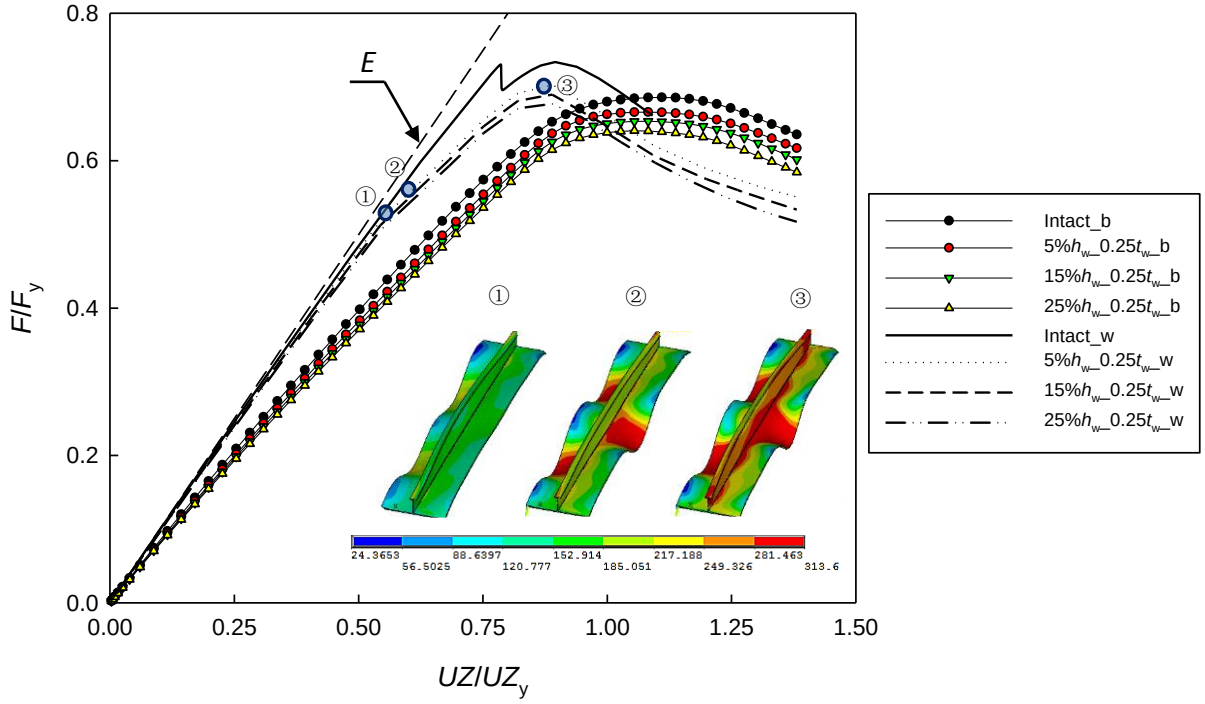

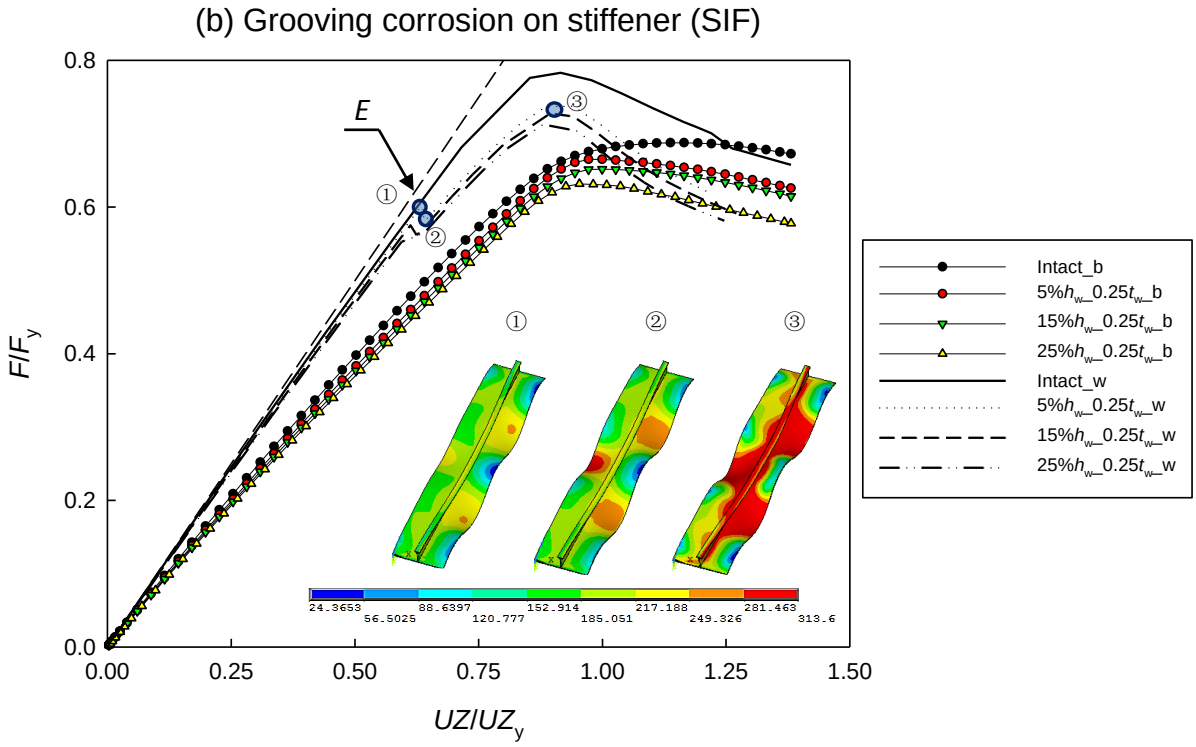

Figure 7.6. Nominal load shortening curves with von Mises stress distributions for (a) PIF and (b) SIF (scaling factor = 10; b: buckling-mode initial deflection; w: weld-induced initial deflection).

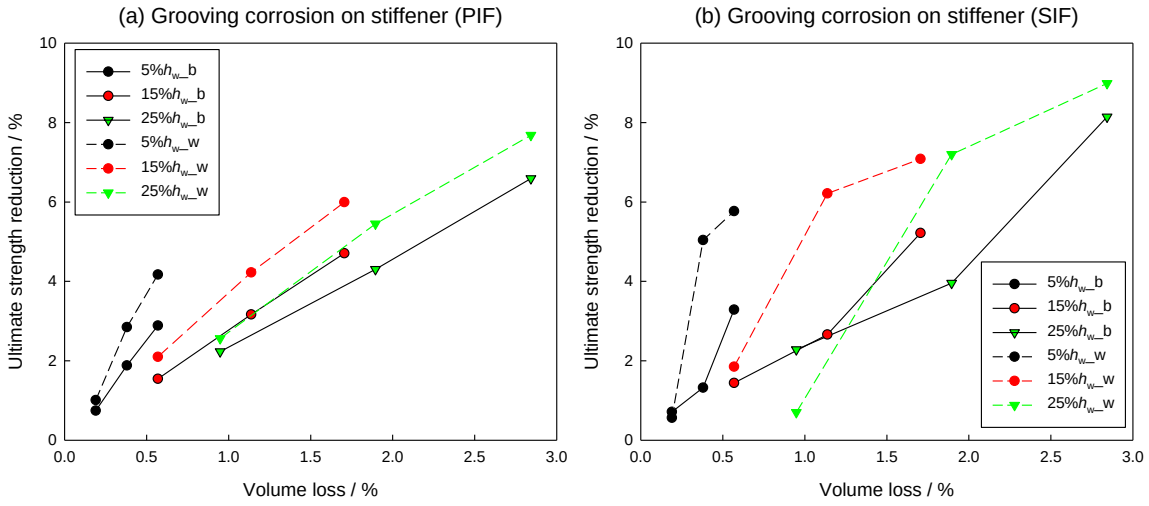

Figure 7.7. Ultimate strength reduction versus volume loss for models without residual stresses for two types of initial deflection and continuous weld (b: buckling-mode initial deflection; w: weld-induced initial deflection).

7.3.3 Influence of weld method and initial column type deflection (PIF/SIF)

The investigation of the weld method effects was carried out considering both initial deflection types and two corrosion locations. However, it was found that the panel with

intermittent welds became highly unstable for the SIF condition even using a high energy dissipation ratio. The accuracy of the numerical results was deemed to be questionable and therefore only the PIF results are presented. Interestingly, when plotting the ultimate strength reduction values versus the volume loss, as shown in Figure 7.8, it is found that the value for intermittent weld increases with increasing volume loss regardless of the corrosion width and depth. Moreover, the slope is higher for welding type deflection compared to the buckling type.

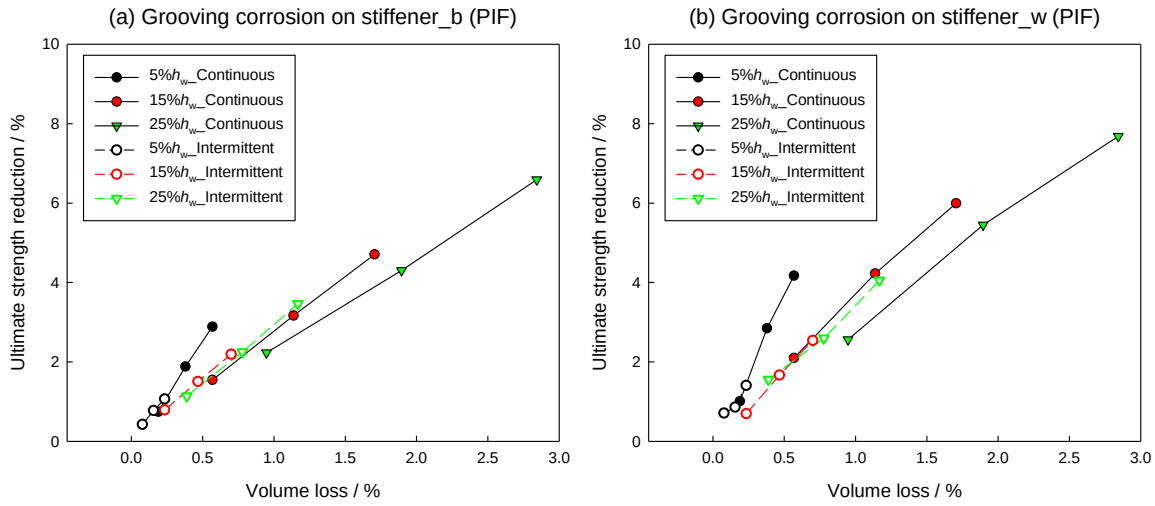

Figure 7.8. Ultimate strength reduction versus volume loss for models without residual stresses for two types of initial deflection and two types of weld (b: buckling-mode initial deflection; w: weld-induced initial deflection).

7.3.4 Influence of weld-induced residual stresses

The influence of weld-induced residual stresses was examined on continuously welded stiffened plate. The application of the residual stresses generally lowers the ultimate strength but tends to stabilise the structure in the post-collapse regions. Compared to the no residual stress condition, similar influences of corrosion location and initial deflection type on the load shortening curves have been observed for models with residual stresses. Figure 7.9 shows the ultimate strength reduction versus volume loss compared to no residual stress condition. It can be seen that the residual stress generally results in a greater strength reduction, with the exception of conditions shown in Figure 7.9 (b) and Figure 7.9 (f). In general, the influence of the residual stresses is enhanced as the volume loss increases. However, the reduction change follows similar trend as the models without residual stresses.

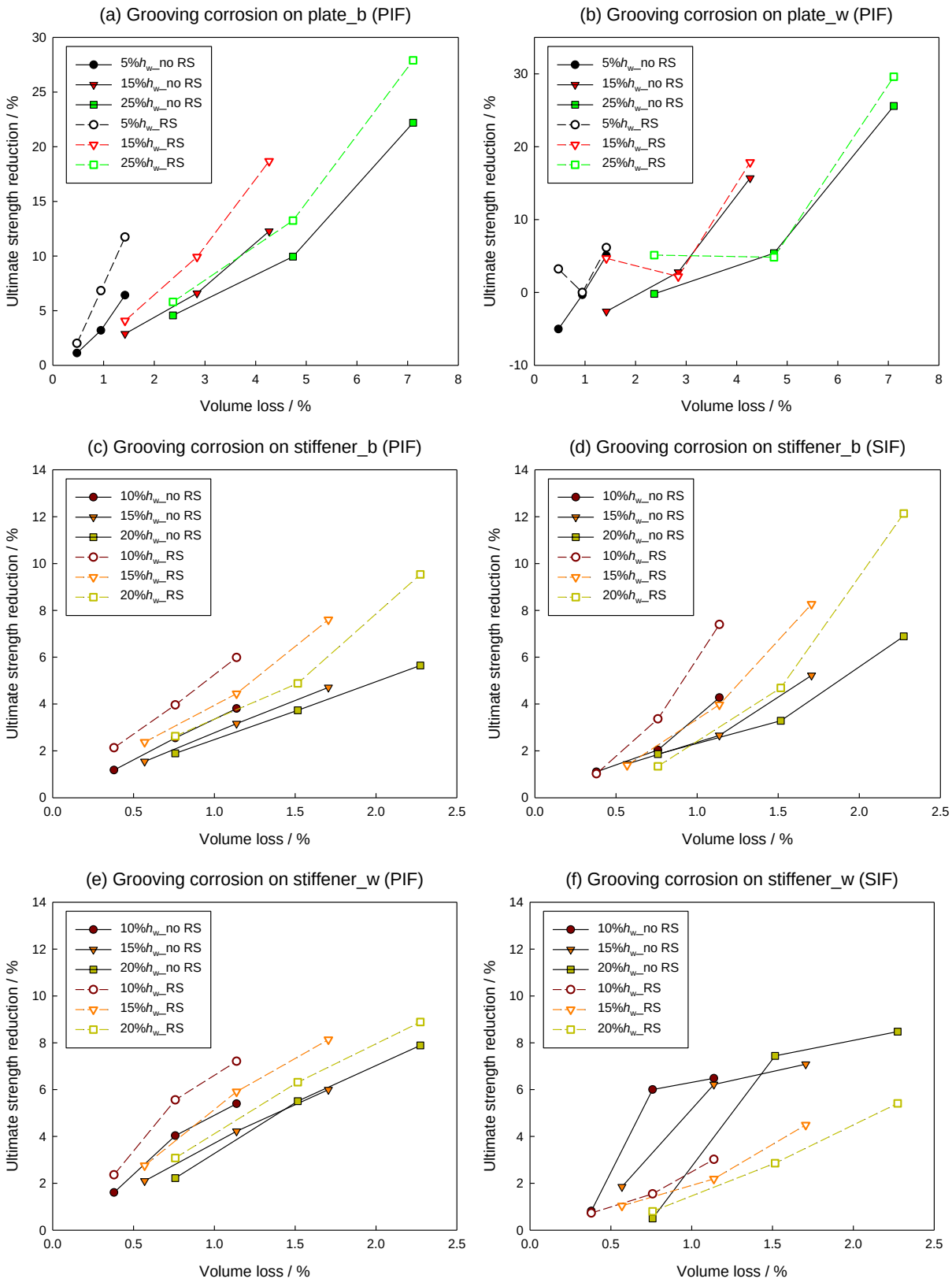

Figure 7.9. Comparison in ultimate strength reduction versus volume loss for models with and without residual stresses (b: buckling-mode initial deflection; w: weld-induced initial deflection; RS: residual stresses).

7.3.5 Influence of weld connection imperfection (root opening)

When considering the weld connection imperfection (root opening), Figure 7.10 shows two examples of the load shortening curves for models with and without the root opening. It has been found that the presence of such imperfection (2 mm gap) induced only a minor variance compared to the perfect weld condition in both elastic and plastic regions, regardless of the corrosion location, corrosion width and initial deflections.

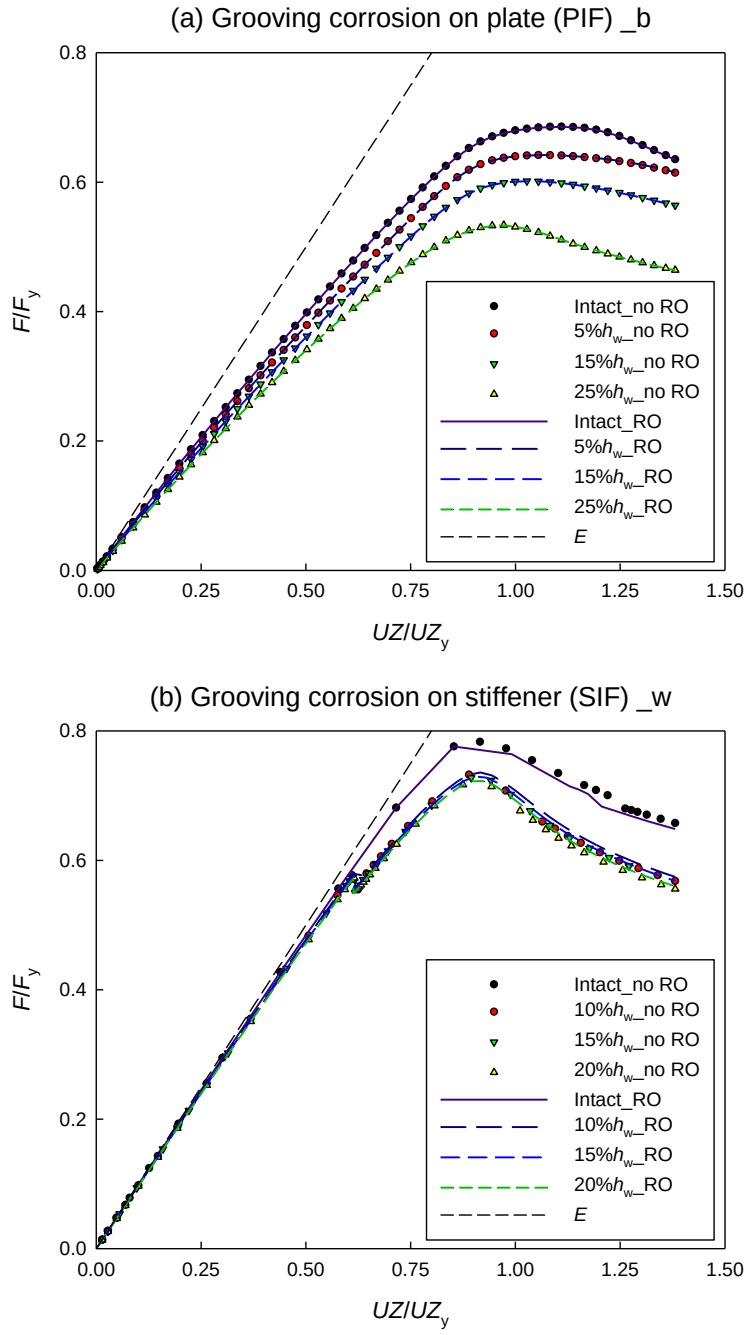

Figure 7.10. Comparison of nominal load shortening curves when corrosion on the plate and stiffener (b: buckling-mode initial deflection; w: weld-induced initial deflection; RO: root opening; *E*: Young's modulus of the material).

The root opening effects on local region of the model were examined on a cross-sectional area located at 1/3 of the plate length. When the structure is in its fully elastic state, for example when the external load = 1.92%σ_y, it can be seen from Figure 7.11 that the overall stress levels are comparable between the model with and without the root opening defect. However, in addition to the stress concentration occurring at the corroded area on the plate (both side of the stiffener) on both models, significantly high stress appears around the root opening.

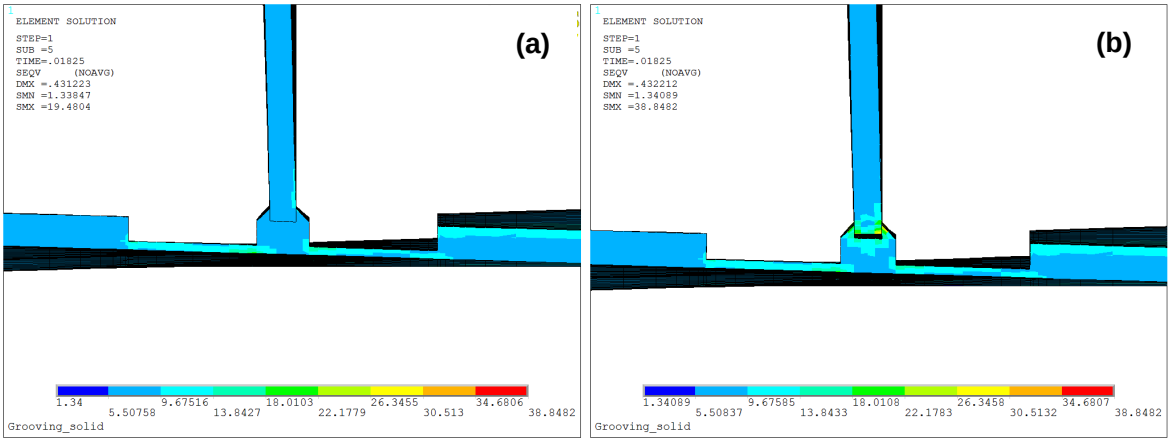

Figure 7.11. Von Mises stress distributions on a cross-section (at 1/3 length) of the stiffened plate model when external load = 1.92%σ_y (corrosion on plate 25%h_w, 0.25t_0; PIF; buckling-mode initial deflection): (a) perfect weld connection; (b) welds with root opening.

When further increasing the external load with development of local plasticity (external load = 6.57%σ_y), greater stress concentration remains around the corrosion feature (Figure 7.12). It is interesting to note that the stress state at the weld connection shows less difference between the two models. This can be confirmed by examining the first principal plastic strain map (Figure 7.13), where the plastic strain starts to emerge around the bottom of the corrosion feature for both conditions. When the models are loaded up to their ultimate strength state, in this case yielding spreads entirely on both the welding interface, independent on the presence of the root opening.

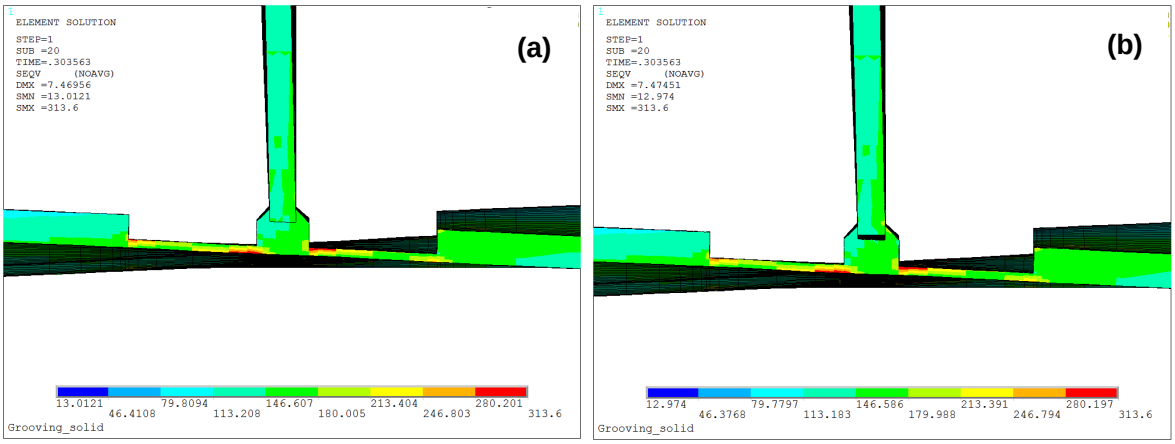

Figure 7.12. Von Mises stress distributions on a cross-section (at 1/3 length) of the stiffened plate model when external load = 6.57%σ_y (corrosion on plate 25%h_w, 0.25t_0; PIF; buckling-mode initial deflection): (a) perfect weld connection; (b) welds with root opening.

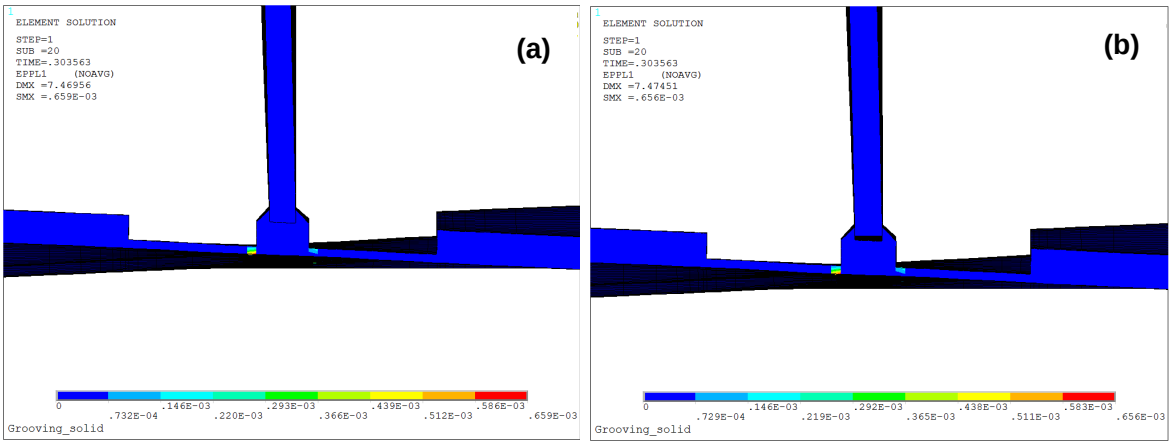

Figure 7.13. First principal plastic strain distributions on a cross-section (at 1/3 length) of the stiffened plate model when external load = 6.57%σ_y (corrosion on plate 25%h_w, 0.25t_0; PIF; buckling-mode initial deflection): (a) perfect weld connection; (b) welds with root opening.

7.4 Discussion

7.4.1 Structural response during the loading procedure

Modelling with the buckling-mode initial deflection indicates that the stiffened plate reaches its ultimate strength when yielding spreads to the stiffener and accelerated by a loss of stiffness due to yielding of the plate. Figure 7.14 shows the yielding on the 1/3-length cross-section with corrosion on the plate and initial deflection towards the stiffener (PIF). Depending on the initial deflection shape, yielding initiates from the bottom of the right groove where the plate is under compression and gradually propagates towards the

weld joints. Similarly, for corrosion on the stiffener under compression (SIF), yielding starts at the bottom of the left groove and spreads towards the stiffener flange. Compared to the intact plate, where the yielding always initiates at the weld joints, the presence of the grooving corrosion determines the early stress concentrations and ultimately the difference in the collapse strength and post-collapse behaviour. Similar phenomena are also discussed in Ref. [100].

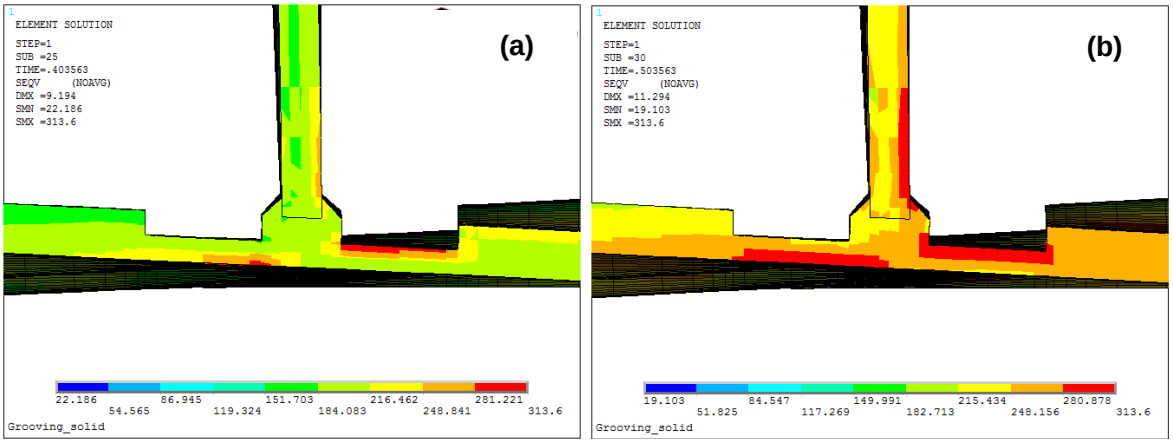

Figure 7.14. Von Mises stress distributions on a cross-section (at 1/3 length) of the stiffened plate model (corrosion on plate 15%h_w, 0.5t_0; PIF; buckling-mode initial deflection): (a) external load = 11.43%σ_y; (b) external load = 41.47%σ_y.

At the ultimate strength state, a stiffening effect can be seen for the weld-induced initial deflection shape in Figure 7.6, which is due to the greater rotation and deflection around the edges and hence larger membrane stresses during the deflection pattern transition [86]. Although the weld-induced deflection results in higher strength, it is followed by a more rigorous unloading, implying a highly unstable post-collapse behaviour. Moreover, the location of the initial buckling deformation is associated with the direction of the initial sideway deformation of the stiffener, which is opposite to the location of the sudden change in the plating deformation. For models considering the weld-induced residual stresses, a much smoother transition from pre- to post-collapse regions has been observed compared to the no residual stress condition, regardless of the corrosion features, primarily due to the stress redistribution during the loading process. The study of the weld connection imperfection indicates that the introduced root opening has little effect on the load shortening curves in both elastic and plastic regimes (Figure 7.10). This behaviour does not vary with different corrosion features and initial deflections. Compared to its minor influence globally, the root opening was found to cause significant stress concentration at the welding area when the model is fully elastically loaded (Figure 7.11). However, the difference in stress/strain distribution diminishes when local plasticity starts

to occur (Figure 7.12). Moreover, by comparing Figure 7.13 and Figure 7.14, it can be seen that the onset of yielding is independent of the existence of a root opening, which may explain the negligible influence on the ultimate strength of the structure. But the early stress concentration at the welds cannot be overlooked, not only for being a potential initiation of cracks but also changing the electrochemical properties of the welds and the base metal. This change may induce corrosion acceleration, which will be discussed in detail in Chapter 8.

7.4.2 Ultimate strength reduction

When examining the ultimate strength reduction versus volume loss for continuous welds, it was evident that for the same volume loss a higher corrosion depth and smaller corrosion width will result in a higher strength reduction (Figure 7.5, Figure 7.7 to Figure 7.9). A similar performance has also been observed in Chapter 5. The difference between different conditions is generally associated with the failure mode change. Table 7.3 and Table 7.4 summarise the out-of-plane deformation plot for all test conditions. For grooving corrosion on the plate with a buckling type initial deflection (Figure 7.5 (a) and (c)), a much greater strength reduction at a large corrosion depth may be explained as the failure mode change, especially the sideway deformation of the stiffener, as indicated in Table 7.3. For both PIF and SIF, a low strength reduction is associated with locally deformed stiffener (No. 1 and 3 in Table 7.3) while a high corrosion depth will lead to an increased deformation (No. 2 and 4 in Table 7.3), and hence a much greater strength reduction. In terms of corrosion on the stiffener, no sudden change can be found in the strength value for PIF, while an increased strength reduction takes place when corrosion depth is $0.25t_{\mathrm{w}}$ for the SIF. For the PIF condition, yielding starts at the corroded area on the stiffener web, followed by a large yielding area on the plate at the ultimate state. As for SIF, the initial yielding also appears on the stiffener web with similar extent/location of the yielded and nearly yielded plate as for PIF when the corrosion depth is low. However, as the remaining thickness is decreased to $0.25t_{\mathrm{w}}$, this area on the plate is narrowed and localised along the joint, implying that a reduced stress redistribution due to the weakened stiffener, and hence a much lower ultimate strength.

When comparing the two initial deflection types for corrosion on the stiffener (Figure 7.7), a similar strength reduction change as the buckling-mode condition for PIF can be seen mainly due to the similar deformation change of the stiffener (No.1 and 2 in Table 7.4). Nevertheless, a marked difference is apparent for SIF when the remaining thickness is

decreased from $0.75t_w$ to $0.5t_w$, due to the significant change of the failure mode (No.6 and 7 in Table 7.4).

Table 7.3. Summary of the failure mode (buckling-mode initial deflection; scale factor = 10; RS: residual stresses)

No	Failure mode	Initial column type deflection	Corrosion condition
1	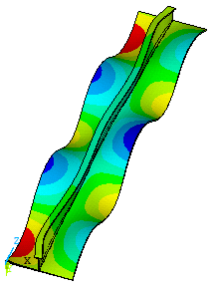	PIF	Intact Plate: 5%-25%h_w, $0.75t_0$ 5%-25%h_w, $0.5t_0$ Stiffener: 5%-50%h_w, $0.75t_w$ 5%-50%h_w, $0.5t_w$ Intact (RS) Plate (RS): 5%-25%h_w, $0.75t_0$ 5%-25%h_w, $0.5t_0$ Stiffener (RS): 10%-20%h_w, $0.75t_w$ 10%-20%h_w, $0.5t_w$
2	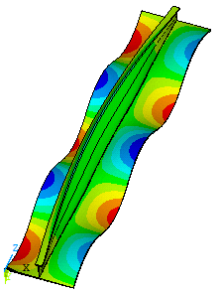	PIF	Plate: 5%-25%h_w, $0.25t_0$ Stiffener: 5%-50%h_w, $0.25t_w$ Plate (RS): 5%-25%h_w, $0.25t_0$ Stiffener (RS): 10%-20%h_w, $0.25t_w$
3	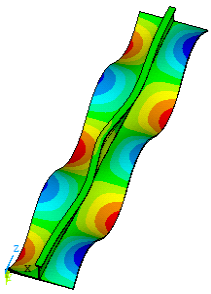	SIF	Intact Plate: 5%-25%h_w, $0.75t_0$ 5%-25%h_w, $0.5t_0$ Stiffener: 5%-50%h_w, $0.75t_w$ 5%-50%h_w, $0.5t_w$ Intact (RS) Stiffener (RS): 10%-20%h_w, $0.75t_w$ 10%-20%h_w, $0.5t_w$
4	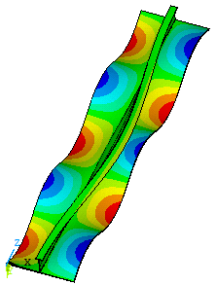	SIF	Plate: 5%-25%h_w, $0.25t_0$ Stiffener: 5%-50%h_w, $0.25t_w$ Stiffener (RS): 10%-20%h_w, $0.25t_w$

Table 7.4. Summary of the failure mode (weld-induced initial deflection; scale factor = 10; RS: residual stresses)

No	Failure mode	Initial column type deflection	Corrosion condition
1	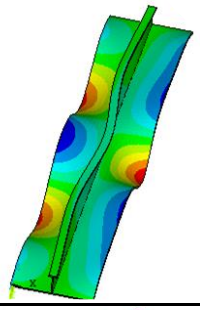	PIF	Intact Stiffener: 5%-50%h_w, 0.75t_w 5%-50%h_w, 0.5t_w Intact (RS) Plate (RS): 5%,15%h_w, 0.75t_0 Stiffener (RS): 10%-20%h_w, 0.75t_w 10%-20%h_w, 0.5t_w
2	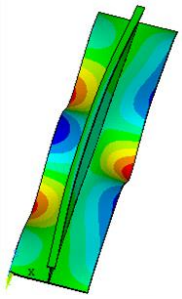	PIF	Stiffener: 5%-50%h_w, 0.25t_w Stiffener (RS): 10%-20%h_w, 0.25t_w
3	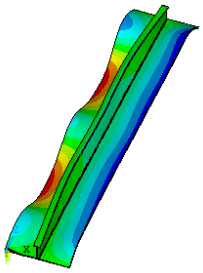	PIF	Plate: 5%-25%h_w, 0.75t_0 5%-25%h_w, 0.5t_0 Plate (RS): 25%h_w, 0.75t_0 5%-25%h_w, 0.5t_0
4	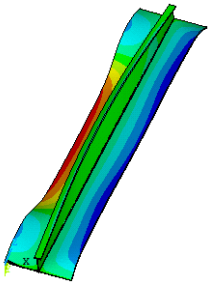	PIF	Plate: 5%,15%h_w, 0.25t_0 Plate (RS): 5%,15%h_w, 0.25t_0
5	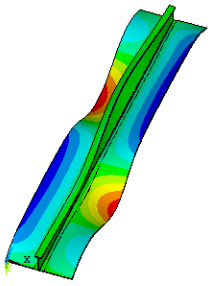	PIF	Plate: 25%h_w, 0.25t_0 Plate (RS): 25%h_w, 0.25t_0

No	Failure mode	Initial column type deflection	Corrosion condition
6	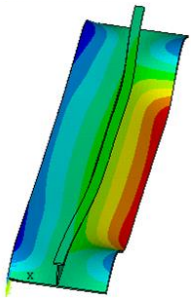	SIF	Intact Stiffener: 5%-50%h_w, 0.75t_w
7	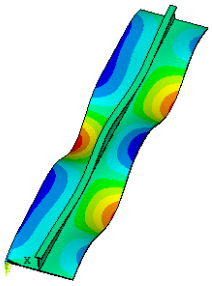	SIF	Stiffener: 5%-50%h_w, 0.5t_w Intact (RS) Stiffener (RS): 10%-20%h_w, 0.75t_w 10%-20%h_w, 0.5t_w
8	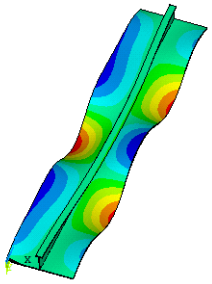	SIF	Stiffener: 5%-50%h_w, 0.25t_w
9	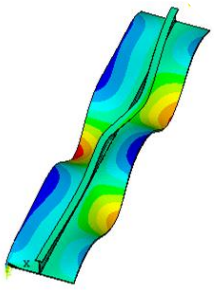	SIF	Stiffener (RS): 10%-20%h_w, 0.25t_w

Compared to the continuously welded stiffened plates, the influence of corrosion width/depth is negligible on the ultimate strength reduction for intermittent weld condition (Figure 7.8). To explain this, the von Mises stress distribution at the ultimate state was investigated and showed that instead of a continuous yielding area at the welds for the continuous weld condition, a discontinuity of the stress distribution was generated for the intermittent welds. Figure 7.15 illustrates the stress distribution at the ultimate strength state, from which a much reduced stress can be seen between the corroded regions. This stress reduction is more obvious for greater corrosion depth, and hence may ease the severity of the corrosion depth effects and lead to a monotonic increase in the strength reduction versus volume loss.

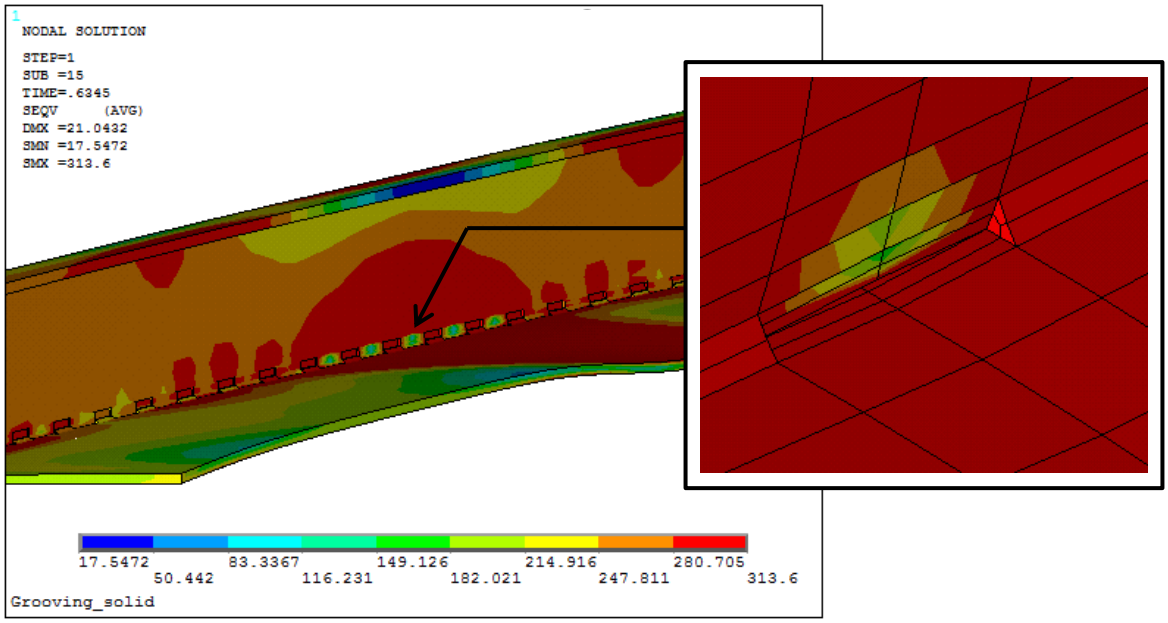

Figure 7.15. Example of von Mises stress distribution of stiffened plate model with intermittent weld and corrosion on stiffener.

Regarding the influence of the residual stresses, for buckling type initial deflection (Figure 7.9 (a), (c) and (d)), the strength reduction is simply increased due to the increased deformation of the structure with the failure mode unchanged (Table 7.3). The welding-induced deflection introduces more complicated failure modes. For low volume loss, corrosion on the plate (Figure 7.9 (b)) along with the residual stresses may even strengthen the structure due to altering from weld-induced to buckling-mode deformation (No.3 to 5 in Table 7.4). The only case when the residual stress lowers the strength reduction (Figure 7.9 (f)) is due to a sudden change of the failure mode for the intact condition without residual stresses whereas no obvious change is detected for the residual stress condition (No.6 and 7 in Table 7.4).

7.4.3 Empirical formulas

Assuming the volume loss is the governing parameter for strength analysis of corroded structures, two empirical formulas proposed by Paik et al. [7] (Equation 7.3) and Huang et al. [95] (Equation 7.4) have been examined together with the present study and plotted in Figure 7.16.

$$\frac{\sigma_{\mathrm{u}}}{\sigma_{\mathrm{u0}}} = \left(\frac{A_0 - A_{\mathrm{r}}}{A_0}\right)^{0.73} \tag{7.3}$$

$$\frac{\sigma_{\mathrm{u}}}{\sigma_{\mathrm{u0}}} = 2.657\left(\frac{\Delta V}{V_0}\right)^2 - 0.0229\left(\lambda_{\mathrm{y}}\right)^2 + 0.143\frac{\Delta V}{V_0}\lambda_{\mathrm{y}} - 2.367\frac{\Delta V}{V_0} + 0.0307\lambda_{\mathrm{y}} + 0.988 \quad (7.4)$$

where σ_{u} and σ_{u0} are the ultimate strength for a structural member with and without corrosion respectively; A_0 is the original cross-sectional area; A_{r} is the smallest cross-sectional area after the plate is damaged by corrosion; λ_{y} is the ratio between the transverse and longitudinal in-plane stresses; ΔV is the corroded volume loss and V_0 is the initial plate volume. It can be seen that Paik et al.'s formula (Equation 7.3) underestimated the strength reduction from the present study while Huang et al.'s formula (Equation 7.4) gives relatively good estimate for small volume loss. However, the two expressions were derived primarily for plates. The Paik et al. formula may be able to represent the lower boundary of strength reductions. The weld-induced initial deflection and the residual stress introduce a greater scatter in the data, due to the more complex failure mode.

To directly represent the contribution of the plate to the strength capacity of a stiffened panel, the concept of effective width has been proposed for structures under compression [86]. Faulkner proposed the following equation to predict the effective width and the ultimate strength capacity for $\beta \geq 1$ [115]:

$$\frac{b_{\mathrm{e}}}{b} = \frac{\sigma_{\mathrm{u}}}{\sigma_{\mathrm{y}}} = \frac{C_1}{\beta} - \frac{C_2}{\beta^2} \quad (7.5)$$

where b_{e} is the effective width of the plate, σ_{y} is the yield stress of the material and β is the slenderness ratio shown in Table 7.1. By taking the initial deflection into account, C_1 = 2 and C_2 = 1, and DNV suggests that C_1 = 1.8 and C_2 = 0.8 when considering both initial deflection and the weld-induced residual stresses [195]. In addition to the slenderness ratio, the column slenderness ratio as defined in Equation 2.11 is another important geometric property for a stiffened plate model. When considering the effective width, A and I are calculated using b_{e}, which leads to an effective column slenderness ratio λ_{e}. Figure 7.17 shows the nominalised ultimate strength ($\sigma_{\mathrm{u}}/\sigma_{\mathrm{y}}$) versus λ_{e}. The values derived from Equation 7.5 and two frequently used empirical formulas, namely Johnson-Ostenfeld formula (Equation 7.6) and Paik and Thayamballi's formula (Equation 7.7) [86] are also presented.

$$\frac{\sigma_{\mathrm{u}}}{\sigma_{\mathrm{y}}} = 1 - \frac{{\lambda_{\mathrm{e}}}^2}{4} \quad (7.6)$$

$$\frac{\sigma_u}{\sigma_y} = \frac{1}{\sqrt{0.995 + 0.936\lambda_e{}^2 + 0.170\beta^2 + 0.188\lambda_e{}^2\beta^2 - 0.067\lambda_e{}^4}} \tag{7.7}$$

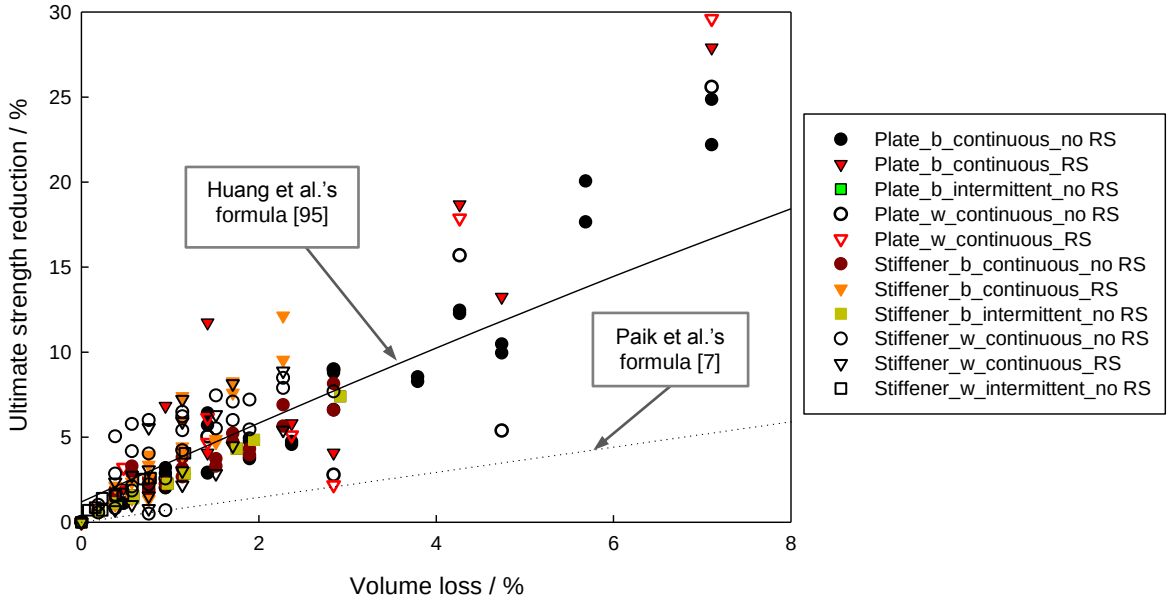

Figure 7.16. Comparison between present results and empirical formulas (b: buckling-mode deflection; w: weld-induced deflection; RS: residual stresses).

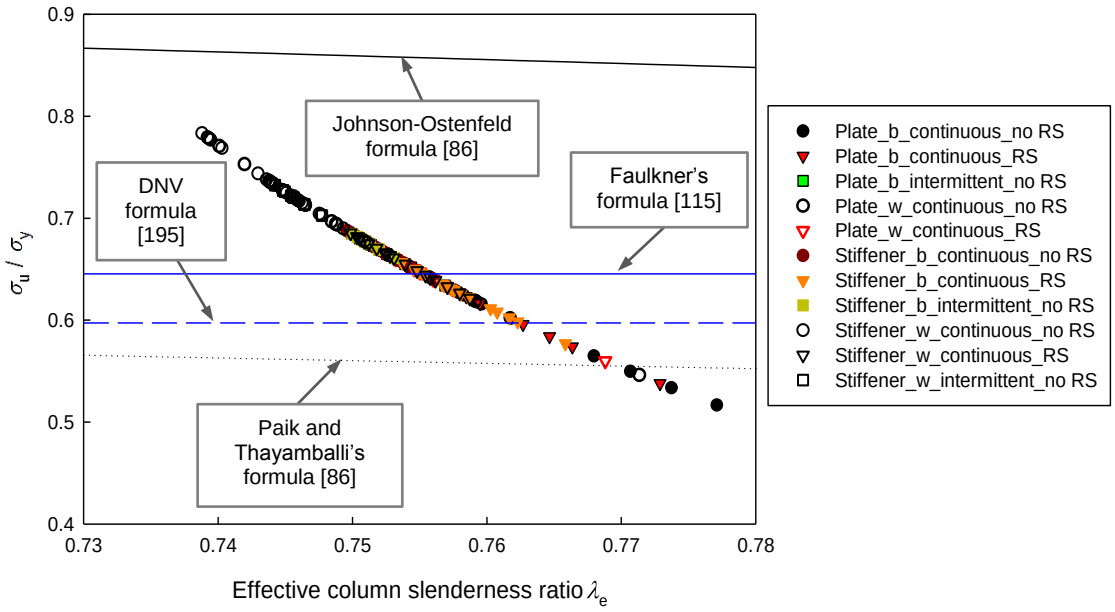

Figure 7.17. Comparison of the ultimate strength formulas for a stiffened plate under uniaxial compression (b: buckling-mode initial deflection; w: weld-induced initial deflection; RS: residual stresses).

It can be seen that the ultimate strength of corroded models remains in the range of the estimated values but drops faster compared to the empirical formulas with increasing λ_e,

which indicates that the grooving corrosion damage would introduce a large fluctuation to the empirical predictions and may not be accurately estimated using the empirical approach.

7.5 Conclusions

This study has analysed the influence of grooving corrosion on the ultimate strength capacity of a stiffened plate considering various initial imperfections (initial deflections, weld-induced residual stresses and a root opening), weld methods and a realistic weld connection. The nonlinear FEA has provided a better understanding of the mechanical behaviour associated with the grooving corrosion, which could occur within aged marine structures and steel bridges. It has been found that the ultimate strength of a stiffened plate model is more affected by the corrosion depth compared to width for the same volume loss. The examined corrosion feature would cause up to 26% reduction in the strength capacity. The strength reduction is mainly related to the failure mode change. In addition, a weld-induced initial deflection may lead to a more complex and sensitive failure mode to corrosion features. An intermittent weld type could provide stress relief between the corroded area especially for narrow and deep damage. In terms of the weld-induced residual stresses, the corrosion effect is enhanced by the application of longitudinal residual stresses. Negligible influence of a root opening was observed on the load shortening curves, however, stress concentrations are greatly increased at an early stage of loading. Overall, caution is needed when using empirical formulas to predict the ultimate strength for structures with grooving corrosion.

Chapter 8 Mechano-electrochemical modelling of corroded steel structures

To date, extensive effort has been made to assess the strength capacity of steel plated structures with localised corrosion features using both experimental and numerical methods. However, only a limited number of studies have addressed the mechanically assisted reactions (often called mechanochemistry) on the corrosion performance of a metallic surface (Section 2.3). It has been realised that when considering a structural system consisting of a number of different structural members, some members will always reach their collapse or ultimate strength first before the whole system collapses. Yet there has been no mechano-electrochemical investigation performed on plated steel structures loaded up to the collapse point. This chapter focuses on the interactions between the mechanical and electrochemical performances of such corroded structures based on the FEA models developed in the previous chapters. By utilising the results obtained numerically, it is possible to predict corrosion acceleration at 'hot spot' locations induced by stress/strain effects and to quantify the corrosion enhancement.

8.1 Problem

Both plate and stiffened plate models have been investigated, which are discussed in Chapter 5 and Chapter 7, respectively. For the plate models, two idealised local pit distributions on one side were considered, as shown in Figure 8.1 with typical mesh patterns. Five DOPs (2%, 5%, 10%, 15% and 25%) and four thickness reductions, t_{p} ($0.2t_0$, $0.25t_0$, $0.33t_0$ and $0.5t_0$, where t_0 is the original plate thickness), were considered. Regarding the stiffened plate model, the grooving corrosion was located on both-sides of the stiffener (Figure 8.2) with a groove width w_{gc} varying between $5\%h_{\mathrm{w}}$ and $50\%h_{\mathrm{w}}$, and the remaining thickness t_{gc} of $0.25t_{\mathrm{w}}$, $0.5t_{\mathrm{w}}$ and $0.75t_{\mathrm{w}}$ (where h_{w} is the stiffener web height and t_{w} is the original stiffener web thickness). A model with the grooving corrosion feature on the plate (w_{gc} = $25\%h_{\mathrm{w}}$, t_{gc} = $0.25t_0$; PIF; buckling-mode initial deflection) and the root opening (2 mm, illustrated in Figure 7.3) was also examined.

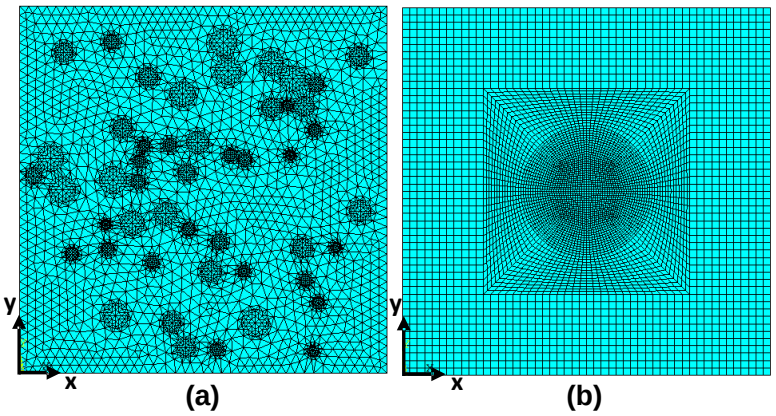

Figure 8.1. Localised pit distributions on a steel plate model of 800 mm × 800 mm × 15 mm: (a) random pitting (with pit radii varying between 10 mm and 30 mm); (b) a single large corrosion feature in the plate middle (170 mm radius).

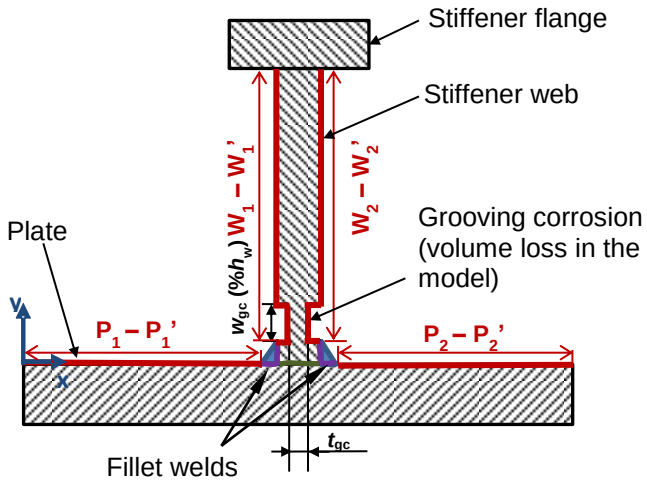

Figure 8.2. The cross section of the stiffened plate model with grooving corrosion features on the stiffener (dimensions refer to Table 7.1), Lines P_1-P_1' to W_2-W_2' are locations to extract results.

8.2 Results

Utilising Equation 3.7, the anodic current density increment ratio (i_a/i_{a0}) can be calculated. Detailed calculation procedures can be found in Section 3.4.

8.2.1 Plate models with pitting corrosion features

An external compressive load was applied in numerous substeps until the model reached the ultimate strength state (collapse). Figure 8.3 shows an example of the anodic current

density increment ratio distribution for a plate with random pitting corrosion (DOP = 15%, pit depth = $0.2t_0$) at two load substeps (43%σ_y and 65%σ_y). When the load was relatively low (43%σ_y), most areas of the plate remained elastic. It can be seen that the anodic current density ratio is increased slightly (approximately 1.3 times) and mainly occurs in the middle of the plate and along the four edges. When the load was increased to 65%σ_y, which equals the ultimate strength of the model, the current density ratio increased markedly (1.5 to 4 times) compared to the unstressed condition, concentrated on the middle area and the unloaded edges. Similar distributions have also been observed for intact plates, as well as plates with a large corrosion feature in the middle. Examining the area along the unloaded edge, as shown in Figure 8.3 (c) and (d), it can be seen that high current density ratio emerges around the pit edges and gradually develops on the bottom of the pits. Moreover, the interactions between the random pits were enhanced as the load increased.

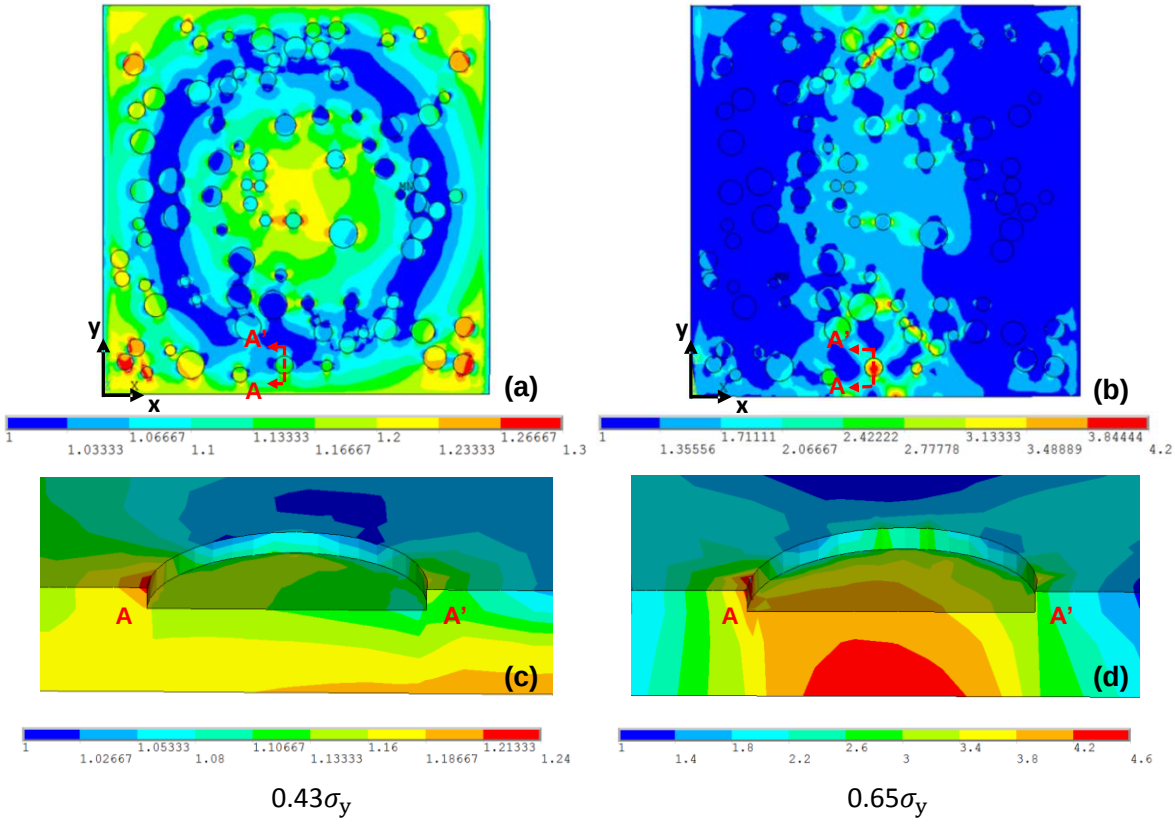

Figure 8.3. Distribution of anodic current density increment ratio i_a/i_{a0} for a plate with random pitting corrosion (DOP = 15%, pit depth = $0.2t_0$): (a) at 43%σ_y top view; (b) at 65%σ_y top view; (c) at 43%σ_y pit cross-section; (d) at 65%σ_y pit cross-section (scale bars indicate i_a/i_{a0} ratio). Modelled using an initial plate defection as detailed in Table 5.1. Loading direction is in *x*-direction. For an activation controlled corrosion process and temperature: 60°C.

To better understand the mechano-electrochemical behaviour of the plate models, Figure 8.4 provides results of hydrostatic pressure, equivalent plastic strain and anodic current density increment ratio for 15% DOP and four pit depths along the plate mid-section with a relatively large corrosion feature in the middle at the ultimate strength stage.

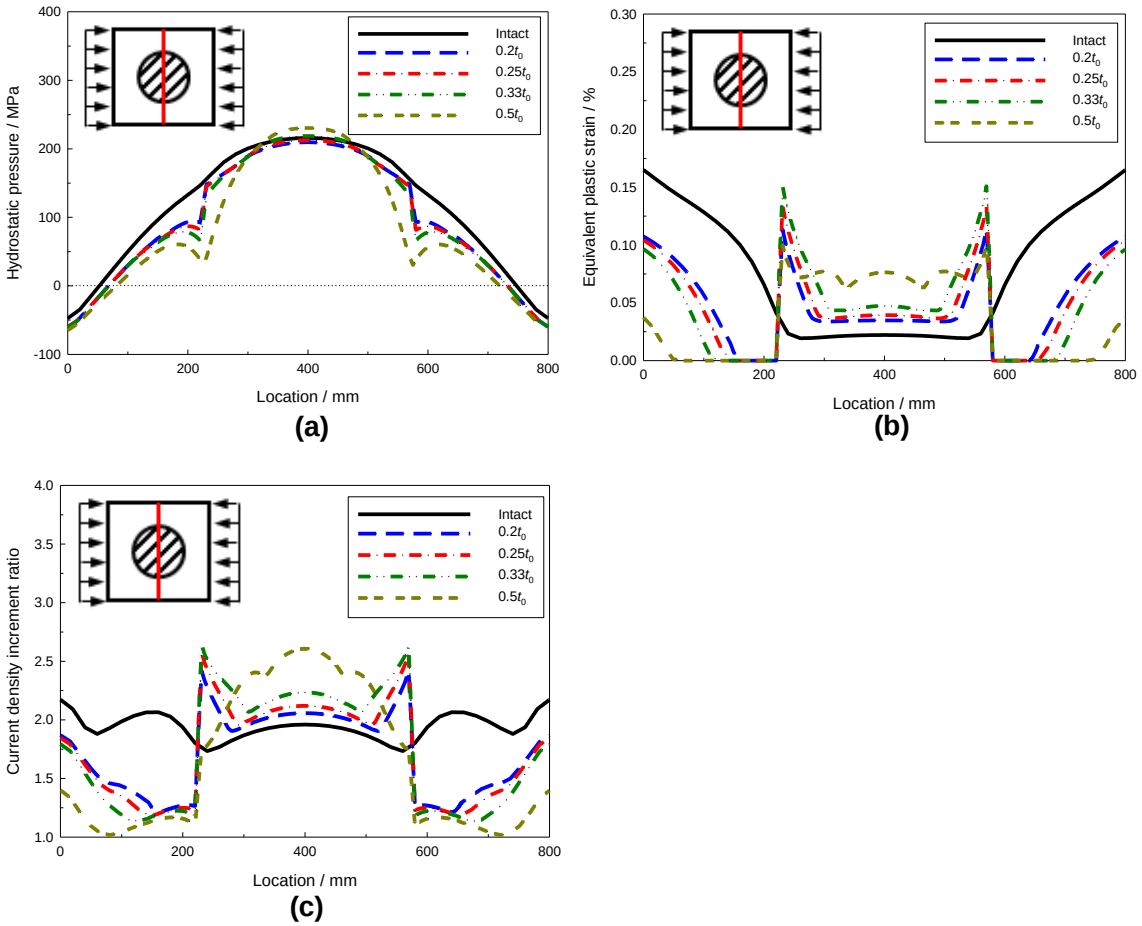

Figure 8.4. Results along line *x* = 400 mm for the plate model with a large corrosion feature in the middle at ultimate strength stage (DOP = 15%): (a) hydrostatic pressure; (b) equivalent plastic strain; (c) anodic current density increment ratio. For an activation controlled corrosion process and temperature: 60°C.

The geometric discontinuity induced by the corrosion defect largely influences the stress/strain values inside and adjacent to the pit edge. As the pit depth increases (from $0.2t_0$ to $0.5t_0$), the hydrostatic pressure shows minor variation in the maximum value in the middle of the plate but a sudden drop at the damage boundaries. Compared to the intact plate, the equivalent plastic strain reaches a maximum value at the boundary of the damage. As the corrosion damage becomes deeper, it is interesting to note that the strain inside the pit is increased accordingly, whereas the value decreases outside the pit. In addition, variation starts to emerge inside the pitted area. The distribution of the anodic current density change follows a similar trend as the plastic strain results. When the

corrosion depth is increased to $0.5t_0$, the location with the highest current density increase moves from the damage boundary towards the centre. However, the profile of the results showed no significant change during the loading process (Figure 8.5 with the load varying from $0.6\sigma_y$ to its ultimate strength). When examining the influence of DOP (Figure 8.6), it was found that for the same corrosion depth, as DOP increased, the current density change inside the pit approached the intact condition while the values outside the damage decreased.

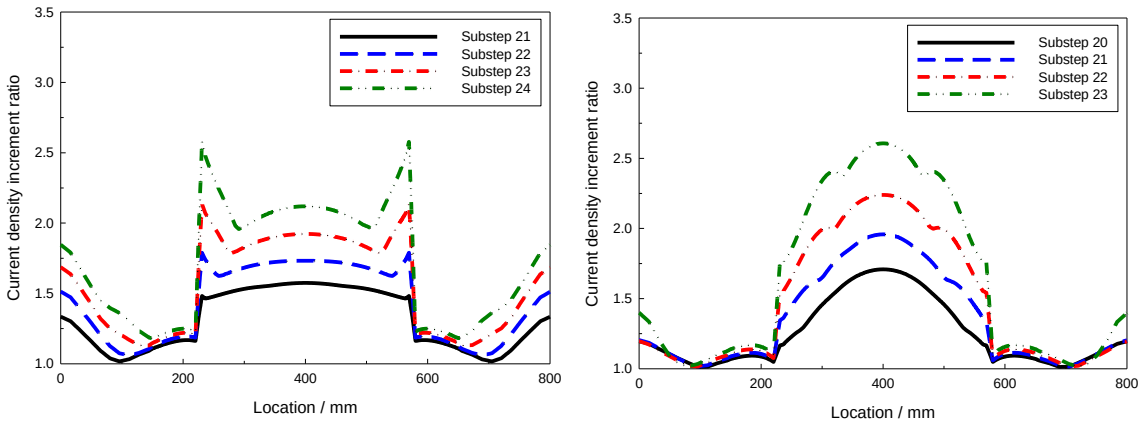

(a) DOP=15%, 0.25t_0 **(b) DOP=15%, 0.5t_0**

Figure 8.5. Anodic current density increment ratio along line *x* = 400 mm for plate model with a large corrosion feature in the middle at different load substeps (DOP = 15%) (Sub: substep number): (a) pit depth = 0.25t_0; (b) pit depth = 0.5t_0. For an activation controlled corrosion process and temperature: 60°C.

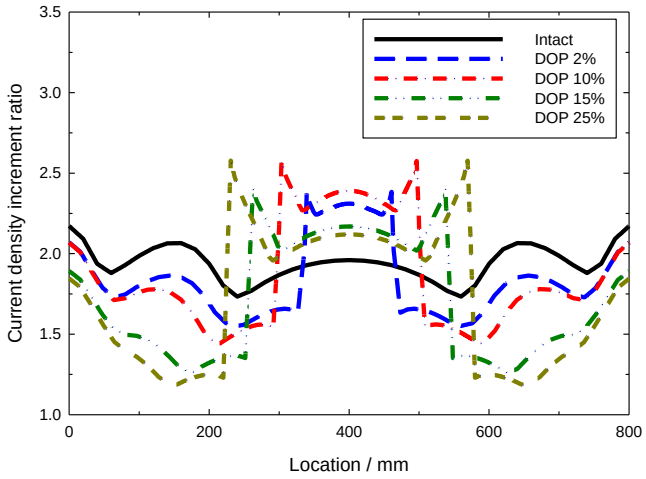

Figure 8.6. Anodic current density increment ratio along line *x* = 400 mm for plate model with a large corrosion feature in the middle and various DOPs (pit depth = 0.25t_0). For an activation controlled corrosion process and temperature: 60°C.

8.2.2 Stiffened plate models with grooving corrosion features

Firstly, for the stiffened plate model, a study was carried out for an unstressed intact condition. Figure 8.7 shows the influence of the longitudinal weld-induced residual stresses on the electrochemical properties. From the anodic current density ratio plot (Figure 8.7 (a)) it can be seen that a higher ratio occurs at the HAZ with maximum tensile stress. When further examining a surface line A-A' (mid-section, half-width from the weld boundary to the plate edge), the element results of longitudinal stress and the equilibrium potential change, $\Delta\varphi_{\mathrm{Total}}$, on the plate surface are also obtained and plotted in Figure 8.7 (b). $\Delta\varphi_{\mathrm{Total}}$ is a summation of the elastic (Equation 2.17) and plastic (Equation 2.20) effects. It clearly shows that the sharp decrease in potential corresponds to the change of the residual stress sign. Accordingly, physical measurement was also carried out across a butt-welded ship grade steel plate using the Scanning Kelvin Probe Force Microscopy (SKPFM) technique. Details of the SKPFM measurement can be found in Appendix 6. It can be seen from Figure A6.2 that the Volta potential difference between the sample surface and the AFM tip has its highest value (approximately 0.143 V) at the weld centre and gradually decreases to 0.006 V at 55 mm from the centreline. Further away from the weld the Volta potential difference stabilises at around 0.012 V. For the plate's flat surface per se, the 6 mV potential difference between the steel plate and the HAZ is comparable with the result obtained from the modelling (3 to 4 mV) shown in Figure A6.2.

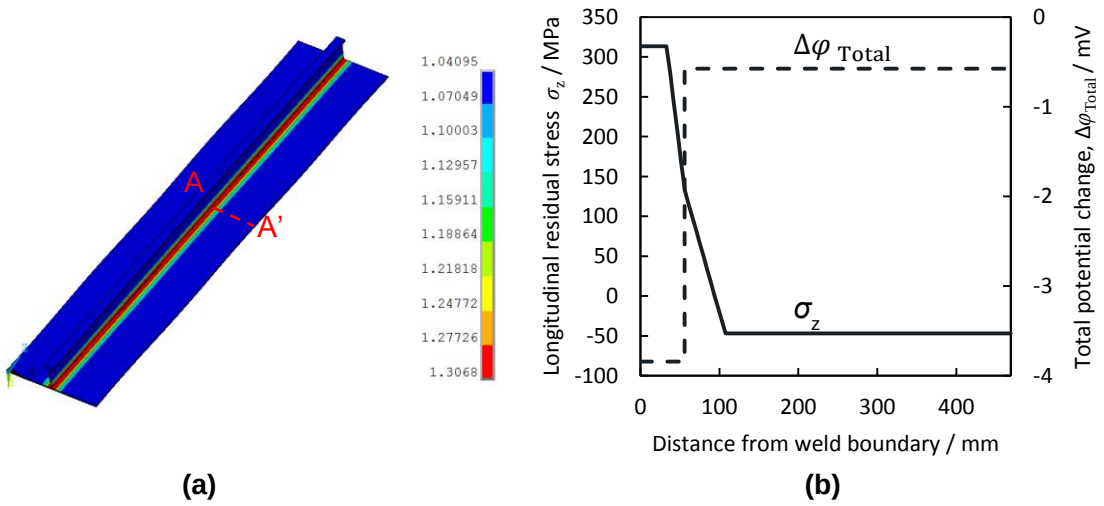

Figure 8.7. An intact stiffened plate with residual stresses in the longitudinal direction: (a) anodic current density increment ratio distribution; (b) longitudinal residual stress and total anodic potential change (summation of elastic and plastic effects) along line A-A' (from weld boundary to plate edge). For an activation controlled corrosion process and temperature: 60°C.

As the structure deforms, a continuous redistribution of the anodic current density has been observed for all conditions during the loading process. Based on the stress/strain relationship, an example of such redistribution is shown in Figure 8.8. At the first load substep (Point 1), when the model is elastically deformed, it can be seen that a slight increase in i_a/i_{a0} appears on the structural surface with the highest i_a/i_{a0} of approximately 1.6 at the corroded region. Regardless of the boundary constraint effect, when further increasing the load with a significant development of plasticity until collapse (Points 2 and 3), a marked rise in the current density occurs not only in the corroded area but also on the intact plate and the flange, mainly concentrated on the mid-section of the model.

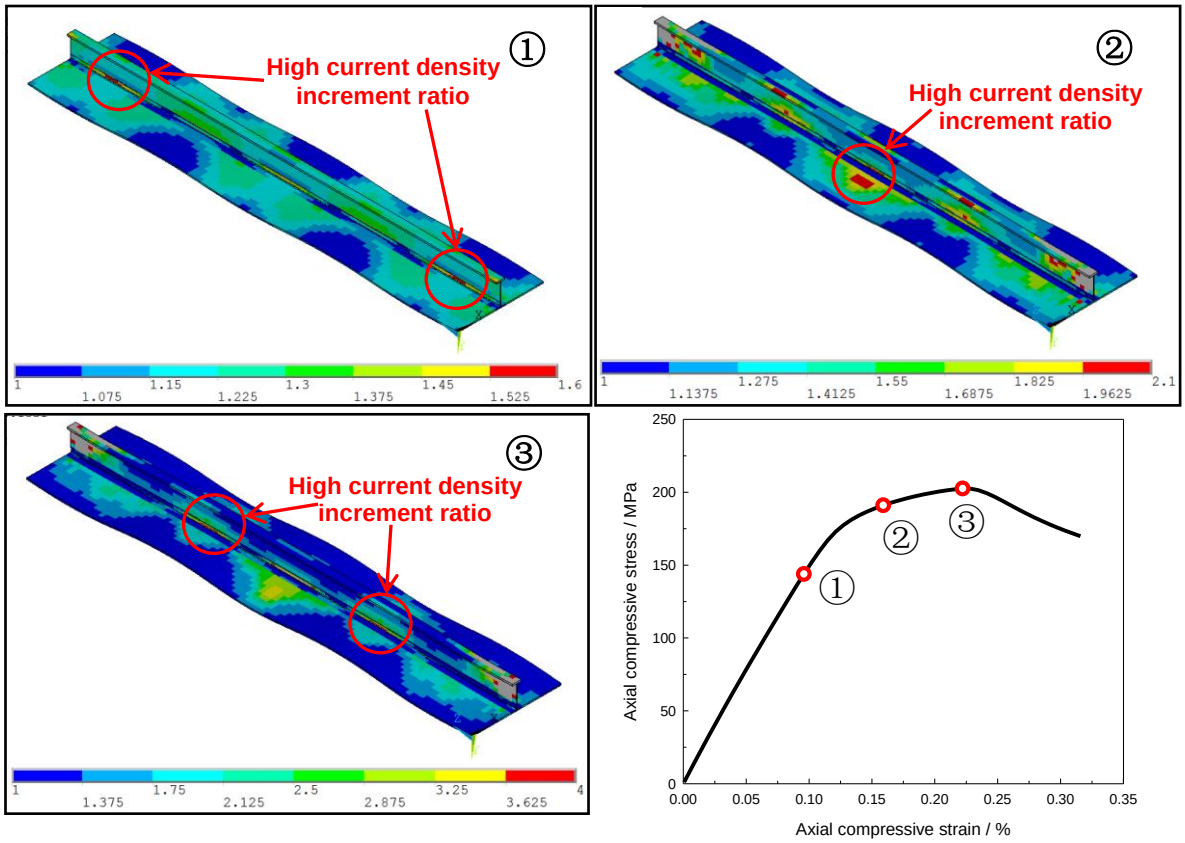

Figure 8.8. Anodic current density increment ratio at different load substeps for a stiffened plate model with grooving corrosion on the stiffener (w_{gc} = 15%h_w; t_{gc} = 0.75t_w). The initial deflection is detailed in Table 7.1. For an activation controlled corrosion process and temperature: 60°C.

Data were also extracted along the mid-section on both sides of the plate and the stiffener, as illustrated in Figure 8.2 (Lines P_1-P_1', P_2-P_2', W_1-W_1' and W_2-W_2'). Figure 8.9 to Figure 8.11 show results for a stiffened plate model at the ultimate strength stage with a fixed corrosion width (10%h_w) and varying the remaining thickness (0.75t_w, 0.5t_w and 0.25t_w).

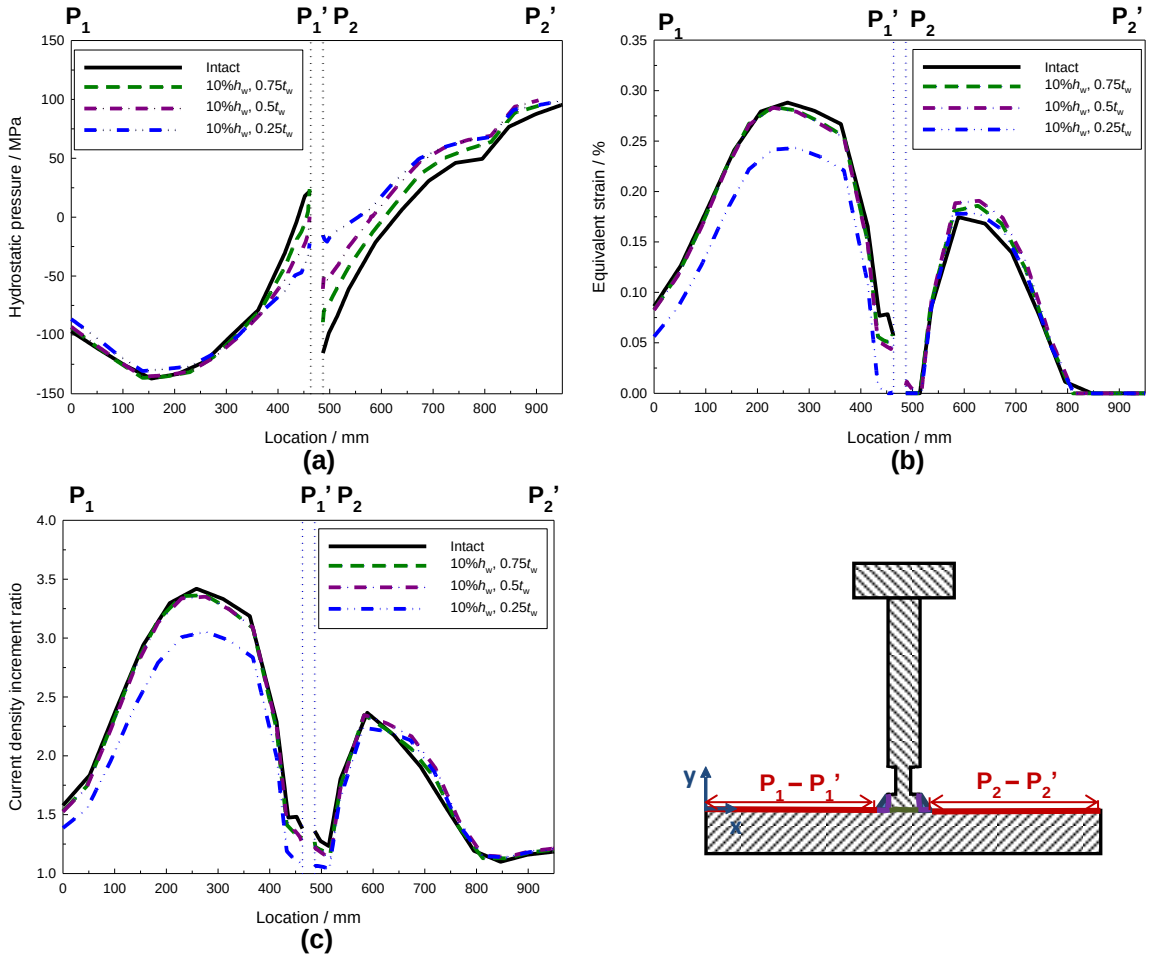

Figure 8.9. Lines P_1-P_1' and P_2-P_2' of a stiffened plate model with grooving corrosion on the stiffener (w_{gc} = 10%h_w; t_{gc} = 0.75, 0.5 and 0.25t_w): (a) hydrostatic pressure; (b) equivalent plastic strain; (c) anodic current density increment ratio. The dashed lines indicate the location of the stiffener. For an activation controlled corrosion process and temperature: 60°C.

For the surface of the plate in the intact model (Figure 8.9), the sign of hydrostatic pressure indicates that Line P_1-P_1' is under compression while P_2-P_2' is under tension (positive hydrostatic pressure). Conversely, the left side of the stiffener (W_1-W_1') is under tension while the right side (W_2-W_2') is under compression (Figure 8.10). The presence of grooving corrosion mainly affects the stress distribution on stiffener surfaces, adding more compression to W_1-W_1' and easing the compressive stress on W_2-W_2'. The influence is much more significant inside the grooves as the corrosion becomes deeper. The equivalent plastic strain reaches its highest value on the plating adjacent to the weld joint. Much larger strain occurs inside the grooves compared to the intact condition with lower values outside the grooves. However, it is interesting to note that when the remaining thickness is only 0.25t_w minimal plastic strain develops inside the grooves at the mid-section location. In terms of the anodic current density ratio, similar distributions can be

seen as the plastic strain for all locations, with maximum current density of 6 to 7 times higher at the corroded area than for the unstressed condition. The results were also compared to models without weld-induced residual stresses. Similar distributions of the stress/strain values were obtained. However, the maximum current density was only 3 to 4 times higher than the unstressed surface and the plastic strain was greatest at the edge of the weld.

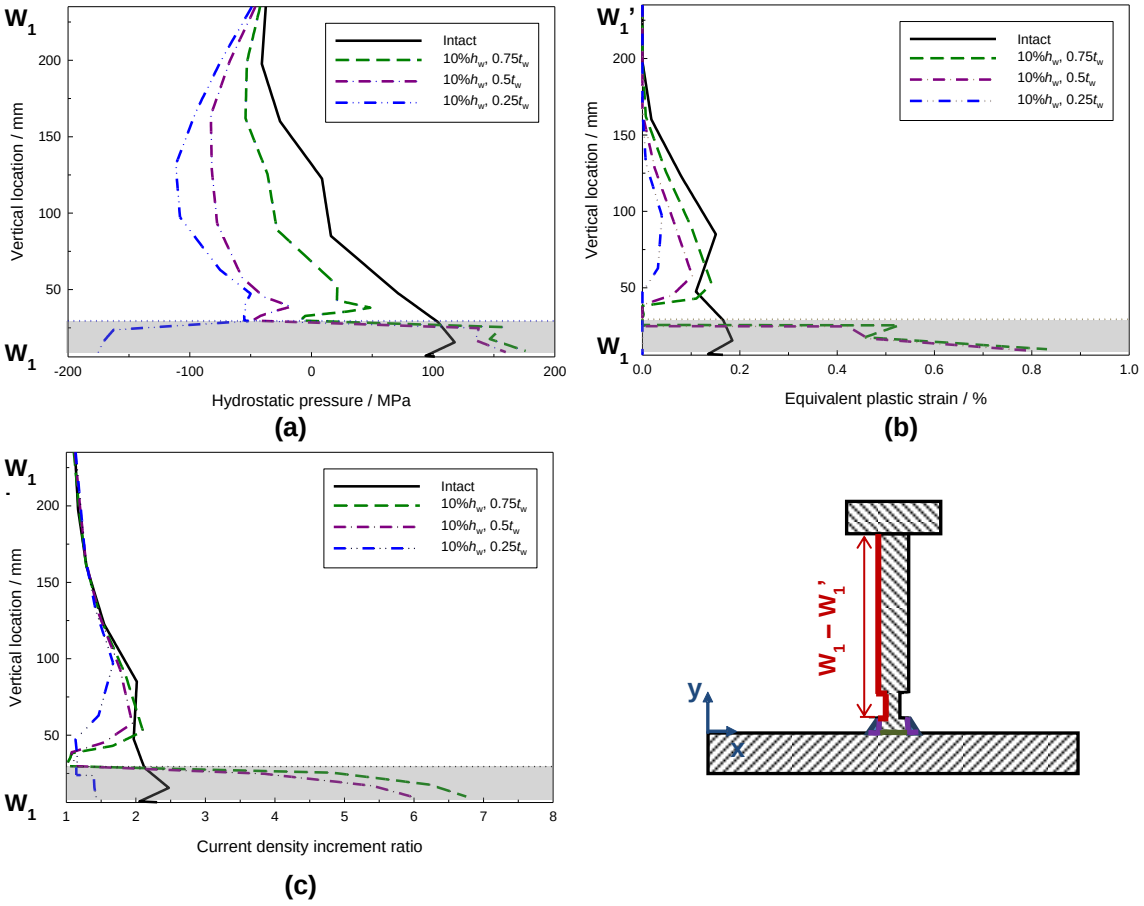

Figure 8.10. Line W_1-W_1' of a stiffened plate model with grooving corrosion (grey area) on the stiffener (w_{gc} = 10%h_w; t_{gc} = 0.75, 0.5 and 0.25t_w): (a) hydrostatic pressure; (b) equivalent plastic strain; (c) anodic current density increment ratio. For an activation controlled corrosion process and temperature: 60°C.

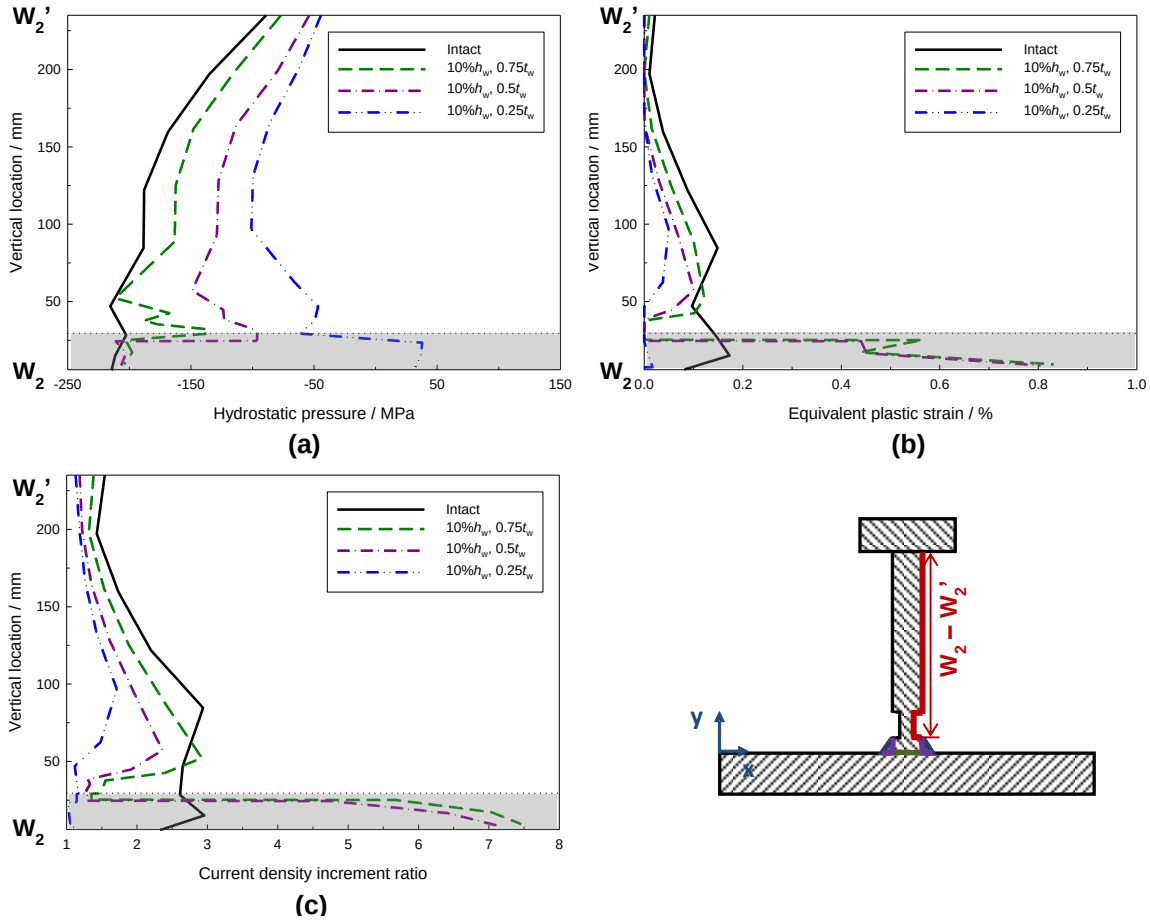

Figure 8.11. Line W_2-W_2' of a stiffened plate model with grooving corrosion (grey area) on the stiffener (w_{gc} = 10%h_w; t_{gc} = 0.75, 0.5 and 0.25t_w): (a) hydrostatic pressure; (b) equivalent plastic strain; (c) anodic current density increment ratio. For an activation controlled corrosion process and temperature: 60°C.

When considering the weld connection defect (root opening), Figure 8.12 shows the comparison of anodic current density increment ratio distribution between models with and without the root opening when elastically loaded (external load = 1.92%σ_y). It can be seen that the increase in the current density is marginal. However, there is a clear difference between the locations of high current density increase. For model with perfect weld connection, the i_a/i_{a0} is more evenly distributed on the cross-section while for model with the root opening, the highest i_a/i_{a0} is concentrated at the bottom of the stiffener.

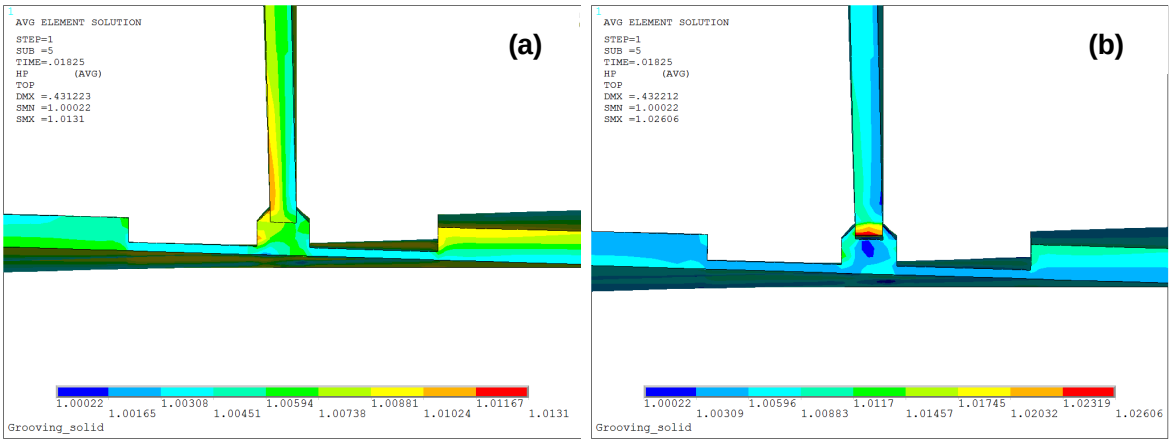

Figure 8.12. Anodic current density increment ratio distributions on a cross-section (at 1/3 length) of the stiffened plate model when external load = 1.92%σ_y (corrosion on plate 25%h_w, 0.25t_0; PIF; buckling-mode initial deflection): (a) perfect weld connection; (b) weld with root opening.

8.3 Discussion

From the mechano-electrochemical evaluation of simple plate models, it is evident that the locations of the stress/strain concentration are closely associated with the applied initial deflection and boundary conditions. When the plates are elastically deformed, higher hydrostatic pressure develops in the middle and four corners of the plate, due to the shape of the initial deflection. The idealised corrosion features have added extra complexity to the stress distribution, which determines the anodic current density distribution at the elastic stage, as shown in Figure 8.3 (a). As the model further deforms, plastic strain starts to develop along the unloaded edges and propagates to the centre (Figure 8.3 (b)), due to the development of the membrane stress in the central area. With the presence of corrosion damage, the highest plastic strain and hence i_a/i_{a0} always occurs at the damage boundary initially (Figure 8.3 (c)), as also reported in Ref. [186]. However, as the external load further increases, the strain or i_a/i_{a0} quickly increases at the bottom of the pits (Figure 8.3 (d)). This finding is of great importance since when plasticity has spread to a large extent on a structure, not only the area with geometric discontinuity but also the area adjacent to it become more anodic. The subsurface at the corrosion feature is therefore more likely to experience corrosion acceleration.

From the results at half-length of the plate, Figure 8.4 clearly shows that the development of plastic strain plays a major role in altering the current change profile, leading to much higher values. In addition, at the ultimate strength stage, the corrosion damage results in a plastic strain increase inside the corroded area and a decrease in the surrounding intact

area compared to the uncorroded condition (Figure 8.4 (b)). This phenomenon becomes more obvious as the pit depth increases, implying a more localised plastic strain distribution. This is due to the lower membrane tensile stress in the middle of the plate surface induced by corrosion damage, which leads to a less effective stress/strain redistribution in the plastic regime and a much increased local deformation. A similar distribution of equivalent stress has also been reported before, which is explained as stress concentration in the elastic region [143]. Ultimately, the concentrated hydrostatic pressure and the equivalent plastic strain would result in a more localised anodic current density increase, indicating that a more severe corrosion enhancement is expected at the corrosion site leaving the surrounding intact region less of an issue. The localised corrosion enhancement is also observed for small DOPs, as shown in Figure 8.6. However, when increasing DOP, the current density increment decreases both inside and outside the pit, due to a greater influence of the larger corrosion area on the stress/strain redistribution along the unloaded edges. It is noticeable that when the pit depth is up to $0.5t_0$, there is a profile change mainly in the plastic strain, leading to a much greater current density increase in the middle of the corroded region compared to at the boundaries. This higher strain is primarily caused by the greatly reduced strain at the centre of both unloaded edges in addition to the yielded intact area around the pit. However, for every DOP and corrosion depth, the distribution profile of the stress/strain and the current density remains unchanged during the loading process (Figure 8.5). Also, minor variation in the distribution shape is obtained for different DOP, suggesting that the location of corrosion acceleration is largely determined by corrosion depth instead of the external load or DOP. Thus, pit depth not only has a greater impact on the strength capacity reduction, but also on the mechano-electrochemical performance.

The stiffened plate model investigation shows higher complexity due to the application of residual stresses, various initial deflections and the connection between the stiffener, weldment and plating. Specifically, the residual stresses in the longitudinal direction cause a negative potential shift (Figure 8.7 (b)) at the HAZ, which could operate as active anodes. The potential variation was confirmed by the SKPFM measurements (Figure A6.2 in Appendix 6). However, compared to the slight potential changes on the flat plate surface away from the weld, it can be seen that a more significant negative shift was detected at the weld boundary compared to the centre of the weld (up to 0.1 V). A similar distribution was reported in the literature from experiments [127,145]. Clearly the SKPFM measurements show a much more complex picture compared to the modelling results (Figure 8.7), which again demonstrates that the mechanisms of grooving corrosion is a combination of mechanical effects, variance in the composition of the welds and the base

metal and the altered microstructure, which ultimately leads to knife-line corrosion attack. From the electrochemical standpoint, this experimental result again rationalises the location of the grooving corrosion in the stiffened plate models. However, it cannot be used as a direction validation of the model.

From Figure 8.8 it can be seen that the distribution of the changed anodic current density is not only dependent on the corrosion location but also affected by the structural deformation. As the external load increases, the increased mechano-electrochemical effect is more affected by the plastic behaviour and becomes more localised along the weld joint, implying a smaller contribution of elastic deformation to the mechanochemical corrosion.

From Figure 8.9 to Figure 8.11 it is apparent that weld-induced residual stresses not only enhance the mechano-electrochemical performance of corroded structures, but also cause stress/strain redistribution during loading, resulting in a much lower plastic strain along the welds on both sides of the plate. However, the low plastic strain inside the grooves when the remaining thickness is down to $0.25t_{\mathrm{w}}$ was found to be induced by the change in the failure mode of the stiffener. This phenomenon affects the difference in plastic strain distribution over the structural surface. For example, the plastic strain development for models with remaining web plate thickness of $0.75t_{\mathrm{w}}$ and $0.25t_{\mathrm{w}}$ (Figure 8.13) shows that plastic strain develops in the groove at the mid-section area for $0.75t_{\mathrm{w}}$ but at the adjacent area for $0.25t_{\mathrm{w}}$, which directly affects the mechano-electrochemical properties.

From the previous study on the root opening effect (Section 7.3.5), it was found that such weld connection defect would primarily influence the local stress state in the elastic region (Figure 7.11). The mechano-electrochemical results (Figure 8.12) again show the less effect of elastic stress on the current density increment. However, the root opening-induced early stress concentration led to a marked $i_{\mathrm{a}}/i_{\mathrm{a0}}$ concentration at the bottom of the stiffener. Therefore, in addition to a potential crack initiation, the electrochemical properties will also be altered due to the weld defect.

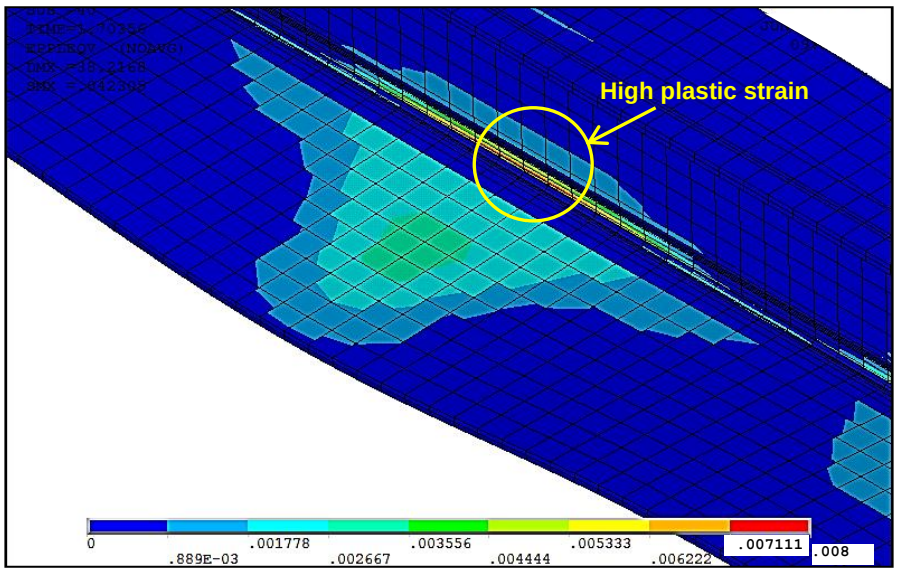

(a) 10%h_w–0.75t_w

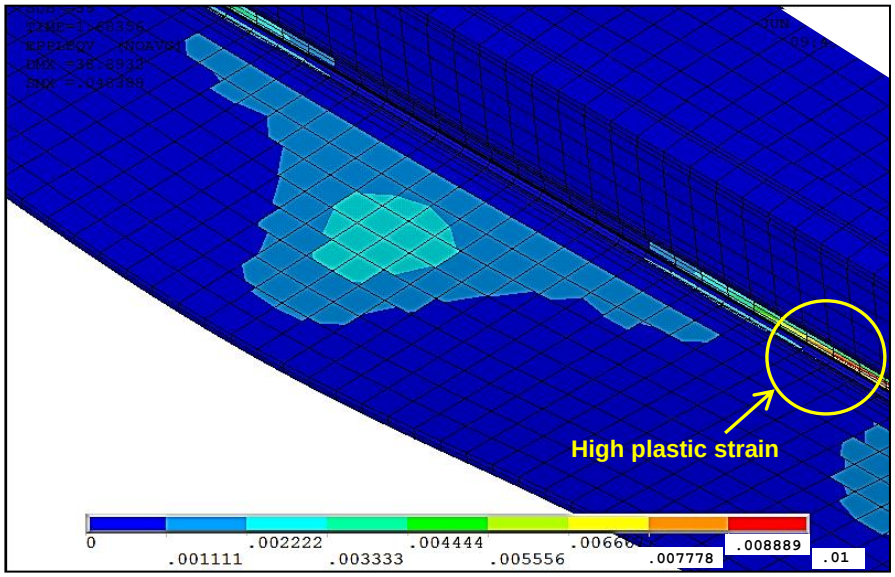

(b) 10%h_w–0.25t_w

Figure 8.13. Equivalent plastic strain at the mid-section of a stiffened plate model with grooving corrosion at the ultimate strength stage: (a) 0.75t_w and (b) 0.25t_w. For an activation control corrosion process and temperature: 60°C.

8.4 Conclusions

A numerical methodology has been established to evaluate the mechano-electrochemical performance of local corroded steel structures subject to external loading and weld-induced residual stresses. The SKPFM measurements revealed a similar potential change on the base metal in comparison with the modelled meausrements. However, a much more complex potential variation was aobserved across the weldment, HAZ and base

metal. Considering that some structural members will always reach their collapse or ultimate strength first before the whole system collapses, various states of deformation up to post-collapse region have been investigated for such local structural members. In general, a rise in the anodic current density is induced by elastic/plastic deformation. In addition to parameters such as the ambient temperature and the yield stress of the material, the current density increment ratio for a multi-component stress system is largely dependent on the hydrostatic component of the stress tensor and the equivalent plastic strain.

Moreover, for both plates and stiffened panels, the distribution of the mechano-electrochemical properties follows a similar profile as the plastic strain, indicating that the mechanochemical corrosion is more related to the plastic deformation, resulting in highly localised areas being more susceptible to enhanced anodic dissolution. It has been found that a change in the external load, weld connection condition and/or the cross-sectional area of a structure could lead to a stress state change and alter the electrochemical behaviour. In addition, the existing corrosion damage could introduce extra localised stress/strain, which intensifies the mechanochemical corrosion. Areas with significantly increased anodic current density are more likely to become anodes leaving the surrounding areas more cathodic in character.

For ship surveys, the actual physical realisation of either corrosion current or potential measurements can only provide an integration of these quantities distributions over a surface, which will mask the identification of singular features in the vicinity of any damage. Likewise, there are limitations in specimen size and loading/boundary conditions within a laboratory. In comparison, numerical modelling is shown here to be able to provide localised stress and strain information under a complex stress state. Although idealised in this study (with the exclusion of coatings and the simplified corrosion processes under specific loading and boundary conditions), the methodology proposed is considered to be able to identify the ‘hot spot' locations of accelerated corrosion and quantify the increased anodic current ratio. The utilisation of this information could thus lead to more targeted corrosion inspections and optimised maintenance schedules, along with enhanced ship surveys. However, other influencing factors such as the oxide film deformation due to stress/strain cannot be neglected. Also, further work is needed to investigate the influence of the changed surface state on future corrosion development and the strength capacity of a structure.

Chapter 9 Conclusions and recommendations for future work

Based on the identification of the corrosion issues and a review of the related research in the literature, a comprehensive and systematic investigation has been presented throughout this thesis, focusing on the interactions between mechanical and electrochemical performances of thin-walled steel structures (mainly for marine applications) with corrosion damage. Both numerical (FEA) and experimental (TSA and DIC) methods were adopted to provide more reliable and detailed information to allow the author to better understand the corrosion-induced stress concentration, strength capacity degradation, structural deformation and mechano-electrochemical property change. In this final chapter, conclusions from all studies will be summarised, based on which recommendations will be provided for further analysis.

9.1 Conclusions

This thesis has firstly introduced the fundamentals of typical corrosion mechanisms and corrosion patterns of steel structures in marine environment (Sections 2.1.1 and 2.1.2). It has been establisehd that while the general corrosion mechanism for steel has been extensively explored, the application of corrosion protection systems, welds and the service stresses have presented uncertainties in terms of localised corrosion (pitting and weld-induced grooving corrosion). Researchers have proposed numerous statistical/empirical models to predict marine corrosion damage over time (Section 2.1.3). However, the accuracy of such predictions is dependent on either the collected corrosion data or understanding of the corrosion mechanisms. The former is obtained from surveys; but it shows large scatter patterns predominantly due to the complex environmental and operational conditions, or indeed any associated human and gauging error, which are normally not noted in a survey report. Predictions relying on mechanistic principles (Melchers' model) are not able to consider the coating deterioration and lacking validation. More uncertainties were raised in terms of correcting the models with environmental (temperature, oxygen, salinity, pH and water velocity) and operational factors (coating condition, cargoes, ballast condition and tank cleaning). It has been realised that the corrosion prediction models have convenience in structural reliability analysis and helped the author gain a greater insight into the corrosion phenomenon in marine environment (large structural/time scale). However, due to the abovementioned issues, simply

choosing a particular model seems to overlook the complexity of marine corrosion problem. Knowing that the corrosion mechanisms are still not fully understood, and there is a lack of up-to-date survey data, the author decided to focus initially on the mechanical performance of structures subject to corrosion damage at discrete time points.

When considering a system consisting of a number of different structural members, some will always reach their collapse/ultimate strength first before the whole system collapses. Thus, to understand the ULS of individual structural members it is essential to concentrate on the corrosion features in order to ultimately determine the overall integrity of a structural system. With an understanding of the fundamentals (Section 2.2.1), previously published ultimate strength analysis has been reviewed covering both experimental and numerical methods (Sections 2.2.2 and 2.2.3). In the literature, there are a limited number of experiments, which only provide a stress-strain relationship at discrete locations on specimens, with no information of the stress/strain distribution on an irregular surface. Numerical methods (mainly FEA) are widely used to assess the ultimate strength thanks to the increasing computational ability. The nonlinear FEA enables researchers to not only consider the material and geometrical nonlinearities but also vary structural geometries, corrosion extent, loading/boundary conditions and structural initial imperfections. However, the studied corrosion features need to be closely related to what is found on-board marine structures. The modelling techniques, which may significantly influence the result accuracy, are often not clearly stated and validated. Also, it is not clear that if such mechanical property change would induce a change in the existing corrosion performance.

Therefore, another interesting field has in due course been realised from the literature, namely the mechano-electrochemical performance of a metallic surface (Section 2.3). From the literature it shows that the influence of elastic stress and plastic strain vary significantly owing to the selection of materials, test solutions and loading conditions. A better understanding of synergistic effect of mechanical and chemical/electrochemical properties of a metal surface is needed for an accurate estimation of the enhanced corrosion rate or reduced corrosion potential.

To finally identify a clear scope of this investigation, the author collected classification rules and regulations for corrosion inspection and repair (Section 2.4). The minimum allowable thickness together with coating failure scale diagrams were used to inform the studied corrosion features. Overall, the literature review has been a solid foundation for the author to carry out novel studies in order to better understand the problem and enhance the efficiency of finding solutions.

Nonlinear FEA was chosen to be the primary method. As a start, a systematic validation was achieved to gain familiarity and confidence in using such method (Chapter 4). The initial eigenvalue buckling analysis provided valuable knowledge of shell/solid element behaviour (frequently used for thin-walled structures), as well as constraining methods, selection of element type, element size/shape, number of elements through thickness, and integration strategies. It was found that apart from the commonly used shell element, solid-shell and solid element could be used for a more detailed modelling of structural defects. Using appropriate integration strategies, shear locking and hourglassing problems could be avoided. Regarding the nonlinear FEA procedure considering both geometric and material nonlinearities, the validation was achieved by replicating a series of steel structural members published in the literature, including plates, plate-stiffener combinations and a two-bay/two-span panel. The proposed method to explicitly apply a residual stress matrix to a plate model was also verified using both shell and solid elements. Although good agreements were obtained between replicated models and those published in the literature, the most reliable validation is always via experiments and physical observations. As discussed in the review, experimental data (stress or strain) to date have only been obtained at discrete locations over specimen surfaces. This study has brought in novel techniques (TSA and DIC) to overcome such limitations (Chapter 6) for corroded structure analysis. Based on the initial modelling study (Chapter 5), a range of steel specimens with idealised corrosion defects were tested. TSA successfully captured a full-field stress map when the specimen was elastically loaded. It not only validated the mesh quality of the new FEA models but also physically revealed early stress concentrations on an irregular surface. Another full-field technique, 3D DIC, was proven to be of great potential to provide a displacement/strain map for a specimen under compression until failure. It also demonstrated the reliability of the nonlinear FEA method for collapse and post-collapse behaviour.

Regarding the modelling work, two types of localised corrosion feature (pitting and grooving corrosion) were considered on a steel plate (Chapter 5) and a stiffened plate model (Chapter 7), respectively. The coating failure scale diagrams and reported immersion trials were used to inform the corrosion patterns for the plate models, including one-side localised corrosion damage (diameters in the order of tens of mm), bench-shape pits induced by MIC and a localised rough surface. It gave the parametric FEA a novel and more realistic physical meaning for ship structures, but equally this approach could also be utilised for other marine platforms and steel bridges. The main conclusions drawn from the plate model study are as follows:

(1) Corrosion on the unloaded edge or at the corner could potentially lead to a much lower ultimate strength compared to other corrosion locations (up to 20% reduction for a 800 mm × 800 mm × 15 mm plate with 25% locally corroded area and 3.75 mm remaining thickness);
(2) The existence of benches will further reduce the strength; however, the overall effect of benches diminishes with increasing volume loss;
(3) The strength reduction is greatly influenced by the corrosion size (especially pit depth), the formation of the bench geometry and the corrosion location;
(4) In terms of the post-ultimate strength, corrosion at the plate corner shows a more unstable behaviour in general, which may weaken a structural system when the rest of the structural members have not yet failed;
(5) Greater attention is needed during survey and maintenance when such pitting features occur at the corner/edge of plate structures, especially when bench-shape pits are formed;
(6) A rough surface at the corroded area has little impact on the ultimate strength and post-collapse behaviour but will introduce extra stress concentration and localised plastic strain even when the structure is elastically loaded, which may lead to cracking and corrosion acceleration;
(7) Based on the conclusions from Ref. [196] in local plastic strain analysis, it has been found that the plastic strain distribution is not only dependent on the external load and the damage location, but also largely associated with the morphology of a corroded surface. Moreover, when the structure enters its plastic regime, the location of high plastic strain depends on the location with minimum remaining thickness.

In the stiffened plate modelling, contact elements were used for a more realistic fillet weld simulation. The study covered weld-induced grooving corrosion features, different initial deflections, weld-induced residual stresses and weld connection imperfections (root opening). The key findings are as follows:

(1) Grooving corrosion depth has a greater influence on the ultimate strength reduction in comparison with corrosion width for the same volume loss. Such corrosion damage could cause up to 26% ultimate strength reduction of a stiffened plate (4750 mm × 950 mm × 15 mm) with corrosion of a width of 59 mm and a remaining thickness of 3.75 mm;
(2) For plates with weld-induced initial deflection, the failure mode is more complex and sensitive to corrosion features;

(3) An intermittent weld method can provide stress relief between the corroded area and hence ease the influence of narrow but deep corrosion damage;
(4) Consideration of the weld-induced residual stresses results in a lower ultimate strength value and a greater reduction compared to the intact structure, indicating the influence of corrosion is enhanced;
(5) Negligible influence of a root opening have been detected on the load shortening curves for models with different corrosion features and initial deflections. However, at the early stage of loading (fully elastic), the markedly increased stress concentration at the welding interface may lead to cracking and surface state change;
(6) The ultimate strength of corroded models remains in the range of the empirically estimated values but decreases faster when increasing λ_e, compared to the empirical formulas, indicating that the grooving corrosion damage would introduce a large fluctuation to the empirical predictions and needs to be treated with caution.

Having a better understanding of the mechanical performance of local structural members subject to various corrosion features, the final attempt was to investigate the mechanically altered corrosion performance (mechano-electrochemistry) of a metallic surface (Chapter 8). Analytical formulas were explicitly imbedded in the modelling study to calculate the anodic current density increment ratio due to mechanical stress/strain. In general, a rise in the anodic current density is induced by elastic/plastic deformation. In addition to parameters such as the ambient temperature and the yield stress of the material, the current density increment ratio for a multi-component stress system is dependent on the hydrostatic component of the stress tensor and the equivalent plastic strain, with plastic strain playing a major role. A change in the external load, weld connection condition and/or the cross-sectional area of a structure could lead to a stress state change and alter the electrochemical behaviour. In addition, the existing corrosion damage could introduce extra localised stress/strain, which intensifies the mechanochemical corrosion. Areas with significantly increased anodic current density are more likely to become anodes leaving the surrounding areas more cathodic.

The research highlights of the thesis are summarised as follows:

(1) A systematic validation of nonlinear FEA in ANSYS has been carried out;
(2) Full-field measurement techniques (TSA and DIC) on assessing the strength of plate specimens with various defects up to collapse point;
(3) The identification of localised corrosion features were related to ship survey (pitting/grooving corrosion) and immersion trials (bench-shape pits);

(4) A localised rough surface was introduced to the plate model;
(5) Grooving corrosion feature was studied together with a more realistic weld simulation, initial deflections, weld-induced residual stresses and a root opening;
(6) Detailed analysis has been presented looking at not only the ultimate strength but also the local stress/strain distributions;
(7) Mechano-electrochemical analysis was carried out based on the modelling results for a multi-component stress condition.

9.2 Recommendations for future work

The recommendations for future work are divided into two sections. The first relates to the investigation of mechanical performance of corroded thin-walled structures, and the second relates to the mechano-electrochemical analysis.

9.2.1 Mechanical performance analysis

It has been shown that modelling (FEA) is indeed a powerful tool and can be continuously used for future mechanical analysis. However, as the software and elements keep updating, it is vital to carefully examine the element behaviour and the calculation algorithm. The structural members studied so far have been plates and plate-stiffener combinations of ships with a fixed dimension. However, the scantling varies depending on the locations and the types of structures (ships, offshore platforms and bridges). The basic structural member of interest can be extended from a simple plate to a complex stiffened panel and even a box girder to allow researchers to gradually build up the knowledge of corrosion effects both locally and globally. Because of the selection of structural locations, there is expected to be a change in the boundary and loading conditions. Therefore, it is important to study the corrosion effect under typical and extreme loading condition, such as dynamic loading and fatigue problems. While steel is still the major material used for merchant ships, aluminium alloys have been increasingly used for their lightweight property. Although the corrosion rate of aluminium alloys is markedly controlled by a thin oxide film, once the oxide film is damaged, pitting corrosion could be generated. Also, the 5000 series aluminium alloys can become sensitised and vulnerable to intergranular corrosion, exfoliation and stress corrosion cracking especially in the HAZ. There has not been such study focusing on the corrosion effects on the strength capacity of aluminium alloy structures. In the current investigation, localised corrosion features were idealised

defects. It would be interesting to simulate natural localised corrosion morphology on plate but also stiffener-plate combination models. Also, edge corrosion needs to be studied for flange and web plates. From the classification rules in Section 2.4, either epoxy compound or welding is needed for corrosion repair. Assessing the efficiency of such repair methods is of importance for improving the maintenance. Ultimately, a collection of load-shortening curves considering corrosion and various structural parameters would contribute to the assessment of the ultimate strength of the entire structural system (for example a hull girder), which leads to a reliability analysis linking the understanding of corrosion mechanisms and the mechanical performances. Even if reliability analysis cannot be applied in the daily design practice, the results are useful for rule calibrations.

No matter how advanced the numerical models can be, experimental work is always essential for mechanical analysis and validation of the models. Since the full-field techniques (TSA and 3D DIC) have been proven to be able to assess a steel specimen with corrosion features, more effort is needed to look at natural corrosion morphology, different loading and explore the technique settings (speckle patterns, design of rigs, noise, et cetera) especially for the area with geometrical discontinuities. The experiments can also be performed on stiffened plate and welded structures. In addition to the laboratory environment and specimens of a reduced scale, it is interesting to see if such techniques can be applied *in situ*.

9.2.2 Mechano-electrochemical analysis

Being a complicated yet intriguing field, mechano-electrochemistry has gradually gained interest over the last several decades. It bridges the corrosion aspects and mechanical properties. However, from the literature the influence of elastic stress and plastic strain varied significantly owing to the selection of materials, solutions and loading types, not to mention the added confusion of stress corrosion cracking and oxide film conditions. Theoretical methods have been proposed together with empirical estimations. However, most validations of such protocols are unclearly stated and it is not certain if the parameters have been appropriately determined. Greater effort is thus needed to understand the fundamentals of the mechano-electrochemical phenomenon, with the help of carefully controlled corrosion experiments on stressed specimens (or surfaces with residual stresses). The current investigation has shown a numerical approach using analytical formulas to estimate the corrosion acceleration locations and magnitude. Although validation of the formulas was presented in the literature, it needs to fully verify

the numerical approach by means of experiments. Also, other aspects such as coating, concentration controlled process and temperature should be considered. Ultimately, it is important to utilise the results for more targeted corrosion inspections and optimised maintenance schedules.

List of References

[1] Centre of Documentation, Research and Experimentation on Accidental Water Pollution (CEDRE), "Erika", November 2009, Available online: http://www.cedre.fr/en/spill/erika/erika.php (August 2013).

[2] C. Canfield, "'Super-rust' in Castor leads to calls for more stringent inspections", March 2007, Avalibale online: http://www.professionalmariner.com/March-2007/Super-rust-in-Castor-leads-to-calls-for-more-stringent-inspections/ (August 2013).

[3] D.J. Howarth, J. Zhang, Corrosion: its impact on modern shipping with particular reference to crude oil tankers, in: Lloyd's Register Technology Days 2011, 2011.

[4] DNV. Casualty information: grooving corrosion on ship's side – serious leakage, Available online: https://exchange.dnv.com/CasualtyInformation/Documents/EmbeddedDownload/28http://www.eagle.org/eagleExternalPortalWEB/appmanager/absEagle/absEagleDesktop?_nfpb=true&_pageLabel=abs_eagle_portal_rules_guides_download_page&pub_id=49 (November 2013)

[5] N. Khurram, E. Sasaki, H. Katsuchi, H. Yamada, Finite element investigation of shear capacity of locally corroded end panel of steel plate girder, International Journal of Steel Structures, 13 (2013) 623-633.

[6] C. Guedes Soares, Y. Garbatov, A. Zayed, G. Wang, Corrosion wastage model for ship crude oil tanks, Corrosion Science, 50 (2008) 3095-3106.

[7] J.K. Paik, J.M. Lee, M.J. Ko, Ultimate compressive strength of plate elements with pit corrosion wastage Proceedings of the Institution of Mechanical Engineers, Part M: Journal of Engineering for the Maritime Environment, 217 (2003) 185-200.

[8] J.K. Paik, R.E. Melchers, Condition assessment of aged structures, Woodhead Publishing Limited, Cambridge England, 2008.

[9] IACS, Requirements concerning survey and certification, in, Internatinoal Association of Classification Societies Revolution. 11, 2013, Available online: http://www.iacs.org.uk/document/public/Publications/Unified_requirements/PDF/UR_Z_pdf1890.pdf. (August 2013).

[10] K.R. Trethewey, J. Chamberlain, Corrosion for Science and Engineering, 2 ed., Longman Scientific & Technical, UK, 1995.

[11] DNV, Allowable thickness diminution for hull structure, in: No.72.1, Hovik, Norway, 2013.

[12] R.E. Melchers, The changing character of long term marine corrosion of mild steel, in: Research report No. 277.04.2010, Centre for Infrastructure Performance and Reliability, New South Wales, Australia, University of Newcastle, 2010.

[13] Y. Waseda, S. Suzuki, Characterisation of Corrosion Products on Steel Surfaces, Springer, Berlin, 2006.

[14] C.P. Gardiner, R.E. Melchers, Corrosion analysis of bulk carriers, Part 1: operational parameters influencing corrosion rates, Marine Structures, 16 (2003) 547-566.

[15] C.P. Gardiner, R.E. Melchers, Corrosion of mild steel by coal and iron ore, Corrosion Science, 44 (2002) 2665-2673.

[16] C.P. Gardiner, R.E. Melchers, Aspects of bulk carrier hold corrosion, in: Report AME CRC C 98/6, The Royal Institution of Naval Architects, London, 1998.

[17] T. Nakai, H. Matsushita, N. Yamamoto, H. Arai, Effect of pitting corrosion on local strength of hold frames of bulk carriers (1st report), Marine Structures, 17 (2004) 403-432.

[18] C.R. Southwell, J.D. Bultman, J.C. Hummer, Estimating of service life of steel in seawater, Seawater Corrosion Handbook, (1979) 87-374.

[19] L.A. Terry, R.G.J. Edyvean, Influences of microalgae on corrosion of structural steel, in: Corrosion and Marine Growth on Offshore Structures, Ellis Horwood, Chichester, 1984.

[20] R.E. Melchers, Long-term corrosion of steels exposed to marine environments, European Journal of Environmental and Civil Engineering, 13 (2009) 527-546.

[21] R. Jeffrey, R.E. Melchers, The changing topography of corroding mild steel surfaces in seawater, Corrosion Science, 49 (2007) 2270-2288.

[22] W. Magelssen, Corrosion / Corrosion protection - What impact will this have on modern ship design?, in, DNV, 2000.

[23] SRAJ, Study on cargo oil tank corrosion of oil tanker, in: Report of Ship Research Panel 242, The Shipbuilding Research Association of Japan, Tokyo, 2002.

[24] K. Katoh, S. Imai, D.T. Yasunaga, H. Miyuki, Y. Yamane, H. Ohyabu, Y. Kobayashi, M. Yoshikawa, Y. Tomita, Study on localised corrosion on cargo oil tank bottom plate of oil tanker, in: World Maritime Technology Conference, San Francisco, USA, 2003.

[25] A. Forsgren, Corrosion control through organic coatings, Taylor & Francis Group, LLC, 2006.

[26] ABS, Guidance notes on the inspection, maintenance and application of marine coating systems, American Bureau of Shipping, 2007. Available online: http://www.eagle.org/eagleExternalPortalWEB/appmanager/absEagle/absEagleDesktop?_nfpb=true&_pageLabel=abs_eagle_portal_rules_guides_download_page&pub_id=49 (March 2013).

[27] C. Kato, Y. Otoguro, S. Kado, Y. Hisamatsu, Grooving corrosion electric resistance welded steel pipe in sea water, Corrosion Science, 18 (1978) 61-74.

[28] IMO, Hull and Structural Surveys, Compendium Volume 2 Part B, in, International Maritime Organisation, London, UK, 2004.

[29] A. Rahbar-Ranji, Ultimate strength of corroded steel plates with irregular surfaces under in-plane compression, Ocean Engineering, 54 (2012) 261-269.

[30] A.P. Teixeira, C. Guedes Soares, Ultimate strength of plates with random fields of corrosion, Structural and Infrastructure Engineering: Maintenance, Management, Life-Cycle Design and Performance, 4 (2008) 363-370.

[31] A.P. Teixeira, C. Guedes Soares, G. Wang, Probabilistic modelling of the ultimate strength of ship plates with non-uniform corrosion, Journal of Marine Science and Technology, 18 (2013) 115-132.

[32] TSCF, Condition evaluation and maintenance of tanker structures, Tanker Structure Co-operative Forum, 1992.

[33] T. Nakai, H. Matsushita, N. Yamamoto, Pitting corrosion on epoxy-coated surface of ship structures, in: Shipbuilding Technology ISST 2007, Osaka, 2007.

[34] R. Melchers, Corrosion uncertainty modelling for steel structures, Journal of Constructional Steel Research 52 (1999) 3-19.

[35] DNV, Corrosion protection of ships, in, Recommended Practice, DET NORSKE VERITAS, Hovik, Norway, 2000.

[36] J.K. Paik, D.K. Kim, Advanced method for the development of an empirical model to predict time-dependent corrosion wastage, Corrosion Science, 63 (2012) 51-58.

[37] J.K. Paik, S.K. Kim, S.K. Lee, Probabilistic corrosion rate estimation model for longitudinal strength members of bulk carriers, Ocean Engineering, 25 (1998) 837-860.

[38] J.K. Paik, J.M. Lee, Y. Park, J.S. Hwang, C.W. Kim, Time-variant ultimate longitudinal strength of corroded bulk carriers, Marine Structures, 16 (2003) 567-600.

[39] Y. Garbatov, I. Vodkadzhiev, C. Guedes Soares, Corrosion wastage assessment of deck structures of bulk carriers, in: Proceedings of the 7th International Conference on Marine Science and Technology, Union of Scientists of Varna, 2004, pp. 24-33.

[40] Y. Garbatov, C. Guedes Soares, Corrosion wastage modelling of deteriorated bulk carrier decks, International Shipbuilding Progress, 55 (2008) 109-125.

[41] S. Harada, N. Yamamoto, A. Magaino, H. Sone, Corrosion analysis and determination of corrosion margin, in: IACS discussion paper, 2001.

[42] J.K. Paik, G. Wang, A.K. Thayamballi, J.M. Lee, Y.I. Park, Time-dependent risk assessment of aging ships accounting for general/pit corrosion, fatigue cracking and local denting damage, in: 2003 SNAME Annual Meeting, San Francisco, 2003.

[43] G. Wang, J. Spencer, H. Sun, Assessment of corrosion risks to aging ships using an experience database, Journal of Offshore Mechanics and Arctic Engineering, 127 (2005) 167-174.

[44] C. Guedes Soares, Y. Garbatov, Reliability of maintained, corrosion protected plates subjected to non-linear corrosion and compressive loads, Marine Structures, 12 (1999) 425-445.

[45] M. Ohyagi, Statistical survey on wear of ship's structural members, in, NK Technical Bulletin, Tokyo, 1987.

[46] A.F. Mateus, J.A. Witz, On the post-buckling of corroded steel plates used in marine structures, RINA Transaction, 140 (1998) 165-183.

[47] J.K. Paik, A.K. Thayamballi, The strength and reliability of bulk carrier structures subject to age and accidental flooding, SNAME Transactions, 106 (1998) 1-40.

[48] J.K. Paik, A.K. Thayamballi, Ultimate strength of ageing ships, Proceedings of the Institution of Mechanical Engineers, Part M: Journal of Engineering for the Maritime Environment, 216 (2002) 57-78.

[49] M. Ahmmad, Y. Sumi, Strength and deformability of corroded steel plates under quasi-static tensile load, Journal of Marine Science and Technology, 15 (2010) 1-15.

[50] N. Yamamoto, K. Ikegami, A study on the degradation of coating and corrosion of ship's hull based on the probabilistic approach, Journal of Offshore Mechanics and Arctic Engineering 120 (1998) 121-128.

[51] N. Yamamoto, Probabilistic corrosion model of ship structural members, in: The IMAS 97: Ships - The Ageing Process, The Institute of Marine Engineers, London, UK, 1997.

[52] Y. Garbatov, C. Guedes Soares, G. Wang, Nonlinear time dependent corrosion wastage of deck plates of ballast and cargo tanks of tankers, Journal of Offshore Mechanics and Arctic Engineering, 129 (2007) 48-55.

[53] L.D. Ivanov, J. Spencer, G. Wang, Probabilistic evaluation of hull structure renewals for aging ships in: Proceedings of the 8th International Marine Design Conference (IMDC), Athens, Greece, 2003, pp. 393-406.

[54] C. Guedes Soares, Y. Garbatov, A. Zayed, Effect of environmental factors on steel plate corrosion under marine immersion conditions, Corrosion Engineering, Science and Technology, 46 (2011) 524-541.

[55] C. Guedes Soares, Y. Garbatov, A. Zayed, G. Wang, Influence of environment factors on corrosion of ship structures in marine atmosphere, Corrosion Science, 51 (2009) 2014-2026.

[56] S. Qin, W. Cui, A discussion of the ultimate strength of ageing ships, with particular reference to the corrosion model, Proceedings of the Institution of Mechanical Engineers, Part M: Journal of Engineering for the Maritime Environment, 216 (2002) 155-160.

[57] S. Qin, W. Cui, A new corrosion model for the deterioration of steel structures in marine environments, in: The 1st International ASRANet Colloquium, 2002.

[58] S. Qin, W. Cui, Effect of corrosion models on the time-dependent reliability of steel plated elements, Marine Structures, 16 (2003) 15-34.

[59] R.E. Melchers, Mathematical modelling of the diffusion controlled phase in marine immersion corrosion of mild steel, Corrosion Science, 45 (2003) 923-940.

[60] R.E. Melchers, Development of new applied models for steel corrosion in marine applications including shipping, Ships and Offshore Structures, 3 (2008) 135-144.

[61] R.E. Melchers, T. Wells, Models for the anaerobic phases of marine immersion corrosion, Corrosion Science, 48 (2006) 1791-1811.

[62] R.E. Melchers, Extreme value statistics and long-term marine pitting corrosion of steel, Probabilistic Engineering Mechanics, 23 (2008) 482-488.

[63] R.E. Melchers, Statistical characterisation of pitting corrosion - 1: Data analysis, Corrosion (NACE), 61 (2005) 655-664.

[64] M.T. Gudze, R.E. Melchers, Operational based corrosion analysis in naval ships, Corrosion Science, 50 (2008) 3296-3307.

[65] R.E. Melchers, Pitting corrosion of mild steel in marine immersion environment - Part 1: Maximum pit depth, Corrosion, 60 (2004) 824-836.

[66] R.E. Melchers, Modelling and prediction of long-term corrosion of steel in marine environments, International Journal of Offshore and Polar Engineering, 22 (2012) 257-263.

[67] R.E. Melchers, Probabilistic models for corrosion in structural reliability assessment - Part 2: models based on mechanics, Transaction of the ASME, 125 (2003) 272-280.

[68] IMO, Performance standard for protective coatings for dedicated seawater ballast tanks in all types of ships and double-side skin spaces of bulk carriers, in: International Maritime Organisation Resolution MSC. 215(82), 2006.

[69] X. Jiang, C. Guedes Soares, Assessment of the uncertainty in corrosion models for ship steels, in: Proceedings of the 27th International Conference on Offshore Mechanics and Arctic Engineering (OMAE 2008), ASME, Estoril, Portugal, 2008.

[70] R. Loseth, G. Sekkesater, S. Valsgard, Economics of high-tensile steel in ship hulls, Marine Structures, 7 (1994) 31-50.

[71] C.P. Gardiner, R.E. Melchers, Bulk carrier corrosion modelling, in: Proceedings of the Eleventh International Offshore and Polar Engineering Conference, Stavanger, Norway, 2001, pp. 609-615.

[72] A.C. Viner, D.R. Tozer, Influence of corrosion on ship structural performance, in: Hull New Construction Division No. 85/29, Lloyd's Register of Shipping, 1985.

[73] RINA, Guide for the structural design of oil tankers, in, The Royal Institution of Naval Architects, 2004.

[74] R.E. Melchers, Effect on marine immersion corrosion of carbon content fo low alloy steels, Corrosion Science, 45 (2003) 2609-2625.

[75] C. Guedes Soares, Y. Garbatov, A. Zayed, G. Wang, Non-linear corrosion model for immersed steel plates accounting for environmental factors, ABS Technical Papers, (2005) 193-211.

[76] Y. Wang, Y. Wang, X. Huang, W. Cui, A simplified maximum pit depth model of mild and low alloy steels in marine immersion environments, Journal of Ship Mechanics, 12 (2008) 401-417.

[77] R.W. Revie, Uhlig's corrosion handbook, 3rd edition, Wiley & Sons, Inc., New Jersey, 2011.

[78] C. Guedes Soares, Y. Garbatov, Reliability of maintained ship hulls subjected to corrosion and fatigue under combined loading, Journal of Constructional Steel Research, 52 (1999) 93-115.

[79] C. Guedes Soares, J.M. Gordo, Compressive strength of rectangular plates under biaxial load and lateral pressure, Thin-Walled Structures, 24 (1996) 231-259.

[80] R.W. Revie, Corrosion and corrosion control, John Wiley, New York, 1985.

[81] L. Korb, D. Olson, Metals Handbook, Corrosion, 13, 9 ed., 1987.

[82] A. Mercer, E. Lumbard, The corrosion of mild steel in water, British Corrosion Journal, (1995) 43-55.

[83] R.E. Melchers, R. Jeffrey, The critical involvement of anaerobic bacterial activity in modelling the corrosion behaviour of mild steel in marine environments, Electrochimica Acta, 54 (2008) 80-85.

[84] R.E. Melchers, Probabilistic models for corrosion in structural reliability assessment - Part 1: empirical models, Transaction of the ASME, 125 (2003) 264-271.

[85] J. Guo, G. Wang, L. Ivanov, A.N. Perakis, Time-varying ultimate strength of aging tanker deck plate considering corrosion effect, Marine Structures, 21 (2008) 402-419.

[86] J.K. Paik, A.K. Thayamballi, Ultimate limit state design of steel-plated structures, John Wiley & Sons, England, 2003.

[87] P.P. Benham, R.J. Crawford, C.G. Armstrong, Mechanics of Engineering Materials: 2nd Edition, Longman Group Limited, London, 1996.

[88] D. Ok, Y. Pu, A. Incecik, Computation of ultimate strength of locally corroded unstiffened plates under uniaxial compression, Marine Structures, 20 (2007) 100-114.

[89] IMO, Performance Standard for Alternative Means of Corrosion Protection for Cargo Oil Tanks of Crude Oil Tankers, in, International Maritime Organisation Resolution MSC.289 (87), 2010.

[90] A.I. Manevich, Effect of strain hardening on the buckling of structural members and design Thin-Walled Structures, 45 (2007) 810-815.

[91] S. Saad-Eldeen, Y. Garbatov, C. Guedes Soares, Effect of corrosion severity on the ultimate strength of a steel box girder, Engineering Structures, 49 (2013) 560-571.

[92] ISSC, Report of Specialist Committee III.1 Ultimate Strength, in: Proceedings of the 17th International Ship and Offshore Structures Congress, Seoul, Korea, 2009, pp. 375-474.

[93] M.R. Khedmati, M.M. Roshanali, Z.H.M.E. Nouri, Strength of steel plates with both-sides randomly distributed with corrosion wastage under uniaxial compression, Thin-Walled Structures, 49 (2011) 325-342.

[94] A. Rahbar-Ranji, Plastic collapse load of corroded steel plates, Sadhana, 37 (2012) 341-349.

[95] Y. Huang, Y. Zhang, G. Liu, Q. Zhang, Ultimate strength assessment of hull structural plate with pitting corrosion damnification under biaxial compression, Ocean Engineering, 37 (2010) 1503-1512.

[96] X. Jiang, C. Guedes Soares, Ultimate capacity of rectangular plates with partial depth pits under uniaxial loads, Marine Structures, 26 (2012) 27-41.

[97] X. Jiang, C. Guedes Soares, A closed form formula to predict the ultimate capacity of pitted mild steel plate under biaxial compression, Thin-Walled Structures, 59 (2012) 27-34.

[98] J.M.R.S. Appuhamy, T. Kaita, M. Ohga, K. Fujii, R. Dissanayake, Experimental and numerical investigation of residual strength of corroded steel plates in tensile force, in: International Symposium on Society for Social Managemenet Systems (SSMS 2010), Kochi, Japan, 2010.

[99] J.M.R.S. Appuhamy, M. Ohga, T. Kaita, R. Dissanayake, Reduction of ultimate strength due to corrosion - A finite element computational method, International Journal of Engineering, 5 (2011) 194-207.

[100] T.E. Dunbar, N. Pegg, F. Taheri, L. Jiang, A computational investigation of the effects of localised corrosion on plates and stiffened panels, Marine Structures, 17 (2004) 385-402.

[101] X. Jiang, C. Guedes Soares, Nonlinear FEM analysis of pitted mild steel square plate subjected to in-plane compression, Journal of Ship Mechanics, 13 (2009) 398-405.

[102] M. Ohga, J.M.R.S. Appuhamy, T. Kaita, K. Fujii, R. Dissanayake, Numerical study on remaining strength prediction of corroded steel bridge plates, in: International Conference on Sustainable Built Environment, Kandy, Sri Lanka, 2010.

[103] S. Saad-Eldeen, C. Guedes Soares, Effect of pitting corrosion on the collapse strength of rectangular plates under axial compression, in: C. Guedes Soares, P.K. Das (Eds.) Analysis and Design of Marine Structures, Taylor & Francis Group, London, UK, 2009.

[104] S. Tamagawa, Y. Kim, Effects of welding residual stress on compressive behaviour and ultimate strength of corroded plate, International Journal of Steel Structures, 10 (2010) 147-155.

[105] M.R. Bahaari, Numerical examination of compressive in-plane strength of corroded plates, in: 4th Structural Specialty Conference of the Canadian Society for Civil Engineering, Montreal, Quebec, Canada, 2002.

[106] M.R. Khedmati, Z.H.M.E. Nouri, M.M. Roshanali, A comparative computational investigation on the effects of randomly distributed general corrosion on the post-buckling behaviour of uniaxially loaded plates, Journal of Mechanical Science and Technology, 26 (2012) 767-783.

[107] T. Nakai, H. Matsushita, N. Yamamoto, Effect of pitting corrosion on the ultimate strength of steel plates subjected to in-plane compression and bending, Journal of Marine Science and Technology, 11 (2006) 52-64.

[108] Z.H.M.E. Nouri, M.R. Khedmati, M.M. Roshanali, Degradation of the compressive strength of unstiffened/stiffened steel plates due to both-sides randomly distributed corrosion wastage, Latin American Journal of Solids and Structures, 7 (2010) 335-367.

[109] M.A.C.E. Silva, Y. Garbatov, C. Guedes Soares, Ultimate strength assessment of rectangular steel plates subjected to a random localised corrosion degradation, Engineering Structures, 52 (2013) 295-305.

[110] M.R. Islam, Y. Sumi, Geometrical effects of pitting corrosion on strength and deformability of steel rectangular plates subjected to uniaxial tension and pure bending, Journal of the Japan Society of Naval Architects and Ocean Engineers, 14 (2011) 9-17.

[111] J.K. Paik, J.M. Lee, M.J. Ko, Ultimate shear strength of plate elements with pit corrosion wastage, Thin-Walled Structures, 42 (2004) 1161-1176.

[112] A. Rahbar-Ranji, Shear buckling strength of corroded steel plates with irregular surfaces, Journal of Zhejiang University-SCIENCE A (Applied Physics & Engineering), (2012) 1-9.

[113] T. Nakai, H. Matsushita, N. Yamamoto, Effect of pitting corrosion on local strength of hold frames of bulk carriers (2nd report) - Lateral-distortional buckling and local face buckling, Marine Structures, 17 (2004) 612-641.

[114] T. Nakai, H. Matsushita, N. Yamamoto, Effect of pitting corrosion on strength of web plates subjected to patch loading, Thin-Walled Structures, 44 (2006) 10-19.

[115] D. Faulkner, A review of effective plating for use in the analysis of stiffened plating in bending and compression, Journal of Ship Research, 19 (1975).

[116] O.F. Hughes, J.K. Paik, Ship structural analysis and design, Society of Naval Architects and Marine Engineers (SNAME), 2010.

[117] D. Ok, Y. Pu, A. Incecik, Artificial neural networks and their application to assessment of ultimate strength of plates with pitting corrosion, Ocean Engineering, 34 (2007) 2222-2230.

[118] Y. Ueda, T. Yao, The influence of complex initial deflection modes on the behaviour and ultimate strength of rectangular plates in compression, Journal of Constructional Steel Research, 5 (1985) 265-302.

[119] C.S. Smith, P.C. Davidson, J.C. Chapman, P.J. Dowling, Strength and stiffness of ships' plating under in-plane compression and tension, RINA, Trans., 130 (1988) 277-296.

[120] M. Kmiecik, The load carrying capacity of axially loaded longitudinally stiffened plates having initial deformation, in: Technical Report No. R80, Ship Research Institute, Trondheim, 1970.

[121] J.J.R. Cheng, A.E. Elwi, G.Y. Grondin, G.L. Kulak, Material testing and residual stress measuremensts in a stiffened steel plate, in: Strength and Stability of Stiffened Plate Components, Ship Structure Committee, Washington, DC, 1996.

[122] ISSC, Report of Specialist Committee III.1 Ultimate Strength, in: Proceedings of the 18th International Ship and Offshore Structures Congress, Rostock, Germany, 2012, pp. 285-363.

[123] ISSC, Report of Specialist Committee III.1 Ultimate Strength, in: Proceedings of the 16th International Ship and Offshore Structures Congress, Southampton, UK, 2006, pp. 353-438.

[124] J.M.R.S. Appuhamy, M. Ohga, T. Kaita, P. Chun, R. Dissanayake, Estimation of corrosion-induced strength deterioration of steel bridge plates – An analytical method, Annual Research Journal of SLSAJ, 11 (2011) 19-25.

[125] J.K. Paik, B.J. Kim, J.K. Seo, Methods for ultimate limit state assessment of ships and ship-shaped offshore structures: Part I - unstiffened plates, Ocean Engineering, 25 (2008) 261-270.

[126] J.K. Paik, B.J. Kim, J.K. Seo, Methods for ultimate limit state assessment of ships and ship-shaped offshore structures: Part II - stiffened panels, Ocean Engineering, 35 (2008) 271-280.

[127] E.M. Gutman, Mechanochemistry of solid surfaces, World Scientific Publishing Co. Pte. Ltd., Singapore, 1994.

[128] W. Chu, R. Ma, C. Hsiao, Stress corrosion cracking of mild streel under compressive stress, National Association of Corrosion Engineers, 43 (1987) 251-254.

[129] X. Liu, G.S. Frankel, Effects of compressive stress on localised corrosion in AA2024-T3`, Corrosion Science, 48 (2006) 3309-3329.

[130] T. Pan, Corrosion behaviour of a duplex stainless steel under cyclic loading: a scanning Kelvin probe force microscopy (SKPFM), Journal of Applied Elctrochemistry, 2012 (2012) 1049-1056.

[131] A.R. Despic, R.G. Raicheff, J.O.M. Bockris, Mechanism of the acceleration of the electrodic dissolution of metals during yielding under stress, The Journal of Chemical Physics, 49 (1968) 926-938.

[132] B.T. Lu, H. Yu, J.L. Luo, Effects of plastic deformation and carbon dioxide on corrosion of pipeline steel in near-neutral pH groundwater, Journal of Materials Engineering and Performance, 22 (2013) 1430-1435.

[133] L.L. Migai, M.A. Vedeneeva, N.P. Zhuk, "Effect of deformation on the corrosion resistance of steel Kh18N10T," Chemical and Petroleum Engineering 7,2 (1971): pp. 133-136.

[134] T.G. Movchan, N.E. Esipova, P.V. Eryukin, N.B. Uriev, A.I. Rusanov, Mechanochemical effects in processes of corrosion of metals, Russian Journal of General Chemistry, 75 (2005) 1681-1686.

[135] S. Zhang, X. Pang, Y. Wang, K. Gao, Corrosion behaviour of steel with different microstructures under various elastic loading conditions, Corrosion Science, 75 (2013) 293-299.

[136] Y.C. Fung, A First Course in Continuum Mechanics (3rd Edition), A Simon & Schuster Componay New Jersey, 1993.

[137] L. Qiao, X. Mao, Thermodynamic analysis on the role of hydrogen in anodic stress corrosion cracking, Acta Metallurgica et Materialia, 43 (1995) 4001-4006.

[138] B.T. Lu, J.L. Luo, P.R. Norton, H.Y. Ma, Effects of dissolved hydrogen and elastic and plastic deformation on active dissolution of pipeline steel in anaerobic groundwater of near-neutral pH, Acta Materialia, 57 (2009) 41-49.

[139] E.M. Gutman, G. Solovioff, D. Eliezer, The mechanochemical behaviour of type 316L stainless steel, Corrosion Science, 38 (1996) 1141-1145.

[140] P.L. Bonora, M. Andrei, A. Eliezer, E.M. Gutman, Corrosion behaviour of stressed magnesium alloys, Corrosion Science, 44 (2002) 729-749.

[141] W. Li, D.Y. Li, Variations of work function and corrosion bahaviours of deformed copper surfaces, Applied Surface Science, 240 (2005) 388-395.

[142] L.Y. Xu, Y.F. Cheng, Corrosion of X100 pipeline steel under plastic strain in a neutral pH bicarbonate solution, Corrosion Science, 64 (2012) 145-152.

[143] L.Y. Xu, Y.F. Cheng, Development of a finite element model for simulation and prediction of mechanoelectrochemical effect of pipeline corrosion, Corrosion Science, 73 (2013) 150-160.

[144] L. Peguet, B. Malki, B. Baroux, Influence of cold working on the pitting corrosion resistance of stainless steels, Corrosion Science, 49 (2007) 1933-1948.

[145] L.T. Han, F. Mansfeld, Scanning Kelvin probe analysis of welded stainless steel, Corrosion Science, 39 (1997) 199-202.

[146] G. Bäck, A. Nazarov, D. Thierry, Localised corrosion of heat-treated and welded stainless steel studied using a scanning Kelvin probe, Corrosion, 61 (2005) 951-960.

[147] F.W. Herbert, K.J. Van-Vliet, B. Yildiz, Plasticity-induced oxidation reactivity on Ni(100) studied by scanning tunneling spectroscopy, MRS Communications, 2 (2012) 23-27.

[148] B. Yildiz, A. Nikiforova, S. Yip, Metallic interfaces in harsh chemo-mechanical environment, Nuclear Engineering and Technology, 41 (2009) 21-38.

[149] J.C. Daidola, J. Parente, M. Rosenblatt & Son, I.R. Orisamolu, K. Ma, Residual strength assessment of pitted plate panels, in, Ship Structure Committee, 1997.

[150] TSFC, Guidelines for the inspection and condition assessment of tanker structures, Tanker Structure Co-operative Forum, 1993.

[151] A.P. Teixeira, C. Guedes Soares, Simulation of inspections on ship plates with random corrosion patterns, Journal of Ship Production, 24 (2008) 168-175.

[152] IMO, Guidelines on procedures for in-service maintenance and repair of coating systems for cargo oil tanks of crude oil tankers, in: International Maritime Organisation Resolution MSC. 1/Circ. 1399, 2011.

[153] J.K. Paik, A.K. Thayamballi, Y.I. Park, J.S. Hwang, A time-dependent corrosion wastage model for seawater ballast tank structures of ships, Corrosion Science, 46 (2003) 471-486.

[154] D.H. Kim, D.K. Park, H.B. Kim, J.K. Seo, B.J. Kim, J.K. Paik, M.S. Kim, The necessity of applying the common corrosion addition rule to container ships in terms of ultiamte longitudinal strength, Ocean Engineering, 49 (2012) 43-55.

[155] LR, Thickness measurement and close-up survey guidance, Lloyd's Register, 2012.

[156] IACS, Common structural rules for double hull oil tankers, International Association of Classification Societies, London, UK, 2006.

[157] LR, Guidance Information - Naval survey guidance for steel ships, Lloyd's Register, 2001.

[158] ANSYS Inc, ANSYS 12.1 Reference Manual, 2009.

[159] W. Thomsen, On the dynamical theory of heat, Transaction of the Royal Society of Edinbourgh, 20 (1853) 261-283.

[160] J.M. Dulieu-Barton, P. Stanley, Development and applications of thermoelastic stress analysis, The Journal of Strain Analysis for Engineering Design, 33 (1998) 93-104.

[161] S.W. Boyd, J.M. Dulieu-Barton, O.T. Thomsen, S. El-Gazzani, Through thickness stress distributions in pultruded GRP materials, Composite Structures, 92 (2010) 662-668.

[162] S.W. Boyd, J.M. Dulieu-Barton, O.T. Thomsen, A. Gherardi, Development of a finite element model for analysis of pultruded structures using thermoelastic data, Composites, 39 (2008) 1311-1321.

[163] Z. Feng, D. Zhang, R.E. Rowlands, B.I. Sandor, Thermoelastic determination of individual stress components in loaded composites, Experimental Mechanics, 1992 (1992) 89-95.

[164] N. Harwood, W.M. Cummings, Thermoelastic stress analysis, IOP Publishing Limited (Adam Hilger), Bristol, 1991.

[165] A.F. Robinson, J.M. Dulieu-Barton, S. Quinn, R.L. Burguete, Paint coating characterisation for thermoelastic stress analysis of metallic materials, Measurement Science and Technology, 21 (2010) 1-11.

[166] T. Hutt, P. Cawley, Feasibility of digital image correlation for detection of cracks at fastener holes, NDT&E International, 42 (2009) 141-149.

[167] J. Kovac, T.J. Marrow, E. Govekar, A. Legat, Detection and characterisation of intergranular stress-corrosion cracking on austenitic stainless steel, Materials and Corrosion, 63 (2012) 664-673.

[168] G. Crammond, S.W. Boyd, J.M. Dulieu-Barton, Evaluating the localised through-thickness load transfer and damage initiation in a composite joint using digital image correlation, Composite: Part A, 61 (2014) 224-234.

[169] V. Savic, L.G. Hector, J.R. Fekete, Digital image correlatino study of plastic deformation and fracture in fully martensitic steels, Experimental Mechanics, 50 (2010) 99-110.

[170] H. Ghadbeigi, C. Pinna, S. Celotto, Quantitative strain analysis of the large deformation at the scale of microstructure: comparison between digital image correlation and microgrid techniques, Experimental Mechanics, 52 (2012) 1483-1492.

[171] T.C. Chu, W.F. Ranson, M.A. Sutton, W.H. Peter, Applications of digital - image - correlation techniques to experimental mechanics, Experimental Mechanics, 25 (1985) 232-244.

[172] M.A. Sutton, J. Orteu, H.W. Schreier, Image correlation for shape, motion and deformation measurements, Springer Science+Business Media, LLC, New York, 2009.

[173] LaVision, DaVis 8.0 Software product manual, 2012.

[174] D.A. Crump, J.M. Dulieu-Barton, J. Savage, Design and commission of an experimental test rig to apply a full-scale pressure load on composite sandwich panels representative of an aircraft secondary structure, Measurement Science and Technology, 21 (2010).

[175] G. Crammond, S.W. Boyd, J.M. Dulieu-Barton, Speckle pattern quality assessment for digital image correlation, Optics and Lasers in Engineering, 51 (2013) 1368-1378.

[176] T. Sakiyama, H. Matsuda, Elastic buckling of rectangular Mindlin plate with mixed boundary conditions, Computers and Structures, 25 (1987) 801-808.

[177] B.C.L. Vanam, M. Rajyalakshmi, R. Inala, Static analysis of an isotropic rectangular plate using finite element analysis (FEA), Journal of Mechanical Engineering Research, 4 (2012) 148-162.

[178] C.M. Wang, Allowance for prebuckling deformations in buckling load relationship between Mindlin and Kirchhoff simply supported plates of general polygonal shape, Engineering Structures, 17 (1995) 413-418.

[179] C.M. Wang, Y. Xiang, J. Chakrabarty, Elastic/plastic buckling of thick plates, International Journal of Solids and Structures, 38 (2001) 8617-8640.

[180] E. Reissner, The effect of transverse shear deformation on the bending of elastic plates, Journal of Applied Mechanics, 12 (1945) A69-A77.

[181] J.K. Paik, J.M. Sohn, Effects of welding residual stresses on high tensile steel plate ultimate strength: nonlinear finite element method investigations, Journal of Offshore Mechanics and Arctic Engineering, 134 (2012) 1-6.

[182] N. Garcia, E. Stoll, Monte carlo calculation of electromagnetic-wave scattering from random rough surfaces, Physical Review Letters, 52 (1984) 1798-1801.

[183] D. Bergström, Rough surface generation and analysis, in MySimLabs, 2007. Available online: http://www.mysimlabs.com/surface_generation.html (Dec 2014).

[184] D.A. Horner, B.J. Connolly, S. Zhou, L. Crocker, A. Turnbull, Novel images of the evolution of stress corrosion cracks from corrosion pits, Corrosion Science 53 (2011) 3466-3485.

[185] M. Cerit, Numerical investigation on torsional stress concentration factor at the semi elliptical corrosion pit, Corrosion Science, 67 (2013) 225-232.

[186] A. Turnbull, L. Wright, L. Crocker, New insight into the pit-to-crack transition from finite element analysis of the stress and strain distribution around a corrosion pit, Corrosion Science, 52 (2010) 1492-1498.

[187] Y. Tajima, S. Rashed, Y. Okumoto, Y. Katayama, H. Murakawa, Prediction of welding distortion and panel bucklign of car carrier decks using database generated by FEA, Transaction of JWRI, 36 (2007) 65-71.

[188] D. Deng, H. Murakawa, FEM prediction of buckling distortion induced by welding in thin plate panel structures, Computational Materials Science, 4 (2008) 591-607.

[189] L. Gannon, Y. Liu, N. Pegg, M.J. Smith, Effect of welding sequence on residual stress and distortion in flat-bar stiffend plates, Marine Structures, 23 (2010) 385-404.

[190] L. Gannon, Y. Liu, N. Pegg, M.J. Smith, Effect of welding-induced residual stress and distortion on ship hull girder ultimate strength, Marine Structures, 28 (2012) 25-49.

[191] M.R. Khedmati, M. Rastani, K. Ghavami, Numerical study on the permissible gap of intermittent fillet welds of longitudinally stiffened plates under in plane axial compression, Journal of Constructional Steel Research, 63 (2007) 1415-1428.

[192] DNV Common structural rules for double hull oil tankers

[193] The Engineer's Handbook: Reference tables – coefficient of friction. Available online: http://www.engineershandbook.com/Tables/frictioncoefficients.htm (Access date: 11/08/2014)

[194] AWS, Structural welding code – steel, D1. 1:2000, American Welding Society, Miami, U.S., 2000.

[195] DNV, Classification Notes No. 30.1: Buckling strength analysis of bars and frames, and spherical shells, DET NORSKE VERITAS, Hovik, Norway, 2004.

Appendices

A1. Matieral compostion for ship grade steels

Table A1.1. Composition of ship grade steels

ASTM	%	C	Mn	Si	P	S	Al	Nb	V	Ti	Cu	Cr	Ni	Mo	N
A	min														
	max	0.21	1.2	0.50	0.035	0.035					0.35		0.3		0.020
B	min		0.8												
	max	0.21	1.2	0.35	0.035	0.035					0.35		0.3		0.020
D	min		0.6												
	max	0.21	1.2	0.35	0.035	0.035					0.35		0.3		0.020
E	min		0.7	0.10											
	max	0.18	1.2	0.35	0.035	0.035					0.35		0.3		0.020
AH32	min		0.9	0.10				0.02	0.05						
	max	0.18	1.6	0.50	0.035	0.035	0.015	0.05	0.10	0.02	0.35	0.2	0.4	0.08	
DH32	min		0.9	0.10				0.02	0.05						
	max	0.18	1.6	0.50	0.035	0.035	0.015	0.05	0.10	0.02	0.35	0.2	0.4	0.08	
EH32	min		0.9	0.10				0.02	0.05						
	max	0.18	1.6	0.50	0.035	0.035	0.015	0.05	0.10	0.02	0.35	0.2	0.4	0.08	
FH32	min		0.9	0.10				0.02	0.05						
	max	0.16	1.6	0.50	0.025	0.025	0.015	0.05	0.10	0.02	0.35	0.2	0.4	0.08	0.009
AH36	min		0.9	0.10				0.02	0.05						
	max	0.18	1.6	0.50	0.035	0.035	0.015	0.05	0.10	0.02	0.35	0.2	0.4	0.08	
DH36	min		0.9	0.10				0.02	0.05						
	max	0.18	1.6	0.50	0.035	0.035	0.015	0.05	0.10	0.02	0.35	0.2	0.4	0.08	
EH36	min		0.9	0.10				0.02	0.05						
	max	0.18	1.6	0.50	0.035	0.035	0.015	0.05	0.10	0.02	0.35	0.2	0.4	0.08	
FH36	min		0.9	0.10				0.02	0.05						
	max	0.16	1.6	0.50	0.025	0.025	0.015	0.05	0.10	0.02	0.35	0.2	0.4	0.08	0.009

A2. Kirchhoff plate theory and Mindlin-Reissner plate theory

Consider a flat rectangular plate of dimensions $a \times b \times t$ being simply supported along four edges and subject to uniform in-plane compressive stresses in the x direction (Figure A2.1). Assume the plate is free to move inwards as a result of the uniform in-plane compressive loading condition. When the plate width to thickness ratio is in the range of 8:1 to 80:1, thin plate theory, which was first proposed by Kirchhoff in 1850, is normally adopted with the effect of transverse shear being neglected. However, when dealing with thick plate (width to thickness ratio $<$ 8:1), the thin plate theory tends to overestimate the buckling loads and underestimate the deflections. Since the shell elements in ANSYS are

generally based on these two plate theories, it is necessary to derive the exact solutions based on both theories for better comparisons.

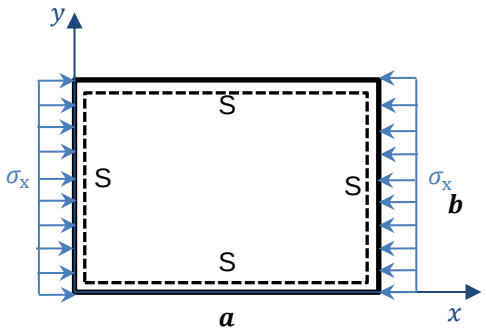

Figure A2.1. Sketch of a plate being simply supported along four edges and subject to uniaxial compressive load.

A2.1 Hypotheses and differential equations

The hypotheses of the Kirchhoff plate theory are [1]:

(1) The material of the plate is elastic, homogenous and isotropic;

(2) Plate thickness t is small compared to the side dimensions;

(3) Stress normal to the middle plane ($z = 0$), is small compared to the other stress components and neglected in the stress-strain relations ($\sigma_z = 0$);

(4) The straight lines which are initially normal to the middle plane before bending remain straight and normal to the middle surface during the deformation, which implies ($\gamma_{xz} = \gamma_{yz} = 0$);

(5) The middle surface remains unstrained ($u(x, y, 0) = v(x, y, 0) = 0$, where u and v are in-plane displacement in the x and y directions respectively);

(6) Change in plate thickness can be neglected and normally undergo no extension ($\varepsilon_z = 0$).

Since $\gamma_{xz} = \gamma_{yz} = 0$, the physical equations for Kirchhoff plates can be reduced to:

$$\sigma_x = \frac{E}{1-\nu^2}\left(\varepsilon_x + \nu\varepsilon_y\right) \tag{1}$$

$$\sigma_y = \frac{E}{1-\nu^2}\left(\varepsilon_y + \nu\varepsilon_x\right) \tag{2}$$

$$\tau_{xy} = \frac{E}{2(1+\nu)}\gamma_{xy} \tag{3}$$

In terms of the geometrical equations, since

$$\gamma_{\mathrm{xz}} = \frac{\partial u}{\partial z} + \frac{\partial w}{\partial x} = 0 \tag{4}$$

$$\gamma_{\mathrm{yz}} = \frac{\partial v}{\partial z} + \frac{\partial w}{\partial y} = 0 \tag{5}$$

where w is the transverse displacement in the z-direction. Integrate the two equations (4) and (5), and the displacements u and v can be expressed as:

$$u = -\frac{\partial w}{\partial x} z + f_1(x, y) \tag{6}$$

$$v = -\frac{\partial w}{\partial y} z + f_2(x, y) \tag{7}$$

where f_1 and f_2 are random functions. Due to the assumption $u(x, y, 0) = v(x, y, 0) = 0$, it can be seen that $f_1(x, y) = f_2(x, y) = 0$. Thus,

$$u = -\frac{\partial w}{\partial x} z \tag{8}$$

$$v = -\frac{\partial w}{\partial y} z \tag{9}$$

The geometrical equations for Kirchhoff plates are:

$$\varepsilon_{\mathrm{x}} = \frac{\partial u}{\partial x} = -\frac{\partial^2 w}{\partial x^2} z \tag{10}$$

$$\varepsilon_{\mathrm{y}} = \frac{\partial v}{\partial y} = -\frac{\partial^2 w}{\partial y^2} z \tag{11}$$

$$\gamma_{\mathrm{xy}} = \frac{\partial v}{\partial x} + \frac{\partial u}{\partial y} = -2\frac{\partial^2 w}{\partial xy} z \tag{12}$$

The main difference between the Mindlin plate theory [2] and the Kirchhoff plate theory is the allowance of the normal (a vector that is perpendicular to the tangent plane to the plate surface) undergoing constant rotations about the middle surface while maintaining straightness. Therefore, a constant shear strain is assumed through the thickness of the plate, and the displacement fields become:

$$u = z\phi_{\mathrm{x}} \tag{13}$$

$$v = z\phi_{\mathrm{y}} \tag{14}$$

$$w = w(x, y, 0) \tag{15}$$

where ϕ_{x} and ϕ_{y} are the rotation rates about y-and x-axes, respectively. Therefore, the geometrical equations for Mindlin plates are:

$$\varepsilon_{\mathrm{x}} = \frac{\partial u}{\partial x} = z\frac{\partial \phi_{\mathrm{x}}}{\partial x} \tag{16}$$

$$\varepsilon_{\mathrm{y}} = \frac{\partial v}{\partial y} = z\frac{\partial \phi_{\mathrm{y}}}{\partial y} \tag{17}$$

$$\gamma_{\mathrm{xy}} = \frac{\partial v}{\partial x} + \frac{\partial u}{\partial y} = z\left(\frac{\partial \phi_{\mathrm{y}}}{\partial x} + \frac{\partial \phi_{\mathrm{x}}}{\partial y}\right) \tag{18}$$

$$\gamma_{\mathrm{xz}} = \frac{\partial u}{\partial z} + \frac{\partial w}{\partial x} = \phi_{\mathrm{x}} + \frac{\partial w}{\partial x} \tag{19}$$

$$\gamma_{\mathrm{yz}} = \frac{\partial v}{\partial z} + \frac{\partial w}{\partial y} = \phi_{\mathrm{y}} + \frac{\partial w}{\partial y} \tag{20}$$

Note that by setting $\phi_{\mathrm{x}} = -\partial w/\partial x$ and $\phi_{\mathrm{y}} = -\partial w/\partial y$, the equations above will be simplified as those for Kirchhoff plates. To compensate for the actual transverse shear strain distribution being parabolic through the thickness, a shear correction factor κ^2 was proposed by Mindlin [2]. Accordingly, the physical equations for Mindlin plates become [3]:

$$\sigma_{\mathrm{x}} = \frac{E}{1-\nu^2}\left(\varepsilon_{\mathrm{x}} + \nu\varepsilon_{\mathrm{y}}\right) \tag{21}$$

$$\sigma_{\mathrm{y}} = \frac{E}{1-\nu^2}\left(\varepsilon_{\mathrm{y}} + \nu\varepsilon_{\mathrm{x}}\right) \tag{22}$$

$$\tau_{\mathrm{xy}} = G\gamma_{\mathrm{xy}} \tag{23}$$

$$\tau_{\mathrm{xz}} = \kappa^2 G\gamma_{\mathrm{xz}} \tag{24}$$

$$\tau_{\mathrm{yz}} = \kappa^2 G\gamma_{\mathrm{yz}} \tag{25}$$

where $G = E/2(1+\nu)$ is the shear modulus. In order to illustrate the force (moment) and stress components over a cross-section of a plate, consider a parallelepiped taken from the plate with the three dimensions being dx, dy and t (Figure A2.2).

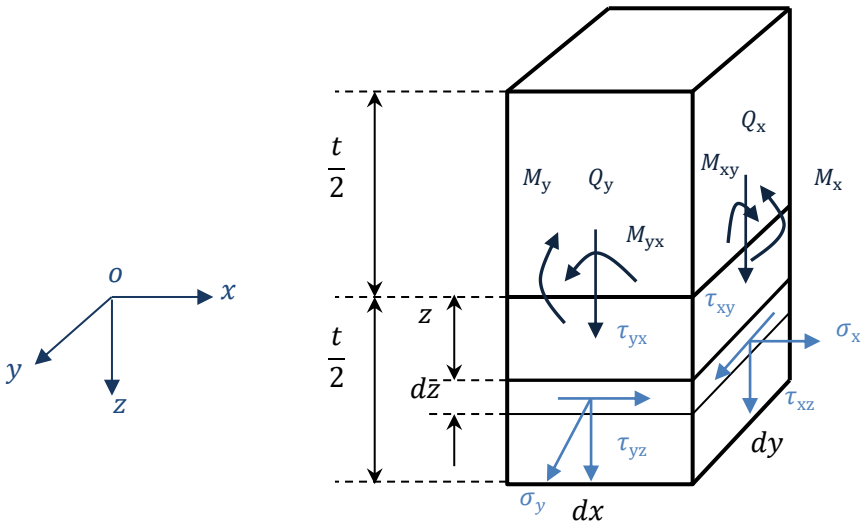

Figure A2.2. Distribution of force/moment and stress (in blue) components.

The values of the moment components per unit width or length can be expressed as:

$$M_{\mathrm{x}} = \int_{-\frac{t}{2}}^{\frac{t}{2}} \sigma_{\mathrm{x}} z dz \tag{26}$$

$$M_{\mathrm{y}} = \int_{-\frac{t}{2}}^{\frac{t}{2}} \sigma_{\mathrm{y}} z dz \tag{27}$$

$$M_{\mathrm{xy}} = M_{\mathrm{yx}} = \int_{-\frac{t}{2}}^{\frac{t}{2}} \tau_{\mathrm{xy}} z dz \tag{28}$$

Similarly, the transverse shear forces can be written as:

$$Q_{\mathrm{x}} = \int_{-\frac{t}{2}}^{\frac{t}{2}} \tau_{\mathrm{xz}} dz \tag{29}$$

$$Q_{\mathrm{y}} = \int_{-\frac{t}{2}}^{\frac{t}{2}} \tau_{\mathrm{yz}} dz \tag{30}$$

A2.2 Governing equations

Figure A2.3 shows an infinitesimal area indicating the middle surface of a plate under the equilibrium condition. Governing equations can be obtained by resolving the equilibrium equations of forces and moments.

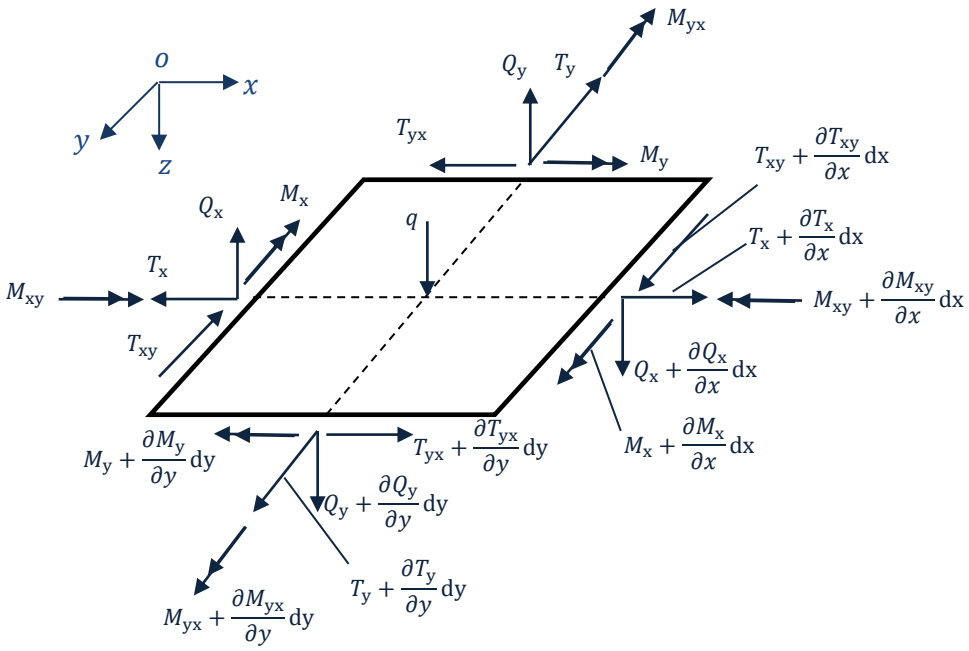

Figure A2.3. Schematic of the middle surface of a plate under equilibrium condition.

By constructing the force equilibrium in x and y directions, a differentiation equation can be derived for Kirchhoff plates:

$$D\nabla^4 w - \left(T_{\mathrm{x}}\frac{\partial^2 w}{\partial x^2} + 2T_{\mathrm{xy}}\frac{\partial^2 w}{\partial xy} + T_{\mathrm{y}}\frac{\partial^2 w}{\partial y^2}\right) = q \tag{31}$$

where $D = Et^3/12(1-\nu^2)$, which is the flexural rigidity of a plate; ∇^4 is the differential operator given by $\nabla^4 = \partial^4/\partial x^4 + 2\,\partial^4/\partial x^2\partial y^2 + \partial^4/\partial y^4$; T_{x} and T_{y} are the in-plane tensile forces in x and y directions, respectively; T_{xy} is shear force along the edges and q is the external transverse load. Energy (Ritz) method is used for Mindlin plate analysis due to its simplicity in implementation. According to Chakrabarty [208], the strain energy of a Mindlin plate is:

$$U = \frac{1}{2}\int \left(\sigma_{\mathrm{x}}\varepsilon_{\mathrm{x}} + \sigma_{\mathrm{y}}\varepsilon_{\mathrm{y}} + \tau_{\mathrm{xy}}\gamma_{\mathrm{xy}} + \tau_{\mathrm{xz}}\gamma_{\mathrm{xz}} + \tau_{\mathrm{yz}}\gamma_{\mathrm{yz}}\right)dV \tag{32}$$

Substitute Equations (16) to (25) into the Equation (32), and integrate through the thickness, the strain energy can be rewritten as:

$$U = \frac{1}{2}\iint \left\{ \frac{Et^3}{12(1-\nu^2)}\left(\frac{\partial \phi_x}{\partial x}\right)^2 + \frac{Et^3}{12(1-\nu^2)}\left(\frac{\partial \phi_y}{\partial y}\right)^2 + \frac{E\nu t^3}{6(1-\nu^2)}\left(\frac{\partial \phi_x}{\partial x}\right)\left(\frac{\partial \phi_y}{\partial y}\right) + \frac{Gt^3}{12}\left(\frac{\partial \phi_x}{\partial y} + \frac{\partial \phi_y}{\partial x}\right)^2 + \kappa^2 Gt\left[\left(\phi_x + \frac{\partial w}{\partial x}\right)^2 + \left(\phi_y + \frac{\partial w}{\partial y}\right)^2\right]\right\} dx\, dy \quad (33)$$

The potential energy for the plate subject to uniform in-plane compressive stresses is given by:

$$V = -\frac{1}{2}\iint \left[\sigma_x t\left(\frac{\partial w}{\partial x}\right)^2 + \sigma_y t\left(\frac{\partial w}{\partial y}\right)^2 + 2\tau_{xy}\left(\frac{\partial w}{\partial x}\right)\left(\frac{\partial w}{\partial y}\right)\right] dx\, dy \quad (34)$$

The total energy is:

$$\Pi = U + V \quad (35)$$

The governing equations can be derived by minimising the total energy function with respect to arbitrary variation of w, ϕ_x and ϕ_y:

$$\frac{\partial \Pi}{\partial w} = 0 \quad (36)$$

$$\frac{\partial \Pi}{\partial \phi_x} = 0 \quad (37)$$

$$\frac{\partial \Pi}{\partial \phi_y} = 0 \quad (38)$$

Three governing equations are generated:

$$\kappa^2 Gt\left(\frac{\partial \phi_x}{\partial x} + \frac{\partial \phi_y}{\partial y} + \nabla^2 w\right) - \sigma_x t\frac{\partial^2 w}{\partial x^2} - \sigma_y t\frac{\partial^2 w}{\partial y^2} - 2\tau_{xy} t\frac{\partial^2 w}{\partial x \partial y} = 0 \quad (39)$$

$$\frac{\partial}{\partial x}\left[\frac{Et^3}{12(1-\nu^2)}\frac{\partial \phi_x}{\partial x} + \frac{E\nu t^3}{12(1-\nu^2)}\frac{\partial \phi_y}{\partial y}\right] - \kappa^2 Gt\left(\phi_x + \frac{\partial w}{\partial x}\right) + \frac{\partial}{\partial y}\left[\frac{Gt^3}{12}\left(\frac{\partial \phi_x}{\partial y} + \frac{\partial \phi_y}{\partial x}\right)\right] = 0 \quad (40)$$

$$\frac{\partial}{\partial y}\left[\frac{Et^3}{12(1-\nu^2)}\frac{\partial \phi_y}{\partial y} + \frac{E\nu t^3}{12(1-\nu^2)}\frac{\partial \phi_x}{\partial x}\right] - \kappa^2 Gt\left(\phi_y + \frac{\partial w}{\partial y}\right) + \frac{\partial}{\partial x}\left[\frac{Gt^3}{12}\left(\frac{\partial \phi_x}{\partial y} + \frac{\partial \phi_y}{\partial x}\right)\right] = 0 \quad (41)$$

where ∇^2 is the Laplacian operator, defined as $\nabla^2 = \partial^2/\partial x^2 + \partial^2/\partial y^2$.

A2.3 Boundary conditions

Based on the Saint-Venant principle, the stress components through the plate thickness are studied in order to satisfy the boundary conditions. For simply supported rectangular plates (Figure A2.1 and Figure A2.2), the boundary conditions are:

$$w(0,y) = M_{\mathrm{x}}(0,y) = \phi_{\mathrm{y}}(0,y) = 0$$
$$w(x,0) = M_{\mathrm{y}}(x,0) = \phi_{\mathrm{x}}(x,0) = 0$$
$$w(a,y) = M_{\mathrm{x}}(a,y) = \phi_{\mathrm{y}}(a,y) = 0$$
$$w(x,b) = M_{\mathrm{y}}(x,b) = \phi_{\mathrm{x}}(x,b) = 0$$

A2.4 Critical buckling load

The displacement and rotations are assumed as follows, in order to satisfy the boundary conditions stated above:

$$w = \sum_{m=1}^{\infty}\sum_{n=1}^{\infty} A_{\mathrm{mn}}^{w} \sin\frac{m\pi x}{a}\sin\frac{n\pi y}{b} \tag{42}$$

$$\phi_{\mathrm{x}} = \sum_{m=1}^{\infty}\sum_{n=1}^{\infty} A_{\mathrm{mn}}^{\phi_{\mathrm{x}}} \cos\frac{m\pi x}{a}\sin\frac{n\pi y}{b} \tag{43}$$

$$\phi_{\mathrm{y}} = \sum_{m=1}^{\infty}\sum_{n=1}^{\infty} A_{\mathrm{mn}}^{\phi_{\mathrm{y}}} \sin\frac{m\pi x}{a}\cos\frac{n\pi y}{b} \tag{44}$$

where A_{mn}^{w}, $A_{\mathrm{mn}}^{\phi_{\mathrm{x}}}$ and $A_{\mathrm{mn}}^{\phi_{\mathrm{y}}}$ are constants. Note that for the case considered in Figure A2.1, $\sigma_{\mathrm{y}} = \tau_{\mathrm{xy}} = T_{\mathrm{y}} = T_{\mathrm{xy}} = q = 0$. For Kirchhoff plates, by substituting Equation (42) into Equation (31), it can be derived that:

$$D\left(\frac{m^2}{a^2} + \frac{n^2}{b^2}\right)^2 - T_{\mathrm{x}}\frac{m^2}{\pi^2 a^2} = 0 \tag{45}$$

i.e.,

$$\overline{T_{\mathrm{cr}}} = \frac{\pi^2 a^2 D}{m^2}\left(\frac{m^2}{a^2}+\frac{n^2}{b^2}\right)^2 = k\frac{\pi^2 D}{b^2} \tag{46}$$

where $k = [mb/a + an^2/(mb)]^2$, is defined as the buckling factor, and is independent of the plate shape. Given $\overline{T_{\mathrm{cr}}}$ is the critical in-plane load along the plate edge per unit length, the total critical buckling load can be derived as:

$$T_{\mathrm{cr\ (Kirchhoff)}} = k\frac{\pi^2 D}{b} \tag{47}$$

For Mindlin plates, the substitution of Equations (42) to (44) into the governing Equations (39) to (41) leads to:

$$\begin{bmatrix} C_{11} & C_{12} & C_{13} \\ C_{12} & C_{22} & C_{23} \\ C_{13} & C_{23} & C_{33} \end{bmatrix} \begin{Bmatrix} A^{w}_{\mathrm{mn}} \\ A^{\phi_{\mathrm{x}}}_{\mathrm{mn}} \\ A^{\phi_{\mathrm{y}}}_{\mathrm{mn}} \end{Bmatrix} = \begin{Bmatrix} 0 \\ 0 \\ 0 \end{Bmatrix} \tag{48}$$

where

$$C_{11} = \kappa^2 Gt\left(\frac{m^2\pi^2}{a^2}+\frac{n^2\pi^2}{b^2}\right) - \sigma_{\mathrm{x}} t\left(\frac{m^2\pi^2}{a^2}\right)$$

$$C_{12} = \kappa^2 Gt\left(\frac{m\pi}{a}\right)$$

$$C_{13} = \kappa^2 Gt\left(\frac{n\pi}{b}\right)$$

$$C_{22} = \frac{Et^3}{12(1-\nu^2)}\left(\frac{m^2\pi^2}{a^2}\right) + \frac{Gt^3}{12}\left(\frac{n^2\pi^2}{b^2}\right) + \kappa^2 Gt$$

$$C_{23} = \left[\frac{E\nu t^3}{12(1-\nu^2)} + \frac{Gt^3}{12}\right]\left(\frac{mn\pi^2}{ab}\right)$$

$$C_{33} = \frac{Et^3}{12(1-\nu^2)}\left(\frac{n^2\pi^2}{b^2}\right) + \frac{Gt^3}{12}\left(\frac{m^2\pi^2}{a^2}\right) + \kappa^2 Gt$$

The total critical buckling load can be determined by deriving the non-trivial solution of the matrix $[C]$ in Equation (48) and thus the value can be expressed as:

$$T_{\mathrm{cr\ (Mindlin)}} = \frac{k\pi^2 Db}{b^2 + \dfrac{kt^2\pi^2}{6\kappa^2(1-\nu)}} \tag{49}$$

References:

[1] S. Timoshenko, S. Woinowsky-Krieger, Theory of plates and shells, McGraw-Hill, New York, 1959.

[2] R.D. Mindlin, Influence of rotatory intertia and shear on flexural motions of isotropic, elastic plates, Transaction of ASME, Journal of Applied Mechanics, 18 (1951) 31-38.

[3] J. Chakrabarty, Applied plasticity, 2nd ed., Springer, New York, USA, 2010.

A3. Plate models

Supplementary results for the studies in Chapter 5 are presented in this section.

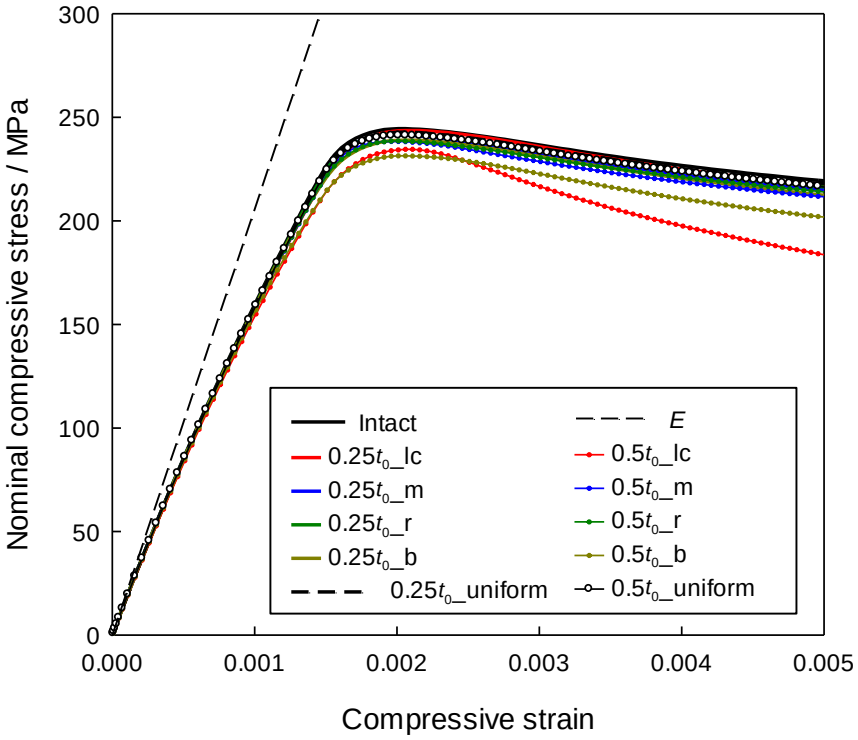

Figure A3.1. Nominal compressive stress-strain relationships (DOP = 2%; pit depth = 0.25t_0 and 0.5t_0) (lc: corrosion at the corner; m: corrosion in the middle; r: random pitting; b: corrosion at the unloaded edge; *E*: Young's modulus of the material).

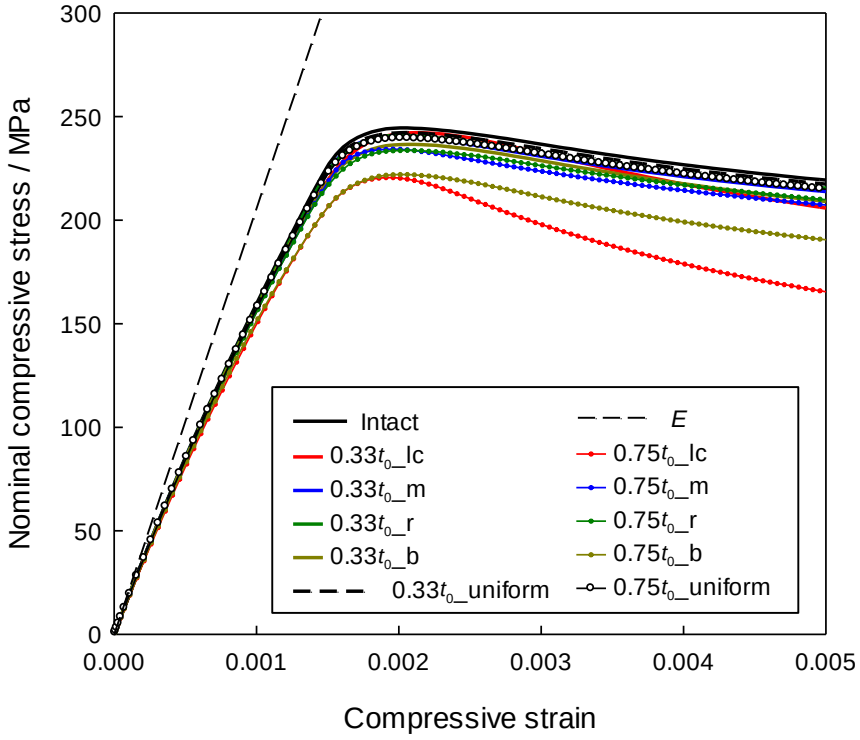

Figure A3.2. Nominal compressive stress-strain relationships (DOP = 2%; pit depth = 0.33t_0 and 0.75t_0) (lc: corrosion at the corner; m: corrosion in the middle; r: random pitting; b: corrosion at the unloaded edge; *E*: Young's modulus of the material).

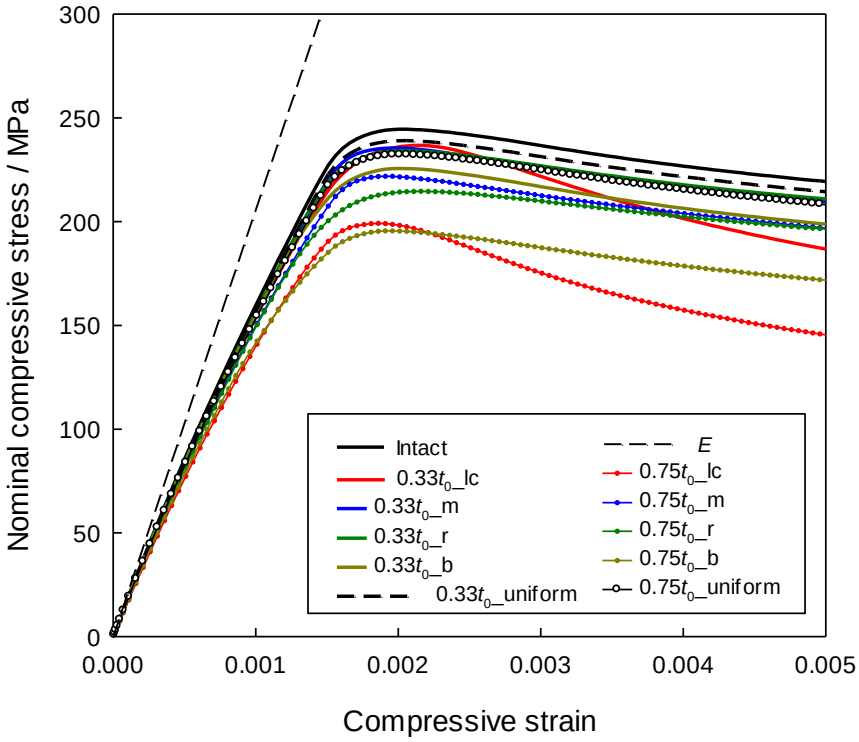

Figure A3.3. Nominal compressive stress-strain relationships (DOP = 5%; pit depth = 0.33t_0 and 0.75t_0) (lc: corrosion at the corner; m: corrosion in the middle; r: random pitting; b: corrosion at the unloaded edge; *E*: Young's modulus of the material).

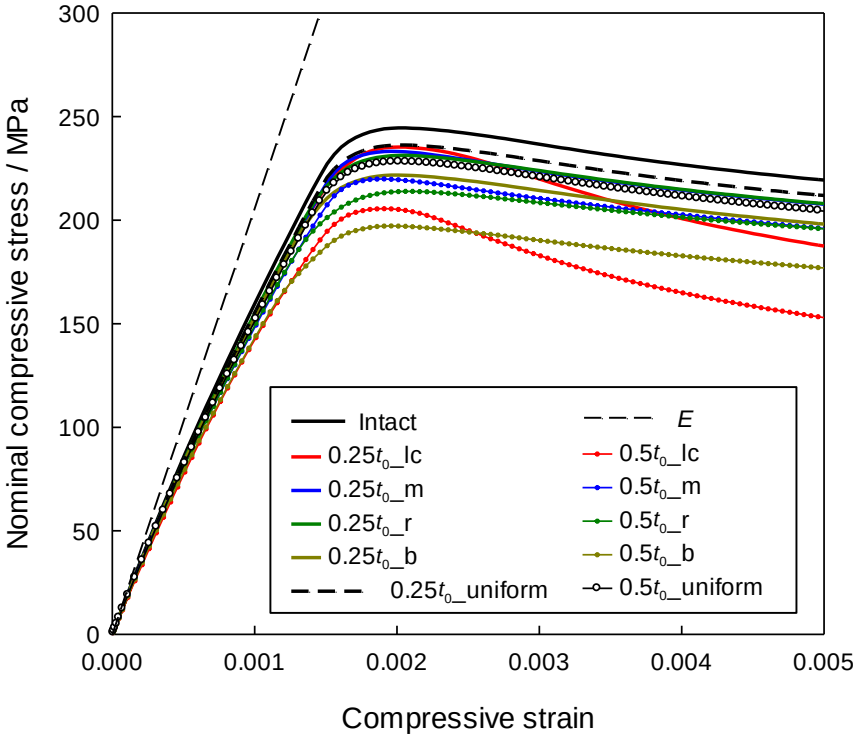

Figure A3.4. Nominal compressive stress-strain relationships (DOP = 10%; pit depth = 0.25t_0 and 0.5t_0) (lc: corrosion at the corner; m: corrosion in the middle; r: random pitting; b: corrosion at the unloaded edge; *E*: Young's modulus of the material).

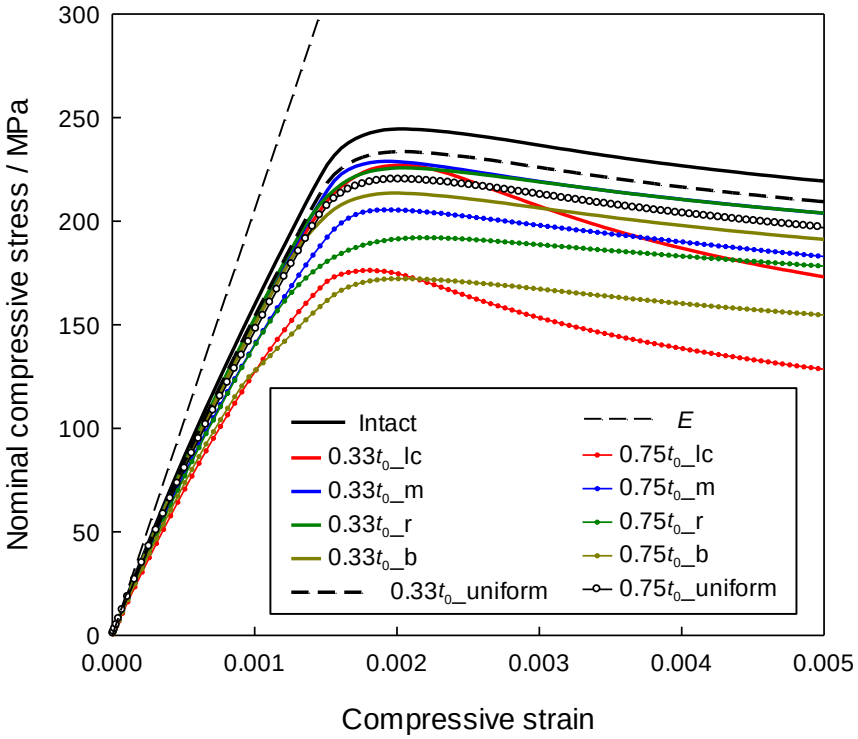

Figure A3.5. Nominal compressive stress-strain relationships (DOP = 10%; pit depth = 0.33t_0 and 0.75t_0) (lc: corrosion at the corner; m: corrosion in the middle; r: random pitting; b: corrosion at the unloaded edge; *E*: Young's modulus of the material).

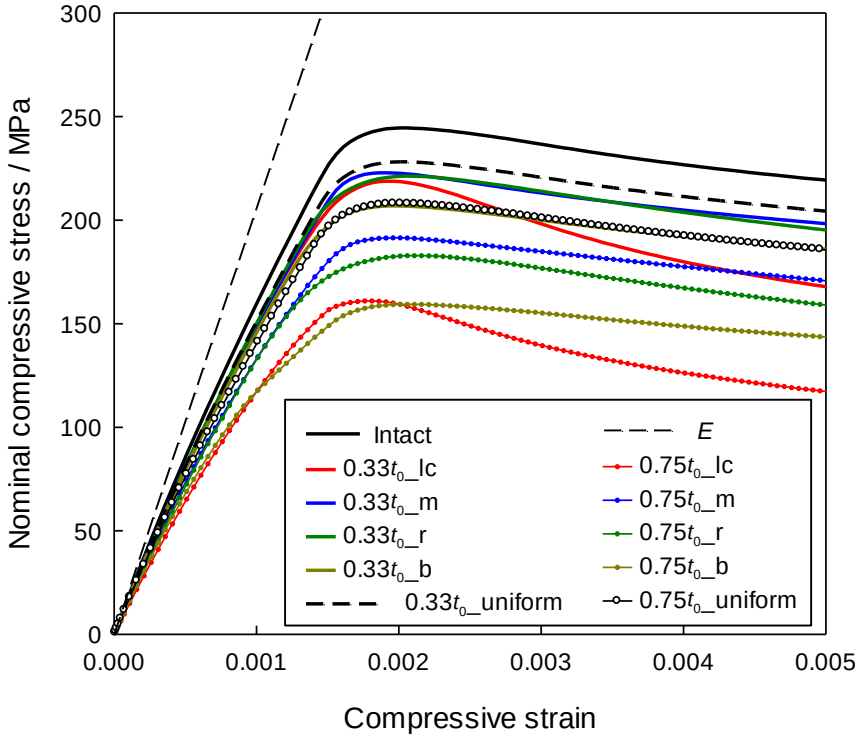

Figure A3.6. Nominal compressive stress-strain relationships (DOP = 15%; pit depth = 0.33t_0 and 0.75t_0) (lc: corrosion at the corner; m: corrosion in the middle; r: random pitting; b: corrosion at the unloaded edge; *E*: Young's modulus of the material).

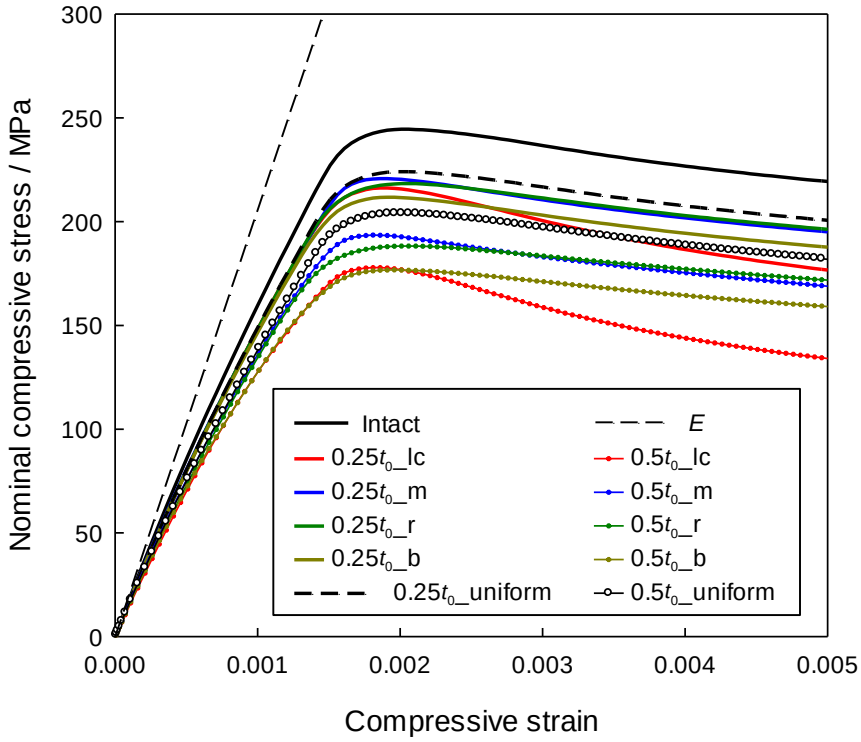

Figure A3.7. Nominal compressive stress-strain relationships (DOP = 25%; pit depth = 0.25t_0 and 0.5t_0) (lc: corrosion at the corner; m: corrosion in the middle; r: random pitting; b: corrosion at the unloaded edge; *E*: Young's modulus of the material).

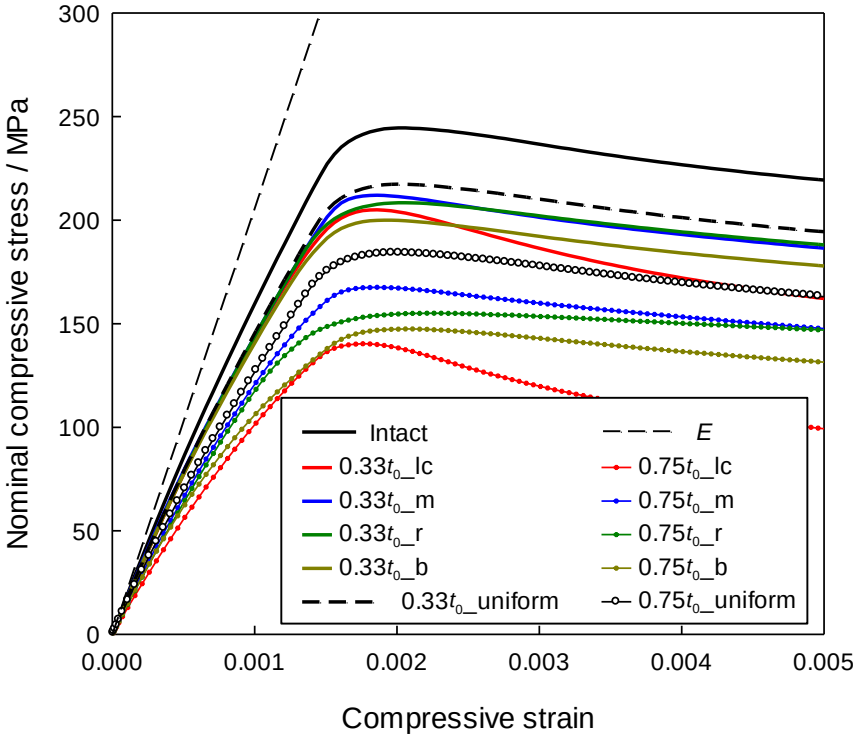

Figure A3.8. Nominal compressive stress-strain relationships (DOP = 25%; pit depth = 0.33t_0 and 0.75t_0) (lc: corrosion at the corner; m: corrosion in the middle; r: random pitting; b: corrosion at the unloaded edge; *E*: Young's modulus of the material).

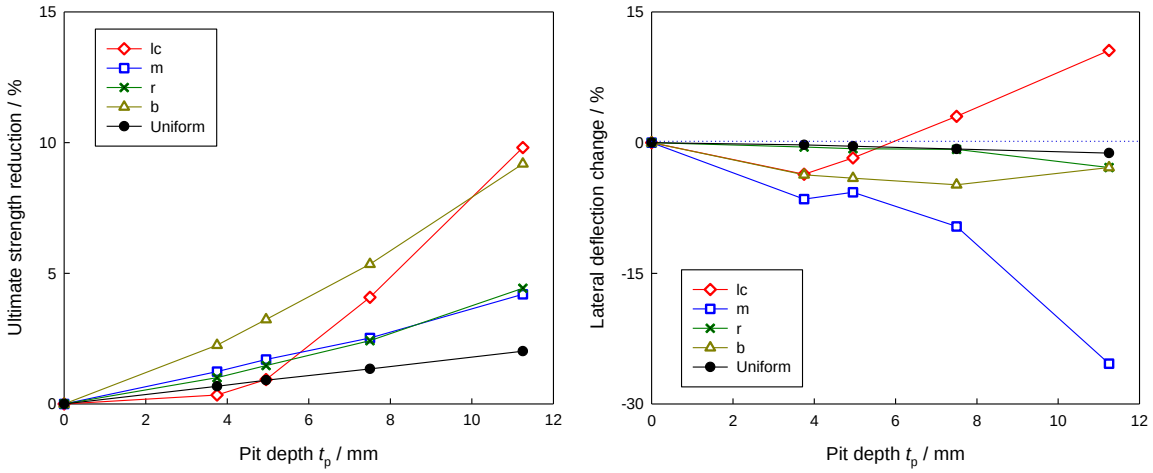

Figure A3.9. Normalised ultimate strength and lateral deflection reductions (DOP = 2%) (lc: corrosion at the corner; m: corrosion in the middle; r: random pitting; b: corrosion at the unloaded edge).

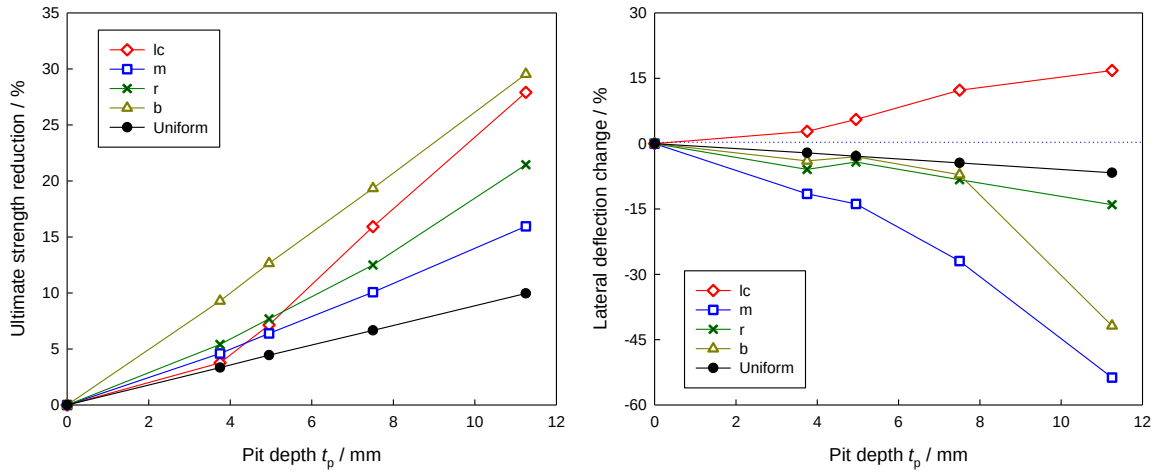

Figure A3.10. Normalised ultimate strength and lateral deflection reductions (DOP = 10%) (lc: corrosion at the corner; m: corrosion in the middle; r: random pitting; b: corrosion at the unloaded edge).

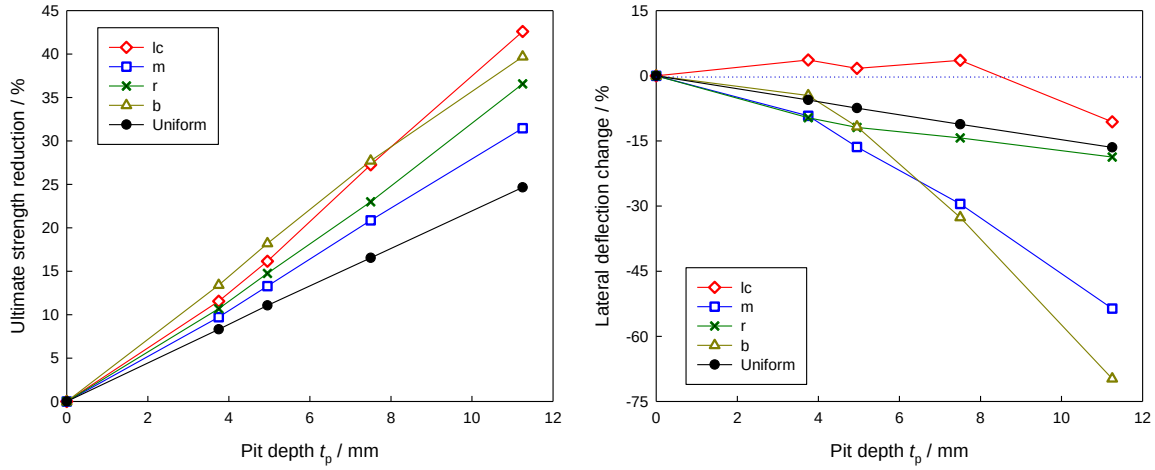

Figure A3.11. Normalised ultimate strength and lateral deflection reductions (DOP = 25%) (lc: corrosion at the corner; m: corrosion in the middle; r: random pitting; b: corrosion at the unloaded edge).

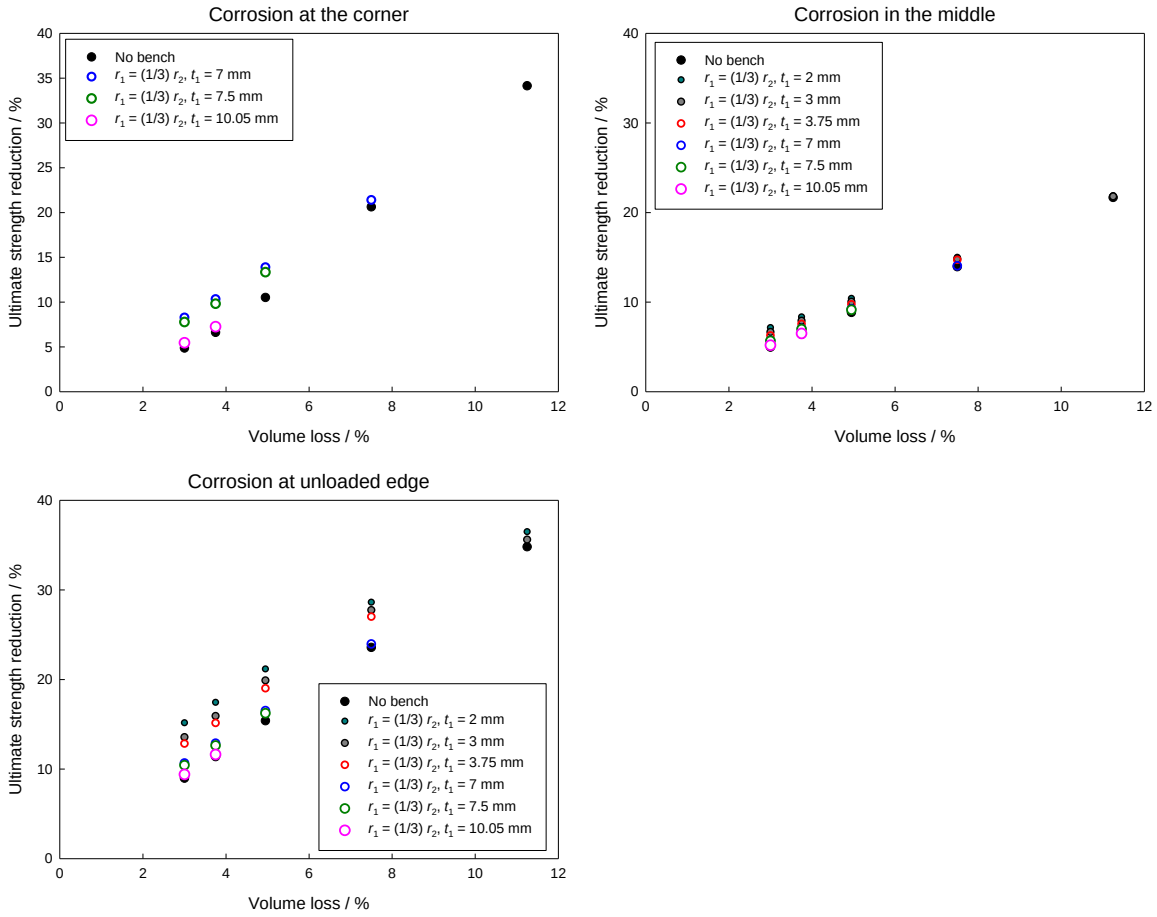

Figure A3.12: Normalised ultimate strength reduction for bench-shape pit study (DOP = 15%; r_1 = (1/3) r_2): (a) corrosion at the corner; (b) corrosion in the middle; (c) corrosion at the unloaded edge.

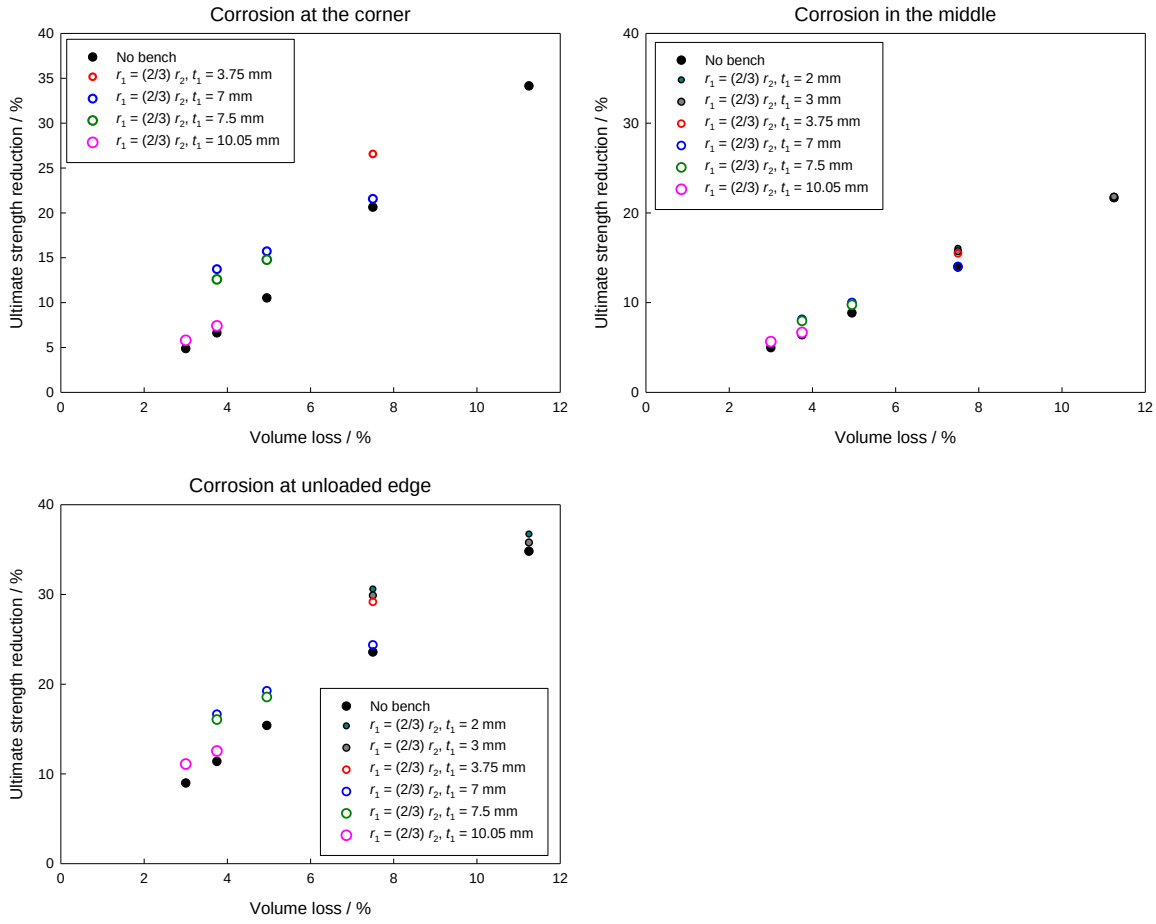

Figure A3.13: Normalised ultimate strength reduction for bench-shape pit study (DOP = 15%; r_1 = (2/3) r_2): (a) corrosion at the corner; (b) corrosion in the middle; (c) corrosion at the unloaded edge.

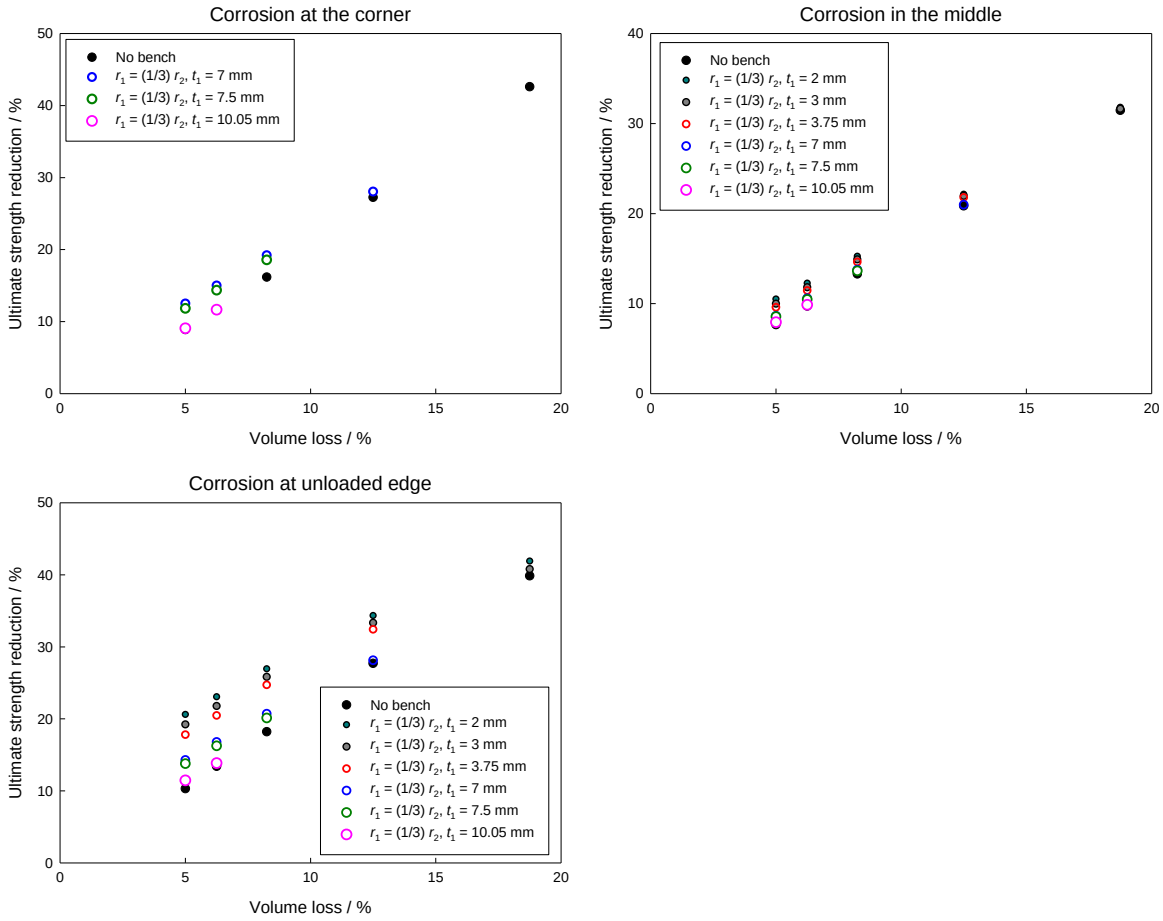

Figure A3.14: Normalised ultimate strength reduction for bench-shape pit study (DOP = 25%; r_1 = (1/3) r_2): (a) corrosion at the corner; (b) corrosion in the middle; (c) corrosion at the unloaded edge.

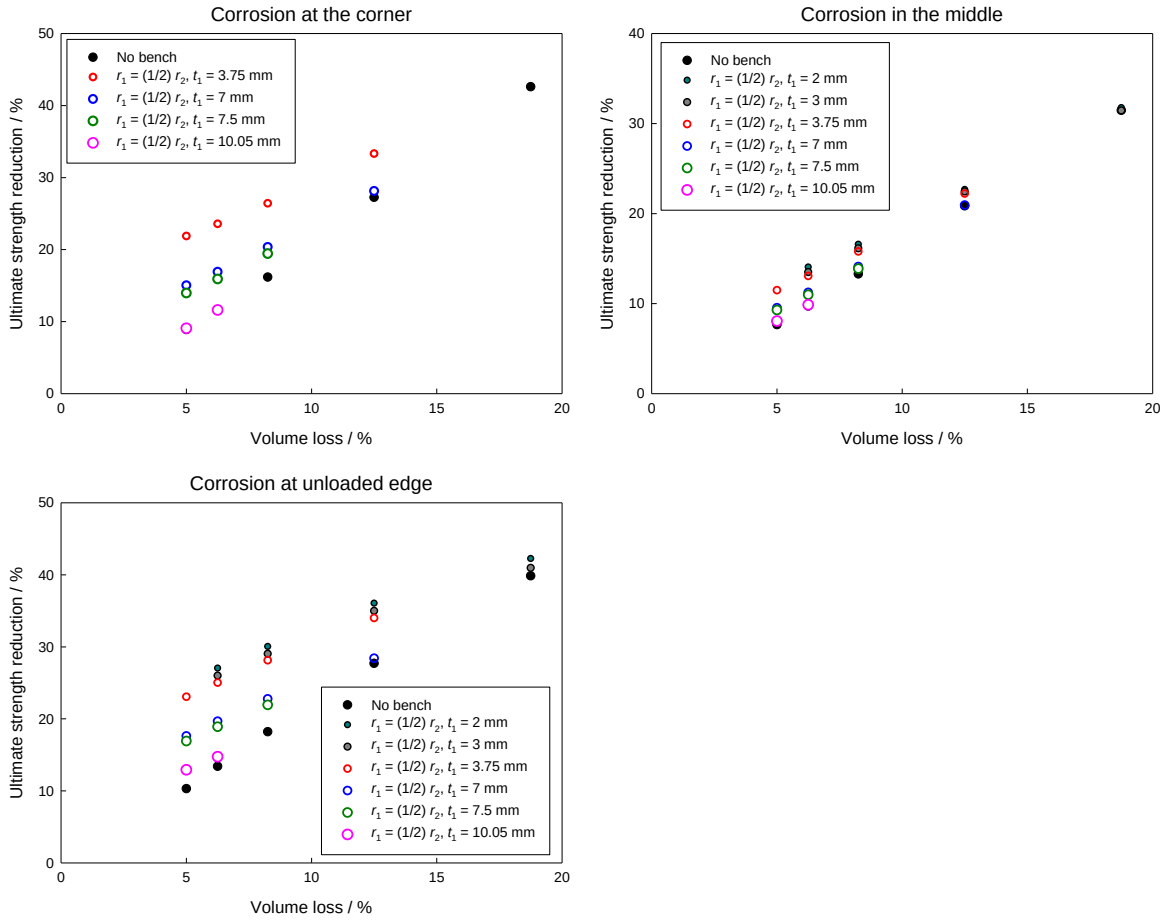

Figure A3.15: Normalised ultimate strength reduction for bench-shape pit study (DOP = 25%; r_1 = (1/2) r_2): (a) corrosion at the corner; (b) corrosion in the middle; (c) corrosion at the unloaded edge.

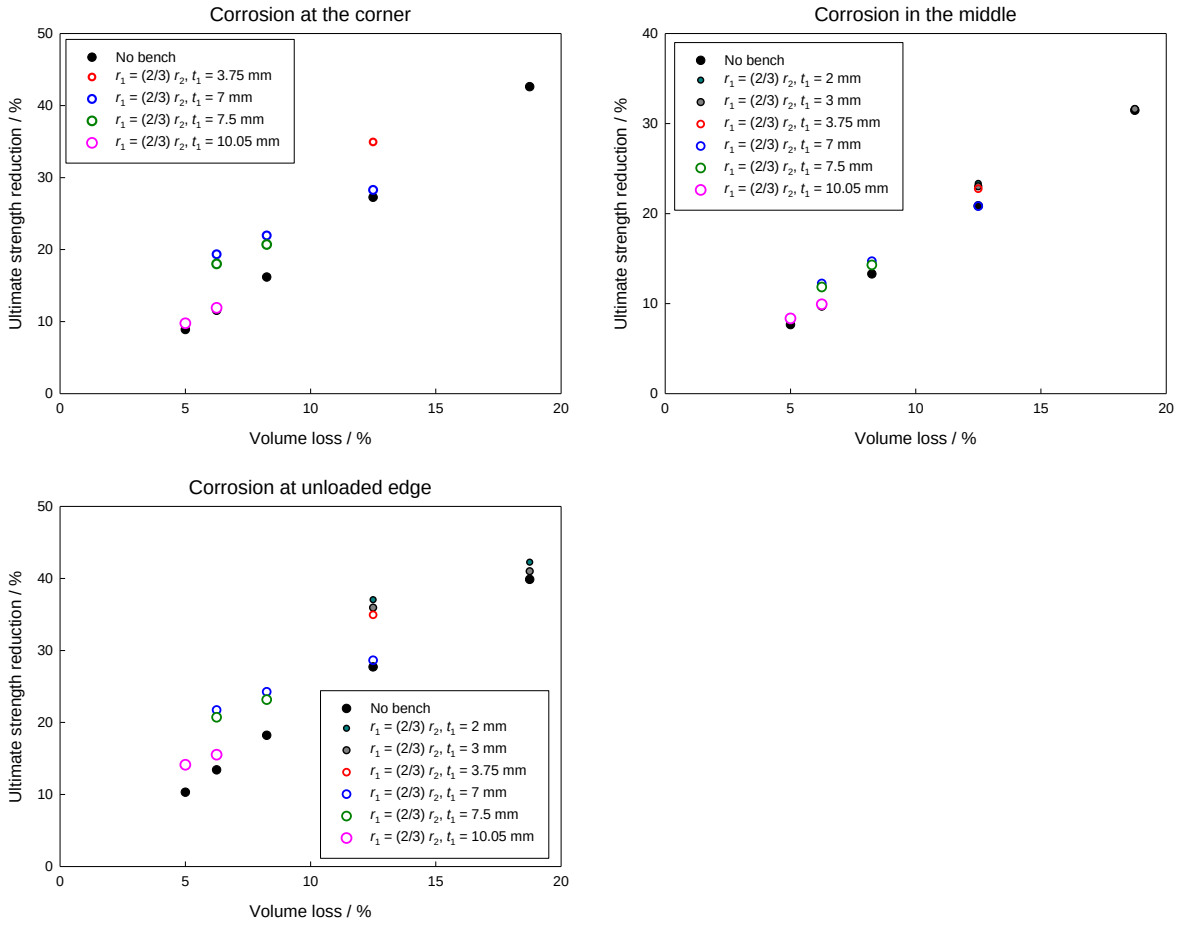

Figure A3.16: Normalised ultimate strength reduction for bench-shape pit study (DOP = 25%; r_1 = (2/3) r_2): (a) corrosion at the corner; (b) corrosion in the middle; (c) corrosion at the unloaded edge.

A4. Initial deflections of DIC specimens

The initial deformations of DIC specimens were measured using a Faro Arm at discrete locations and presented in Figure A4.1. Since the much finer mesh was used for the numerical models, surface fitting was conducted to generate more deformation data points over the specimen surfaces, as shown in Figure A4.2.

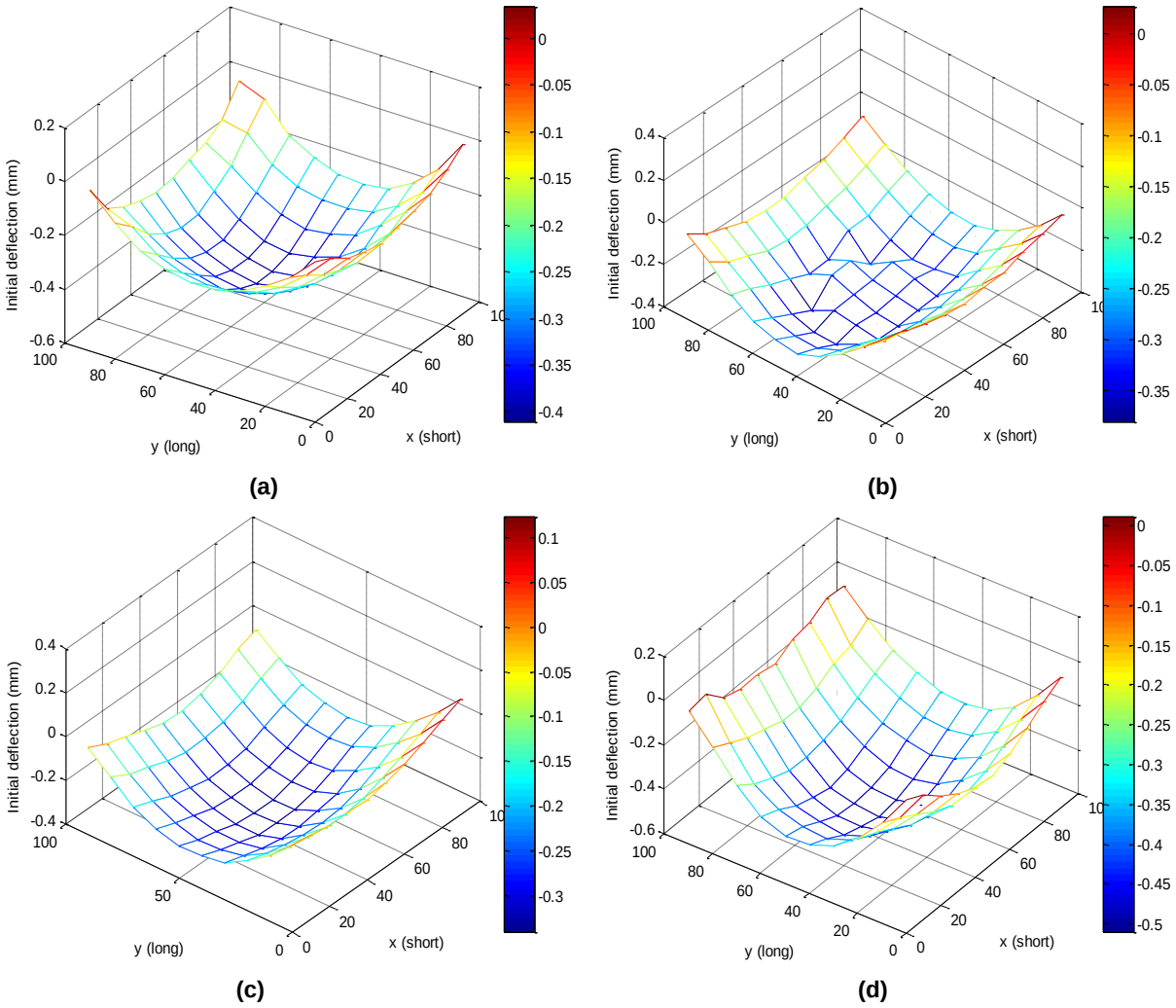

Figure A4.1. Initial deflections measured at discrete locations using Faro Arm: (a) corrosion at the corner; (b) corrosion in the middle; (c) random pitting; (d) corrosion at the unloaded edge.

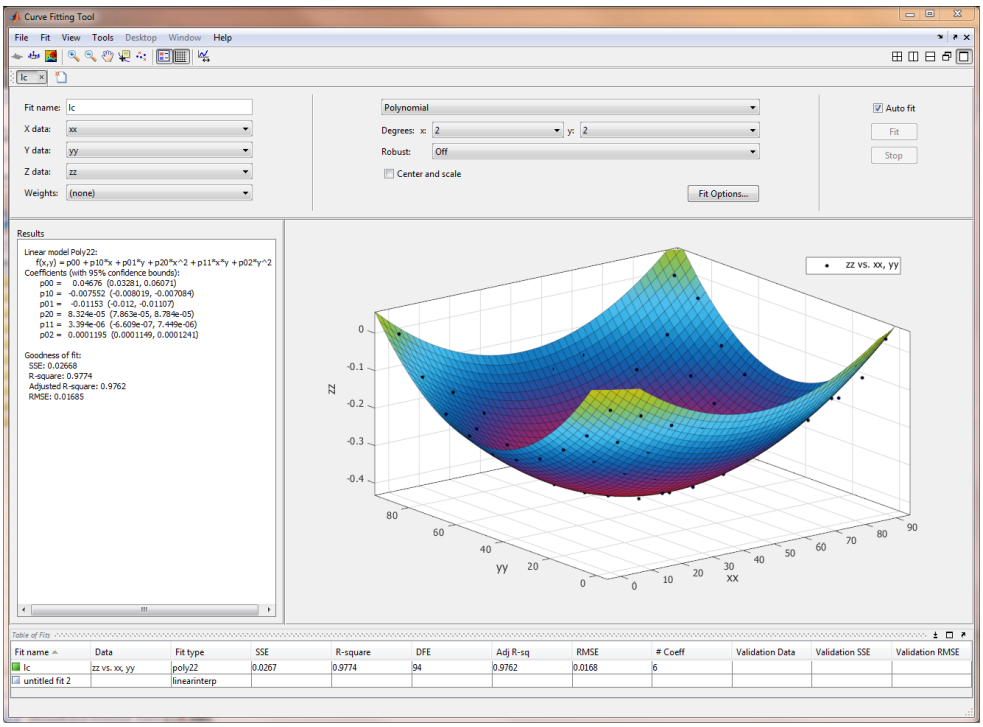
Curve Fitting Tool
File Fit View Tools Desktop Window Help
Fit name: lc
X data: xx
Y data: yy
Z data: zz
Weights: (none)
Polynomial
Degrees: x: 2 y: 2
Robust: Off
Center and scale
Fit Options...
Auto fit
Fit
Stop
Results
Linear model Poly22:
f(x,y) = p00 + p10*x + p01*y + p20*x^2 + p11*x*y + p02*y^2
Coefficients (with 95% confidence bounds):
p00 = 0.04676 (0.03281, 0.06071)
p10 = -0.007552 (-0.008019, -0.007084)
p01 = -0.01153 (-0.012, -0.01107)
p20 = 8.324e-05 (7.863e-05, 8.784e-05)
p11 = 3.394e-06 (-6.609e-07, 7.449e-06)
p02 = 0.0001195 (0.0001149, 0.0001241)
Goodness of fit:
SSE: 0.0268
R-square: 0.9774
Adjusted R-square: 0.9762
RMSE: 0.01685
zz vs. xx, yy
zz
xx
yy
Table of Fits
Fit name | Data | Fit type | SSE | R-square | DFE | Adj R-sq | RMSE | # Coeff | Validation Data | Validation SSE | Validation RMSE
lc | zz vs. xx, yy | poly22 | 0.0267 | 0.9774 | 94 | 0.9762 | 0.0168 | 6
untitled fit 2 | | linearinterp

(a)

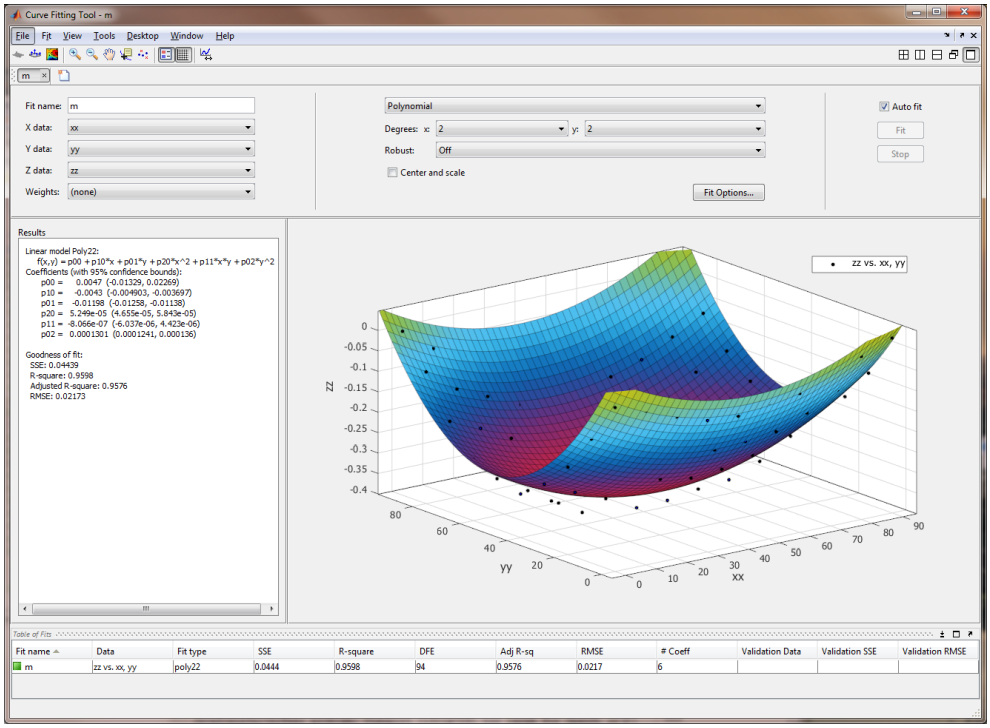
Curve Fitting Tool - m
File Fit View Tools Desktop Window Help
Fit name: m
X data: xx
Y data: yy
Z data: zz
Weights: (none)
Polynomial
Degrees: x: 2 y: 2
Robust: Off
Center and scale
Fit Options...
Auto fit
Fit
Stop
Results
Linear model Poly22:
f(x,y) = p00 + p10*x + p01*y + p20*x^2 + p11*x*y + p02*y^2
Coefficients (with 95% confidence bounds):
p00 = 0.0047 (-0.01329, 0.02269)
p10 = -0.0043 (-0.004903, -0.003697)
p01 = -0.01198 (-0.01258, -0.01138)
p20 = 5.249e-05 (4.655e-05, 5.843e-05)
p11 = -8.066e-07 (-6.037e-06, 4.423e-06)
p02 = 0.0001301 (0.0001241, 0.000136)
Goodness of fit:
SSE: 0.04439
R-square: 0.9598
Adjusted R-square: 0.9576
RMSE: 0.02173
zz vs. xx, yy
zz
xx
yy
Table of Fits
Fit name | Data | Fit type | SSE | R-square | DFE | Adj R-sq | RMSE | # Coeff | Validation Data | Validation SSE | Validation RMSE
m | zz vs. xx, yy | poly22 | 0.0444 | 0.9598 | 94 | 0.9576 | 0.0217 | 6

(b)

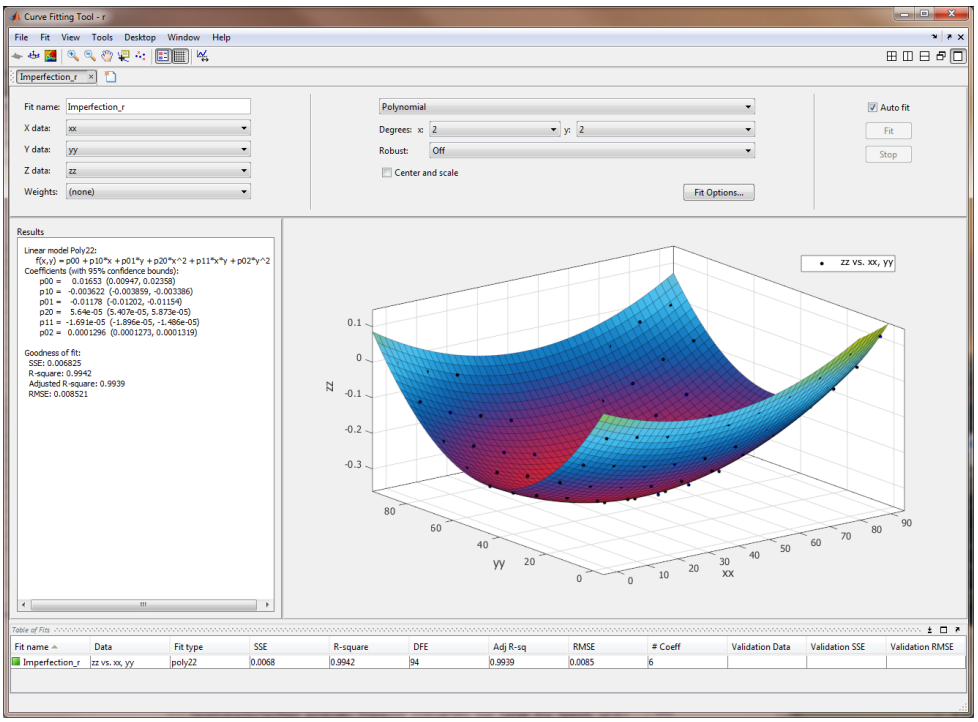

(c)

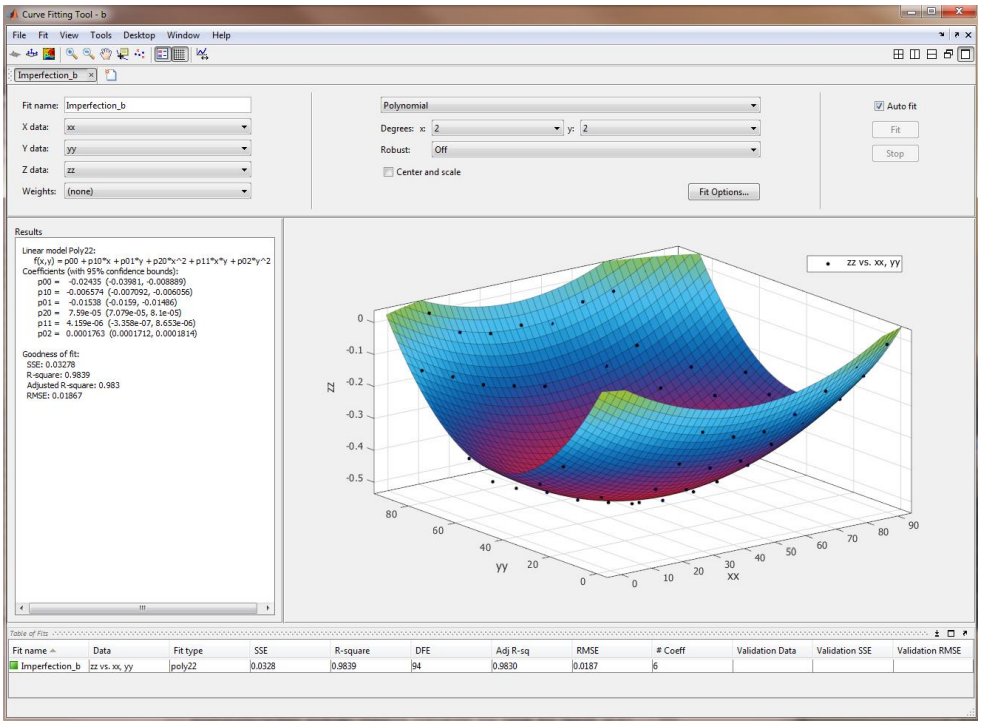

(d)

Figure A4.2. Initial deflections surface fitted using polynomial functions: (a) corrosion at the corner; (b) corrosion in the middle; (c) random pitting; (d) corrosion at the unloaded edge.

A5. Stiffened plate models

Comparison between SHELL181 and SOLID185 for stiffened plate models in Chapter 7 is shown in Figure A5.1. Remaining results for stiffened plate models with root opening in Chapter 7 are presented in Figure A5.2.

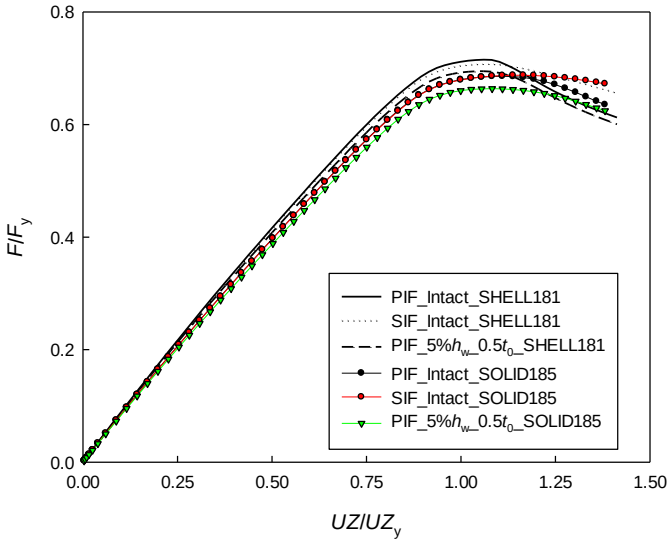

Figure A5.1: Comparison of nominal load shortening curves for shell and solid models with and without corrosion on the plate.

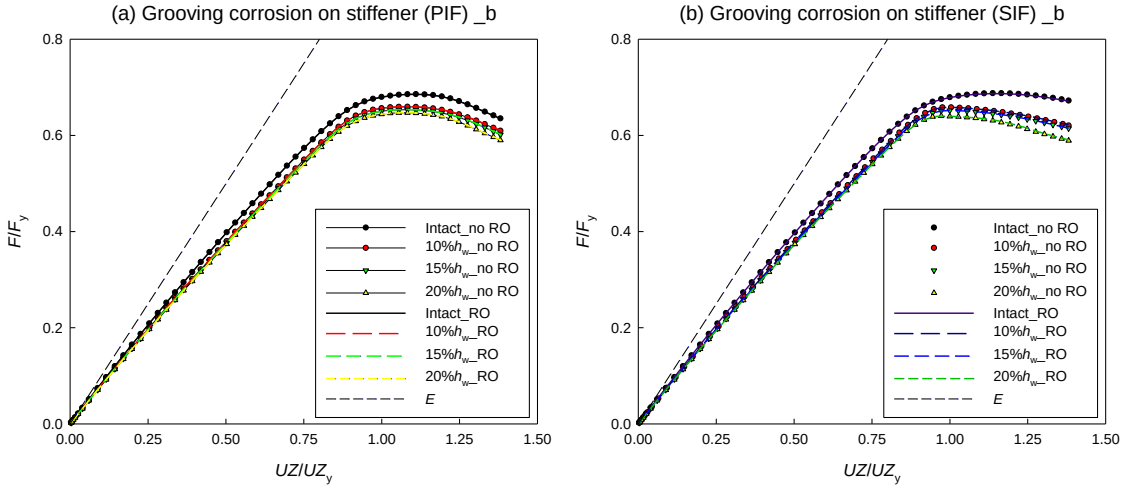

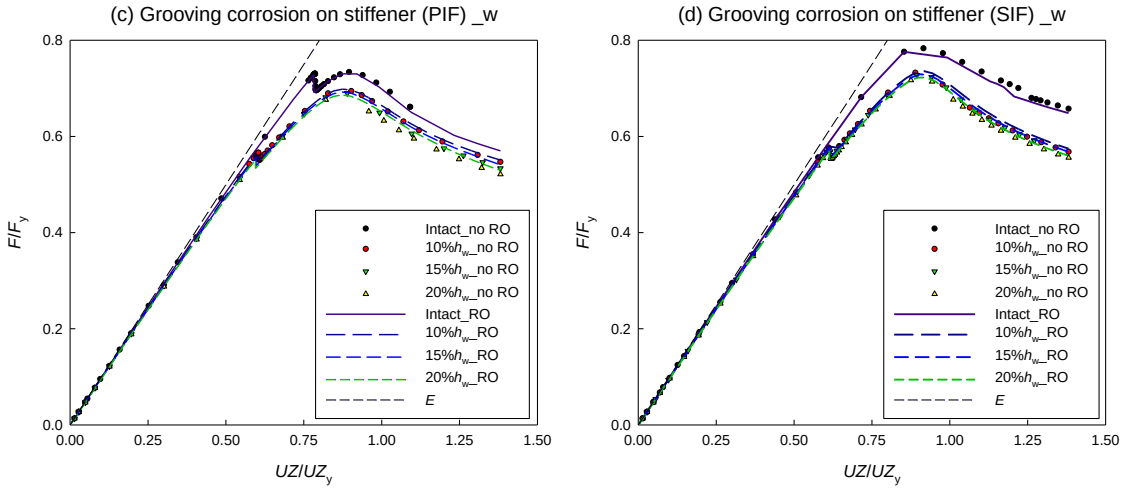

Figure A5.2: Comparison of nominal load shortening curves when corrosion on the stiffener: (b: buckling-mode initial deflection; w: weld-induced initial deflection; RO: root opening; *E*: Young's modulus of the material).

A6. Scanning Kelvin probe force microscopy (SKPFM) measurements

Four square specimens (25 mm × 25 mm × 6 mm) were fabricated from a multi-pass butt welded steel plate (Grade 070M20 for marine applications), as shown in Figure A6.1. MIG wire EN 440 was used for the welding (deposits C – 1.3% Mn weld metal with a copper coat finish and double deoxidised). The welding temperature was 1200℃ to 1300℃ at a speed of 100 mm min^{-1}. The material is widely used for welding low carbon, low alloy steel structures, ship grade steels (A, B, D and E) and equivalent mild steels. Moreover, it is frequently utilised especially for thin plates of ship structures, container buildings, bridges, railway constructions, pressure vessels, etc. Prior to the SKPFM tests, chemical surface cleaning was conducted according to the standard practice ASTM (G1-03) by dipping the sample surfaces into a 1000 mL pickling solution (500 mL 37% HCl, 3.5 g hexamethylenetetramine and deionised water) at room temperature for 10 minutes. No mechanical/chemical polishing was carried out due to its potential influence on the residual stresses and the surface state. Samples were stored in a desiccator before testing. The SKPFM was performed using atomic force microscope (AFM) (MAC Mode III, 5500 Scanning Probe Microscopy, Agilent Technologies, US). PicoView 1.12 and PicoImage Basics 6.0 (Agilent Technologies, US) software were used for data acquisition and image analysis, respectively. Conducting AFM probes, OMCL-AC240TS (from Olympus) with nominal spring constant ~ 2 N m^{-1} were used. Image sizes of 1 × 1 μm^2 were recorded with a resolution of 512 lines at scan rate 2 lines s^{-1}. Measurements were

done along the *y*-axis of the sample every 3 – 5 mm. Topography and surface potential measurements were performed simultaneously in amplitude modulation mode in an environmental chamber. The Volta potential difference between the sample surface and the AFM tip was calculated by averaging potential signal over the whole scan area. As all measurements were performed in air, the effect of oxygen contaminations cannot be excluded. More details on SKPFM technique can be found in Refs. [1,2]. Figure A6.2 presents the Volta potential difference across the butt weld and the plate surface (Figure A6.1) using SKPFM.

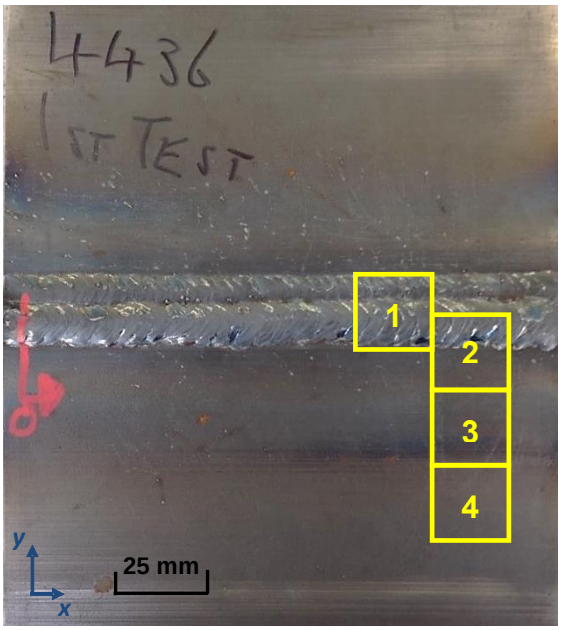

Figure A6.1: Butt welded ship grade steel plate: Samples 1 to 5 in yellow frames are for the SKPFM test (25 mm × 25 mm × 6 mm).

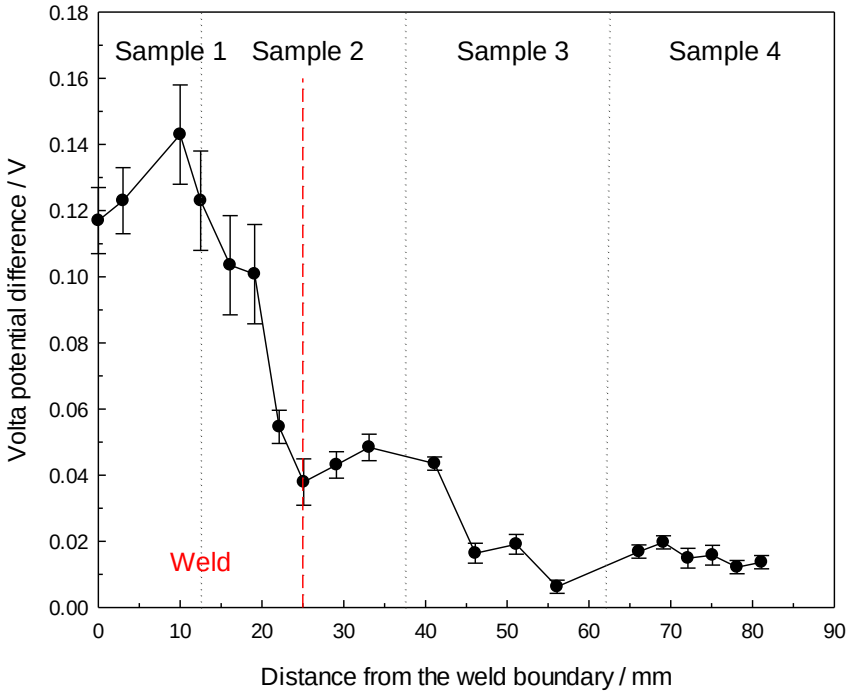

Figure A6.2: SKPFM measurements across a butt-welded steel plate (Samples 1 to 4).

References:

[1] R. Berger, H. Butt, M.B. Retschke, S.A.L. Weber, Electrical modes in scanning probe microscopy, Macromolecular Rapid Communications 30 (2009) 1167-1178.

[2] W. Melitz, J. Shen, A.C. Kummel, S. Lee, Kelvin probe force microscopy and its application, Surface Science Reports, 66 (2011) 1-27.